CZECH TECHNICAL UNIVERSITY IN PRAGUE
Faculty of Civil Engineering
Department of Steel and Timber Structures

TURBULENCE EFFECTS ON WIND-INDUCED FATIGUE OF SLENDER STEEL STRUCTURES

DOCTORAL THESIS

Arsenii Trush

Doctoral study programme: Civil Engineering

Branch of study: Building and Structural Engineering

Doctoral thesis tutor: prof. Ing. Jiří Studnička, DrSc.
doc. Ing. Stanislav Pospíšil, Ph.D.

Prague, 2019

CZECH TECHNICAL UNIVERSITY IN PRAGUE
Faculty of Civil Engineering
Thákurova 7, 166 29 Praha 6

DECLARATION

Ph.D. student’s name: Arsenii Trush

Title of the doctoral thesis: TURBULENCE EFFECTS ON WIND-INDUCED FATIGUE OF SLENDER STEEL STRUCTURES

I hereby declare that this doctoral thesis is my own work and effort written under the guidance of the tutor prof. Ing. Jiří Studnička, DrSc. and doc. Ing. Stanislav Pospíšil, Ph.D.
All sources and other materials used have been quoted in the list of references.

The doctoral thesis was written in connection with research on the project: No. 17-26353J and No. 19-04695S of the Czech Science Foundation (GAČR), CET sustainability project LO1219 (SaDeCET) of the Ministry of Education, Youth and Sport of the Czech Republic.

In Prague on 11.11.2019

signature

Contents:

Abstrakt 3
Abstract 4
1. Introduction... 5
2. Objectives of the doctoral thesis 6
3. State-of-the-art review 8
3.2 Cable types 8
3.3 Fatigue of structural cables... 9
The Miner-Palmgren hypothesis 9
The S-N curve...9
Cable fatigue features: fretting 10
3.4 Wind characteristics 12
Wind flow in Atmospheric Boundary Layer 12
Turbulence intensity...13
Integral length scale of turbulence 14
Taylor’s frozen turbulence hypothesis..15
Auto power spectra used in practice 16
The von Karman turbulence autospectrum model 16
Davenport turbulence autospectrum model 17
Eurocode turbulence autospectrum model 18
Solari turbulence autospectrum model..18
Fichtl–McVehil turbulence autospectrum model 18
Calculating of Integral length scale of turbulence in wind tunnel.........................19
3.5 Types of Wind Induced Vibrations 20
Vortex shedding basic physics..21
Strouhal number 22
Reynolds number...23
Scruton number 23
Effect of free stream turbulence...24
Surface roughness effects 25
3.6 Theoretical models of vortex shedding vibrations 28
Energy-balanced double oscillator mode by Krenk and Nielsen......................28
Eurocode models...30
Vortex-resonance model..30

Spectral model 32

4. First stage of experiments 33

4.1 Experimental setup for first stage of experiments 33

Wind Tunnel 33

Models 33

Turbulence generation in test section 38

4.2 Results 39

Turbulence characteristics 39

Strouhal number 41

Amplitude response 42

Probability density estimation of amplitudes 49

5. Second stage of experiments 52

5.2 Experimental setup for second stage of experiments 52

Wind tunnel 52

Models 53

Dynamic force balance stand 55

Signal denoising 59

Time shift correction 60

Turbulence generation in the wind tunnel 61

5.3 Results 63

Turbulence characteristics 63

Strouhal number 72

Amplitude response 73

Flow-to-structure energy transfer 88

Direct force measurement 93

5.4 Additional testing 95

6. Fatigue analysis based on the experimental data 98

7. Conclusions 102

8. References 105

9. List of publications by the dissertant related to the dissertation115

10. Appendix A: Figures 117

11. Appendix B: Tables 190

12. Appendix C: Matlab code for Comsol Multyphisics 215

Abstrakt

Ověření dynamického zatížení je nutné pro spolehlivý a ekonomický návrh stavebních konstrukcí. Zatížení větrem je často rozhodujícím účinkem pro štíhlé ocelové konstrukce a konstrukční prvky. Navzdory značnému množství nashromážděných poznatků v oboru stavební aerodynamiky však dosud chybí pochopení některých důležitých aspektů tohoto zatížení. Konkrétně je nutná simulace drsnosti v široké škále relativních drsností, zejména s ohledem na standardy používané v České republice. Výpočetní dynamika tekutin stále postrádá přesné simulace atmosférické turbulence a je pro většinu simulačních metod omezená velmi jednoduchou strukturální architekturu. Analytické metody jsou omezeny přísnými předpoklady o okrajových a geometrických podmínkách, často neodpovídajících realitě. Jsou však užitečné pro kvalitativní hodnocení modelů a pro fyzické porozumění danému problému. Testování v aerodynamickém tunelu proto zůstává stále mocným nástrojem pro získávání nových znalostí o chování toku tekutin a jeho vlivu na konstrukce, a slouží také jako ověřovací nástroj pro numerické simulace.

Předkládaná disertační práce je zaměřena především na experimentální výzkum. Zvláštní důraz je přitom kladen na vliv turbulence proudění, jakož i na účinky drsnosti povrchu a ledových akrecí nosných lan.

Výsledky výzkumu ukazují, že indukované víry vibrace lan jsou značně ovlivněné změnami v turbulenci toku a drsnosti povrchu lan. Zejména zvýšení intenzity turbulence přicházejícího proudu způsobuje snížení amplitudy indukované víry vibrace lan s ledovými sedimenty. Akrece ledu způsobuje změnu (zvýšení nebo snížení) amplitudy v závislosti na orientaci ledu pro každou studovanou úroveň intenzity turbulence toku. Drsnost povrchu vinutých lan snižuje rozsah rychlostí lock-in efektu („uzamknutí frekvencí“) ve srovnání s referenčním hladkým modelem, přičemž největším dopad ma zvýšení úhlu vinutí. Tento trend je patrný i v turbulentních tocích s vyšší intenzitou, rovněž vibrace začínají při menších kritických rychlostech, což ukazuje na zvýšení Strouhalova čísla. Hysterézní charakter amplitudové odezvy pro rostoucí a klesající rychlost je pozorovaný u všech modelů a pro všechny intenzity turbulencí. Nejvýraznější je pro případ modelu s vyššími hodnotami drsnosti povrchu a úhlu vinutí.

Uvedené výsledky poskytují projektantům štíhlých ocelových konstrukcí s lany některé důležité poznatky, protože turbulence proudění a drsnost povrchu lan prokazatelně a výrazně ovlivňují indukované víry vibrace lan, což zase může výrazně změnit dynamické vlastnosti a životnost konstrukcí s nosnými lany.

Abstract

Verification of dynamic loads is necessary for reliable and economical design. Wind loads frequently are critical for steel slender structures and structural elements. However, despite the important knowledge in the field, there is a lack of understanding of some important aspects. Computational fluid dynamics still lacks on precise simulations of atmospheric turbulence and it is for the most simulation methods restrained on very simple structural architecture. Analytical methods are limited by strict assumptions about boundary and geometrical conditions, often beyond reality. Nevertheless, they are useful in qualitative assessment of models and in physical understanding of the matter. Hence, wind-tunnel testing still remains a powerful tool for acquiring new knowledge about the fluid flow behavior and its effect on structures, as well as to serve as a validation tool for numerical simulations. Namely, the simulation of the roughness in wide range of relative roughnesses, is needed especially with respect to the codes and standards in the Czech Republic.

Present study focused on experimental research. A particular focus is on the influence of flow turbulence, as well as on the effects of surface roughness and ice accretion of structural cables.

VIV of structural cables proved to considerably modify due to changes in flow turbulence and surface roughness of structural cables. In particular, increasing the turbulence intensity of the incoming flow causes a reduction in the amplitude of VIV of ice-accreted structural cables. The ice accretion causes the peak amplitude to change (increase or decrease) depending on the ice orientation for each studied level of flow turbulence.

According to the results surface roughness of helical strand cables reduces the lock-in range comparing to reference smooth model whereby the greatest impact is an increase of lay angle. This trend remains in turbulent flows with higher intensities, also vibrations starts at lover critical velocities which indicates an increase of Strouhal number. The hysteresis character of amplitude response caused by the direction of velocity change observed for all of models and turbulence intensities. The most pronounced effect was for the case of model with higher values of surface roughness and lay angle.

The reported results provide some important findings for bridge designers, as flow turbulence and cable surface roughness clearly prove to considerably influence VIV of structural cables, which in turn may considerably alter the dynamic characteristics and lifetime of cable-supported bridges.

1. Introduction

Cable stayed and suspended structures have become very popular since the second half of the twentieth century due to their high aesthetics and economy. The rigidity and load-bearing capacity of these structures is provided by tension members. Structural cables are most often used as tension members for high-rise and long-span structures. Structural cables are made of high strength steel (about 1600 MPa compared to 250-750 for the construction steel). Thus, it is more susceptible to brittle failure occurring with the fatigue load [1].

Wind induced vibrations along with traffic loads are the main factors causing fatigue damages. Structural analysis related to the wind impact deals with the problems of static wind loading and dynamic excitation of structures; tall building, bridges, guyed masts, and towers. The wind causes naturally the static and/or dynamic effects on whole structure or on its parts, called substructures. The latter are nonetheless of lower importance. Vibration of essential bearing or supporting element can influence the response of the superstructure (and vice versa) in the form, e.g., of parametric vibration [2], damage, or the consequent destructive vibration of the superstructure itself. Supporting cables are such elements for the cable-supported bridges or guyed masts. They have high flexibility, low damping and therefore often experience oscillations with large amplitudes.

During inspection of suspension and cable stayed bridges after observed strong vibrations as well as regular monitoring inspections numerous cable wires defects of different nature (stress corrosion cracking, pitting, corrosion fatigue, etc.) were detected. Cracked wires could represent a significant percentage of the total number of wires in the cable cross-section and significantly reduce strength. All types of structural cables strand are subjected to fatigue damage in a greater or lesser extent [3]: the wire fractures in locked coil cables were investigated in [4], fractured wires have been observed in numerous bridges, e.g. [5], [6], [7].

One of the particular cases of the fatigue loading is due to wind induced vibrations, especially due to vortices which sheds at the structure and imposes the pressures variation on the surfaces as well as the fluctuation in the wake. This vibration may have destructive effect on the structural elements and consequently on the whole structure. This phenomenon is called Vortex Induced Vibrations (VIV) and it is characteristic for wind speeds with a high probability of occurrence. Therefore, it has a high risk of fatigue damage.

Verification of dynamic loads and loadings cycle counting are necessary for both the reliable and the economical design. Wind loads are often very critical for steel slender structures and structural elements. However, despite the important knowledge in the field, there is a lack of understanding of some important aspects. Namely, the simulation of the unevenness in a wide range of relative roughnesses, especially with respect to the codes and standards in the Czech Republic is needed.

2. Objectives of the doctoral thesis

This work is aimed on one of the challenging problem, namely on the aerodynamics of the cables with geometrically modified (“rough”) surface. It combines the basic research approach with very natural relation to the applications in the civil engineering.

Thus the main objectives of present study are:

- Investigation of simultaneous effect of the free stream turbulence and various parameters of surface roughness of different nature on VIV response of cylinder-like structures.
- Measurement of the rough cylinders wake characteristics with respect to Strouhal number identification and in the specified range of the Reynolds number and in the low, moderate, and highly turbulent flow
- Improvement of testing facilities and developing experimental methodology for laboratory simulation and investigation of air flow conditions around cables with climatic and technological surface roughness with respect to aeroelastic phenomena
- Fatigue risk assessment based on wind tunnel simulations results according to existing building code procedure.

Tools for the analysis of the influence of wind and other climatic parameters on the structure are field experiments, wind-tunnel simulations, as well as mathematical tools like computational fluid dynamics and in some cases also analytical methods. While the field experiments are very accurate provided the long-term observation are carried out, their drawback is a weak controllability and repeatability. Computational fluid dynamics still lacks on precise simulations of atmospheric turbulence and it is for the most simulation methods limited to the very simple structural architecture. Analytical methods are limited by the assumptions about boundary and geometrical conditions, often beyond the reality. Nevertheless, they are useful in qualitative assessment of the models and in physical understanding of the phenomenon.

Therefore, the wind-tunnel testing still remains a very powerful tool for acquiring new knowledge about the fluid flow behavior and its effect on structures, and for validation of numerical simulations of the wind action on structures. This fact is permanently emphasized and documented in many journals and by wind engineering research centers, e.g., [8].

The main focus will be on experimental investigation of aerodynamics and aeroelastic (self-excited vibration) of cylinders with rough surface. The roughness will be categorized into the one caused by the climatic conditions and by the technological processes.

The generation of the conditions for the synergetic wind loading of sectional cylinders using the equipment of the wind tunnel, i.e., turbulence generators, etc.

The constant temperature anemometry technique will be used to measure flow velocity and turbulence characteristics.

The special force balance mechanism allowing elastic fastening of models and fine tuning of frequency and stiffness of dynamic system will be used to study flow-structure interaction.

3. State-of-the-art review

3.2 Cable types

The most common cable structures for guyed masts, roofs, cable stayed and suspension bridges are (see Figure 3.1):

- parallel wire strand: wires are laid parallel and bonded together at the ends with collars/ wrapping, this type of cable has a high strength at low weight, relative cheapness of production (pack can be collected from the individual wires directly on the construction site). The disadvantage is a weaker corrosion resistance. For its increase can be used protective PVC coating. In this case, the cable has a circular cross section with low relative roughness.

- helical wire strand - wire stacked with a certain pitch in the helix. This type characterized by higher corrosion resistance and low bending stiffness. The outer layer of wires is a regular roughness element with $k = 0.5 \cdot D_{wire}$

- locked-coil cable - is a kind of combination of the two previous types, where parallel wire coil is covered with outer helical layer of z-shaped wires. This design reduces the surface roughness and area of the cable and prevents penetration of atmospheric moisture into the inner layers. The problem is the cost and availability of stress concentrators at z-shaped wires reducing fatigue endurance limit.

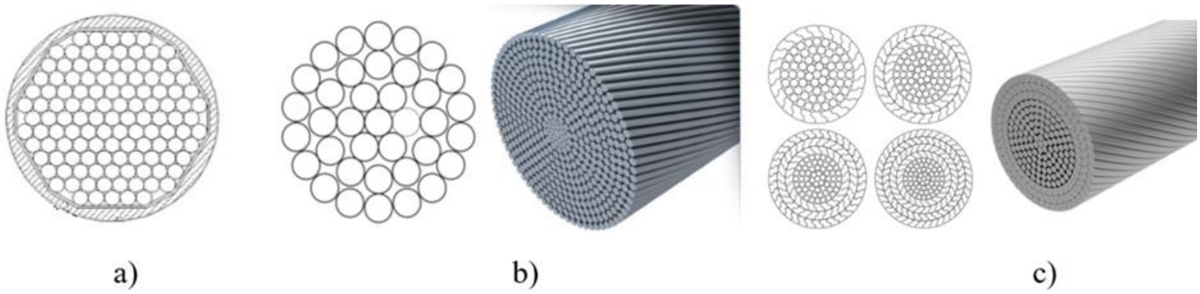

Figure 3.1 Most common cable types: a) parallel wire strand; b) helical wire strand; c) locked-coil cable

3.3 Fatigue of structural cables

The Miner-Palmgren hypothesis

Fatigue is a process of progressive localized structural degradation induced by fluctuating stresses and deformations [9]. One has to distinguish two stages in fatigue process: the fatigue crack initiation and the fatigue crack propagation. The fatigue crack initiation period consists of the nucleation, collecting and growth of microdefects. The fatigue crack propagation period is the crack growth at the macroscopic scale including the crack stable and unstable propagation.

The problem how to link two different stages (or scales) is still open. It is a scale transition problem solved by developing the multiscaling theories [3]. These two stages are applicable to various methods.

Real structures are anyway subjected to variable loads which have to be transformed into equivalent constant cyclic loads. Miner-Palmgren cumulative damage theory is an empirical based approach used for the analysis and prediction of the fatigue crack initiation period. This approach allows to calculate the total fatigue damage related to a stress time history, once the stress cycle histogram has been determined using a cycle-counting method. Such a diagram represents the number of equivalent stress cycles n_i for each amplitude i [9]. The Miner-Palmgren hypothesis and its various improved versions are the most commonly used, see [10].

The S-N curve

The Miner-Palmgren hypothesis for accumulation of fatigue damage from stress time histories with varying amplitudes defines fracture to take place if:

$$D = \sum_i \frac{n_i}{N_i} = 1 \tag{3.1}$$

where n_i is number of cycles with stress range D_i and N_i is the number of cycles to failure for this specific stress range D_i.

The S-N curve is used to define the relationship between number of cycles to failure and the stress range:

$$log\,N = log\,\bar{a} - m \cdot log\ {}_{\Delta}\sigma \tag{3.2}$$

where m defines the slope of the S-N curve, and $log\,\bar{a}$ is the intersection between the log N-axis and the S-N curve. For each stress range D_i in the sampled time interval, the number of cycles to failure for that stress range can be expressed by:

$$N_i = 10^{(log\,\bar{a} - m\,log\,\Delta\sigma_i)} = a \cdot \sigma_i^{-m} \tag{3.3}$$

Damage from one cycle with stress range D_i is:

$$D_i = \frac{1}{N_i} = \frac{\Delta\sigma}{\bar{a}} \tag{3.4}$$

Thus, the total fatigue damage can be calculated by summation of the contributions from all cycles, leading to:

$$D_{tot} = \sum_{i=1}^{N_{tot}} D_i = \sum_{i=1}^{N_{tot}} \frac{1}{N_i} = \sum_{i=1}^{N_{tot}} \frac{\Delta\sigma}{\bar{a}} \tag{3.5}$$

where N_{tot} is the total number of stress ranges in the actual time history.

Cable fatigue features: fretting

The fatigue behavior of structures depends on the interaction between loading sequence, material characteristics and component geometry. Cables are often considered to behave as elements with no bending stiffness, however at connection sites bending moments arise if the cable profile varies. Similarly, in suspended structures, cables are not free to rotate at the end of the deviation saddle, thus originating bending moments that can eventually lead to the fatigue damages and ruptures.

Fretting fatigue cracks are caused by the friction stresses originated by the sliding contact between two tight surfaces (wires) see Figure 3.2, Figure 3.3 [1]. This phenomenon significantly affects endurance limit of structure. In this case fatigue crack originated from the fretting area under alternating load will result in components that appear in the fretting fatigue phenomenon when the alternating stress is lower than the material fatigue limit [11]. During the usage process, the steel wire rope is affected by the axial stress and bending stress, which will cause fretting wear to occur between wires. Fretting accelerates the occurrence of crack in initiation and propagation on the surface of the fretting component.

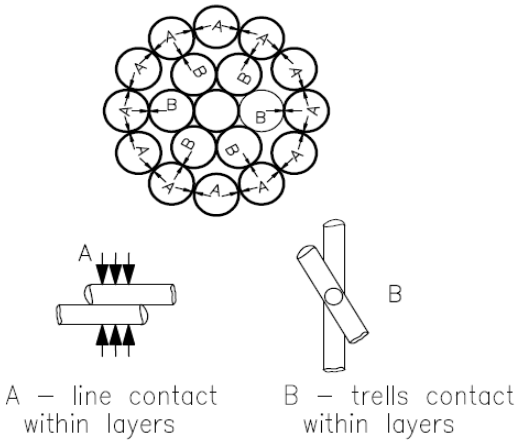

Figure 3.2 Contact points in spiral strand [1].

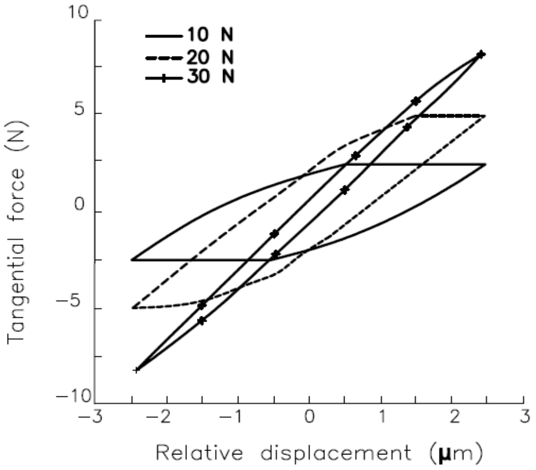

Figure 3.3 Hysteresis loops for fretting condition of relative displacement under different contacts loads [1].

The European standard EN 1993-1-11 [12] provides an $S-N$ curves that are based on this failure mode, see Figure 3.4, related to the 1st or 2nd visible wire fracture.

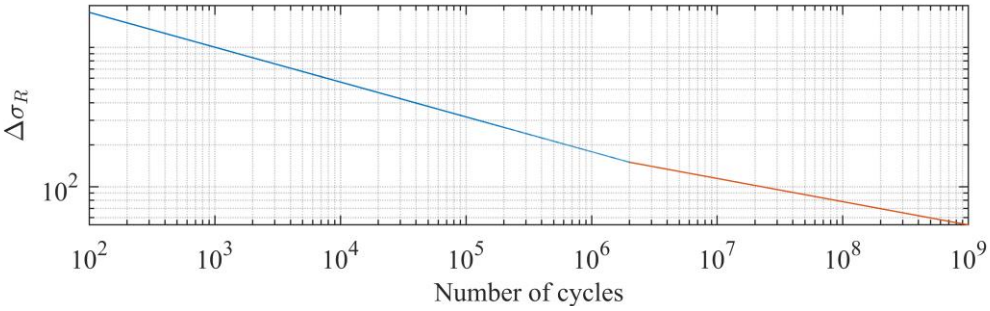

Figure 3.4 Wohler curve for helical strand cables

3.4 Wind characteristics

Wind flow in Atmospheric Boundary Layer

The non-uniform heating of the Earth's surface by the sun radiation lead to thermal stratification of the atmosphere both in the vertical and horizontal direction and, as a result, to the air pressure gradient. Among the causative factors there are: inclination of the earth's axis, daily and annual rotation, the relief features and albedo of the Earth's surface as well as the local atmospheric phenomena preventing the penetration of solar radiation to the Earth's surface, known as clouds. As a result of the interaction of the pressure force gradient, the Coriolis and centripetal forces and the viscous friction (both internal and between wind flow and ground) the spatial air mass transfer phenomenon called the wind occurs [13].

The wind flow near to Earth surface is strongly affected by its topography. The inhomogeneity of the terrain, or in other words Earth surface roughness, generates the frictional force that reduced the flow velocity and promotes mixing of the air masses. As a result, at lower part of the troposphere occurs so-called Atmospheric Boundary Layer (ABL). The upper boundary of ABL is known as a gradient height. The thickness of the ABL is dependent on the topography, thermal stratification and the wind velocity. It can reach up to 1000 meters. Thus, the specificity of the flow in ABL is the leading factor in the wind design for engineering structures.

The following major characteristics of the wind in the ABL can be distinguished according to Simiu and Scanlan [14]:

- The variation of the mean wind speed with height (wind gradient).
- The variation of turbulence intensities and integral length scales with height.
- The spectra and cross-spectra of turbulence in the along-wind, cross-wind, and vertical directions.

The airflow within the atmospheric boundary layer is always turbulent. The absolute velocity (*u, v, w*) is a sum of the mean velocities *u, v, w* and the fluctuating components u', v', w':

x – longitudinal direction $u = \bar{u} + u'$;

y – lateral direction $v = \bar{v} + v'$;

z – vertical direction $w = \bar{w} + w'$;

The relevant characteristic parameters of atmospheric turbulence important in the wind engineering are the turbulence intensity, integral length scale of the turbulence and power spectral density of the velocity fluctuations.

Wind velocity fluctuations caused by turbulence have a short time period, while the average wind speeds are important for assessing of long-term effects. The probability occurrence of the average wind speeds could be described by the Weibull distribution [13], see Figure 3.5

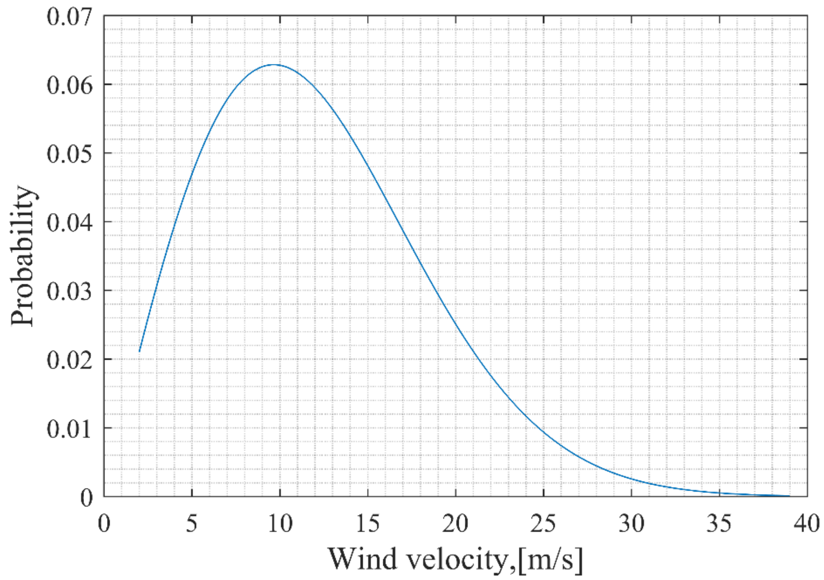

Figure 3.5 Weibull distribution of wind velocity typical for Czech Republic

Turbulence intensity

Turbulence intensity is the one of the main parameters used to describe atmospheric wind speed fluctuations. For the longitudinal direction, the turbulence intensity is given by:

$$I_u(z) = \frac{\sqrt{{u'}^2(z)}}{\bar{u}} \tag{3.6}$$

where:$\bar{u}$ – is the mean velocity value in the longitudinal direction.

$u'(z)$ – is the fluctuation of the mean velocity at the given height;

The same expressions can be written for the lateral and vertical directions:

$$I_v(z) = \frac{\sqrt{{v'}^2(z)}}{\bar{v}} \tag{3.7}$$

$$I_w(z) = \frac{\sqrt{{w'}^2(z)}}{\bar{w}} \tag{3.8}$$

According to Counihan [15] the relations I_v/I_u and I_w/I_u can be written as:

$$\frac{I_v}{I_u} = 0.75\ and\ \frac{I_w}{I_u} = 0.50 \tag{3.9}$$

Integral length scale of turbulence

Apart from intensity of turbulence, another important parameter that characterizes turbulence is it so-called (integral) length scale. Turbulent velocity fluctuations may be considered as result from the passage of eddies sequences. Each eddy is characterized by a periodic motion of circular frequency $\omega = 2\pi f$, where f is the frequency, or equivalently by a wave number $k = 2\pi/\lambda$, where λ is wave length.

The integral length scale represents the average size of vortices or i.e. vortices containing the highest energy in given direction: $L_{u,x}, L_{u,y}$ and $L_{u,z}$ represent the average eddy size in the longitudinal, lateral and vertical direction caused by the wind velocity fluctuations in the longitudinal direction.

Lower frequencies correspond to larger-scale motions, while higher frequencies correspond to small-scale vortexes. Structure of specific size eddies formed by the air flow over a rough surface with time dissipated in smaller eddies. This size dissipation transfers the kinetic energy from the larger eddies to smaller. This process is called the cascade energy transport. Eddies containing the most energy are not the largest.

The area of highest frequencies and the smallest eddies is called the dissipation zone. In that area the transformation of the kinetic energy into heat is dominant. The dissipation zone is usually not interesting for wind engineering. The maximum energy is contained in the middle of the spectrum inertial subrange where the dominant forces are the inertial forces. In that area the law of Kolmogorov is valid:

$$S_u(f) \approx k_w^{-\frac{5}{3}} \tag{3.10}$$

where:

k_w – is the wave number of the eddy.

A scheme of the velocity power spectrum is given in Figure 3.6.

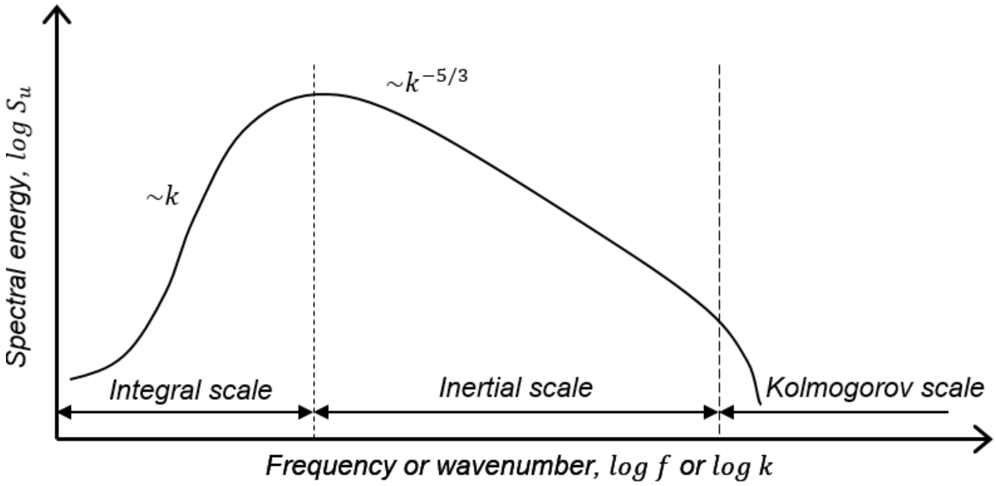

Figure 3.6 . Schematic representation of the energy power spectrum of velocity fluctuations [16]

The distribution of turbulence fluctuation in time as a zero-mean random process is described by so called the spectral density function, or in other words – power spectrum:

$$S_{u,x}(x_1, x_2, f) = \int_{-\infty}^{+\infty} \lim_{t_0 \to \infty} \frac{1}{2t_0} \int_{-t_0}^{t_0} u(x_1, t) u(x_2, t + \Delta t)\, e^{-i2\pi f \Delta t}\, dt\, d\Delta t \tag{3.11}$$

Where:
$u(x)$ – wind velocity in point x,

indices 1 and 2 denote two different positions in space,

Δx – distance between points x_1 and x_2,

Δt – time shift.

The contribution to the mean velocity variance (or square of the standard deviation) in the range of frequencies from f to $f + df$, is given by $Su(f) \cdot df$, where $Su(f)$ is the spectral density function for $u(t)$. Then integrating over all frequencies:

$$\sigma_u^2 = \int_0^{\infty} S_u(f) df \tag{3.12}$$

Where:

σ_u – is standard deviation of the longitudal wind turbulence component u;

In the equation (3.12) integral over time is a corresponding spatial correlation function for velocity fluctuations:

$$R_{u,x}(\Delta x) = \int_{-t_0}^{t_0} u(x_1, t) u(x_2, t + \Delta t)\, e^{-i2\pi f \Delta t}\, dt\, d\Delta t \qquad \textit{(3.13)}$$

According to Sockel [17], $L_{u,x}$ dependency of integral length scale and correlation distance between the fluctuations is given by:

$$L_{u,x} = \int_0^{\infty} R_{u,x}(x + \Delta x) d\Delta x \tag{3.14}$$

$$R_{u,x}(\Delta x) = \frac{u'_1(t) \cdot u'_2(t)}{\sqrt{u'^2_1} \cdot \sqrt{u'^2_2}} \tag{3.15}$$

where the indices 1 and 2 denote two different positions in space.

Taylor's frozen turbulence hypothesis

One of the most important assumptions on which many measurements of developed turbulence are based is a so-called Taylor's frozen turbulence hypothesis [18] according to which in a single-phase flow turbulent vortices are moved by the mean velocity of the main flow without changing.

Under the assumption of Taylor's frozen turbulence hypothesis, the autocorrelation function is used similar to Eq. (2.16) that can be obtained from time history at one spatial measurement only:

$$R_{u,x}(\Delta x) = \frac{u_1'(t) \cdot u_1'(t - \Delta t)}{u_1'^2} = R_{u,x}(\Delta t) \tag{3.16}$$

The integral length scale could be calculated accordingly:

$$L_{u,x} = u \int_0^\infty R_{u,x}(t) d\Delta t \tag{3.17}$$

Where the time shift Δt is:

$$\Delta t = \frac{\Delta x}{u} \tag{3.18}$$

This hypothesis has been confirmed by many experimental studies performed in a single-phase flow behind a turbulence generation grids and with some corrections in developed natural turbulent flows, [19]. Moreover, even for laboratory studies in the absence of 3D Particle Image Velocimetry (PIV) or LIDAR instrument, the application of this hypothesis for determination of the integral length scale of turbulence has practically no analogues [20].

Auto power spectra used in practice

In the engineering practice used auto spectra are widely used to obtain integral length scale values and for dynamic analysis of structures under wind loads in frequency domain. Most often they are based on (semi-)empirical data. The auto power spectrum and the auto-correlation function are interrelated by Fourier transform pairs (the Wiener-Khintchine relations).

The von Karman turbulence autospectrum model

One of the first presented method was obtained by von Karman [21] as statistical interpretation of experimental data from wind tunnel:

$$\frac{f \cdot S_u(f)}{u_*^2} = \frac{4f\beta_u L_u/z}{(1 + 70.78 \cdot f^2 {L_u}^2/z^2)^{5/6}} \tag{3.19}$$

Where:

f *– is frequency*

u_*^2– friction velocity

$\beta_u = \sigma_u^2/u_*^2$ – turbulence intensity coefficient

z – height;

After reduction of intensity coefficient and friction velocity the autospectrum could be presented in dimensionless form as:

$$\frac{f \cdot S_u(f)}{\sigma_u^2} = \frac{4 f_L}{(1 + 70.78 \cdot f_L^2)^{5/6}} \tag{3.20}$$

Where:

f_L – is a dimensionless coordinate

$$f_L = \frac{f \cdot L_{u,x}(z)}{u(z)} \tag{3.21}$$

When frequency tends to zero the integral length scale after differentiating the equation (3.21) can obtained from the peak frequency (frequency with maximal value of spectral density /energy) f_{max}:

$$L_{u,x} = \frac{\sqrt{3/2} \cdot f_u}{\sqrt{70.78}} = \frac{0.146 \cdot u(z)}{fmax} \tag{3.22}$$

Where:

f_{max} – is frequency with the maximum $f \cdot Su(f)$;

$L_{u,x}$ – integral length scale.

This autospectrum is based on experimental data obtained in wind tunnel for grid generated turbulence. The Von Karman model has good coincidence with nearly isotropic artificial generated turbulence as well as ABL turbulence in energy containing and dissipation ranges. Until now, it is one of the most widely used power spectra models in laboratory studies, although for practice its application is limited, because in comparison with other models the von Karman turbulence model gives a higher estimation of the energies that carry large vortices. It has application in the safety design of engineering structures with low damping and low structure- to-flow mass relation and in some regulatory documents, such as Australian Code [22], Japanese Wind Code [23].

Davenport turbulence autospectrum model

The Davenport autospectrum is used in National Building Code of Canada [24]:

$$\frac{f \cdot S_u(f,z)}{\sigma_u^2(z)} = \frac{2}{3} \frac{{f_L}^2(f,z)}{(1 + {f_L}^2(f,z))^{4/3}} \tag{3.23}$$

Where:

f_L – is nondimensional frequency:

$$f_L = \frac{f \cdot L_{u,x}(z)}{u(z)} \tag{3.24}$$

$u(z)$ – is 10-minute average wind speed at height 10 m from ground,

L=1200 m.

Eurocode turbulence autospectrum model

In the Eurocode [25] is used model based on dimensionless form of Kaimal autospectrum:

$$\frac{f \cdot S_u(f,z)}{\sigma_u^2(z)} = \frac{6.8 f_L(f,z)}{(1 + 10.2 \cdot f_L \ (f,z))^{5/3}} \tag{3.25}$$

And the integral length scale determined according to:

$$L_{u,x}(z) = L_t \left(\frac{z}{z_t}\right)^{\alpha}, for\ z \geq z_{min} \tag{3.26}$$

$$\alpha = 0.67 + 0.05 \ln(z_0) \tag{3.27}$$

$$L_{u,x}(z) = L_{u,x}(z_{min}) \quad , for\ z < z_{min} \tag{3.28}$$

Where:

$L_t = \ 300\ m$– is reference integral length scale,

z_0 – roughness parameter,

$z_t = 200\ m$– is reference height,

z_{min} – minimal height from table 4.1 [25].

Solari turbulence autospectrum model

The model proposed by Solari spectrum is applied in American Wind Code [26]. This model is similar to used in the Eurocode model and expressed as:

$$\frac{f \cdot S_u(f)}{\sigma_u^2} = \frac{6.868 f_L}{(1 + 10.3022 \cdot f_L)^{5/3}} \tag{3.29}$$

Fichtl–McVehil turbulence autospectrum model

The spectral model was developed by Fichtl and McVehil [27] is suitable for the turbulence in natural ABL, in the simulated boundary layer in wind tunnels with floor situated roughness elements and barriers as well as for nearly isotropic turbulence generated by mesh arrays of different geometry:

$$\frac{f \cdot S_u(f)}{u_*^2} = \frac{A_j f}{(1 + B_j \cdot f^{\gamma_j})^{5/3\gamma_j}} \tag{3.30}$$

In most cases abovementioned autospectra have the same curve character and differs mostly by constants. The fitting parameters A_j, B_j, γ_j should be defined for the specific flow turbulence conditions. In case of $A_j = 4\beta_j L_j / z$ is taken similar to von Karman model and after reduction autospectrum becomes:

$$\frac{f \cdot S_u(f)}{\sigma_u^2} = \frac{4 f_L}{(1 + B_j \cdot f^{\gamma_j})^{5/3\gamma_j}} \tag{3.31}$$

Calculating of Integral length scale of turbulence in wind tunnel

Thus, the integral length scale can be determined in various ways, based on physically different interpretations:

- Spectral techniques define integral length scale as vortex size corresponding to the maximum spectral energy. Peak frequency corresponding to max. energy obtained from fitting of empirical or semi-empirical turbulence models to measured turbulence spectrum.

- Auto-(cross-) correlation zero crossing method refers to correlated turbulence structures: in this case integral time scale is obtained when correlation coefficients, see Eq. (3.16), drop to zero. Next according to Taylor's hypothesis time scale is recalculated to integral length scale.

- Exponential method: It is similar to zero crossing method, however in this case the period of time when correlation dropped to a value 1/e is used as integral time scale. It helps to avoid problems in integral length determining scale when correlation function does not cross zero due to random fluctuation component [28].

When indicating the results of the measured values of turbulence integral time or length scales, it is also necessary to indicate the method according to which they were calculated.

3.5 Types of Wind Induced Vibrations

Wind aerodynamic forces can be divided into the following groups: the forces originated directly by the impact of the wind on the cable (drag forces, buffeting) and so called aeroelastic phenomena- the interaction between the cable and the air flow (vortex shedding, galloping, rain-wind induced vibrations, etc.), that pose a particular risk because of the large number of loading cycles.

The oscillations of cylinders are in the most cases induced by the wind which forms the regions of the disturbed flow around a body. Usually, four regions are distinguished:

- region of the retarded flow in front of the body,
- two boundary layers regions attached to the cylinder,
- regions above and below the cylinder with the accelerated flow,
- the wake with the separated flow, e.g., [29].

The flow conditions in each of the regions affect the vibration, i.e., fluctuating in-plane pressures called buffeting, or by vortices, shed at the cable surface and imposing the out-of-plane pressures and the oscillating wake flow, see, e.g., [30]. The vibration can affect the stability of supported structure; it may also cause the high stresses in the cables (or the individual strands of a cable) and high internal forces in structural members. Very important is the fatigue damage [31] caused by the cyclic loads, leading to normal stress in the cables or to the fretting friction damage. This is a disadvantage of use of the of steel cables with high tensile strength, because it is accompanied with a reduction in ductility and an increase in susceptibility of cable wires to brittle failure due to fatigue [1], [32]. During inspection of bridge suspension cables defects of different nature are observed, e.g., cracking, pitting, fretting, fatigue, etc., see [33], [34].

- Vortex excited vibration is a well described phenomenon [8], [29]. However much knowledge still rely upon the empirical realm and experimental works [[35], [36] 22. [37], [38], [39]. The vortex-induced vibration is a result of interaction between fluid and structure. It is due to alternating vortices shed at the cylinder surface which produce the periodic forcing. If the damping and structure-air mass relations, expressed by the non-dimensional parameter called Scruton number (Sc) is low the structural motion influences the flow field. The analysis of the cylinder response requires the knowledge of the vortex shedding frequency which is commonly expressed as non-dimensional Strouhal number. This expression helps to transfer the results among different experiments and studies on vibrating bluff cross-section with different geometries and fluid properties. The Strouhal number is necessary for determination of the critical wind velocity at which the resultant vibration of the cylinder is at or nearly to resonant one. The value of Strouhal number (St) depends on the shape (geometry) of the cylinder, surface roughness of the cylinder, turbulence intensity, and on the Reynolds number (Re) determining the flow regimes for structures with circular cross-section or the non-circular cylinders.

- Wind-rain induced vibrations occur with the simultaneous exposure to rain and wind due to a pulsating load from water rivulets flowing down the cable surface. Vibrations can reach significant amplitudes [40].

- Galloping is another type of aeroelastic vibration phenomena occurring on cables with even slight deviation from the circular shape [41] [42] [43], [44]. It is a motion induced vibration and develops as the consequence of an asymmetric, e.g., climatic roughness (ice accretion), on the cable surface that yields asymmetric airflow characteristics around the cable and thus an oscillation of the pressures on the cable surface. The prediction of galloping instability is commonly based on a quasi-steady approach, [45], where instantaneous wind forces are derived from static aerodynamic force coefficients obtained usually in wind-tunnel experiments. The work [39] compares background hypotheses of different galloping models and respective results focusing on ice-accreted bridge cables. It indicates the necessity of establishing a benchmark study to allow for further elucidation of this issue. In [46], the authors report a good agreement between cable instabilities determined using the quasi-steady theory and dynamic tests, while some discrepancies in results indicate certain limitations of this theory. The ice-accreted bridge cable is particularly sensitive to changes in wind direction, as even small changes in wind incidence angle are sufficient to considerably alter dynamic behavior of the bridge cable. Emphasis needs to be placed on the shape of ice as well, as it also may cause modifications in aerodynamic behavior of cable. Previously, effects of ice accretion were predominantly studied with respect to aerodynamics of transmission lines [47], [48] and wind turbines, [49]. More work is however still required in bridge engineering and guy-supported structures, [50].

Vortex shedding basic physics

Vortex-induced vibrations occur when vortices are shed alternately from opposite sides of an object. In result of alternately sheds of vortices from opposite sides of bluff body and related to this changes of high and low pressure zones a harmonically varying lift force with the same frequency as the frequency of the vortex shedding acts on object [51].

The frequency f_{St} of the lateral load caused by vortex shedding is:

$$f_{St} = \frac{St \cdot U_{mean}}{b} \tag{3.32}$$

Where:

St – is the Strouhal number,

U_{mean} – is the mean wind velocity,

b – is the cross-wind dimension (diameter) of the structure considered.

In case of coincidence of the natural frequency f_n of cross-wind mode shape and dominating frequency of vortex shedding f_{St} significant vibrations may occur as result of resonance phenomenon. Therefore, if $f_{St} = f_n$, the resonance wind velocity U_{cr} is:

$$U_{mean} = U_{cr} = \frac{f_n \cdot b}{St} \tag{3.33}$$

It was experimentally found that there exists velocity range when the structure motion induces a feedback in flow and the value of dominant vortex shedding frequency remains close to the natural frequency of certain mode shape in in the cross wind direction even in case when the nominal Strouhal frequency shifts. This phenomenon is known as lock-in effect, see Figure 3.7.

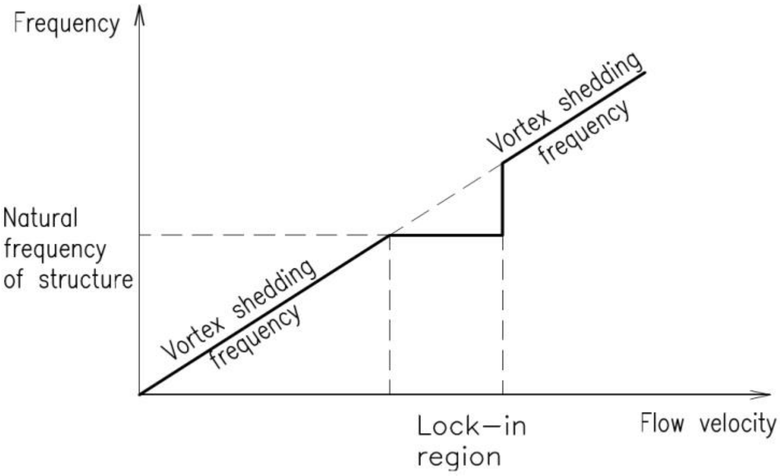

Figure 3.7 Lock-in effect

Strouhal number

Within a certain range of flow velocities, a stationary bluff body sheds alternating vortices into the trailing wake at regular frequencies according to the Strouhal relation. The term “Strouhal number” was introduced by Rayleigh in the theoretical description of Czech physics Vincence Strouhal experimental studies of wind sound generation in flow around cylinders.

The Strouhal number is a dimensionless proportional constant which relates the predominant vortex shedding frequency f_{St}, the free stream velocity and the cylinder diameter. The Strouhal number of a stationary circular cylinder is given by:

$$St = \frac{f_{St} \cdot b}{U_{mean}} \tag{3.34}$$

In description of self-oscillations of bluff bodies in flow Strouhal number actually is a dimensionless frequency of object and depends on cross-section geometry and Reynolds number.

For such kind of structures like bridge and mast anchor cables, steel chimneys, etc. velocity range of interest corresponds to subcritical mode lies between $300 < \mathrm{Re} < 3.0 \cdot 10^5$, where the vortex shedding is the strongest. Strouhal number for circular cylinders is approximately 0.20.

Reynolds number

The Reynolds number is defined as the ratio of the inertial force and the viscous force in liquid. For every kind of liquid exists critical Reynolds number – criteria of the laminar-to-turbulent mode transition. The Reynolds number, Re is given by:

$$Re = \frac{\rho \cdot U \cdot D}{\mu} = \frac{U \cdot D}{v} \tag{3.35}$$

Where:

U – the wind velocity

ρ – the flow density

μ – the coefficient of fluid viscosity

Scruton number

Scruton number is parameter proportional to the structural damping and to the ratio between the vibrating mass and the mass of the air displaced by the structure, and it is defined as:

$$Sc = \frac{2\delta_s \cdot m_e}{\rho \cdot b_{ref}^2} \tag{3.36}$$

Where:

ρ – is the air density,

δ_s – quantifies the structural damping by the logarithmic decrement which can be approximately expressed as $\delta_s = 2\pi\zeta_s$, where ζ_s is the structural damping coefficient, and the effective mass m_e per unit length is given by:

$$m_e = \frac{M_g}{\int_0^h \Phi^2(z)dz} \tag{3.37}$$

Where:

$\Phi\,(z)$ – is the mode shape, the integral in the denominator is taken over the structural part with length h exposed to vortex shedding forces;

M_g – is the modal mass, which for a line-like structure of length *L* may be expressed as:

$$M_g = \int_0^L m_l(z)\psi^2(z)dz \tag{3.38}$$

where $m_l(z)$ – is the vibrating mass per unit length.

Effect of free stream turbulence

Studying the effects of free stream turbulence on the flow around cylinders began in the late 1970s-1980s [52]. Results of these studies often lead to ambiguous conclusions.

The free stream turbulence has an effect on the transitions in the boundary layers. It is relatively well documented that the transition state can occur in a turbulent stream in a range of Re where the transition in free shear and boundary layers does not take place in the smooth stream [53]. However, only limited data are available for the effects on free shear layers located in the near wake of a cylinder [54]. Apart of the influence on the location of the separation point and the free shear layer and the near wake of a cylinder, free stream turbulence influence also the aeroelastic response. For example, [55] investigated vortex shedding from freely vibrating circular cylinder in turbulent flow. Freely vibrating horizontal model was tested in “smooth” flow with minimal turbulence and in isotropic turbulence generated by the grid. For a stationary cylinder, the tests demonstrated slightly increasing the total lift and broaden its spectrum under isotropic turbulence. The effect of amplitude on total lift shows broadening of the spectrum with turbulence and the narrowing of it with amplitude accompanied by an increase in r.m.s. of total lift. Also experiments with vertical cylinder in boundary layer simulated by roughness elements and grid generated turbulence were carried out.

Turbulence effects on rectangular cylinders have been investigated by T. Miyata and M. Miyazaki in [56]. Elastic mounted models were used for vortex induced vibrations. It has been noted that the main effect of turbulence is to increase the growth rate of the shear layers for bluff bodies. Experiments demonstrate that turbulence scale as well as intensity significantly affects the unsteady lift forces due to vortex shedding and galloping.

Research held by A. Kareem and T. Wu [57] demonstrates that turbulence in range of the body scale can enhance or weaken vortex shedding depending on the body geometry.

A study focused on slender structures and structural elements was initiated and coordinated by Giovanni Solari at Department of Structural and Geotechnical Engineering from University of Genoa in Italy. This study extended the concepts defined by Davenport for alongwind to crosswind and torsional responses, crosswind forces and torsional moments due to vortex shedding were superposed by considering these as independent of turbulence actions [58]. Alongwind, crosswind and torsional responses analyzed as uncoupled and only dependent on the related fundamental modes of vibration, were determined in closed forms [59], [60] by the generalized spectrum technique [61].

The effect of turbulence on vortex-induced vibrations has been considered experimentally by Vickery and Krenk and Nielsen [62]. At the present time the most accurate model for vortex shedding resonance including the impact of large scale turbulence was designed by Krenk and Nielsen.

In some conservative cases, the large-scale atmospheric turbulence may be interpreted as a slowly varying mean wind velocity. When the mean wind velocity for a short period of time is equal to the resonance wind velocity, the amplitudes will grow slowly, but as soon as the mean wind velocity has changed away from the resonance wind velocity, large amplitudes will not grow up. The actual amplitudes will be of stochastic nature, i.e. increase when the wind velocity is close to the resonance wind velocity and reduce when this is not the case [63], [64].

Small scale turbulence can occur in wake of structures and construction elements – e.g. behind of arranged ahead cables, pylons etc. Vortex resonance approach of Eurocode [25] take into account interference excitation of closely spaced (a/b less than 10), but not suitable in case of different shape and larger separation distance.

Surface roughness effects

For both theoretical and numerical investigations, the structural cables are often assumed to have perfectly circular cross-sections. In contrast to the aerodynamic bodies (wings) and the bodies with sharp edges (rectangular profiles), the circular cylinders, which may be classified as semi-aerodynamic, have the varying flow separation point at the surface. This point depends on the free-stream velocity, turbulence intensity and flow profile, and roughness of the body's surface [65]. Even dry wrapped or coated structural cables have usually not ideally smooth surface. Roughness elements on surface produce turbulence affecting boundary layer in close way as free-stream turbulence.

Location of the flow separation point is very important especially for the cables created from individual steel wires and with no coated protection as it is the case of guy ropes. In case of covering the steel strands by the polyethylene (HDPE) tubing, even this is expected to exhibit local alterations of its inherent surface roughness, resulting from mechanical damage, manufacturing, creep, and exposure to the atmospheric pollution and solar activity. Such geometrical deviations, corrosion and other types of such surface changes can be defined as a technological roughness. Such microscopic changes on the body's surface can induce macroscopic changes in the flow around it [53] and thus they are important to be analyzed. In close relation to the flow separation on the cable surface is the Reynolds number being a governing parameter of the transitions (critical state) occurring in the disturbed regions, which are the wake, in the shear layer and the boundary layer [66]. This critical state in the boundary layer has attracted most research attention, as in this range of the Reynolds numbers one can expect significant changes in the aerodynamic coefficients [29]. They are provoked by changes of the flow and by the occurrence of the flow instabilities expressed as the drop in the drag coefficient and the simultaneous appearance of a steady lift, [53]. In [67] a demonstration of the influence of cable surface roughness on the force coefficients and their variations due to wind incidence angle is presented. Another author [68] investigated roughness generated by sand paper, wire mesh screen and ribs. The authors of

[69], [70], [71] reported drag coefficient data for rough cylinders and the change in the critical Reynolds number.

In [72] two types of cylinder roughness were classified and tested. In [73] surface roughness used to shift vortex shedding to post-critical regimes. Furthermore [67], present a theoretical and experimental work focused on the wind-induced response of a full-scale yawed bridge cable section model, for varying Reynolds numbers and wind angles-of-attack. Using the drag and lift coefficients, determined in static conditions for an identical cable model as the one used for passive-dynamic tests, the in-plane aerodynamic damping is evaluated by employing a one-degree-of-freedom quasi-steady model.

In recent years, a particular focus is put upon the vibration of flexible cables, e.g. [74]; [75]. Authors present an overview of the recent studies on this topic. The review by Williamson and Govardhan [8] summarizes fundamental discoveries concerning vortex-induced vibration.

The changes of the roughness may also augment a cable wettability which consequently increase the probability of the creation and development of the rain–wind induced rivulets [76]. Moreover, in the case of freezing conditions, the rain and wind may produce the ice accretion of different type.

The ice accreted on the cable surface, but also for example the water rivulets in the rainy condition, considerably alter its aerodynamics expressed by the drag and lift force coefficients. For example, vibration amplitudes at the Great Belt Bridge, Denmark, were reported to be 1.4 m in the cross wind and 1.0 m in the along wind direction for ice-accreted bridge hangers, while such an excessive amplitudes are not present in case of a dry cable, see [77]. Also, the difference of the temperature between the ambient and the surface can be the reason for the separation point relocation [78] creating false roughness. With respect to the above mentioned can be defined as the climatic roughness category. Atmospheric icing is a large problem for many structures located in regions with cold climate [79]. In the literature, there exist specific papers concerning the identification of amplitude of the wind-induced vibration [48] the investigations of the aerodynamic coefficients, [80]. However, because of a relatively small outer diameter of electrical power cables, as well as a different shape of the ice, these results are not really appropriate for cables of the cable-supported bridges with larger diameters. Unlike in cases of the airplane wings and wind turbine blades [81] there are not many experiments focusing on the ice accretion laboratory creation on cables and ropes. Recently, some papers [39], [50] described pioneering work on the effects of ice accretion due to in-cloud icing on the aerodynamics of vertical and inclined cylinder models of bridge hangers or stay cables. In these papers, extensive studies are reported on the ice accretion processes and the final shapes of the ice on these models. The mean aerodynamic force coefficients of the iced bridge cables were also measured. It was found that they are significantly affected by the characteristics of ice accretion, depending on the climatic conditions, and that ice accretion can lead to instability phenomena of bridge cable. It should be noted that the literature on the influence of icing on the aerodynamics of the cables of cable-supported bridges is still insufficient, and it is therefore important to conduct further studies to quantify the aerodynamic variation due to ice accretion on cables.

Withal until todays insufficient attention has been paid to the simultaneous impact of the free stream turbulence and surface roughness.

3.6 Theoretical models of vortex shedding vibrations

Energy-balanced double oscillator mode by Krenk and Nielsen

The basic idea is that the fluid oscillator associated with an internal degree of freedom that interacts with structure as two coupled oscillators. First attempts were undertaken by Hartlen R.T. and Currie I.G. [82], Iwan W.D. and Blewins R.D. [83], Skop R.A. and Griffin O.M. [84]

The model presented in [62] based on exact transfer of energy from fluid to structural oscillator, what allows to determine accurately determine resonance and lock-in region, and represents the structural element and the motion of fluid mass, that introduced as a generalized displacement variable.

The equation of transverse motion of the cylinder defined as:

$$m_0(\ddot{x} + 2\zeta_S\omega_0\dot{x} + \omega_0^2) = \frac{1}{2}\rho U^2 Dl \frac{\dot{w_{fl}}(t)}{U}\gamma \tag{3.39}$$

Where:

m_0 – sum of structural and added mass,

x – transverse displacement of structure,

ζ_s – structural damping ratio(relative-to-critical),

ω_0 – undamped natural angular frequency,

ρ – air density,

U – undisturbed flow velocity

D – diameter of solid cylinder,

l – length of solid cylinder,

w_{fl} – equivalent transverse fluid displacement,

γ – nondimensional coupling parameter.

The equation of motion of the coupled structure fluid oscillator can be written:

$$m_f\left[\ddot{w} + 2\zeta_f\omega_s\left(1 - \frac{w^2 + w^2/\omega_s^2}{w_0^2}\right)\dot{w} + \omega_s^2 w\right] = \frac{1}{2}\rho U^2 Dl \frac{\dot{x}(t)}{U}\gamma \tag{3.40}$$

Where:

m_f - equivalent mass of fluid oscillator,

x - transverse displacement of structure,

ζ_f - damping ratio of equivalent fluid oscillator,

ω_f - Strouhal angular frequency,

w_0 - reference transverse fluid displacement.

During the vibration, the energy flow over a full period consists of energy generation by the negative damping in the fluid (left hand side of Eq. (3.40)), extraction (gain) of the energy from the fluid oscillator (right hand side of Eq. (3.40)), transfer of energy to mechanical oscillator (right hand side of Eq. (3.40)), and energy dissipation by the structural damping. The rate of the energy exchange expressed with the right-hand sides of equations is $\frac{1}{2}\rho UDl\gamma\dot{w}\dot{x}$.

The coupled differential equations can be written in dimensionless forms by introduction nondimensional parameters (Eq. (3.41), (3.42)) and the mass ratio μ_f (relative mass of fluid and cylinder):

$$y = \frac{x}{D} \tag{3.41}$$

$$v = \frac{w}{w_0} \tag{3.42}$$

Where:

y - nondimensional transverse displacement of structure,

v - nondimensional transverse displacement of fluid.

And nondimensional reference fluid displacement v_0:

$$v_0 = \frac{w_0}{D} \tag{3.43}$$

Coupled equations in this case take form:

$$\ddot{y} + 2\zeta_0\omega_0\dot{y} + \omega_0^2 y = \mu_f c_0 \omega_s \dot{v} \tag{3.44}$$

$$\ddot{v} + 2\zeta_f\omega_s[1 - v^2 - (\dot{v}/\omega_s)^2]\dot{v} + \omega_s^2 v = -v_0^{(-2)} c_0 \omega_s \dot{y} \tag{3.45}$$

where c_0 – normalized coupling coefficient.

Presenting the structure and fluid (y, y', v, v') phase variables in terms of the amplitude and the phase angle $(A, \Phi, B\ \Psi)$ the solution of this equation gives the formula for the normalized structural amplitude A:

$$A = \frac{1}{2}\mu_f \left(\frac{U}{D\omega_0}\right)^2 C_L \left\{\left[1 - \left(\frac{\omega}{\omega_0}\right)^2\right]^2 + 4\zeta_0^2 (\frac{\omega}{\omega_0})^2\right\}^{-1/2} \tag{3.46}$$

where:

- μ_f- fluid-to-structure mass ratio,
- C_L - lift coefficient.

Eurocode models

Eurocode [25] proposes two approaches for predicting vortex-induced vibrations of structures.

Vortex-resonance model

Approach 1 is based on the vortex-resonance model. Amplitude of vibration reaches maximum value when vortex shedding frequency is equal to the natural frequency of the particular vibration mode of structure. It is assumed that the maximum value of cross-wind load does not occur along the whole structure in one time. This factor is taken into account by using the correlation coefficient.

Maximal amplitude could be found using:

$$\frac{y_{F,max}}{b} = \frac{1}{St^2} \cdot \frac{1}{Sc} \cdot K \cdot K_w \cdot C_L \tag{3.47}$$

where:

St - Strouhal number,

Sc - Scruton number,

K_w - correlation length coefficient,

K - shape mode,

C_L - lateral force coefficient.

$$K = \frac{\sum_{j=1}^{m} \int_{l_j} |\Phi_{i,y}(s)| ds}{4 \cdot \pi \cdot \sum_{j=1}^{m} \int_{l_j} |\Phi_{i,y}{}^2(s)| ds} \tag{3.48}$$

Where:

$\Phi_{i,y}$ – is the mode shape *i*

l_j –is length of the structures between two nodes

n – is the number of regions where vortex excitations occursat the same time

m – is the number of antinodes of the vibrationg forthe modeshape $\Phi_{i,y}$

s – is coordinate along structure axis

$$K_W = \frac{\sum_{j=1}^{n} \int_{L_j} |\Phi_{i,y}(s)| ds}{\sum_{j=1}^{m} \int_{l_j} |\Phi_{i,y}{}^2(s)| ds} \tag{3.49}$$

Where:

L_j – is the correlation length, the value of which depends on the ratio calculated as the amplitude of the oscillations divided by the characteristic dimension b of the cross section, see Table 3.1:

Table 3.1 Effective correlation length as function of vibration amplitude

$y_F(s_j)/b$	L_j/b
<0.1	6
$0.1 \div 0.6$	$4.8+12 \cdot y_F(s_j)/b$
>0.6	12

Then, according to the calculated amplitude of the oscillations, the distributed inertial load is determined as:

$$F_W(s) = m_l(s) \cdot \left(2 \cdot \pi \cdot f_{n,i}\right)^2 \cdot \Phi_{i,y}(s) \cdot y_{F,max} \tag{3.50}$$

Where

m_l – is vibrating mass per unit length

Number of cycles for fatigue analysis could been found using:

$$N = 2 \cdot T \cdot f_{n,y} \cdot \varepsilon_0 \cdot \left(\frac{v_{crit}}{v_0}\right) \cdot \exp(-\left(\frac{v_{crit}}{v_0}\right)^2) \tag{3.51}$$

Where:

$f_{n,y}$ - structure eigenfrequency [Hz],

v_{crit} - critical wind velocity [m/s],

v_0 - 2x the value of the mode Weibull probability predicted for wind speed [m/s],

T - lifetime in seconds,

ε_0 - bandwidth coefficient, could be taken from 0.1 to 0.3.

Bandwidth coefficient allows rough estimation of turbulence effects.

Spectral model

Approach 2 is based on the spectral model. It avoids underestimation of the rare event response neither the other frequent event responses. Spectral model is mostly suitable for relatively stiff structures.

Characteristic maximum amplitude could be expressed as:

$$y_{max} = \sigma_y \cdot k_p \tag{3.52}$$

Where:

- σ_y is the standard deviation of the displacement,
- k_p - maximum value coefficient.

The standard displacement deviation is calculated using expression:

$$\frac{\sigma_y}{b} = \frac{1}{St^2} \cdot \frac{C_c}{\sqrt{\frac{Sc}{4 \cdot \pi} - K_a \cdot (1 - (\frac{\sigma_y}{b \cdot a_L})^2)}} \cdot \sqrt{\frac{\rho \cdot b^2}{m_e}} \cdot \sqrt{\frac{b}{h}} \tag{3.53}$$

Where:

- C_c - is aerodynamic coefficient,
- K_a- aerodynamic damping parameter,
- a_L - normalized amplitude limiting deflection,
- St - Strouhal number,
- Sc -Scruton number,

ρ - air density,
m_e - effective mass per unit length,
h, b - height and width of structure.

The influence of large scale taken into account by introducing the aerodynamic damping parameter. The value of aerodynamic damping depends upon the turbulence intensity. Aerodynamic damping coefficient K_a decreases with the increasing turbulence intensity. The critical Scruton number, at which the regime with small oscillation changes into the large ones, depends strongly on the low frequency turbulence with large scales, however, it does not depend much upon the high frequency turbulence characterized by the small vortices.

4. First stage of experiments

Experimental part was made in two stages. The first stage of dynamic tests was carried out to evaluate the selected experimental set and the measurement and data processing methodology.

4.1 Experimental setup for first stage of experiments

Wind Tunnel

Dynamic tests were carried out in wind tunnel of the Boundary Layer Wind Tunnel Laboratory at the Ruhr-University of Bochum. It is a subsonic open-return type wind tunnel with rectangular testing cross section. Scheme of this wind tunnel is presented at Figure 4.1.

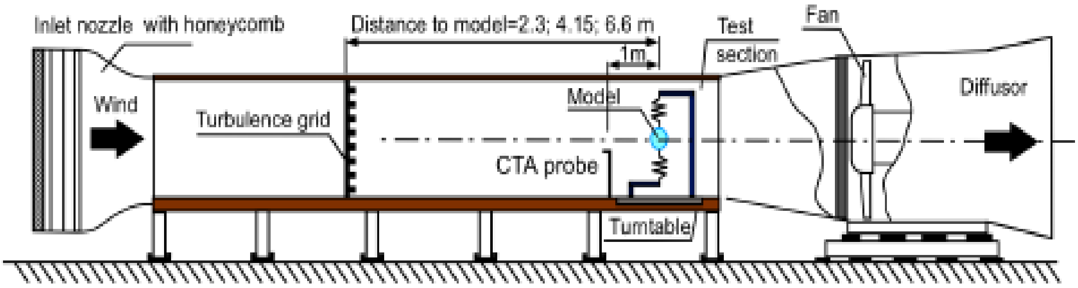

Figure 4.1 Wind tunnel experimental setup in Ruhr University, Bochum

Models

For the purpose of this study, frequently occurring types of cables for suspended structures were selected:

- Cylinder with helical strands with relative roughness k/D = 2.5% and a strand pitch angle of γ=11.5°, representing supporting guy ropes;
- Smooth circular cross section with relative roughness k/D = 0.06%, representing dry structural cables;
- Ice-accreted cylinder with a rough surface approximately covering the section at a 120° angle with a maximal of k/D = 10% in form of ice accretions, representing structural cables in the freezing weather conditions.

Parameter k is the average roughness height and D is the cylinder diameter. Relative roughness of helical strand model is calculated according to [29] as $d_{wire}\ /\ 2D$. The model of the ice-accreted structural cables were tested at three flow incidence angles: a) α=0°; b) α=90°; and; c) α=180°.

The shape of ice formations used in present study were obtained during tests in the Climatic Wind Tunnel of the Institute of Theoretical and Applied Mechanics, see [85]. This is a Gottingen-type closed-circuit boundary-layer wind tunnel with two test sections. The 2.5 m wide, 3.9 m high and 9.0 m long rectangular climatic section is used for modelling precipitation and freezing effects on structures. The shape of the ice accretion was created in this test section using the ice-formation experiments with water sprinkling onto precooled model of a cable covered with a high-density polyethylene protecting coating. The ice was classified as wet ice accretion, (glaze-dominant type of ice that often occurs in Central Europe when temperature is around 0°C) according to [86]. The ice-accretion process yielded an asymmetric and irregularly iced cross-section of the cable model with rounded edges of the ice ribs accreted at the bottom surface of the cable model.

Figure 4.2 Model of structural cable in Climatical section [87]

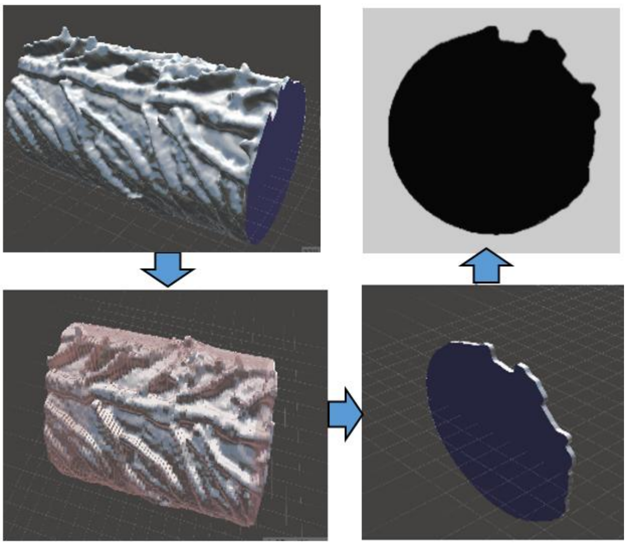

Figure 4.3 The cross-section of polystyrene model obtained from 3d model of iced cable

The sectional cylinders tested were made of polystyrene with length = 800 mm. Diameter of the cylinders was 200 mm. The length-to-width ratio of used models is 4:1 which is acceptable according to West and Appelt [88].

The blockage ratio is the ratio of the area of the model and other equipment to the total area of wind tunnel cross-section. This value should not exceed 10-15%. Otherwise narrowing of the effective cross section causes compression, distortion and local acceleration of the flow. The experiments were carried out at the blockage

6%, in accordance with West and Appelt [88], whereas the entire experimental hardware in the test section was taken into account when calculating this blockage value.

The total vibrating mass was m_v = 3.923 kg with a Scruton number of Sc = 5.702. The measurement of the response was carried out in the range of reduced velocity $U/(f \cdot D) = U_{red} \in (3.90 \div 7.77)$. The amplitudes were registered by the laser optical displacement measuring system Micro-Epsilon OptoNCDI. The Reynolds number Re range was from $6.5 \cdot 10^4$ to $1.2 \cdot 10^5$. For Re in range from 10^3 to 10^5 the Strouhal number proved to be almost constant nearly equal to St = 0.2 in agreement with values commonly reported for smooth cylinders, e.g., [53]. Nevertheless, some experimental studies determined the value of the Strouhal number closer to St = 0.18, e.g. [89], [90], [85].

Figure 4.4 Helical strand model surface

Figure 4.5."Iced"-model in test section on dynamic balance stand

The cylinders were fixed to the special force balance stand allowing adjustment of principal dynamic characteristic of the cylinder, see Figure 4.6. Namely, the fixed frequency of vertical oscillations was set as f_n=5 Hz which corresponds to the actual values. Logarithmic decrement was measured to be δ=0.028.

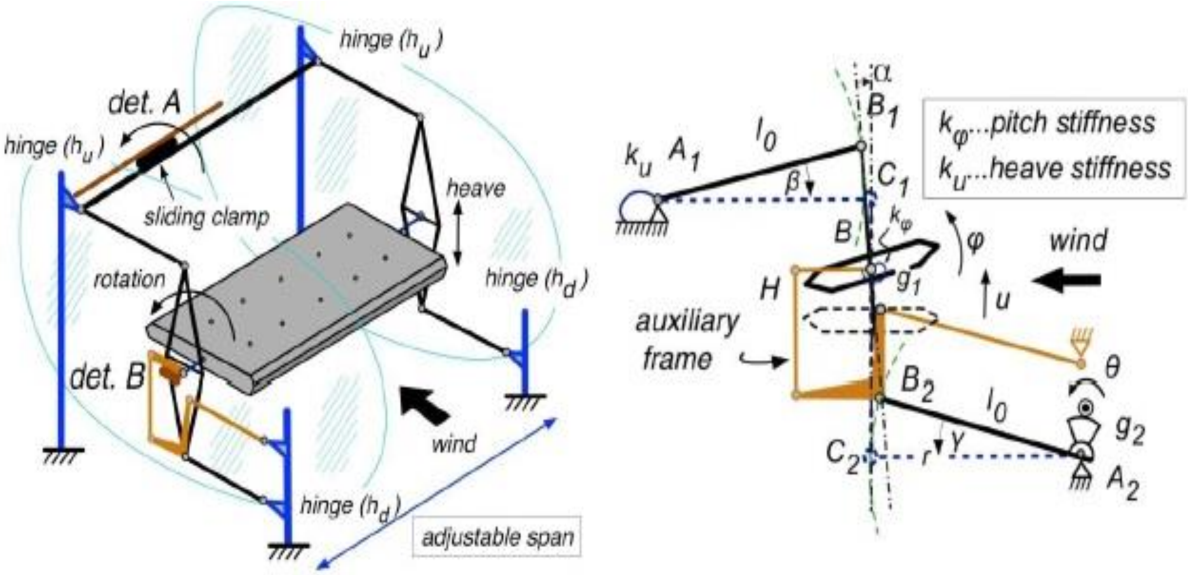

Figure 4.6 Multipurpose stand for aeroelastic tests [91]

Figure 4.7 Model on balance stand in wind tunnel test section

Flow velocity at 1 m upwind of the cable model and at the height of 0.8 m above the test-section floor was measured using a Prandtl tube. Time histories of flow velocity were measured using the Constant Temperature Anemometer (CTA) installed 1 m upwind of the cylinder. The acquisition rate was 1000 Hz and the duration of each measurement was 132 s.

Calibration of CTA probes was held in calibration wind tunnel (chamber), see Figure 4.8. Fan connected to electric motor (on the right) blows air into segmented plexiglas tube. Honeywell is installed inside the tube to decrease incoming flow turbulence. Air outlet contraction (on the left side) increases flow rate and additionally reduces turbulence.

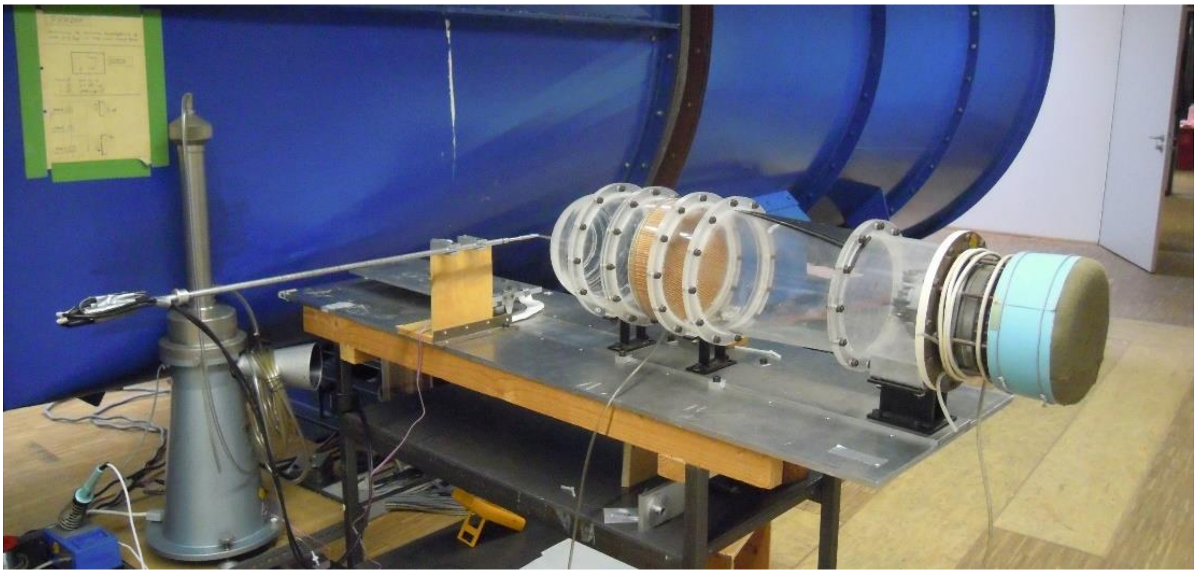

Figure 4.8 Calibration wind chamber for CTA probes

Obtained data were interpolated to obtain calibration function, see Figure 4.9.

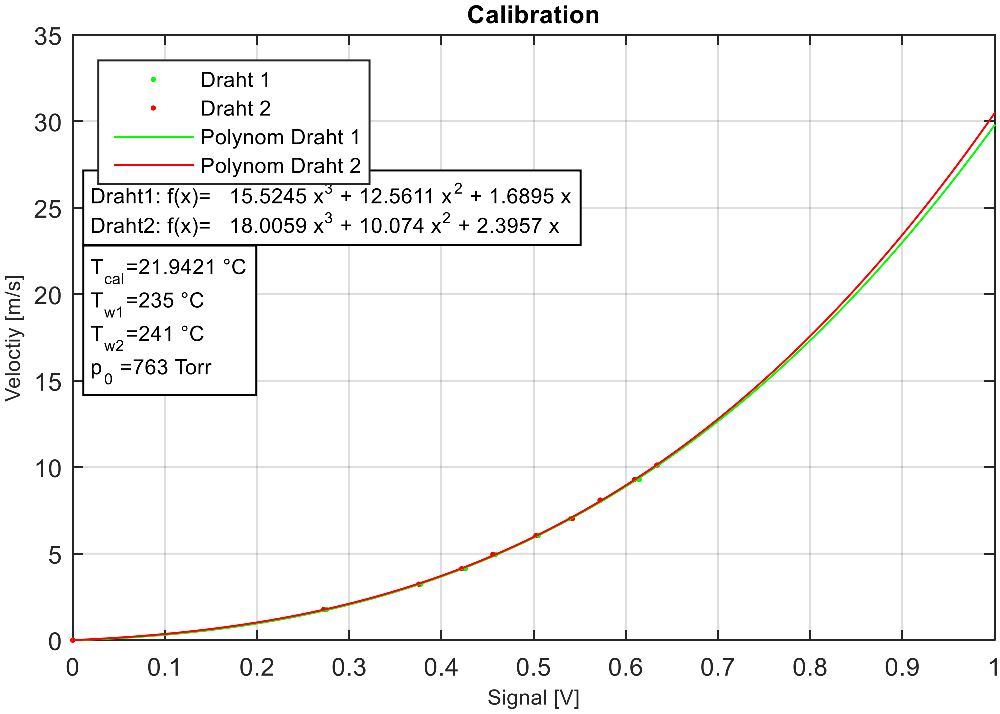

Figure 4.9 Calibration of CTA single wire probe by polynom function fitting

Turbulence generation in test section

All configurations were loaded by the low-turbulent flow with turbulence intensity I_u= 1.5%, further on named as “low” and consequently to the turbulent flow generated by square mesh arrays of rectangular bars with different levels of turbulence intensity. According to multiple sources, see e.g. [92], the method of turbulence modelling used with the described grid creates nearly isotropic turbulence. Nevertheless, the primary focus of the present work is on flow and turbulence in the main x-direction. The distance between the bars was 180 mm, and the bars were 55 mm wide and 25 mm thick, see Figure 4.10a)

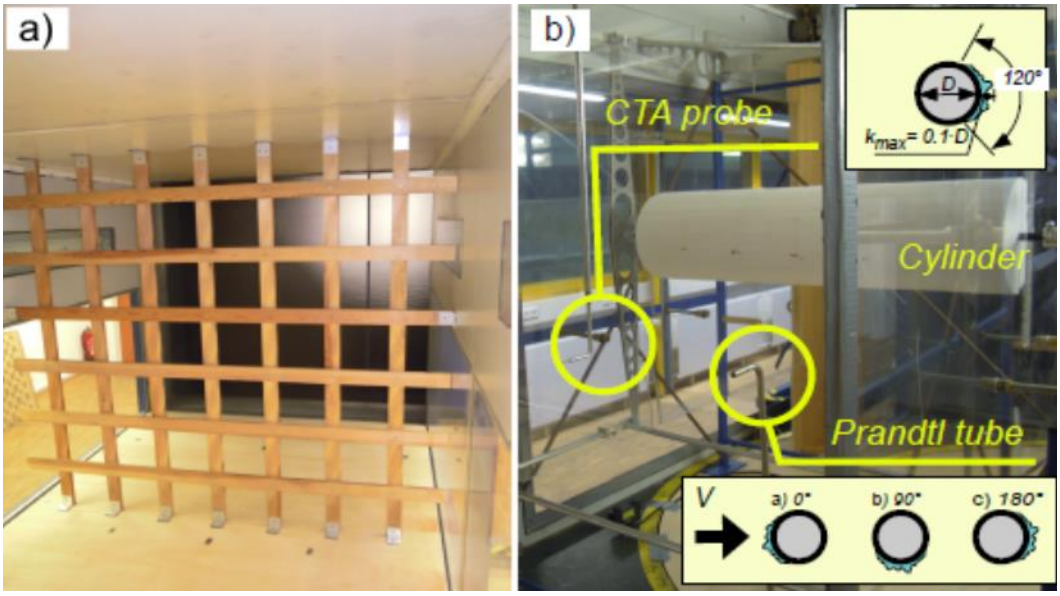

Figure 4.10 a) View of the wooden turbulence grid. B) Arrangement of the experiment in a wind tunnel and the schematic view of the wind direction with respect to the ice-accreted cylinder

The time history of recorded flow velocity (for the consequent evaluation of velocity spectra) and the vibration tests were carried out simultaneously.

Preliminary arrangement and distance from turbulence grid to model calculated using expressions (4.1) and (4.2) from [92] to obtain values of integral length scale equal to 0.075, 0.1, 0.125 m:

$$\frac{L_{u,x}}{d} = I(x/d)^{\frac{1}{2}} \tag{4.1}$$

$$I_{u,x} = C(x/d)^{-\frac{5}{7}} \tag{4.2}$$

Where:

$L_{u,x}$ – integral length scale (measure of the largest eddy size in a turbulent fluid);

I– empirical constant, for SMS I = 0.2 (see [92]);

d – characteristic dimension of bars/rods in turbulence generation grid;

$I_{u,x}$– turbulence intensity in mean direction;

C – function of grid geometry.

4.2 Results

Turbulence characteristics

Experimental data from CTA probe have been used to obtain turbulence intensity and integral length scale. Integral length scales were obtained by fitting of von Karman model for nearly isotropic turbulence to measured normalized power spectrum (Fig. 7.7). Data were divided into 1-sec blocks, for each block were calculated spectra. Obtained mean spectrum was used for fitting. Experimental values were lower than expected. According to the obtained dependence integral length scale values for real position of the model were calculated and are 0.056, 0.081, 0.099 m for distance 2.3, 4.15, 6.4 m.

The von Kármán velocity-spectrum model, was fitted using the nonlinear least-square method to determine the peak spectral frequency, see Figure 4.11. The results of the fitting process are reported in Figure 4.12, Figure 4.13 and Table 4.1.

Table 4.1 Turbulence intensity and integral length scale. The distance of the model from the grid is x_1 while the distance of the CTA probe from the grid is x_2. I_{u1}, $L_{u,x1}$ and I_{u2}, $L_{u,x2}$ are corresponding turbulence intensity and length scale.

	Parameter					
	Grid distance		Turbulence intensity		Turbulence length scale	
Configuration	x_1,[m]	x_2,[m]	I_{u1},[%]	I_{u2},[%]	$L_{u,x1}$, [m]	$L_{u,x1}$, [m]
T1	2.30	1.30	10.2	15.5	0.057	0.038
T2	4.15	3.15	6.7	8.1	0.081	0.069
T3	6.60	5.60	4.8	5.5	0.099	0.094

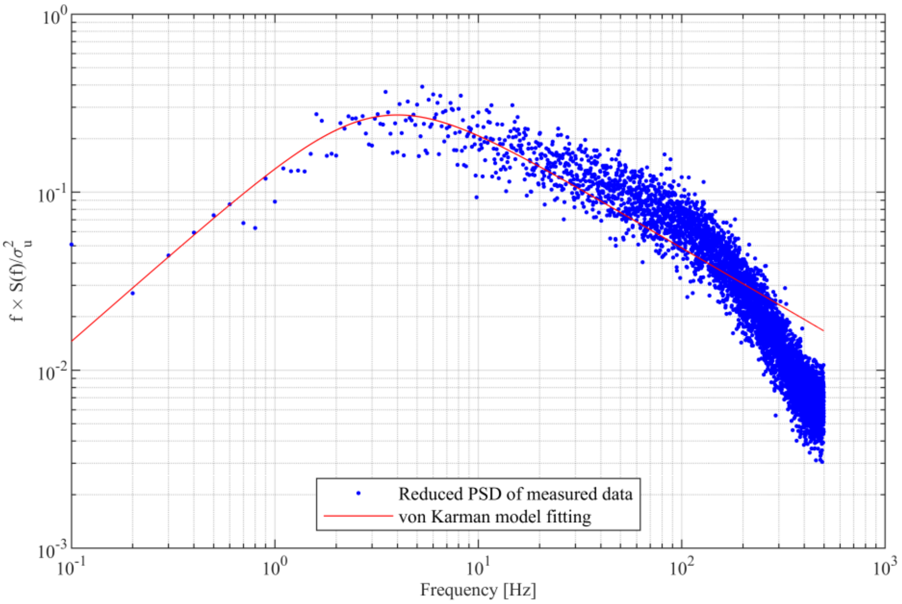

Figure 4.11 Example of fitting von Karman turbulence model to normalized power spectrum of measured data

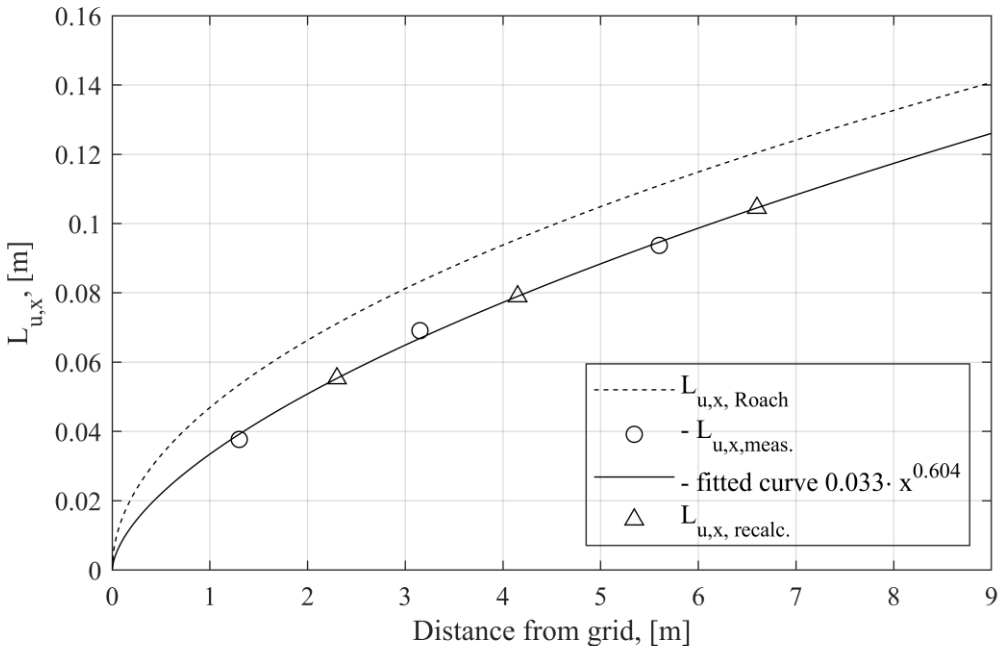

Figure 4.12 Dependence of integral length scale in wind tunnel on distance from grid calculated and obtained empirically

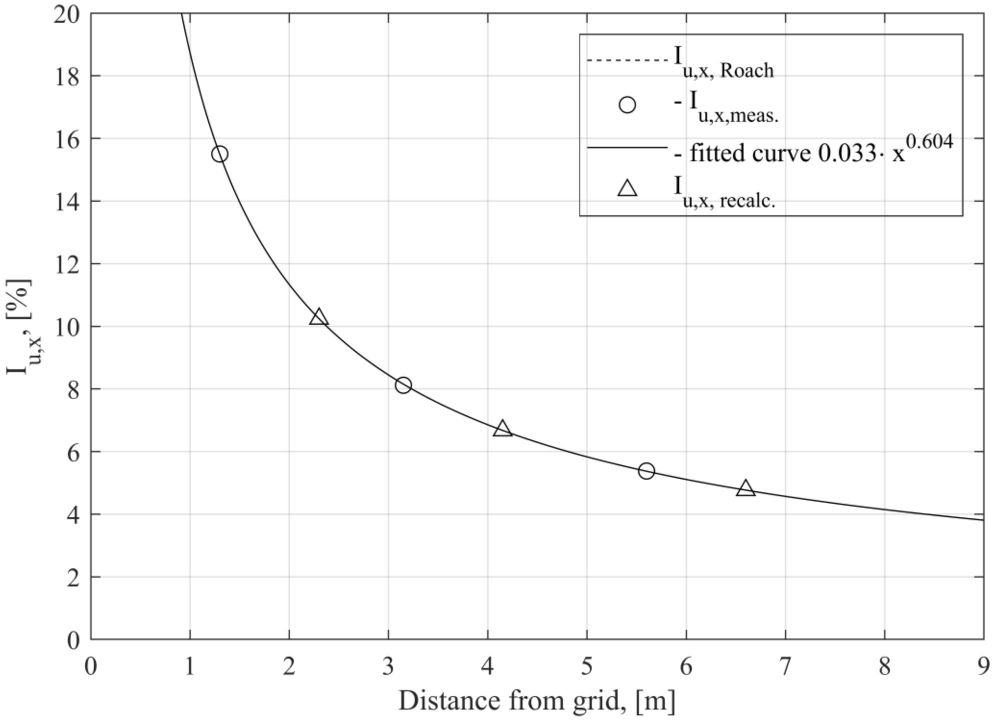

Figure 4.13 Dependence of turbulence intensity in wind tunnel on distance from grid obtained empirically

Strouhal number

During first stage of experiments no CTA probes were installed behind the model to measure the vortex shedding frequency. As it was mentioned in the section 3.5 the critical speed corresponding to the beginning of lock-in range occurs when the natural frequency of structure and frequency of vortex shedding and coincide. Based on this assumption values of Strouhal were obtained in an indirect way as:

$$St = \frac{f_n \cdot b}{U_{cr}} \tag{4.3}$$

The results are presented in the Table 4.2:

Table 4.2 Strouhal number calculated for velocity corresponding to beginning of "lock-in" range

Model name	flow turbulence intensity, I_u	Strouhal number St, []
Smooth cylinder	1.5%	0.196
	4.6%	0.21
	6.7%	-
	10.2%	-
Helical strand	1.5%	0.208
	4.6%	0.22
	6.7%	0.217
	10.2%	0.212
Iced model, α=0°	1.5%	0.185
	4.6%	0.22
	6.7%	0.19
	10.2%	0.19
Iced model, α=90	1.5%	0.200
	4.6%	0.228
	6.7%	0.235
	10.2%	0.23
Iced model, α=180	1.5%	0.212
	4.6%	0.23
	6.7%	0.22
	10.2%	0.227

Amplitude response

For the determination of the resonance domain/lock-in region, the velocity range from 0,9·U_{cr} (theoretically predicted critical velocity) till the velocity of upper lock-in limit was selected. With an increase in the flow velocity, the following patterns of vibration response were observed, Figure 4.14.

The sub-critical and post-critical domains related to the critical flow velocity are defined as:

a) Sub-critical domain, velocity is smaller than the critical velocity $U_{cr} = f \cdot D/St$: vortex-shedding frequency smaller than the set natural frequency of cylinders, significant vibrations do not occur;

b) Vortex-induced resonance with stable vibrations and maximal amplitudes;

c) Lock-in regime of self-sustained (chaotic, amplitude modulated) oscillations;

d) Post-critical domain (velocity is larger than the critical velocity) of forced (non-resonant) vibrations due to vortex shedding with a frequency larger than the natural frequency of the model; no significant vibrations were observed.

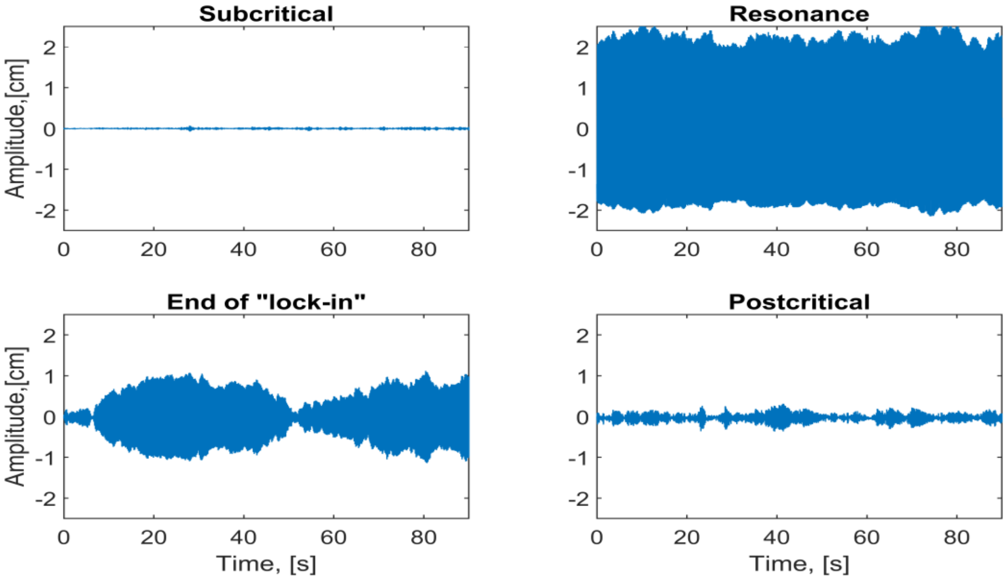

Figure 4.14 Vibration responses of the cylinder with ice accretion at the bottom surface(α=90°), I_u=4.8% in subcritical domain (U_{red}=4.127, top left); vortex induced resonance (U_{red}=4.886, top right), "lock-in" region (U_{red}=5.935, bottom left), and postcritical domain (U_{red}=7.110, bottom right).

The non-dimensional vibration amplitudes of the cylinders as a function of the reduced wind velocity U_{red} are reported in Figure 4.15-Figure 4.19.

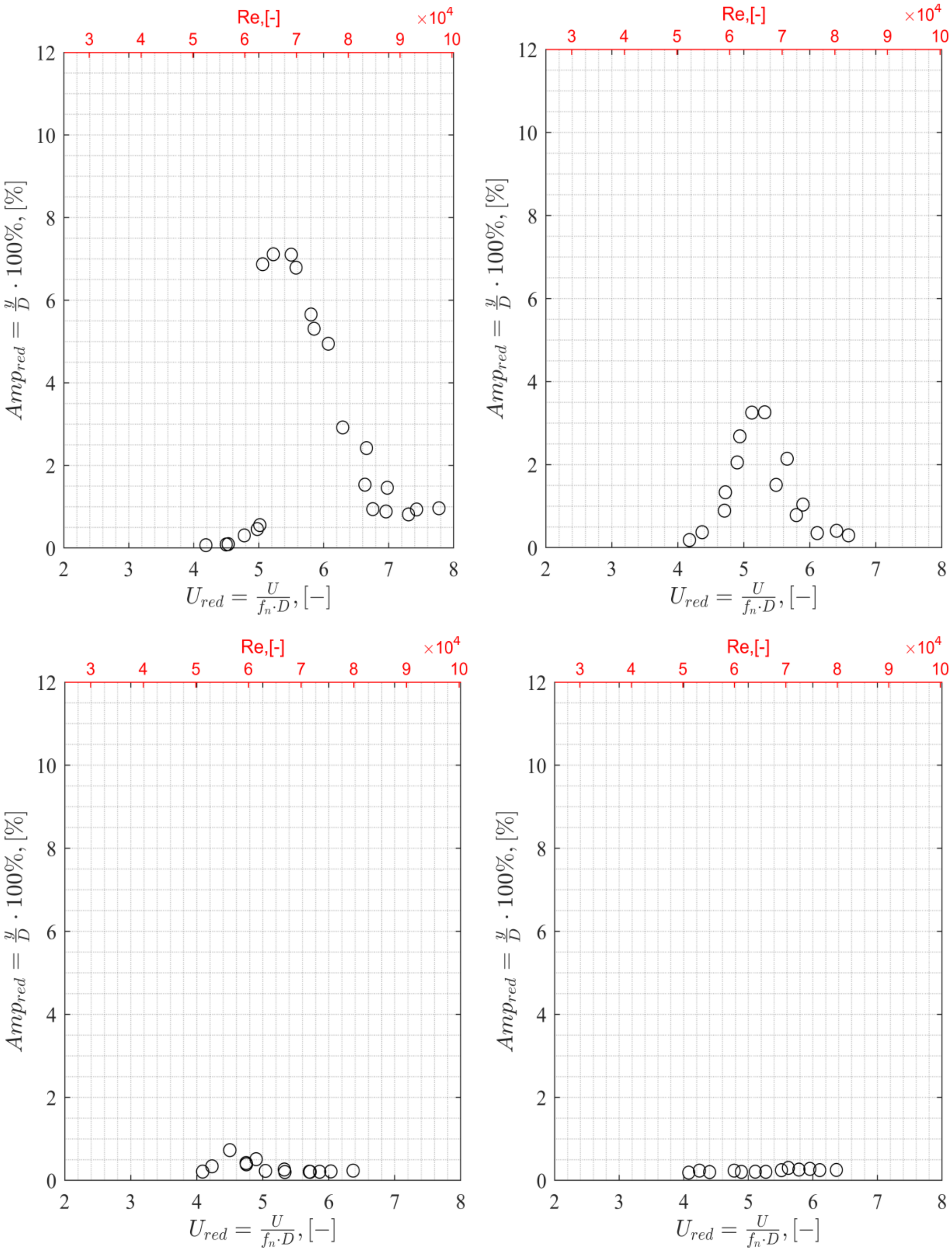

Figure 4.15 Amplitude response plot of smooth surface cylinder model in smooth flow I_u=1.5% (top left), turbulent flow I_u=4.8% (top right), turbulent flow I_u=6.7% (bottom left), turbulent flow I_u=10.2% (bottom right)

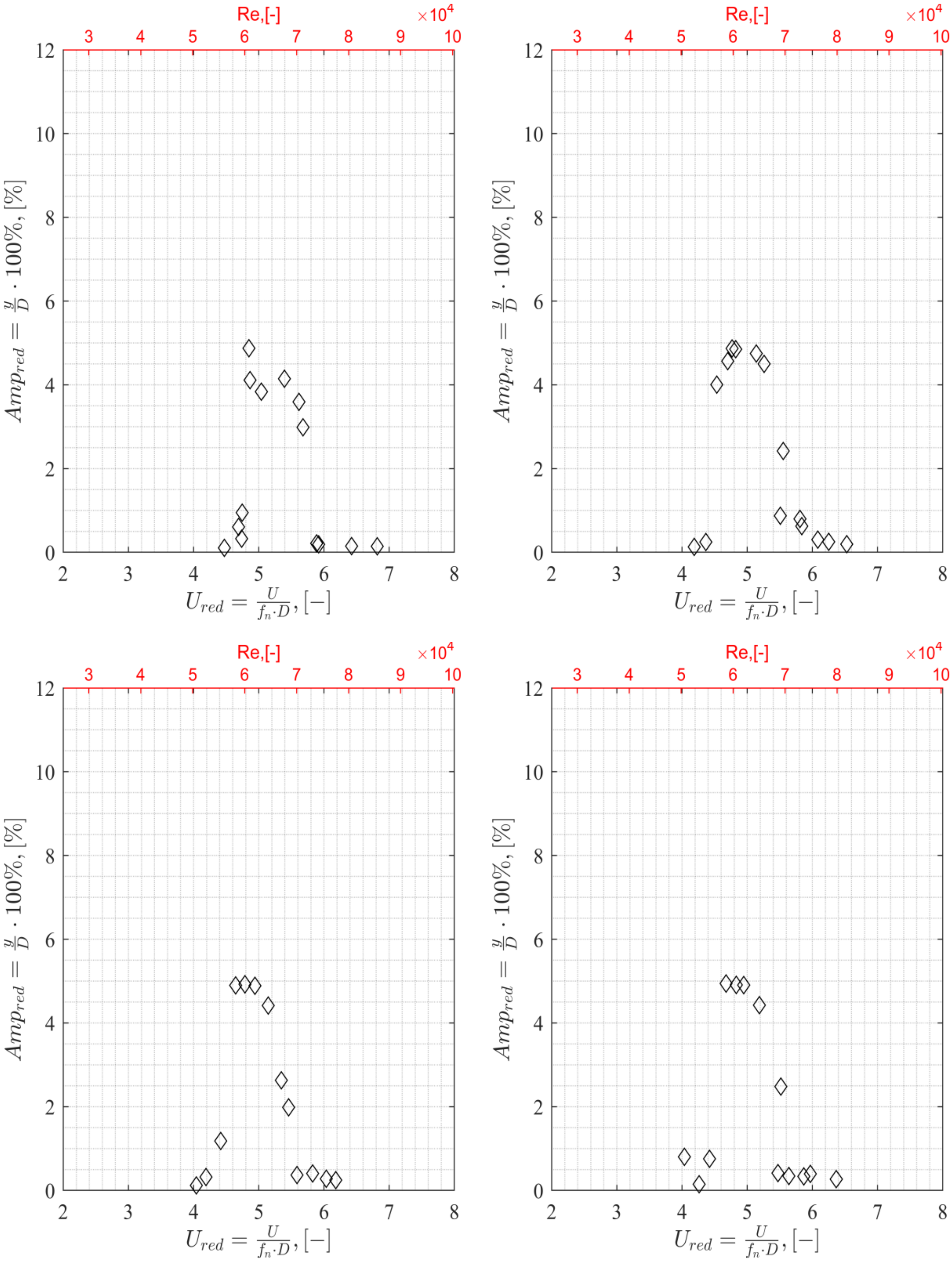

Figure 4.16 Amplitude response plot of helical strand cable model in smooth flow I_u=1.5% (top left), turbulent flow I_u=4.8% (top right), turbulent flow I_u=6.7% (bottom left), turbulent flow I_u=10.2% (bottom right)

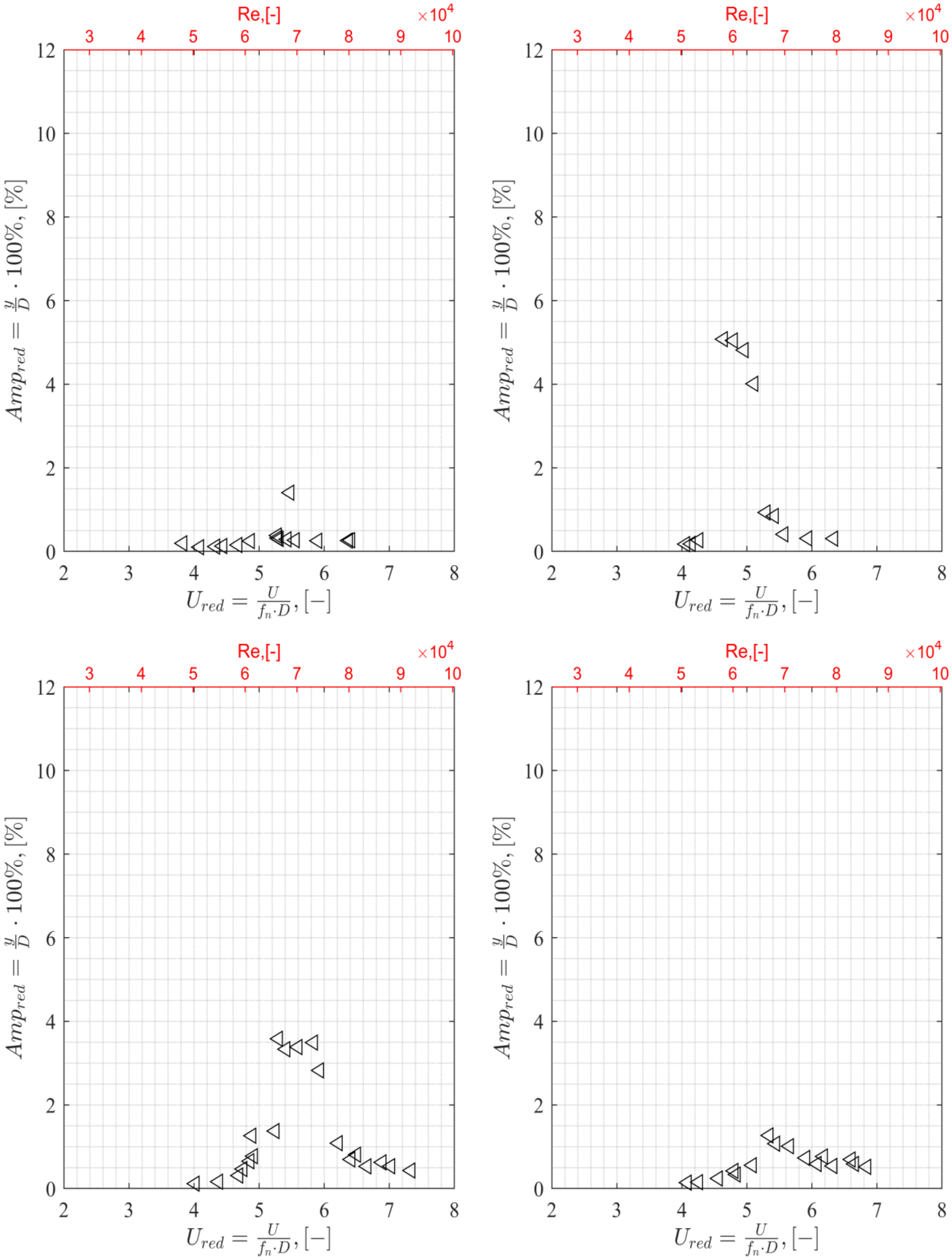

Figure 4.17 Amplitude response plot of iced cable, α=0° model in smooth flow I_u=1.5% (top left), turbulent flow I_u=4.8% (top right), turbulent flow I_u=6.7% (bottom left), turbulent flow I_u=10.2% (bottom right)

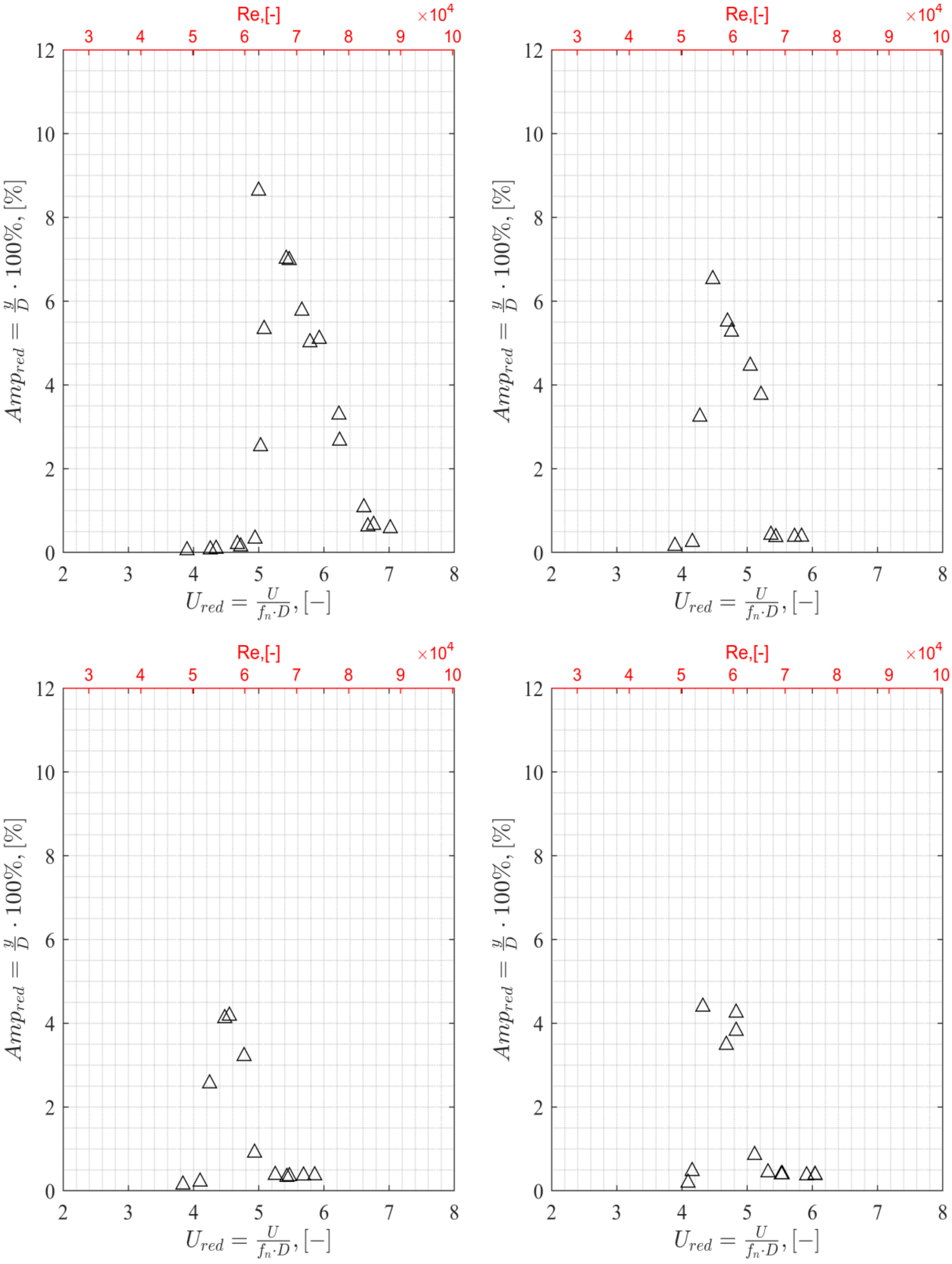

Figure 4.18 Amplitude response plot of iced cable, α=90° model in smooth flow I_u=1.5% (top left), turbulent flow I_u=4.8% (top right), turbulent flow I_u=6.7% (bottom left), turbulent flow I_u=10.2% (bottom right)

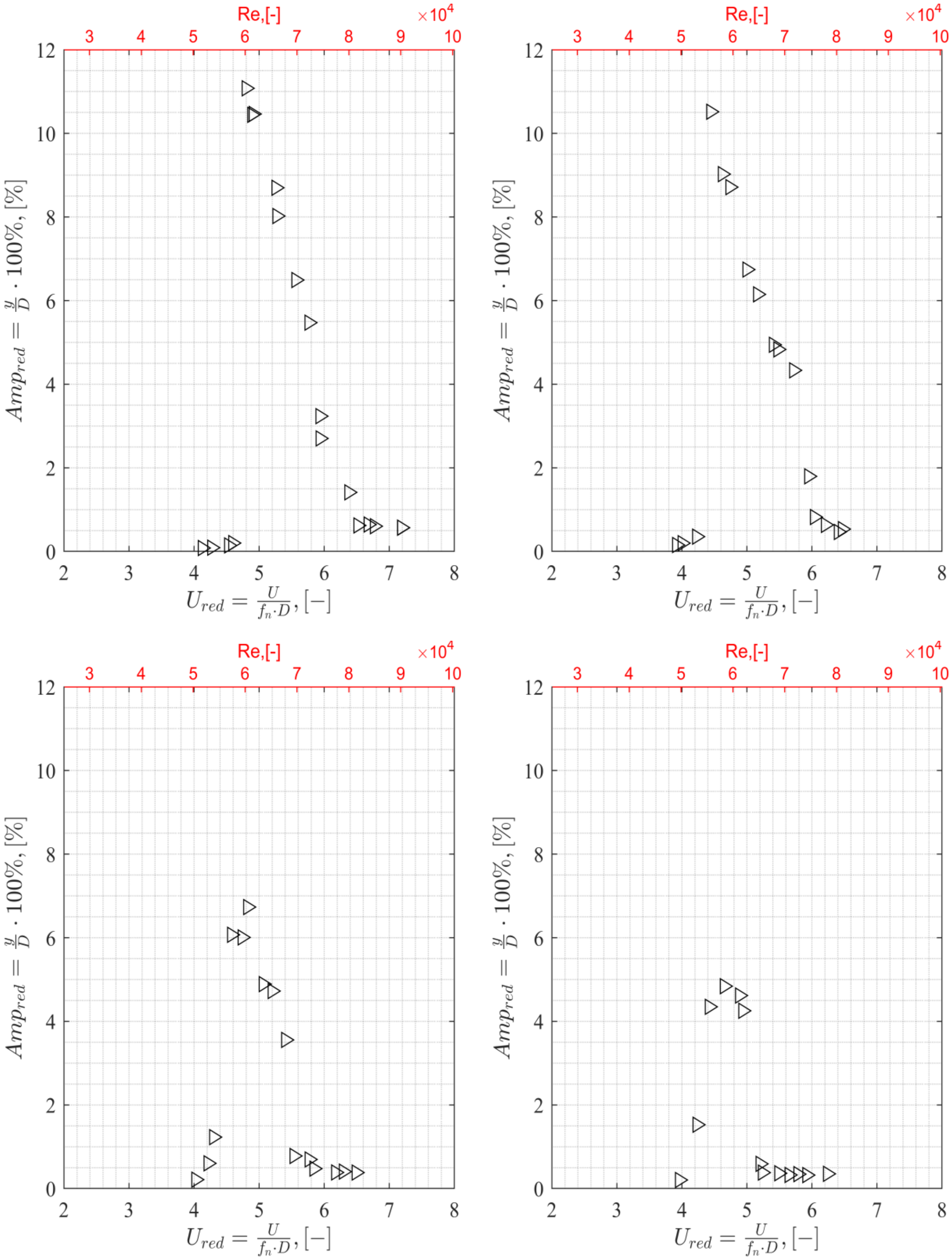

Figure 4.19 Amplitude response plot of iced cable, α=180° model in smooth flow I_u=1.5% (top left), turbulent flow I_u=4.8% (top right), turbulent flow I_u=6.7% (bottom left), turbulent flow I_u=10.2% (bottom right)

In most cases, there is a steep increase of the oscillation amplitudes after entering the lock-in region. Also with the reference to time samples in Figure 4.14, it can be observed that the response consists of deterministic and almost periodic random components. Further increase in the flow velocity leads to a small frequency detuning of the self-exciting oscillations and forced vibration response, which results in quasi-periodic regime. This quasi-periodic behavior becomes shorter with further increasing the wind speed as far as the upper limit of the lock-in domain is reached where the quasi-periodic response disappears completely. At that point, only random component of the response remains in action.

For the smooth cylinder, used as a reference, the beginning of the resonance vibrations corresponds to the Strouhal number $St = 0.2$ in the low turbulent flow (I_u = 1.5%). After exceeding the critical velocity, the lock-in vibrations occur and they are characterized by similar amplitudes and a decrease in response. The shape of curve is similar to [35]. In the low-turbulent flow (I_u = 1.5%), a decrease in vibration amplitudes and a lower velocity limit for the lock-in occurrence was observed for the helical strand cylinder in comparison to the smooth one.

The response of the cylinder with partial ice roughness depends strongly on the wind incidence angle. Unlike for the smooth cylinder, large amplitude vibrations last only few seconds at one particular velocity at 0°. For the cylinder with ice oriented at 180°, the response is characterized by significantly larger amplitude and a lock-in regime. In this case, the lock-in region manifests by almost linearly decreasing response beyond the critical velocity. The iced model at 90° has the same response characteristics as the 180° arrangement along with lower amplitudes. For the moderate turbulent flow (I_u = 4.8% and I_u = 6.7%) an increase in the response was observed for all ice-accreted cylinders in contrast to the smooth cylinder.

The response curve changes for the smooth cylinder, i.e., it gradually decreases and has a narrower lock-in region than in the low-turbulent flow. The shape of the response curves for the rough cylinder models exposed to moderate turbulent flow remains similar to the low turbulent flow but with smaller amplitudes. There is a significant increase in the response at the 0° arrangement of the iced model, where the amplitude reaches values similar to those in the case of the helical strand model. An increase in the freestream turbulence intensity and a reduction of the turbulence length scale lead to a decrease in response and narrowing of the lock-in domain. This applies to all types of iced cylinders and to a large extent to the smooth cylinder model as well. The response of the cylinder with the helical strands remained nearly the same for all tested turbulence levels. For the case with larger turbulence intensity I_u = 10.2%, significant vibrations of the smooth cylinder did not occur.

Probability density estimation of amplitudes

As can be seen from Figure 4.14 the obtained response amplitudes for models of cable with ice formation in lock-in range have non stable values. The density maps of amplitude distributions were prepared to analyze response along the measured range of velocities.

To construct the density functions, each of the measured datasets was approximated using the Kernel Density Estimator (KDE). The KDE creates a function to represent the probability distribution as:

$$\widehat{f}_h(y) = \frac{1}{nh}\sum_{i=1}^{n} F\left(\frac{y - y_i}{h}\right); -\infty < y < \infty \tag{4.4}$$

Where:

$y_{i,(i=1\ldots n)}$ sample of response amplitudes from the test,

F = kernel function (Gaussian) giving weighted density to each observation y_i.

Thus, the resulting probability density function value at point y is the sum of weighted local density estimates of each observation y_i, which was based on optimal bandwidth h, e.g. [93]. Subsequently, all probability density functions for the single experimental set with discrete velocities were consolidated into two dimensional (2D) maps using bicubic interpolation. Typical distribution maps are shown in the following figures where on the x-axis is the reduced velocity U_{red} and on y-axis is the nondimensional amplitude Amp_{red}.

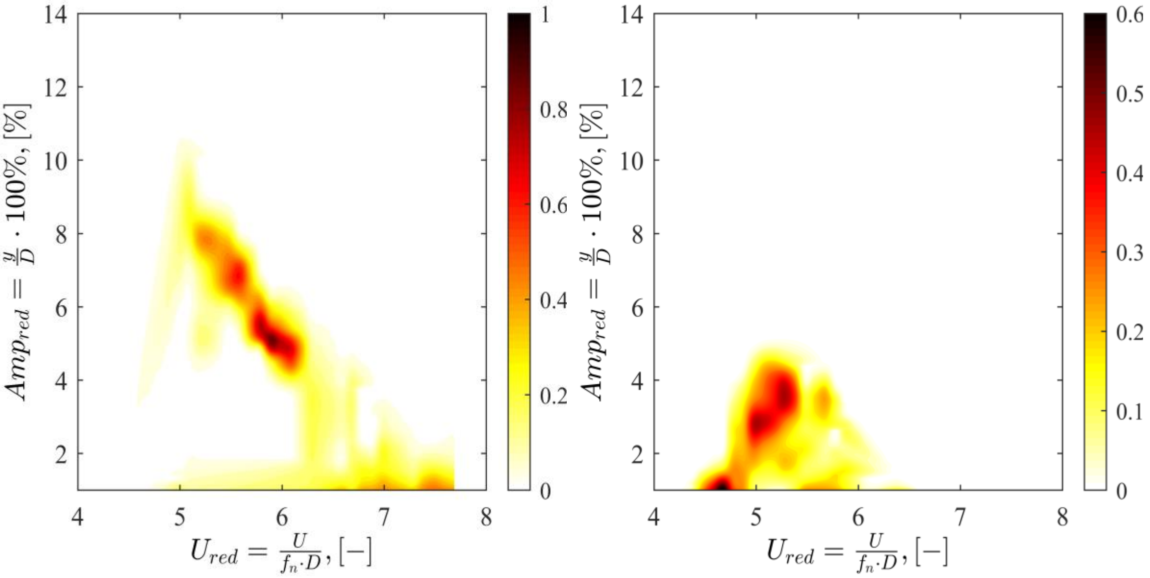

Figure 4.20 Joint probability density of vibration amplitudes of smooth cylinder in smooth flow I_u=1.5% (left), in turbulent flow I_u=4.8% (right)

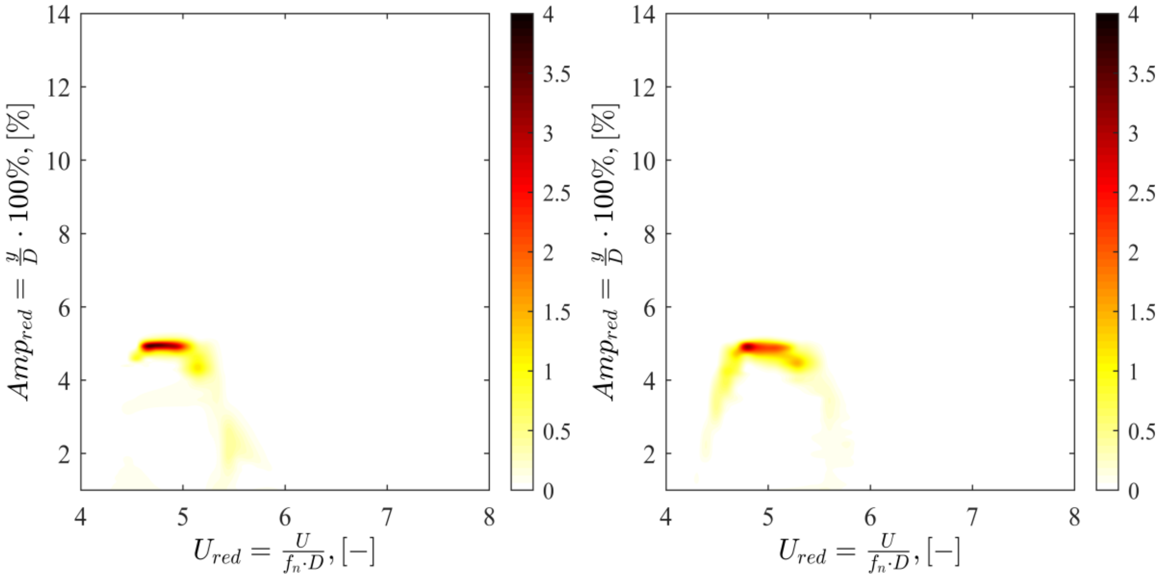

Figure 4.21 Joint probability density of vibration amplitudes of helical strand model in turbulent flow I_u*=6.7%(left),* I_u*=10.2%(right)*

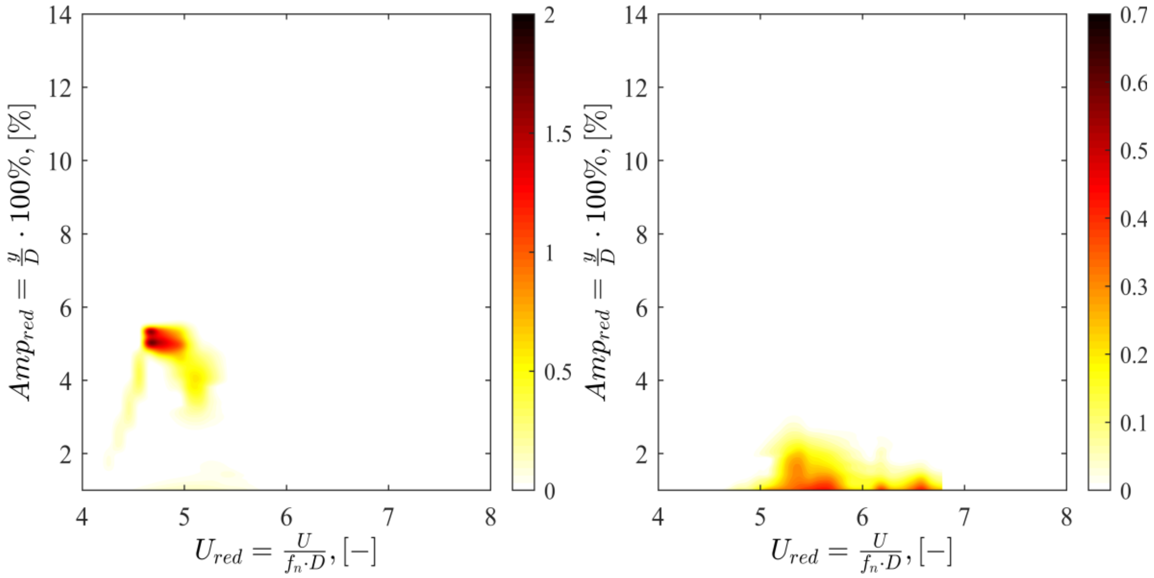

Figure 4.22 Joint probability density of vibration amplitudes density of vibration amplitudes of iced model (α=0°) in turbulent flow I_u*=4.8% (left),* I_u*=10.2% (right)*

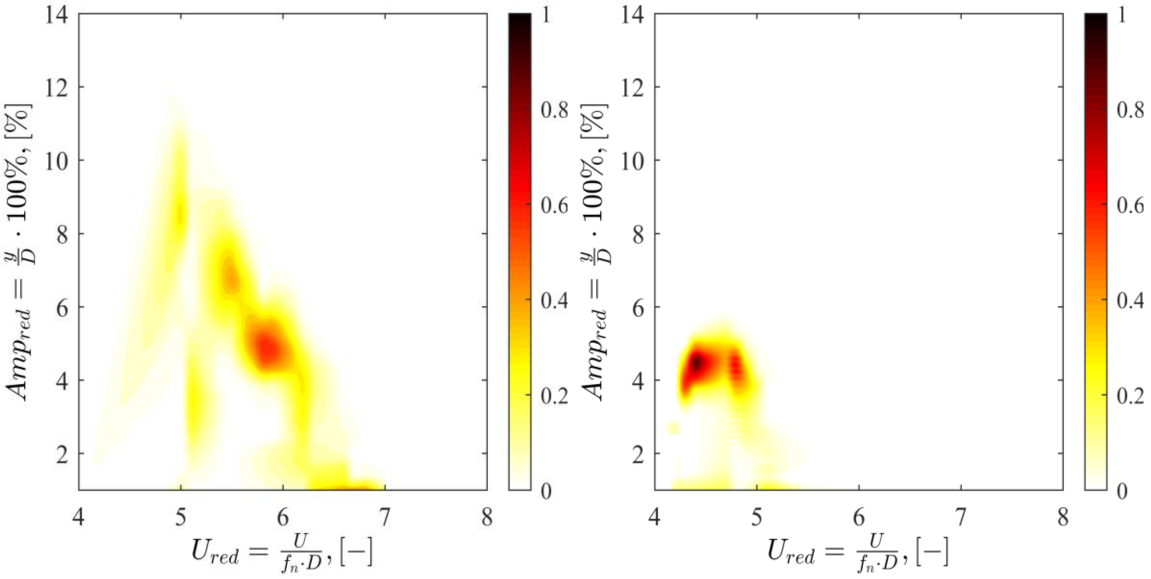

Figure 4.23 Joint probability density of vibration amplitudes of iced model (α=90°) in smooth flow I_u=1.5% (left), in turbulent flow I_u=10.2%(right)

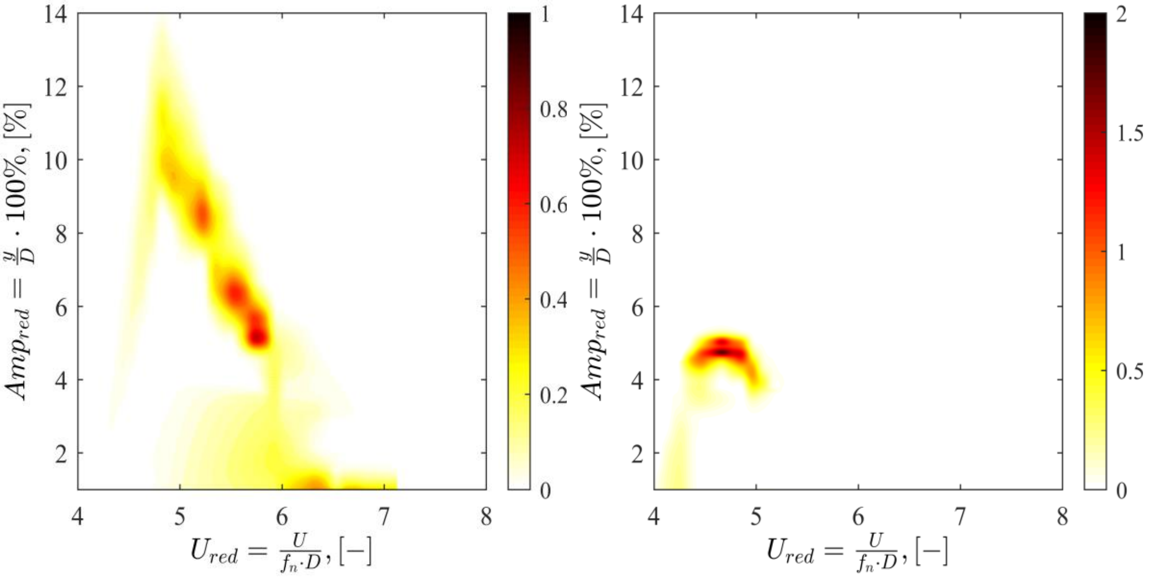

Figure 4.24 Joint probability density of vibration amplitudes of iced model (α=180°) in smooth flow I_u=1.5% (left), in turbulent flow I_u=10.2%(right)

Among all the models, the helical strand has the smallest range of peak amplitudes and at the same time the most stable Strouhal number.

5. Second stage of experiments

The rotor of engine used at Ruhr University in Bochum to drive the fan was regulated by rheostats and strongly depended on the incoming voltage fluctuations. Stability of mean flow velocity are critical for cases with free stream and surface generated turbulence when synchronization of vortex shedding and structure vibration need a longer time. In this case synchronization also could be complicated by a relatively low aspect ratio of the models.

Based on the results of the first stage of measurements carried out in the wind tunnel of Ruhr University in Bochum (RUB), a new measurement was prepared and carried out. The task of the new series of experiments was to use the optimal model parameters and improved facilities to make detailed measurements of the mechanical response and frequency characteristics of the turbulent incoming wind flow and wake flow characteristics of cable models.

Experiments were carried out in the wind tunnel of the Institute of Theoretical and Applied Mechanics in Telč, Czech Republic.

5.2 Experimental setup for second stage of experiments

Wind tunnel

The closed-circuit Climatic Wind Tunnel is the experimental device for flow and turbulence modelling (considering the optimal size-to-economy factor) and for the described problematics. It is designed to serve for experimental simulations of the atmospheric boundary layer flow and wind effects on structures.

The axial ventilator with the 200 kW power has the and the diameter of 2.2m. Asynchronous motor with frequency regulation of power/revolutions through the control software. This allows to achieve high stability of the rotor speed of the engine and, consequently, the flow rate.

Initially, the wind tunnel in Telč speed adjustment step was set to approximately 0.3 m/s. For more detailed testing, the controller was reconfigured to obtain the minimum speed control step equal to 0.03 m / s. The small increment step allows very detailed testing procedure.

Wind tunnel has two testing sections:

- Climatic section – experiments related to wind effects with features like freeze, heat radiation and rain. The climatic section is a rectangular cross-section of 2.5×3.9 m with length of 9.0 m. In this section, the wind speed ranges from 0.8 to 20 m/s (depending on the position of the vertically moveable ceiling and flow nozzle). The rain intensity together with the size of drops is regulated to simulate the effects corresponding to drizzle or heavy rain. The radiation system with four infrared lamps with total power of 8kW and maximal incidence of 60° to the floor is available. Precipitation analyzer is available in the laboratory. The temperature in this section can be controlled in the range -10°C to +40°C.

Aerodynamic section - experiments in the field of wind effects on structures, wind characteristics, aero-elastic structural response. The aerodynamic section with turntable and has rectangular cross section area of 1.9×1.8m. The total length of the test section is 11.0 m. The simulation of the atmospheric boundary layer with required characteristics is based upon turbulent elements, such as spires, grids, barrier and floor roughness. The wind speed can be regulated in the range 0,06 m/s-50 m/s.

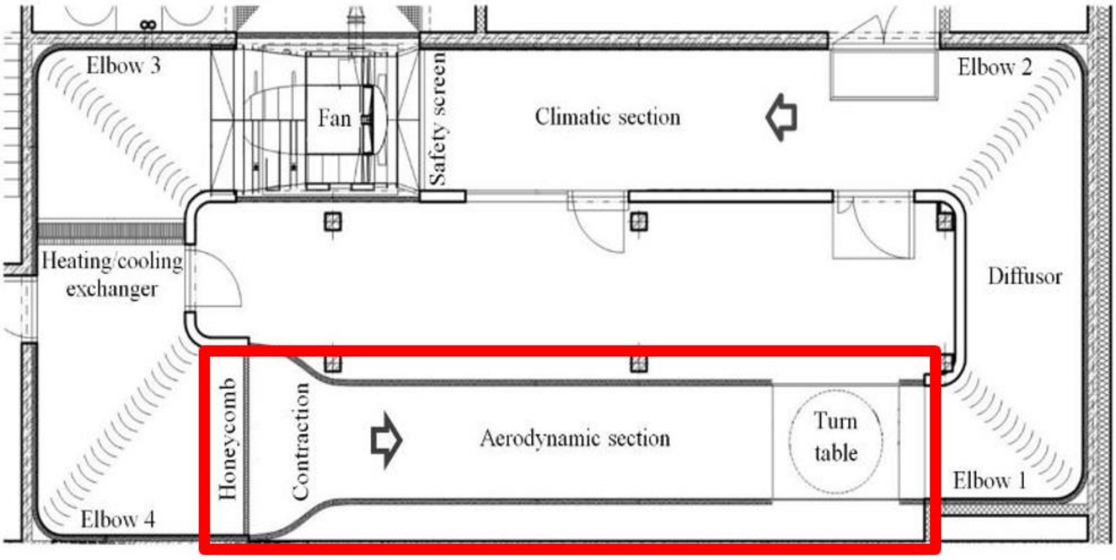

Figure 5.1 Closed circuit wind tunnel with climatic section in Center Telč Institute of Theoretical and Applied Mechanics of the Czech Academy of Sciences

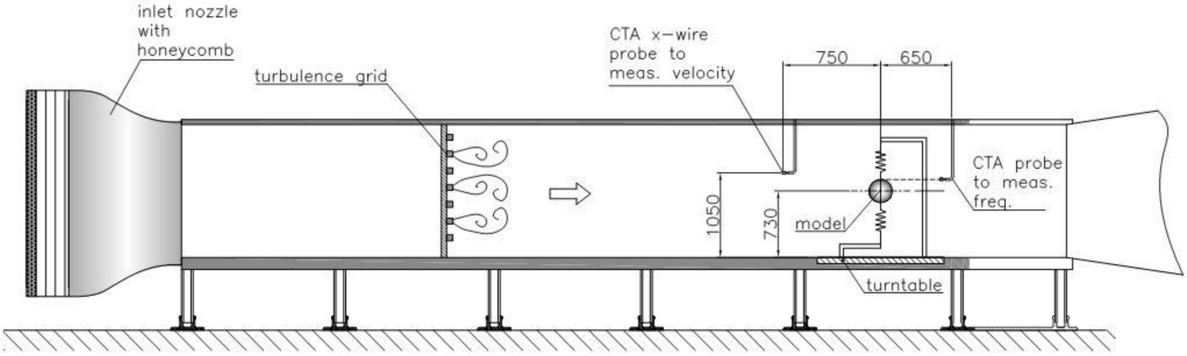

Figure 5.2 Arrangement of the experiment in the aerodynamic test section of wind tunnel

Models

Open wire helical strand cables were selected as the object of the analysis of fatigue load created by the wind. In order to evaluate separately impact of lay angle and surface roughness factors models with next parameters were produced:

- model of helical strand (construction 1x61 according ISO 17893:2004) cable with relative surface roughness k/D = 5.6% and lay length l = 12·D;
- model of helical strand cable (construction 1x61), k/D = 5.6%, l = 24·D;

- model of helical strand cable (construction 1x91), k/D = 4.5%, l = 12·D;
- circular cylinder, used as reference model.
- Iced cable model with identical shape used in previous experiments [94].

In the Table 5.1 some examples of using helical strand cables as structural elements are presented.

All models were made from polystyrene, polished and varnished. The length of models were 1.27 m, diameter D = 0.13 m (for circular part in case of iced cable model). The length-to-diameter ratio≈10. A rigid carbon fiber tube with outer diameter 13 mm and 2 mm wall thickness was used as an axis that can be fixed to the experimental stand.

The real cables have diameters usually lying in the range of 30-60 mm. The increased scale of models diameter were used to obtain Reynolds number range corresponding to averaged velocity with the highest probability, see Figure 3.5.

Table 5.1 Models of helical strand cables used in present study

Model of cable (ISO 17893:2001€):	1x91	1x61	1x61
Number of wire layers in cable	6	5	5
Number of wires in outer layer	30	24	24
Roughness k/D, [%]*	4.55%	5.56%	5.56%
Pitch (l/D)	12	12	24
Kojal mast	✓		
Křešín mast	✓	✓	
Javořice mast	✓		
Mass of model, [kg]	0.4668	0.3978	0.434

The choice of polystyrene as a material for models was based on the practical issues. It can be easily cut and shaped, it has sufficient strength to transfer the load to the rigid carbon axles and next to the dynamic force balance stand. Also, very low specific density made it possible to achieve a low mass of the model at a given size and thereby reduce inertial forces during vibrations which could influence the measurement of the aerodynamic lift. Models were hand-made, sanded, varnished with water-based varnish and sanded again to reduce residual surface roughness from manual processing of the model.

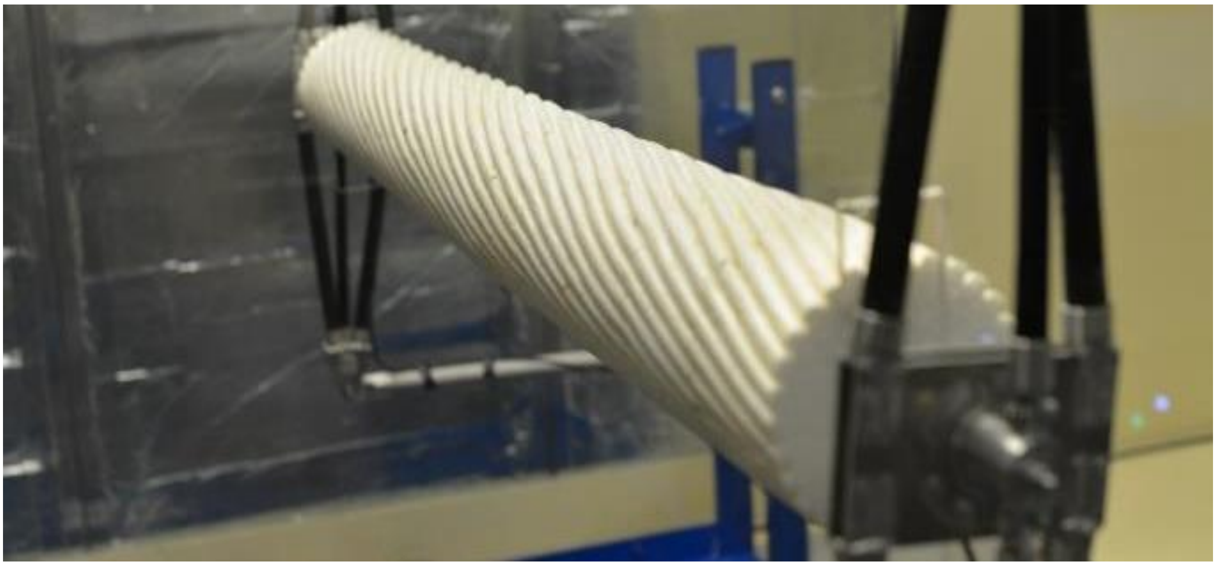

Figure 5.3 Model of 1x91 cable on the dynamic force balance stand

Dynamic force balance stand

To take into the consideration the measurement specific requirement, the available dynamic force balance, see Král et al. [91], has been remodeled and upgraded as follows:

- The spring mechanism responsible for setting the frequency of torsion vibrations and the axes on the rolling bearings were dismantled, which allowed to reduce the oscillating mass of the stand by 0.8 kg.
- On both arms of the stand, instead of rotation axes, embedded parts for thermal compensated 6 component force transducers ATI Nano25 [95] were fixed, with the ability to adjust the angle. The force sensors themselves are installed between the arms of the stand and the axis of the model in such a way to be able to perceive the resulting forces F_{tot} from vortex induced vibrations, see Figure 5.4 Sensor arrangement on a balance stand F_{tot} in this case, consisting of two components : lift (aerodynamic) force and inertia force from nearly-harmonic changing the acceleration model with fluctuations relative to force balance stand arms.
- On the arm which is near to the observer, high precision single axis capacitive low profile DC accelerometer was installed. It is Kistler 8302B2S1 type with measuring range ±2g, transverse sensitivity ≤2%, sensitivity 2500 mV/g, noise (10-100Hz) 25µg_{rms}, max zero offset 10mg, and resonant frequency 1.2 kHz. Data from this accelerometer is used to calculate the inertial force during VIV.

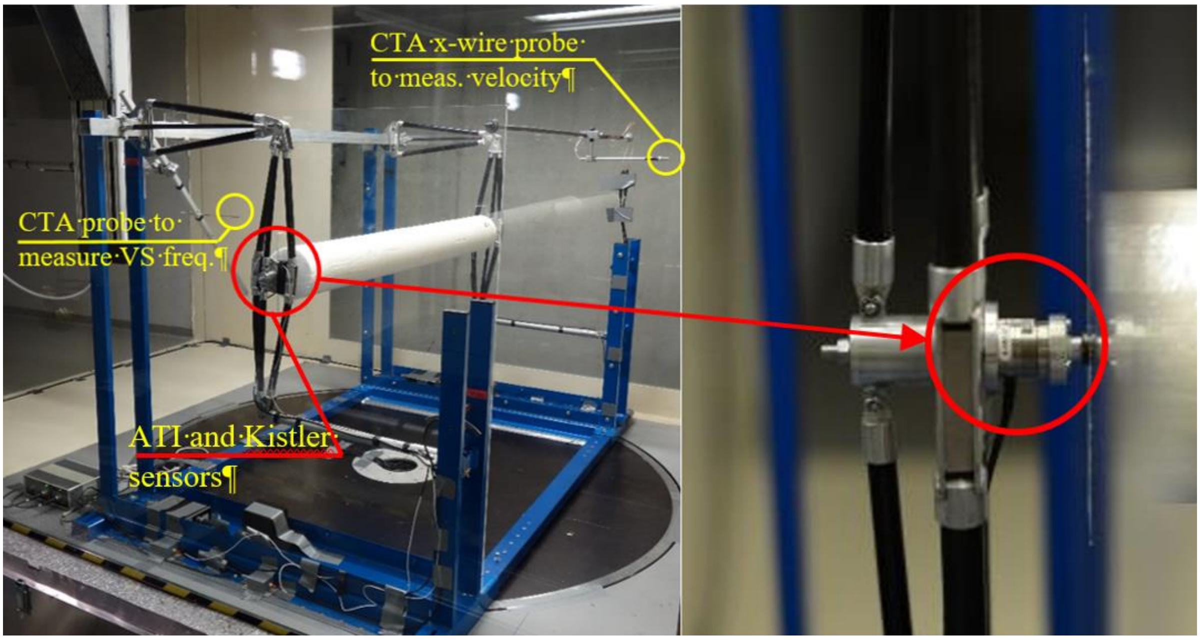

Figure 5.4 Sensor arrangement on a balance stand

While calculating the inertia force, the following corrections were used:

- The weight correction for the Archimedean force acting on the model in the atmosphere.
- the local gravity acceleration value has been calculated according to International Gravity Formula [96] based on latitude and Free Air Correction determined by altitude of the location of the experiment [97]:

$$IGF80 = 9.780327\,(1 + 0.0053024 sin^2\Phi - 0.0000058 sin^2 2\Phi) \tag{5.1}$$

$$FAC = -3.086 \cdot 10^{-6} \cdot h \tag{5.2}$$

$$g = IGF + FAC = 9.80822 \tag{5.3}$$

Where:

g - theoretical local gravity,

IGF – international gravity formula,

FAC – free air correction,

Φ=49°11'30.2"N – latitude,

h=514 m – height relative to sea level

The cable models were mounted on the stand and the frequency of vertical oscillations was tuned to *f* = 4.9 Hz. The damping decaying tests were carried out without installed model to avoid influence of aerodynamic damping and aerodynamic added mass. Mass of the model was compensated by additional weights. The decay tests were conducted with rigid carbon axis to maintain the stiffness of balance, see Figure 5.5.

The logarithmic decrement of structural damping obtained from the vibration decay δ = 0.035, see Figure 5.6.

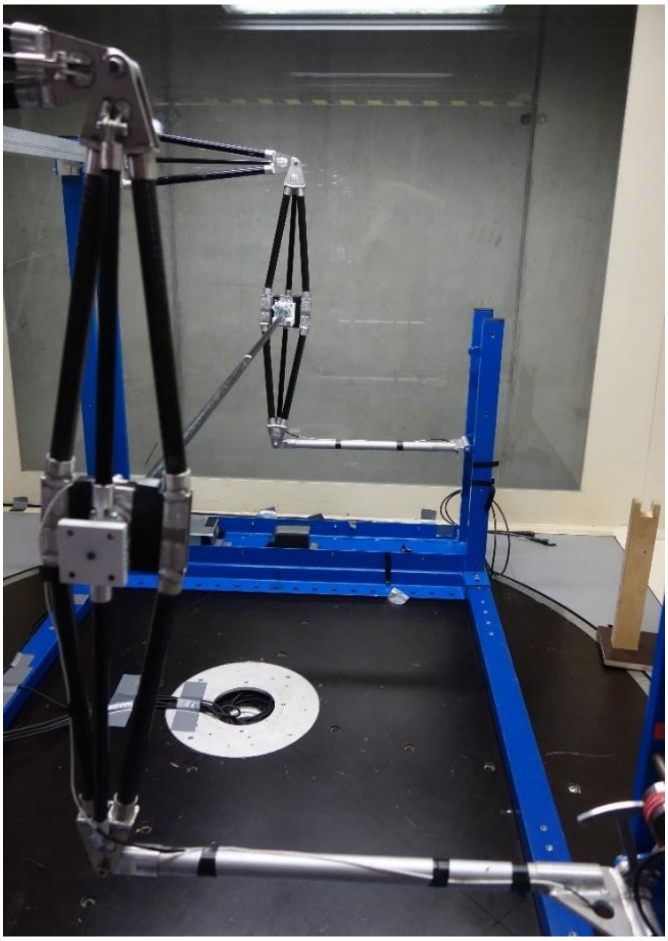

Figure 5.5 Balance stand setup for measurement of structural damping

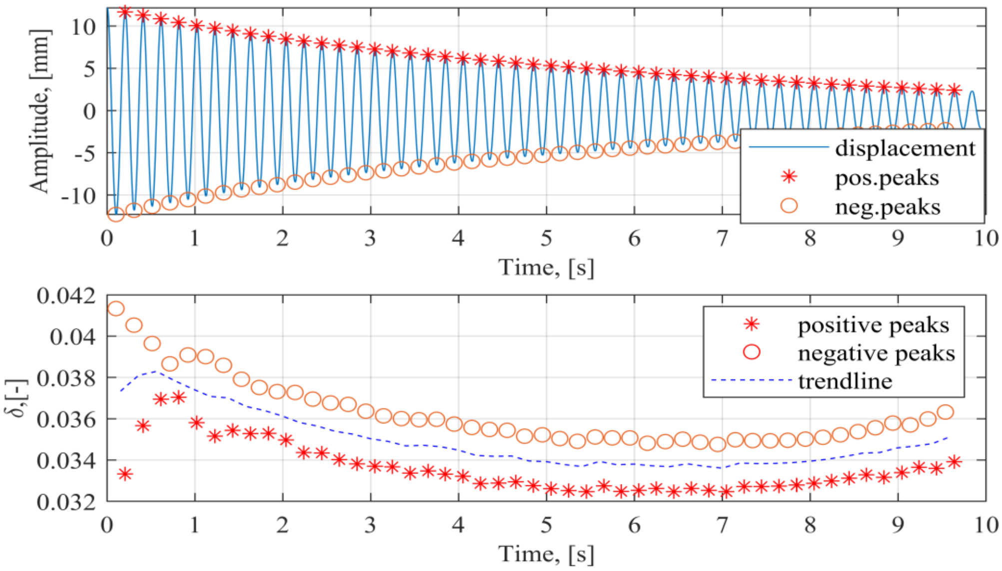

Figure 5.6 Free vibration decay (top) and values of logarithmic decrement (bottom)

To create conditions for two dimensional flow on both sides of the model were fixed plexiglass screens with clearance ≤2mm. Also, to assess the effect of the flow on parts of the stand in the flow, attenuation tests in the moving air flow were carried out according to which this effect was determined to be negligible.

The Scruton number value for models was about Sc = 6.4. The duration of each measurement was 120 seconds. The measurement of the response was carried out in the range of reduced velocity $U/(f \cdot D) =$ 2 ÷ 8 and the Reynolds number Re = $1.12 \cdot 10^4 \div 4.5 \cdot 10^4$. The lock-in range was measured in two directions:

- velocity was increased in steps from the value lower than theoretically predicted critical velocity till resonant vibrations was obtained end next till the end of lock-in vibrations;
- further after the end of lock-in range velocity was changed in the opposite direction: (decreased) to obtain lock-in vibrations.

Signal denoising

To improve the effective resolution of the sensors, noise reduction algorithms were applied. ATI Nano25 sensors have measuring ranges within ±125 N or ±250 N depending on the supplied calibration. In present study were used sensors with SI-250-6 Metric Calibrations operated by Controller F/T System. Direct output from F/T Controller connected to Data acquisition system DEWETRON DEWE-801 which the simultaneous sampling includes 24-bit A/D conversion with anti-aliasing filtering and signal conditioning. This connection option allows to achieve higher resolution when using filtering (up to 1/24 N for 16-Bit DAQ,) than using standard F/T Controller software (1/12 N).

The accelerometer Kistler 8302B2S1 was used as a reference instrument. The electrical signals of both sensors were normalized to their respective R.M.S. values. Thus, it is assumed that in the absence of additional influences, the signal of the force sensor should be similar to the signal of the accelerometer.

Signal to Noise Ratio (SNR) of raw force signal was 18.6908 dB. The following denoising algorithms were analyzed in software complex Matlab R2018a:

- Locally weighted smoothing quadratic polynomial regression, SNR=20.2644 dB,
- Savitzky-Golay filter, SNR=19.9778 dB,
- Cubic smoothing spline interpolation, SNR= 20.199 dB,
- Wavelet Interval-dependent denoising, SNR=20.0093.

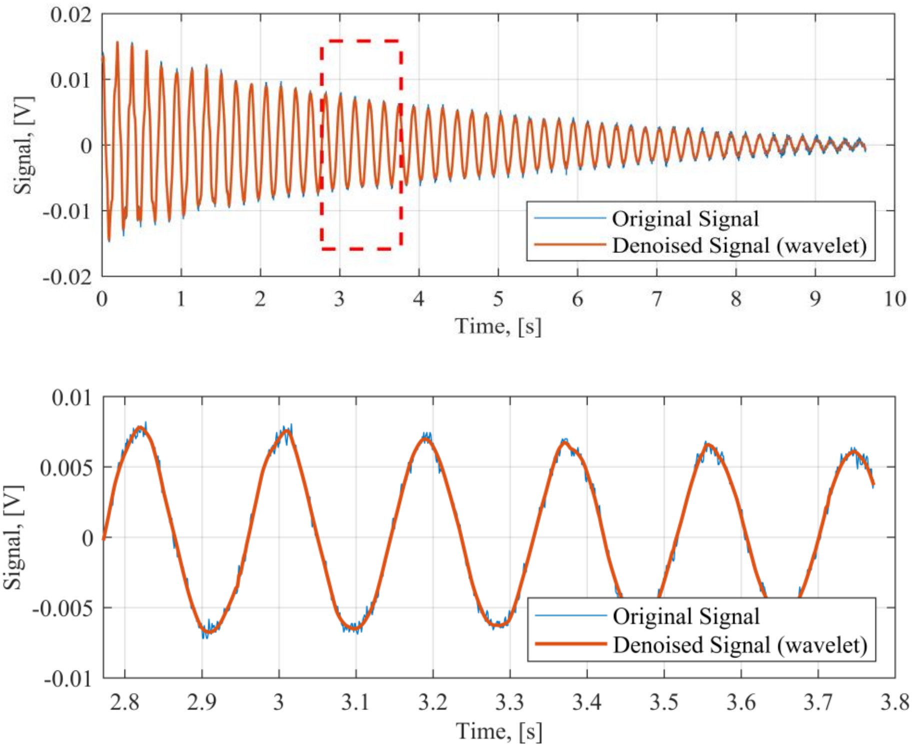

Figure 5.7 Wavelet denoising of force sensor signal

During the test, a total of 1304 measurements were carried out lasting 120 seconds with 1000Hz acquisition rate. Denoising algorithm based on wavelet transformations has a significant advantage because of from 2 to 5 times reduction in computational time and the absence of the need to select the optimal smoothening / robust parameter, despite a slightly lower accuracy compared to other algorithms.

Time shift correction

After denoising of signal a delay in the signal of the force sensors with respect to the accelerometer signal was detected. It was caused by different transition time intervals along the amplification / conditioning circuits. To compensate for the delay of the signal, the phase shift was determined, and the compensation of time shift was calculated and applied. This procedure allowed us to reduce the Signal to Noise Ratio (SNR) of already denoised force sensor to accelerometer signal nearly by 7.5 dB, see Figure 5.8:

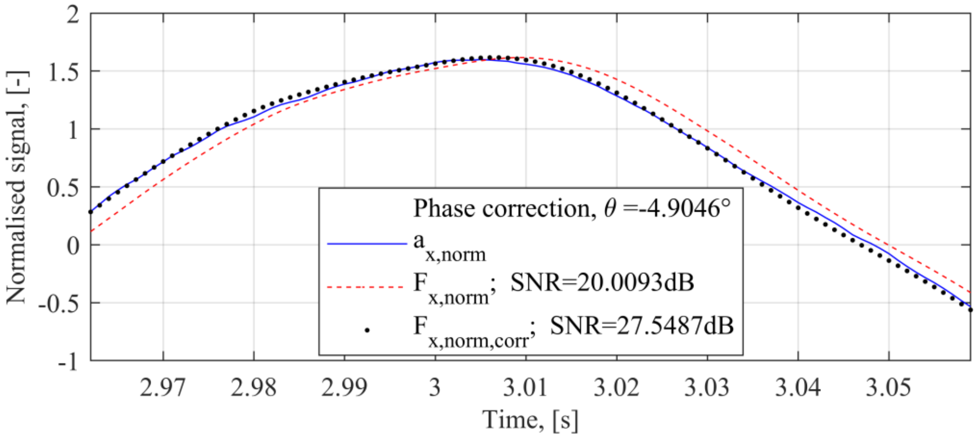

Figure 5.8 Correction of phase (time) shift of force signal to accelerometer signal

Turbulence generation in the wind tunnel

All configurations were tested in tunnel with in flow with the free stream turbulence I_u = 0.75% of incoming flow for “empty” wind tunnel and turbulent flows generated by square mesh arrays of rectangular bars mounted in front of models.

Figure 5.9 Wooden grid for turbulence generation

Multichannel CTA system by Dantec Dynamics with one x-wire and one single wire CTA probes were used to measure time series of velocity and in the wake. CTA probes were calibrated by Dantec Dynamics StreamLine Pro Automatic Directional Calibrator.

Figure 5.10 Multichannel CTA system by Dantec Dynamics and StreamLine Pro Automatic Directional Calibrator

To obtain a detailed picture of turbulence in the tested part, the flow profiles were measured with a step of 75 mm along the model axis in the speed range from 2 to

20 m / s. Inlet flow rate measurements were performed using x-wire CTA probe to separate longitude component of flow velocity. The measurements were carried out in empty test section without installed model at distances 2.1, 4.6 and 7.1 m at which the model axis will be located in the future, as well as intermediate distances 1.35, 3.85, 5.1, 5.9 и 8.4 meters.

The same x-wire probe was installed to measure wind flow velocity during mechanical response tests with model in test section in distance 0.75 m upwind of the cylinder with acquisition rate 1000 Hz.

The second single wire probe were installed in wake at the level of the horizontal tangent to model at distance 650 mm to measure vortex shedding frequency.

5.3 Results

Turbulence characteristics

The intensity and integral length scale of the turbulence were measured over a wide range of velocities along the model axis, also close to wind tunnel walls where wall's boundary layer may affect structure of grid generated turbulence. In these cases, the method of determining the scale by fitting von Karman model to measured spectra is less accurate. Therefore, a comparative analysis of von Karman and Fichtl-McVehil autospectra model and autocorrelation methods (zero crossing and exponential) was carried out.

The autospectra models showed good fitting results in high and moderate turbulence flows with moderate velocities, see Figure 5.11 and Figure 5.12. Under lower velocities autospectra curve shapes differ from spectrum distributions due to greater flexibility and quantity of fitting coefficients Fichtl-McVehil model better fits in area of high spectra energies, see Figure 5.14, Figure 5.20, while von Karman models more accurately corresponds to the measured spectrum in flow with high velocity, see Figure 5.18. Methods based on covariance coefficients work equally well for flows with all measured velocities and turbulence intensities, see Figure 5.13, Figure 5.16, Figure 5.19, Figure 5.22. The exponential method gives more stable distance-to-scale dependency with smaller deviations, see Figure 5.24 and Figure 5.25, therefore hereinafter will be considered in the results obtained according to this method, see Table 5.2. Dependency of turbulence intensity on distance is shown in Figure 5.23.

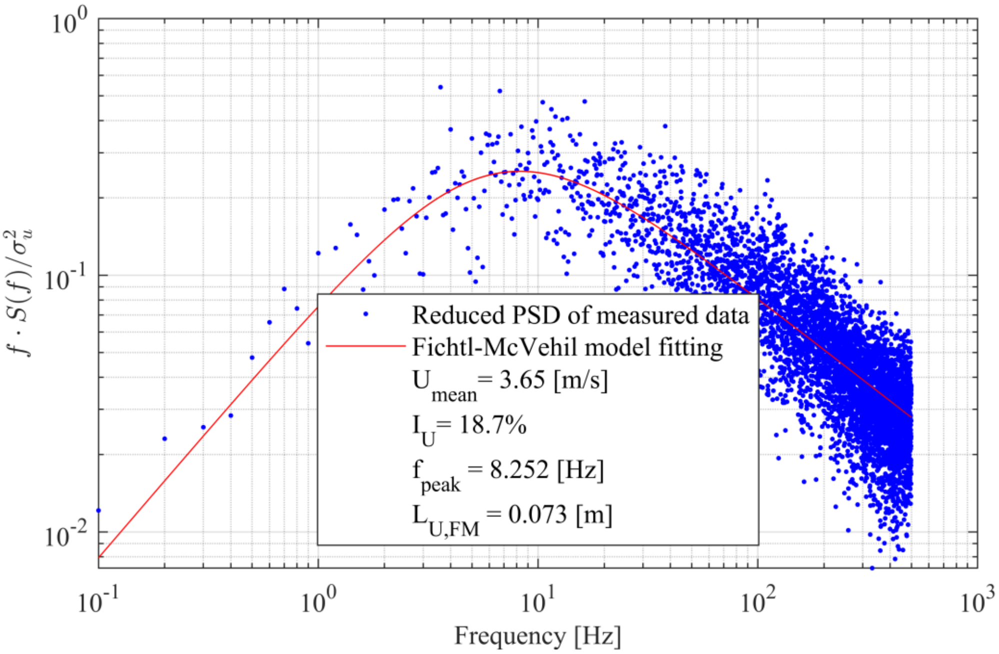

Figure 5.11 Fitting of Fichtl-McVehil turbulence model to measured normalized power spectrum

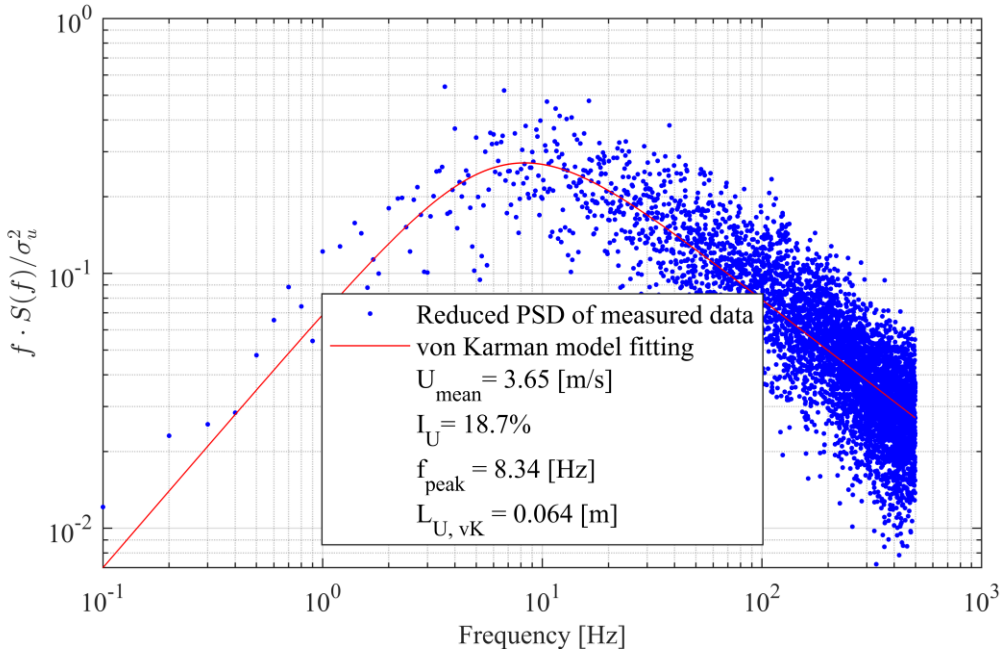

Figure 5.12 Fitting of von Karman turbulence model to measured normalized power spectrum

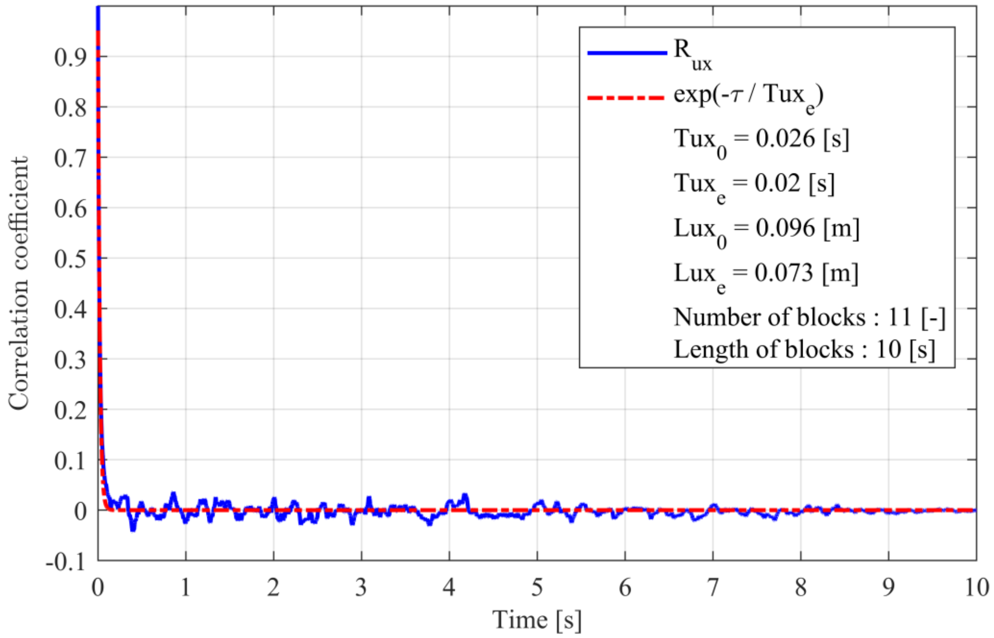

Figure 5.13 Determination of turbulence integral length scale by cross-covariance zero crossing and exponential decay methods

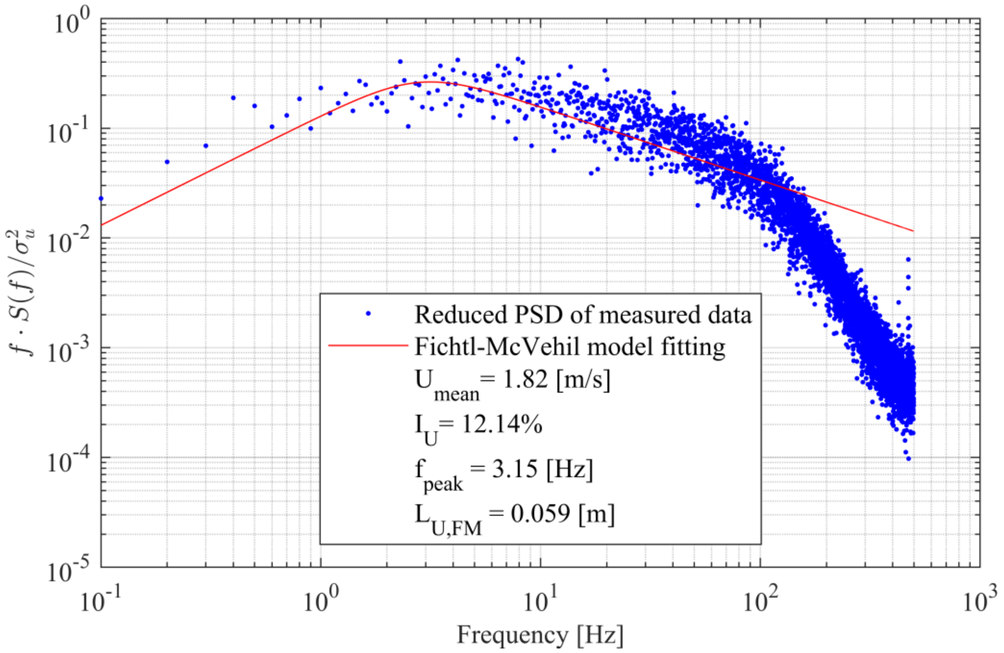

Figure 5.14 Fitting of Fichtl-McVehil turbulence model to measured normalized power spectrum

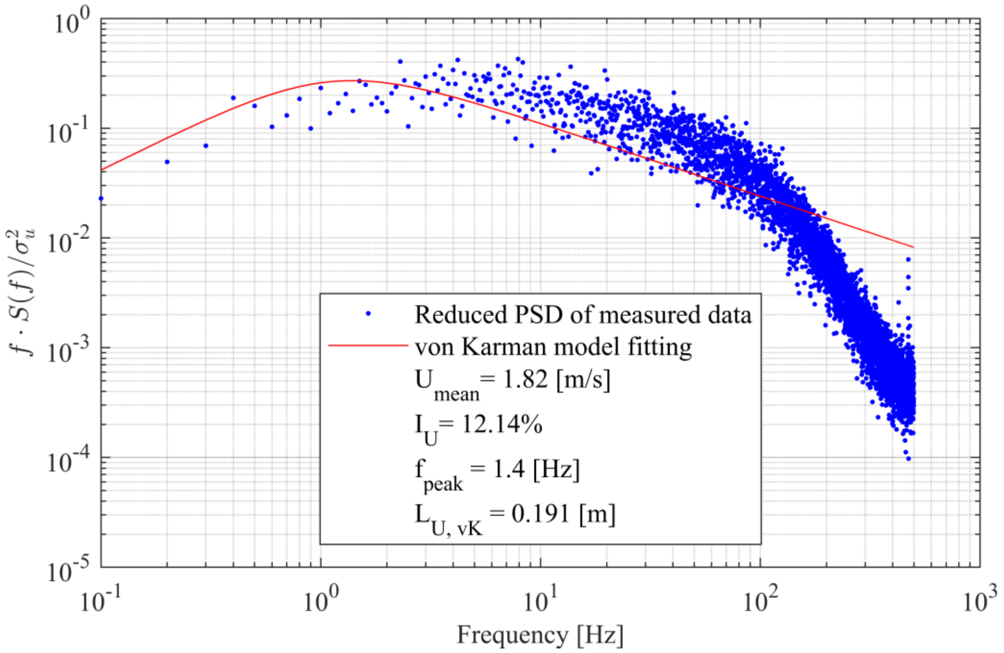

Figure 5.15 Fitting of von Karman turbulence model to measured normalized power spectrum

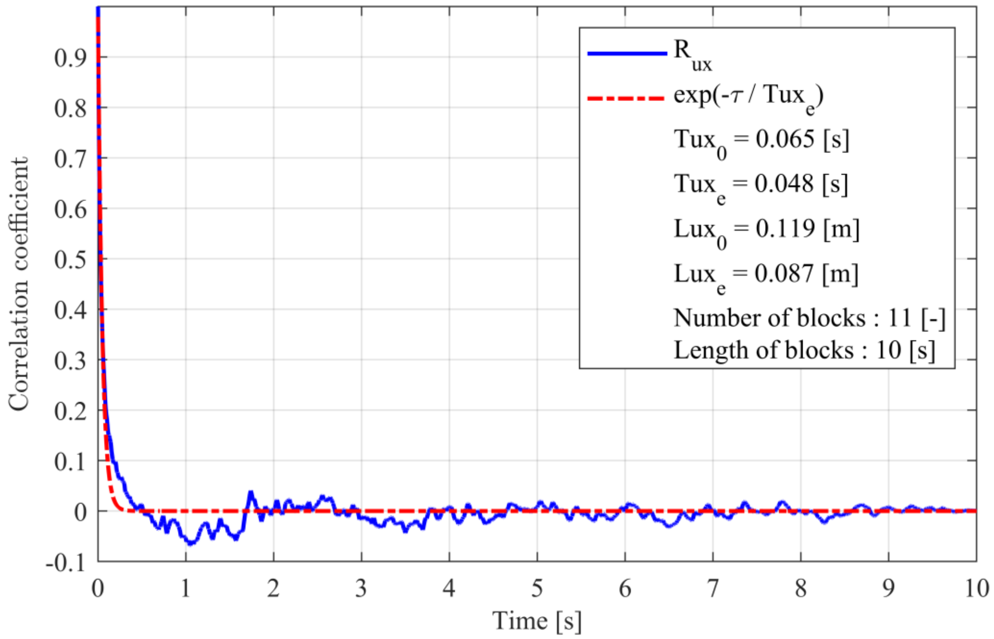

Figure 5.16 Determination of turbulence integral length scale by cross-covariance zero crossing and exponential decay methods

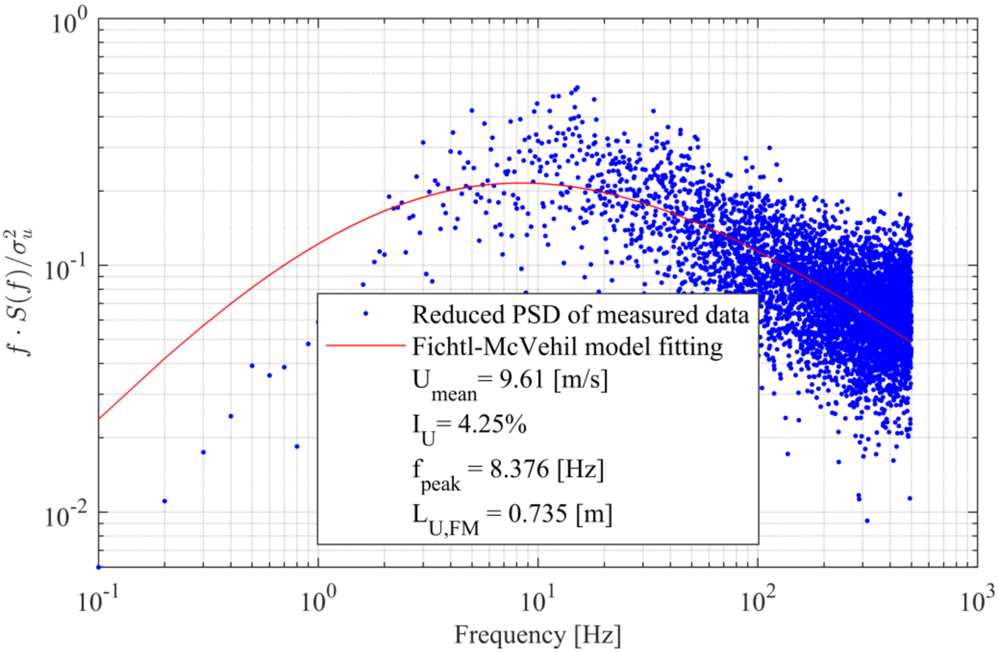

Figure 5.17 Fitting of Fichtl-McVehil turbulence model to measured normalized power spectrum

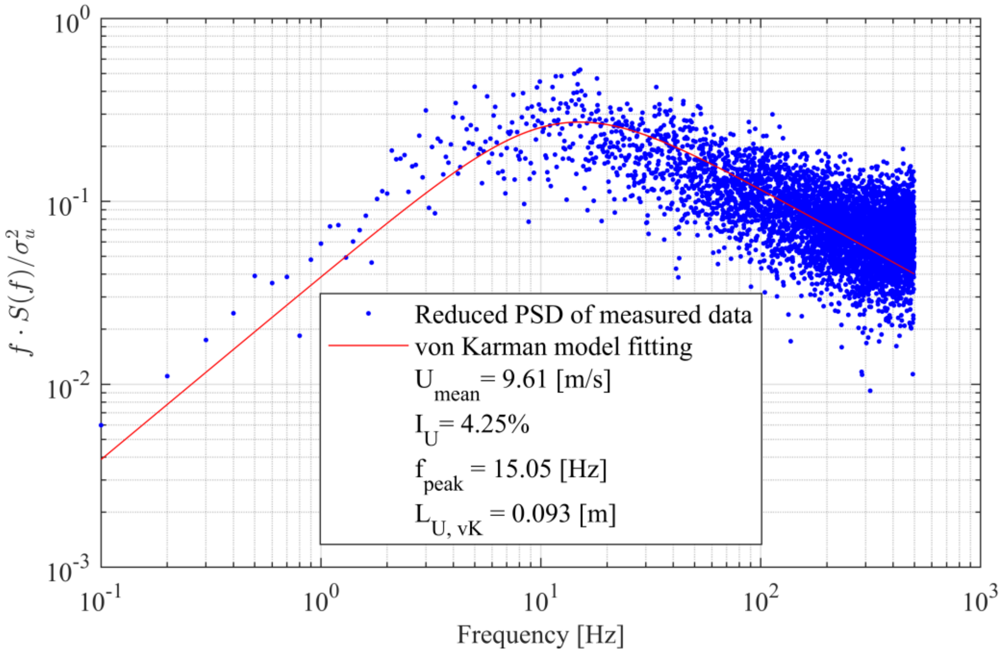

Figure 5.18 Fitting of von Karman turbulence model to measured normalized power spectrum

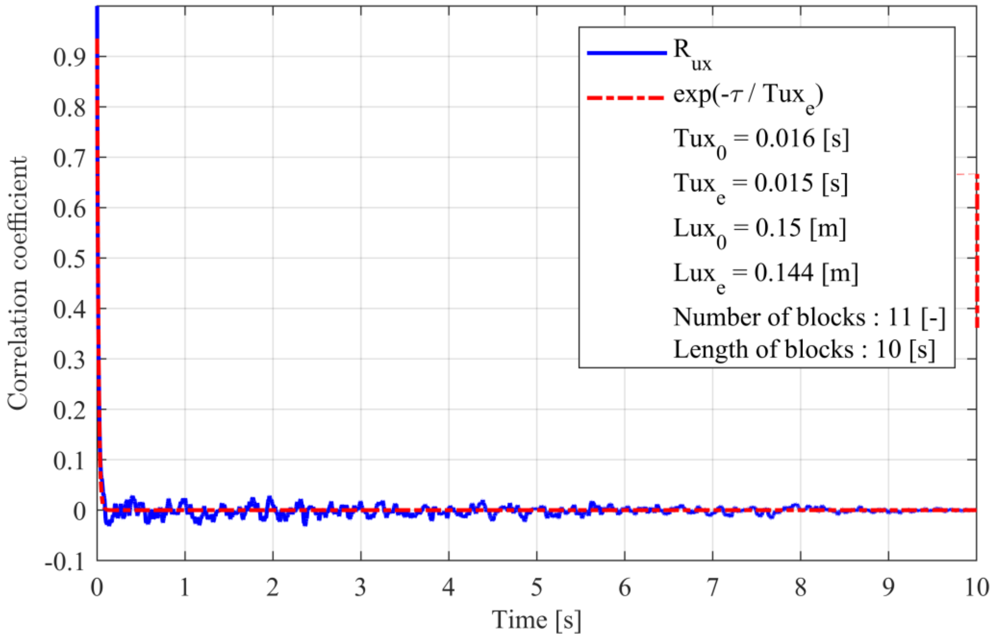

Figure 5.19 Determination of turbulence integral length scale by cross-covariance zero crossing and exponential decay methods

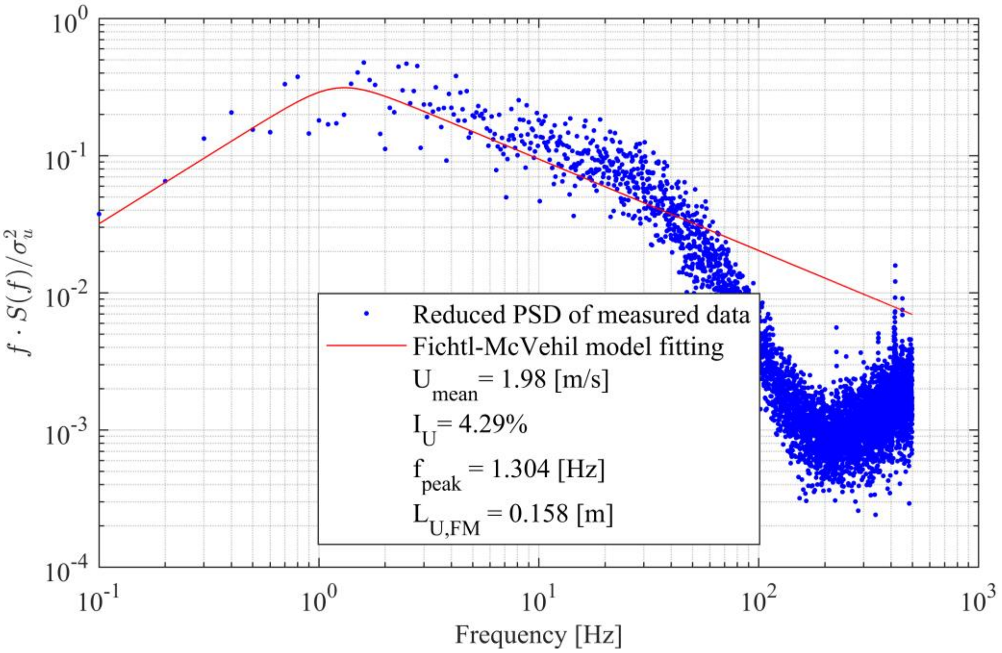

Figure 5.20 Fitting of Fichtl-McVehil turbulence model to measured normalized power spectrum

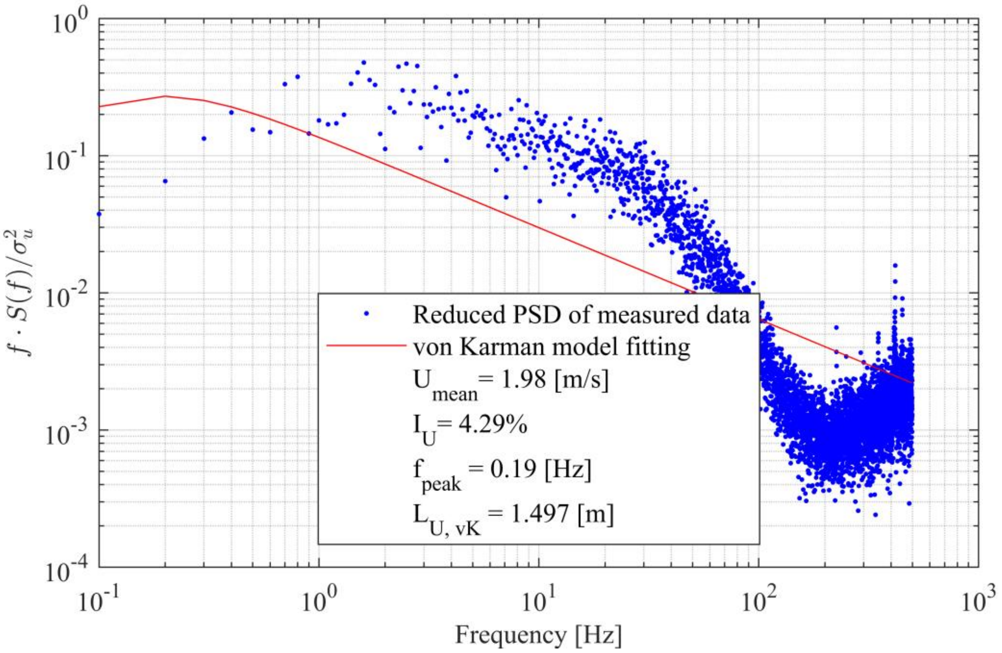

Figure 5.21 Fitting of von Karman turbulence model to measured normalized power spectrum

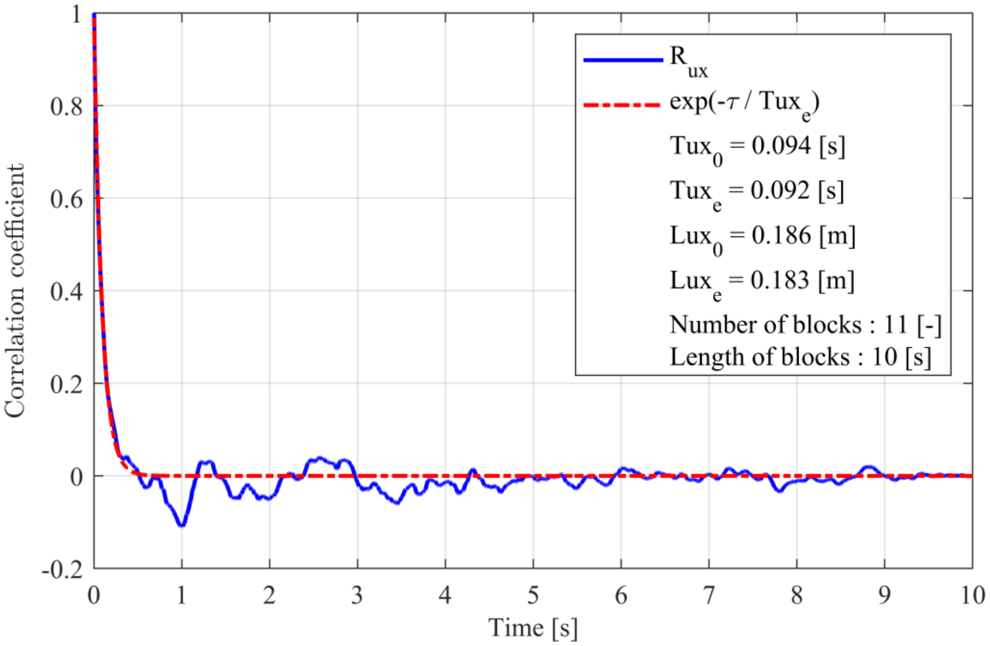

Figure 5.22 Determination of turbulence integral length scale by cross-covariance zero crossing and exponential decay methods

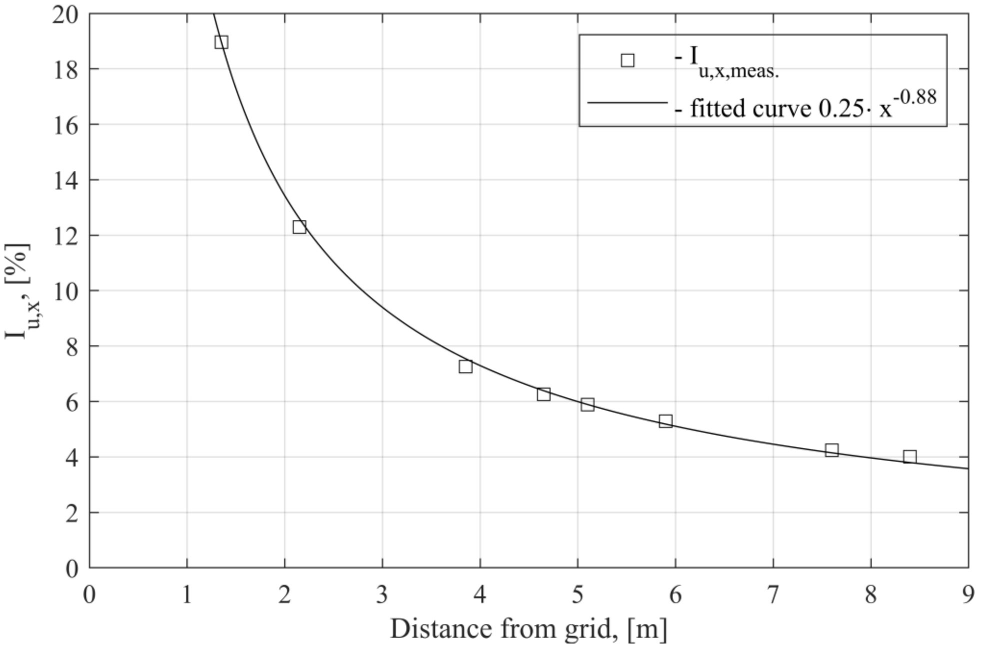

Figure 5.23 Dependence of turbulence intensity in wind tunnel on distance from grid obtained empirically

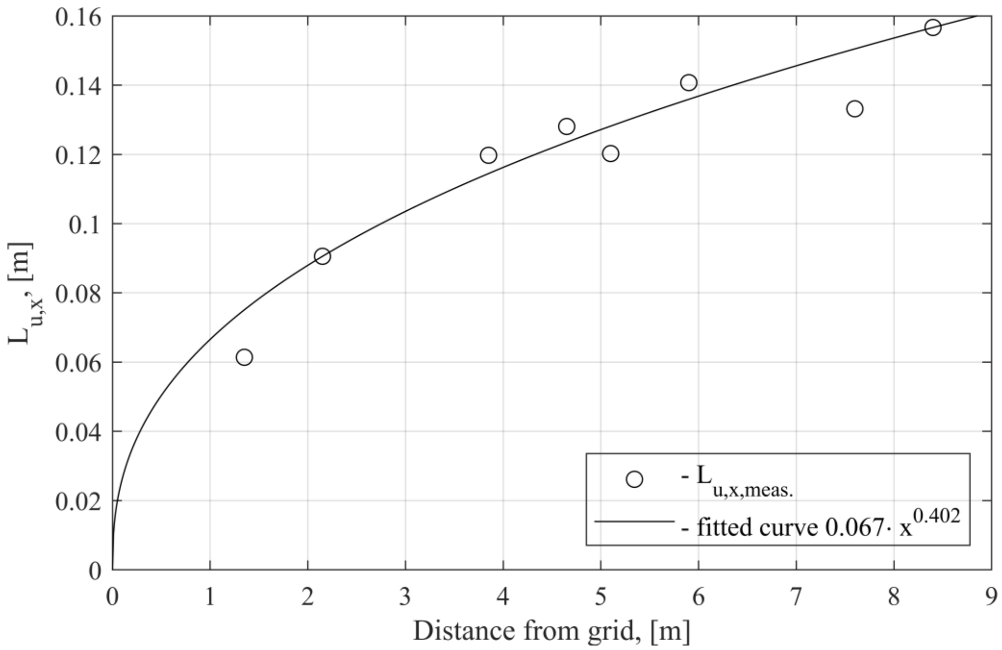

Figure 5.24 Dependence of integral length scale in wind tunnel on distance obtained by zero-crossing method

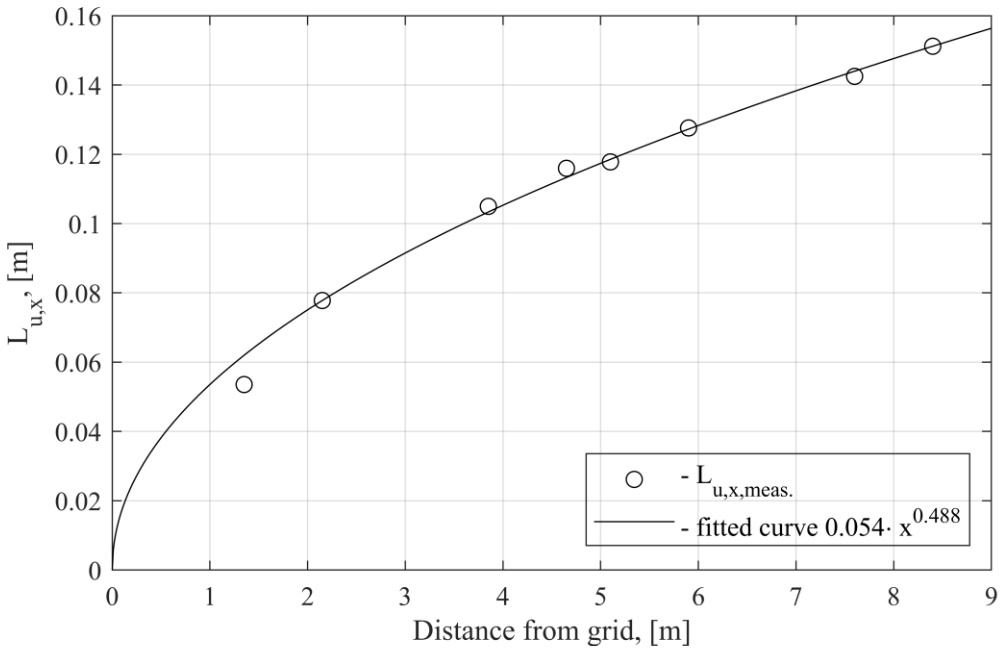

Figure 5.25 Dependence of integral length scale in wind tunnel on distance obtained by exponential method

Table 5.2 Turbulence intensity and integral length scale (obtained by exponential method) at the location used in the mechanical response experiments

Parameter		
Grid distance	Turbulence intensity I_u,[%]	Turbulence length scale $L_{u,x}$, [m]
7.1	*4.5*	*0.141*
4.6	*6.5*	*0.114*
2.1	*12.3*	*0.078*

As the reported experiments are performed for turbulence length scales that are small in comparison to those of the full-scale wind, and the tested cylinder is close to the full-scale dimensions, the future work would respectively need to address more realistic physical conditions as well.

Strouhal number

Vortex shedding frequency was measured with CTA probe mounted in wake. The lock-in range was measured in two directions:

- At first velocity was increased in steps from value about 30% lower than theoretically predicted critical velocity to beginning of vortex induced resonance and next till the end of lock-in vibrations.
- Next velocity decreased to obtain vortex induced vibrations from the value higher than lock-in range.

The measurement time period of 120 seconds was used to obtain steady amplitude of oscillation for each step after changing of flow velocity in wind tunnel.

Results are presented at Figure 10.1-Figure 10.56 of Appendix A: Figures.

The St for smooth cylinder in low turbulent flow (I_u=0.75%) was nearly equal to 0.2 what corresponds to values presented at [53] and grows with increasing of turbulence intensity up to 0.3. Models with the helical strands have larger St values both in low and high turbulence flow. Moreover, in the low-turbulent flow it is almost the same for all types of cylinders maintaining the value St=0.22. In the high-turbulent flow values of Strouhal number grows for all models. Turbulence has the most noticeable effect models for higher relative surface roughness and short lay length. The model with surface roughness k/D = 5.6% and lay length $l = 12 \cdot D$ has the maximal St values about 0.4 in high turbulent flow I_u=12.3%.

The widest lock-in range was also observed for smooth cylinder in the low-turbulent flow. Lock-in range decreases with increasing of turbulence intensity of the flow. Cable models have the similar trend of reduced lock-in range with increasing turbulence. The width of lock-in range of helical strand cable models was most affected by shortening of the lay length.

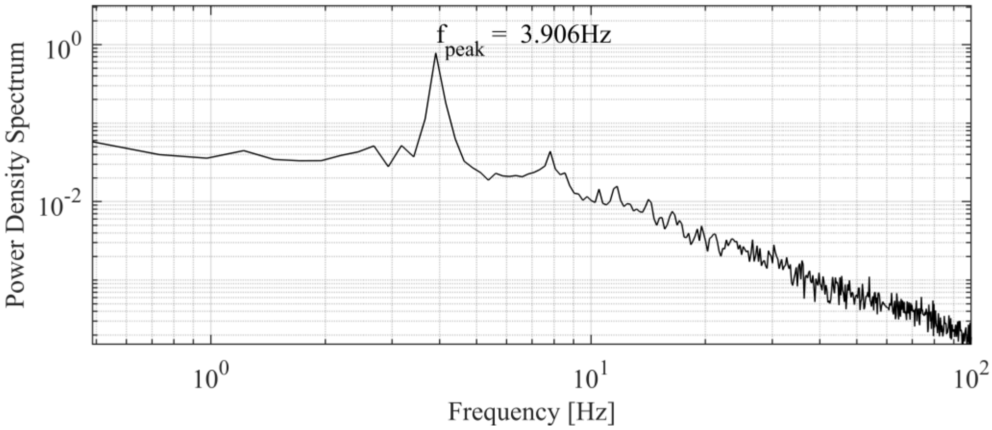

Figure 5.26. PDS of signal from CTA probe installed in wake of model, corresponding to Strouhal number 0.228 for iced model with ice accretion, α=90°

Amplitude response

The experimental results of smooth circular cylinder are shown in Figure 5.27-Figure 5.30, model of cable with ice accretions in Figure 5.31-Figure 5.42, models of: 1x91 cable with lay length 12·D (Figure 5.43-Figure 5.46), 1x61 cable with lay length l = 24·D (Figure 5.47-Figure 5.50), 1x61 cable with lay length 12·D (Figure 5.51-Figure 5.54), in the form of graphs of dimensionless amplitude vibration y/D·100% in range of reduced wind velocities. The measurements taken during gradual increasing of velocity are indicated by the empty markers and measurements taken during gradual decreasing of velocity – by the filled markers.

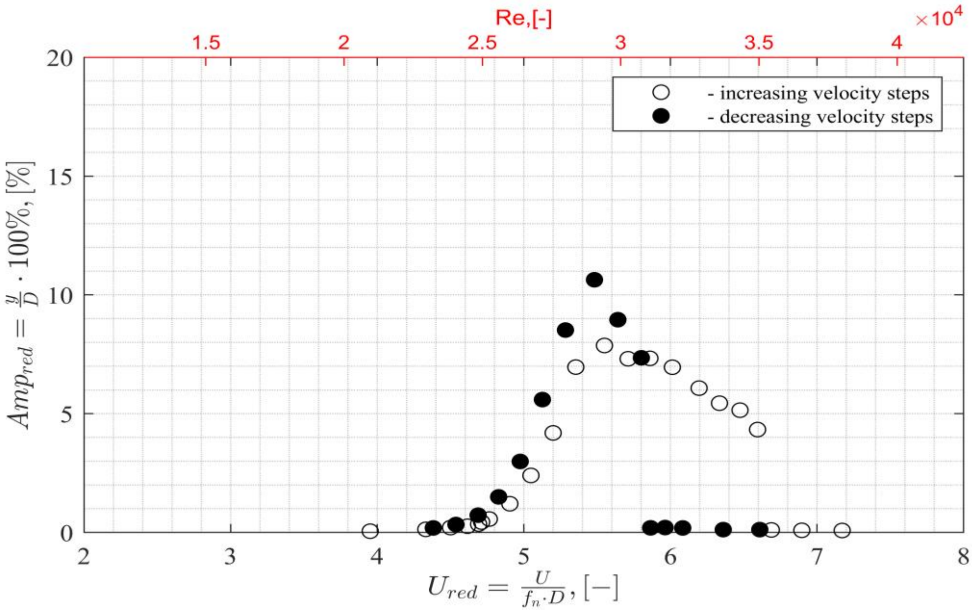

Figure 5.27 Amplitude response plot of smooth surface cable model in smooth flow I_u=0.75%

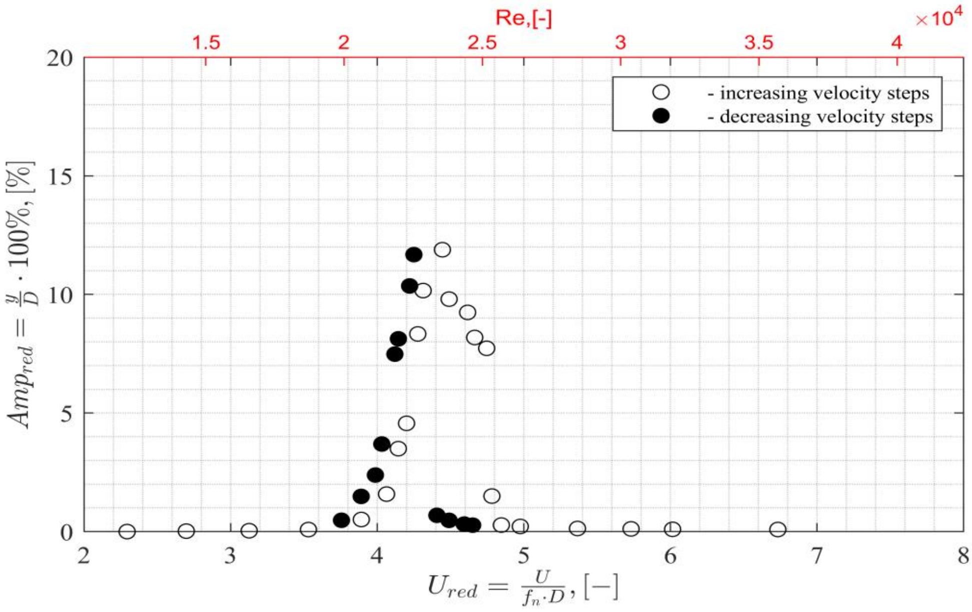

Figure 5.28 Amplitude response plot of smooth surface cable model in turbulent flow I_u=4.5%

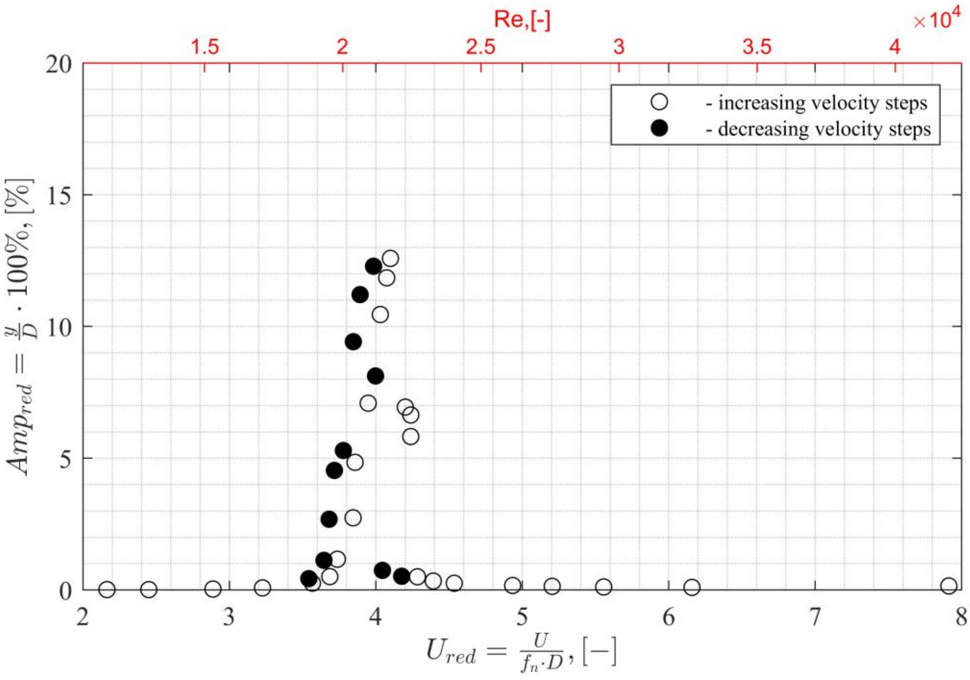

Figure 5.29 Amplitude response plot of smooth surface cable model in turbulent flow I_u*=6.5%*

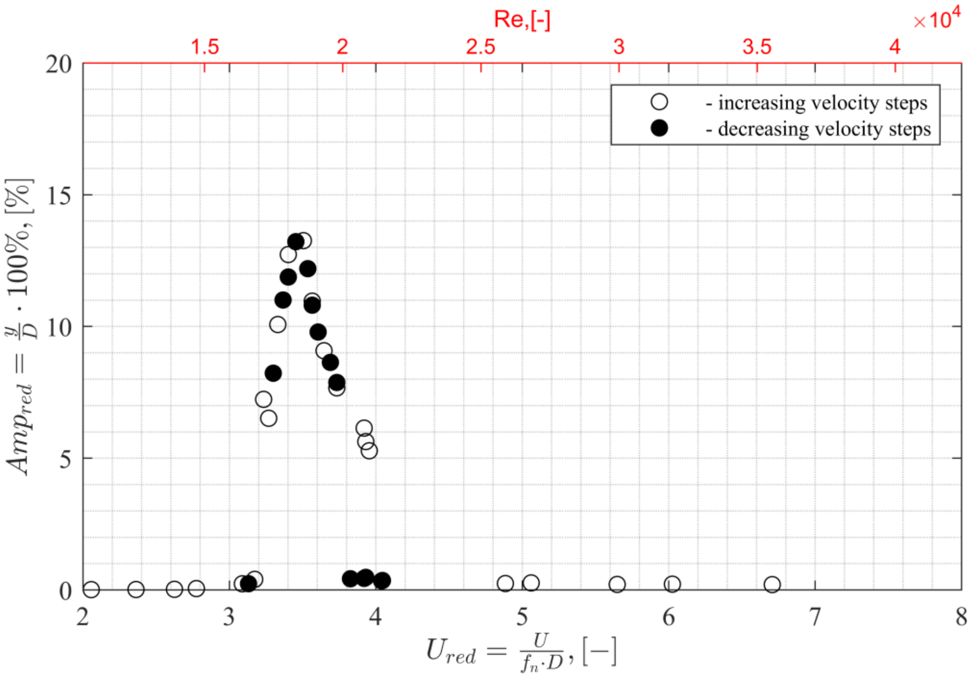

Figure 5.30 Amplitude response plot of smooth surface cable model in turbulent flow I_u*=12.3%*

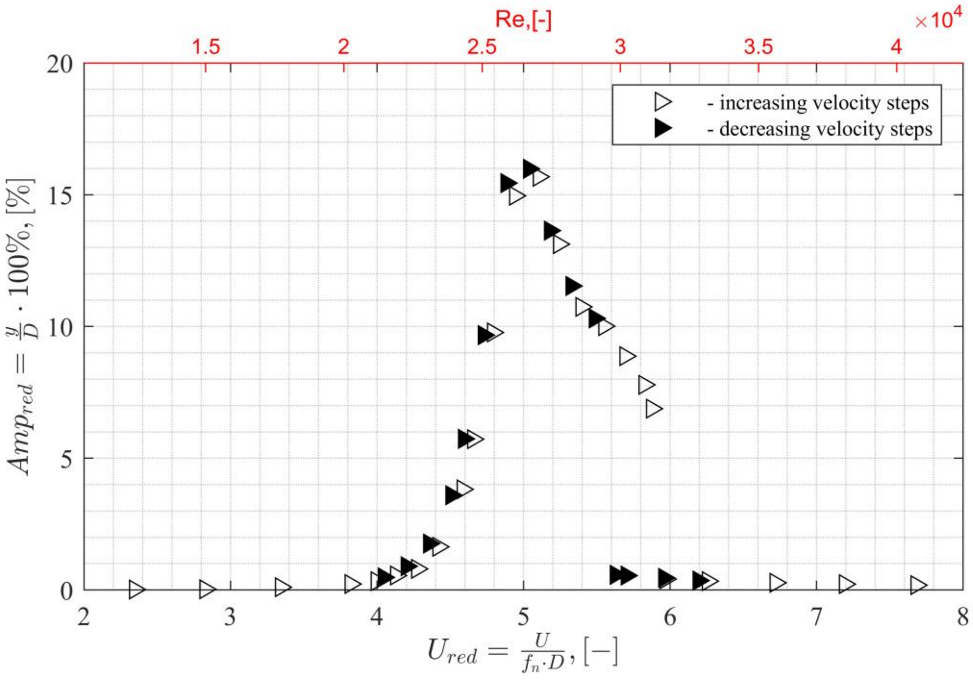

Figure 5.31 Amplitude response plot of iced cable, α=180° model in smooth flow I_u*=0.75%*

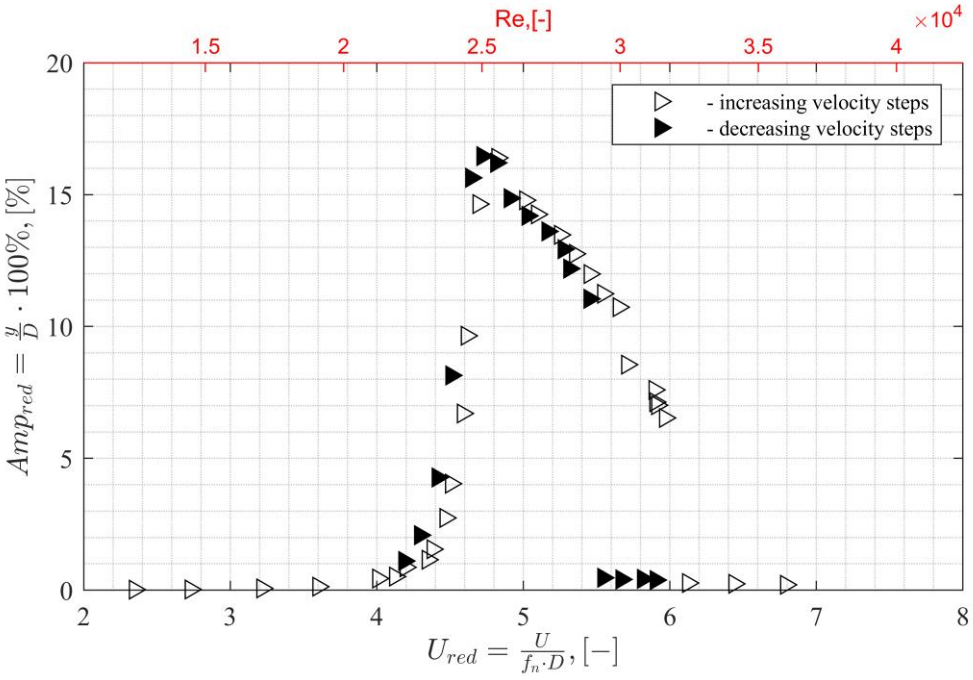

Figure 5.32 Amplitude response plot of iced cable, α=180° model in turbulent flow I_u*=4.5%*

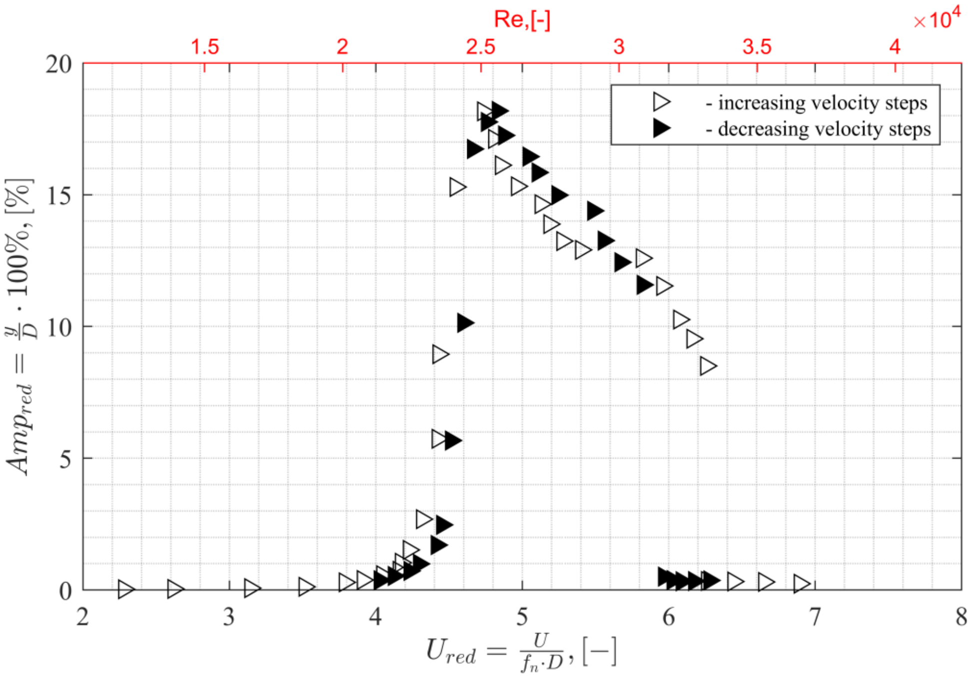

Figure 5.33 Amplitude response plot of iced cable, α=180° model in turbulent flow I_u*=6.5%*

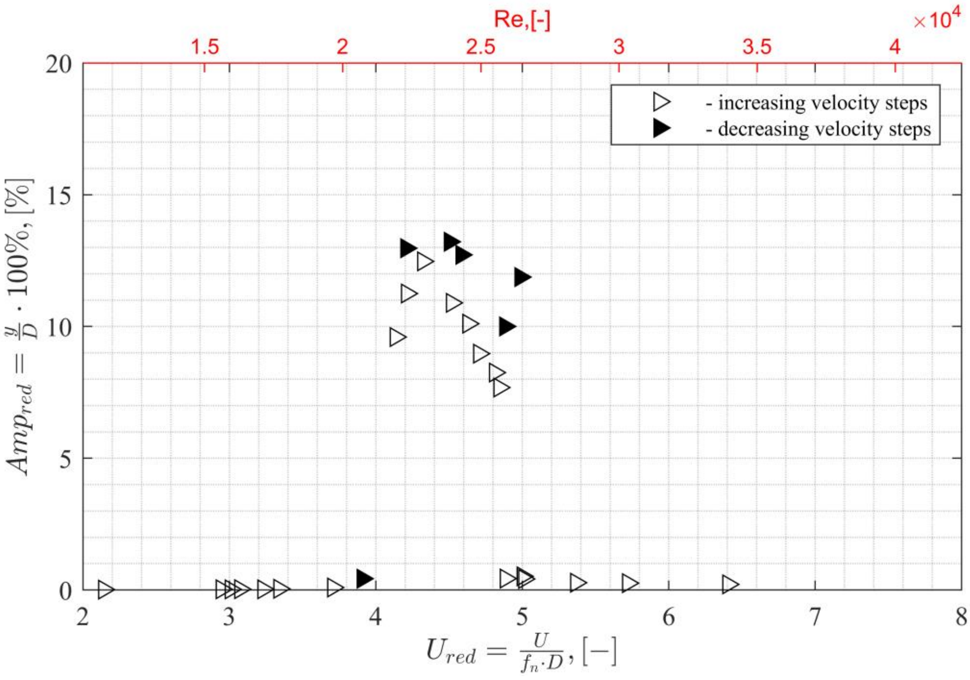

Figure 5.34 Amplitude response plot of iced cable, α=180° model in turbulent flow I_u*=12.3%*

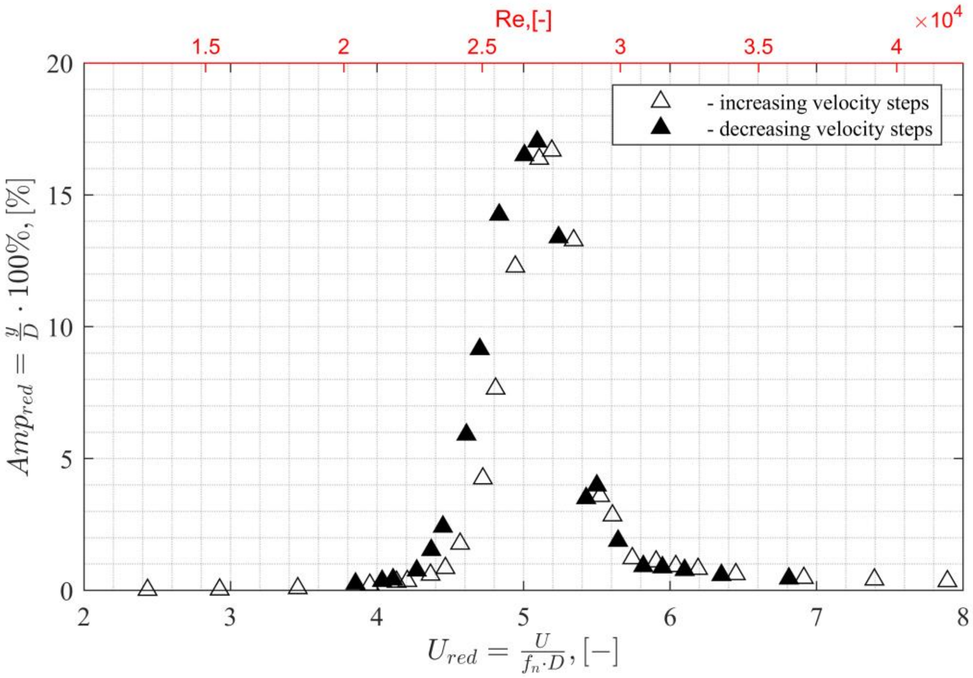

Figure 5.35 Amplitude response plot of iced cable, α=90° model in smooth flow I_u*=0.75%*

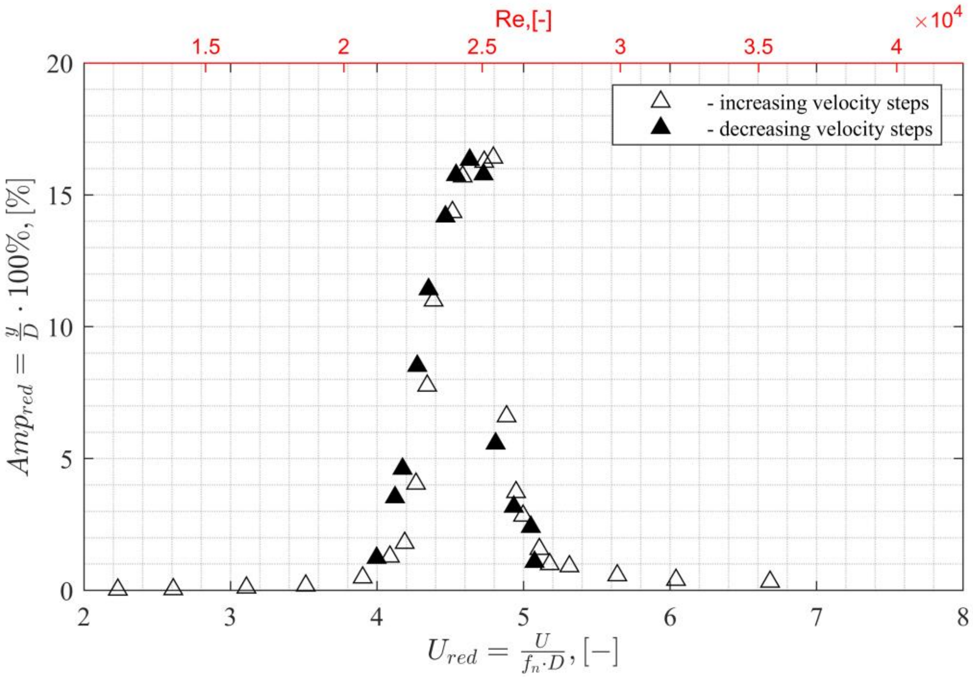

Figure 5.36 Amplitude response plot of iced cable, α=90° model in turbulent flow I_u*=4.5%*

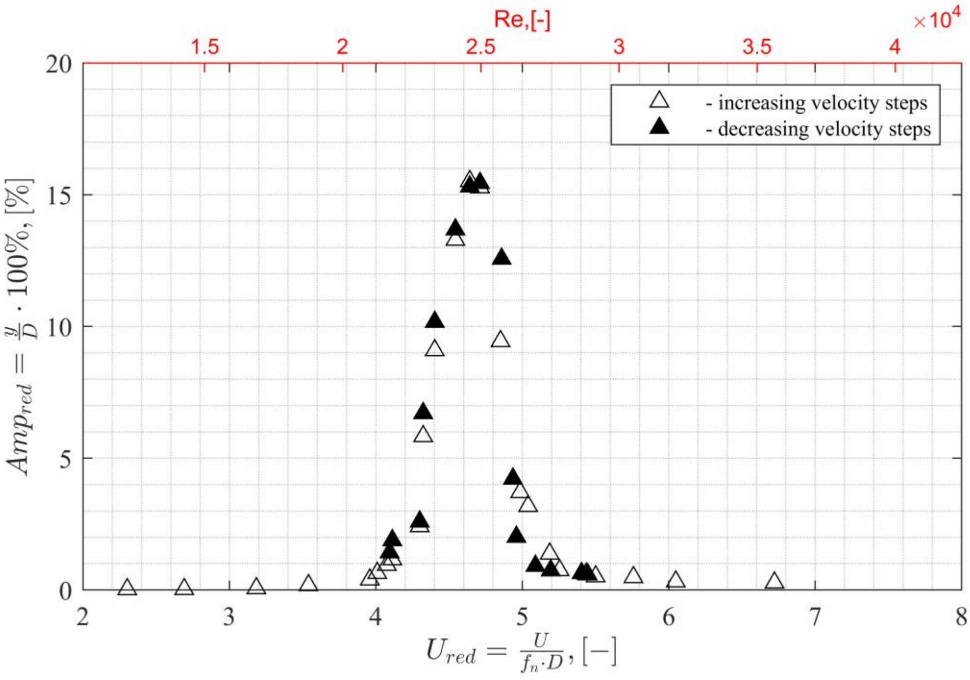

Figure 5.37 Amplitude response plot of iced cable, α=90° model in turbulent flow I_u=6.5%

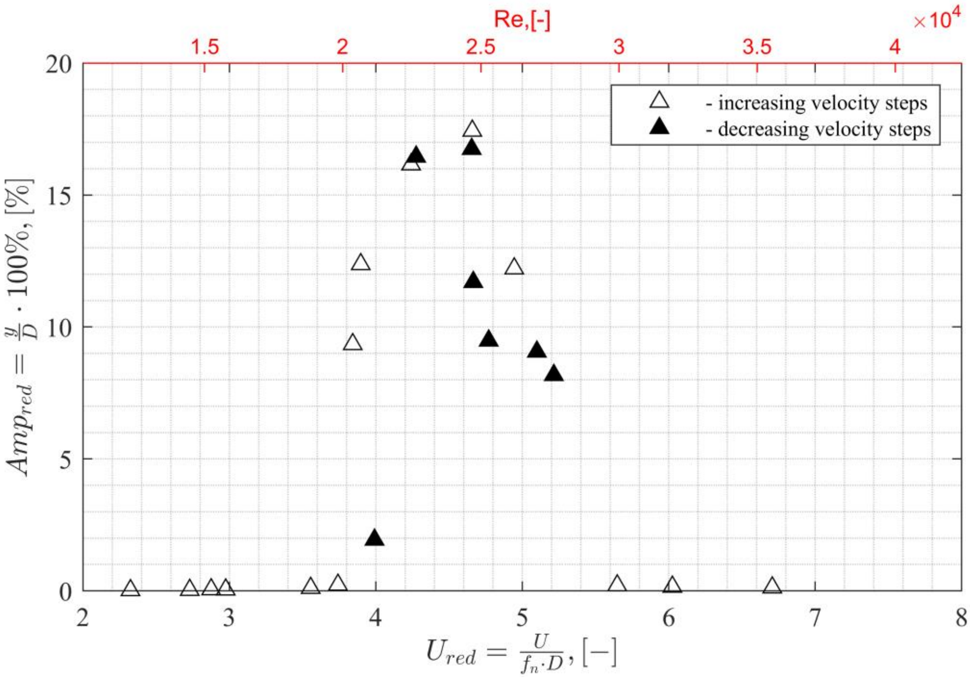

Figure 5.38 Amplitude response plot of iced cable, α=90° model in turbulent flow I_u=12.3%

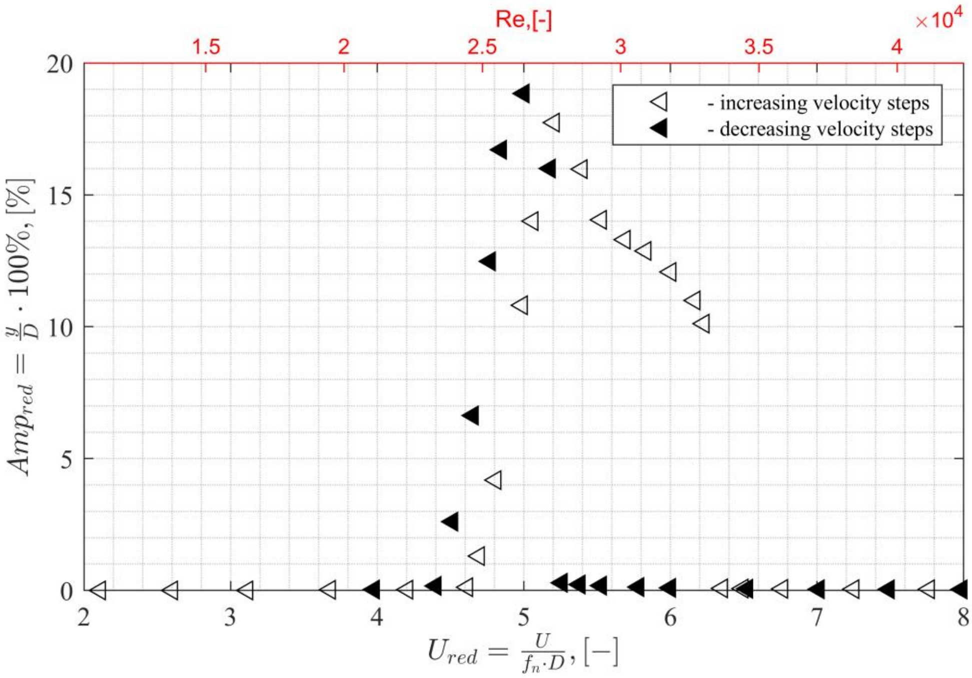

Figure 5.39 Amplitude response plot of iced cable, α=0° model in smooth flow I_u*=0.75%*

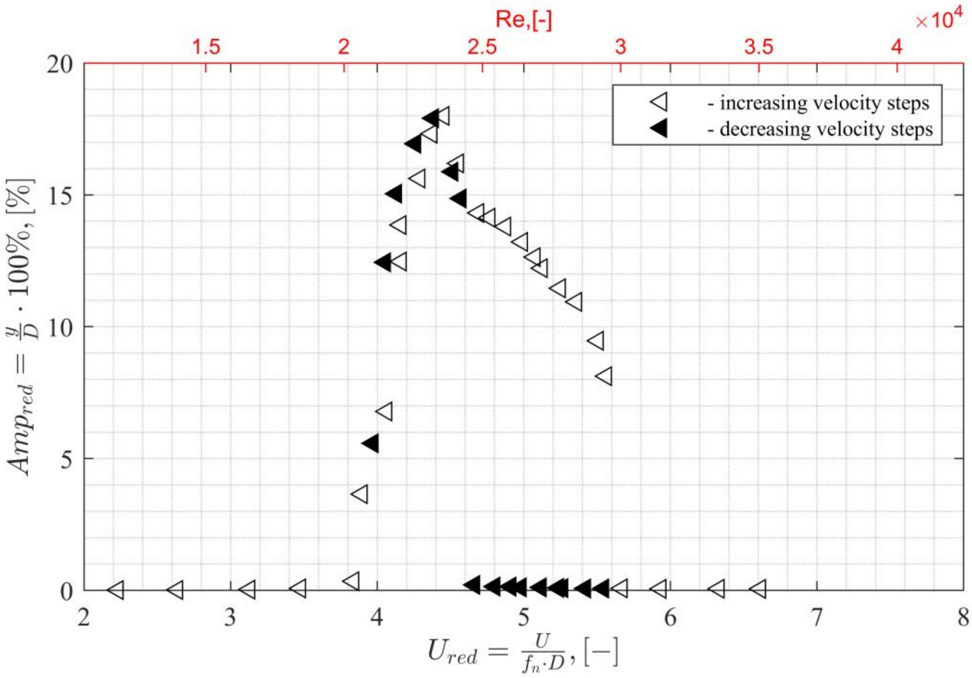

Figure 5.40 Amplitude response plot of iced cable, α=0° model in turbulent flow I_u*=4.5%*

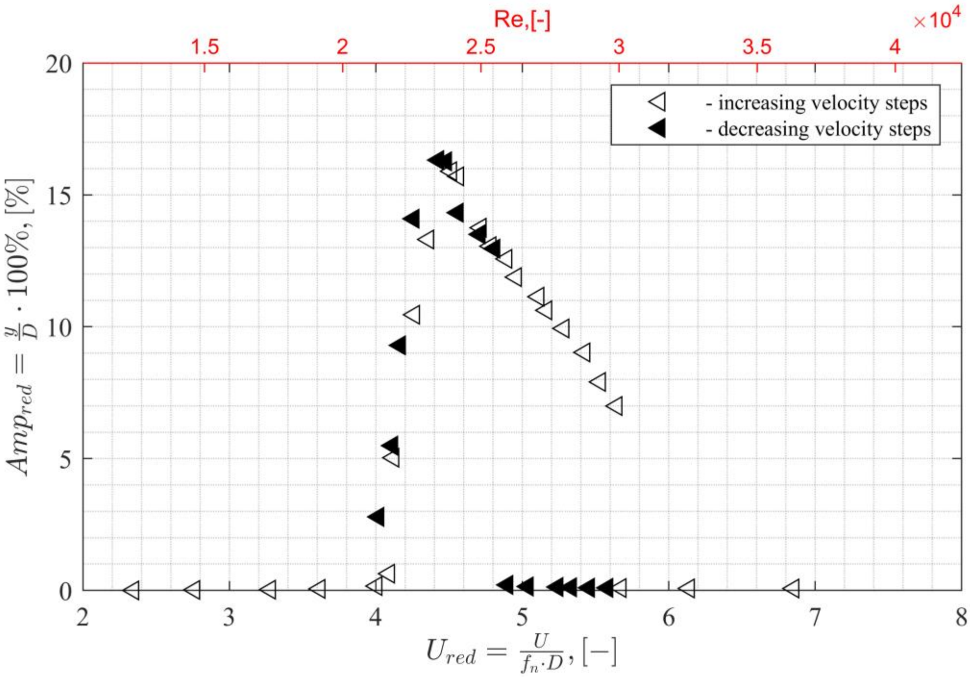

Figure 5.41 Amplitude response plot of iced cable, α=0° model in turbulent flow I_u*=6.5%*

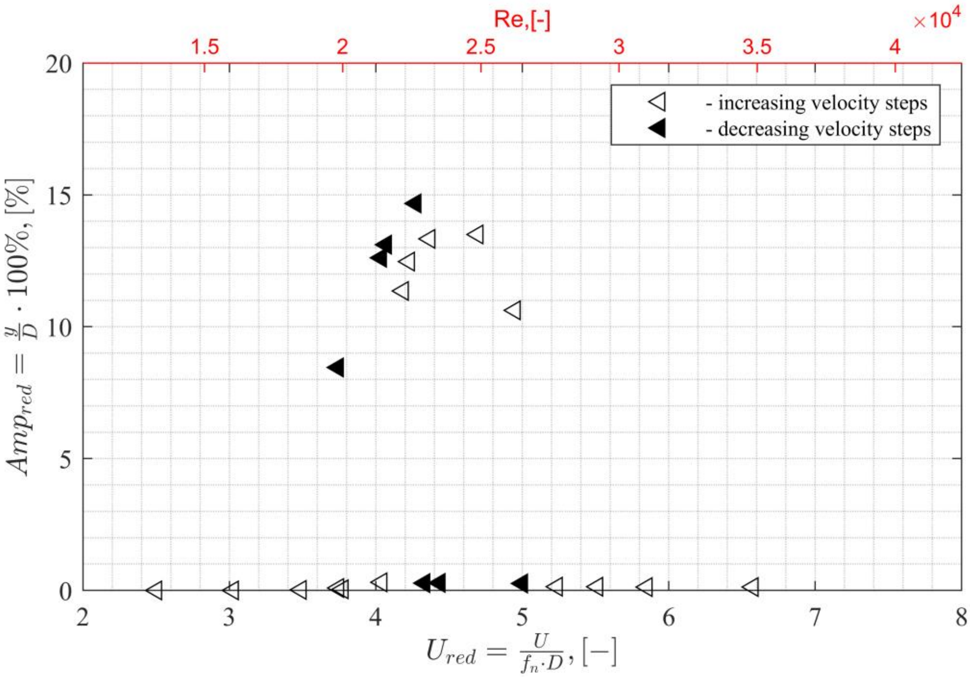

Figure 5.42 Amplitude response plot of iced cable, α=0° model in turbulent flow I_u*=12.3%*

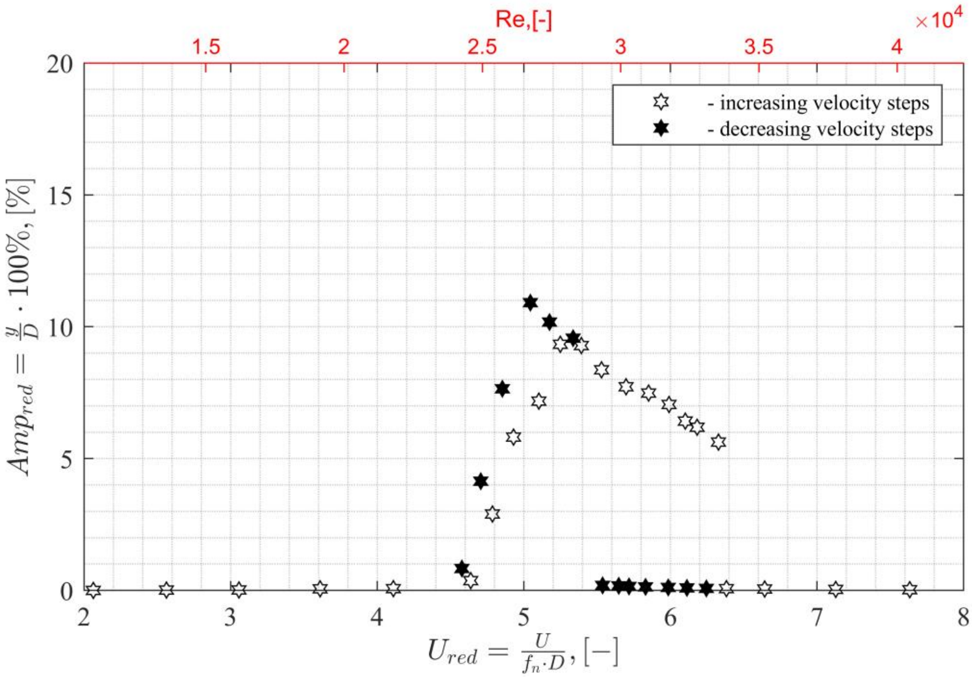

Figure 5.43 Amplitude response plot of helical cable 1x91-12 model in smooth flow I_u=0.75%

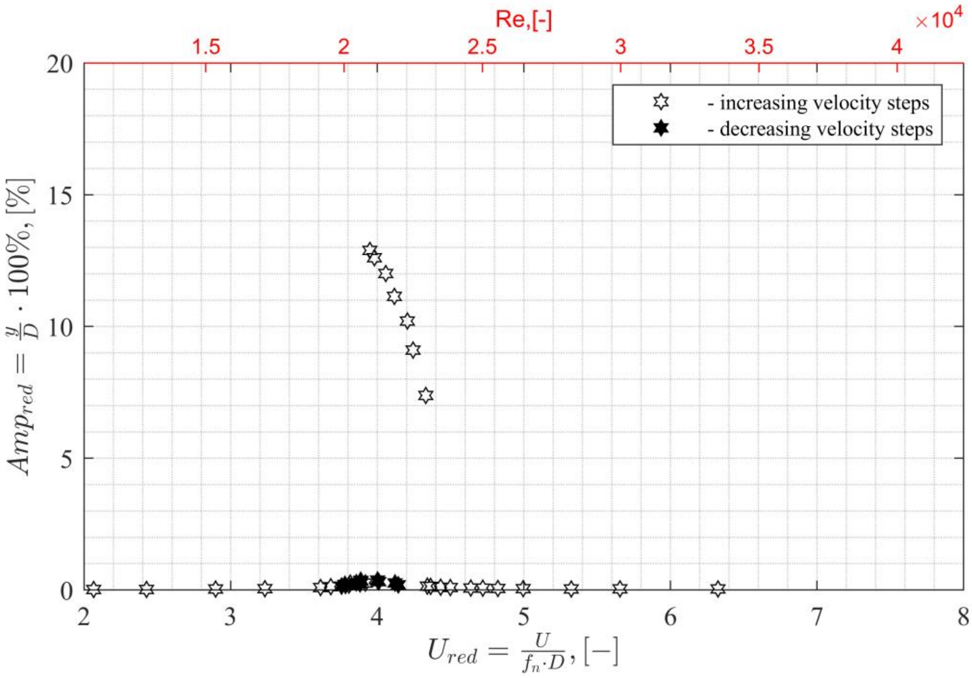

Figure 5.44 Amplitude response plot of helical cable 1x91-12 model in turbulent flow I_u=4.5%

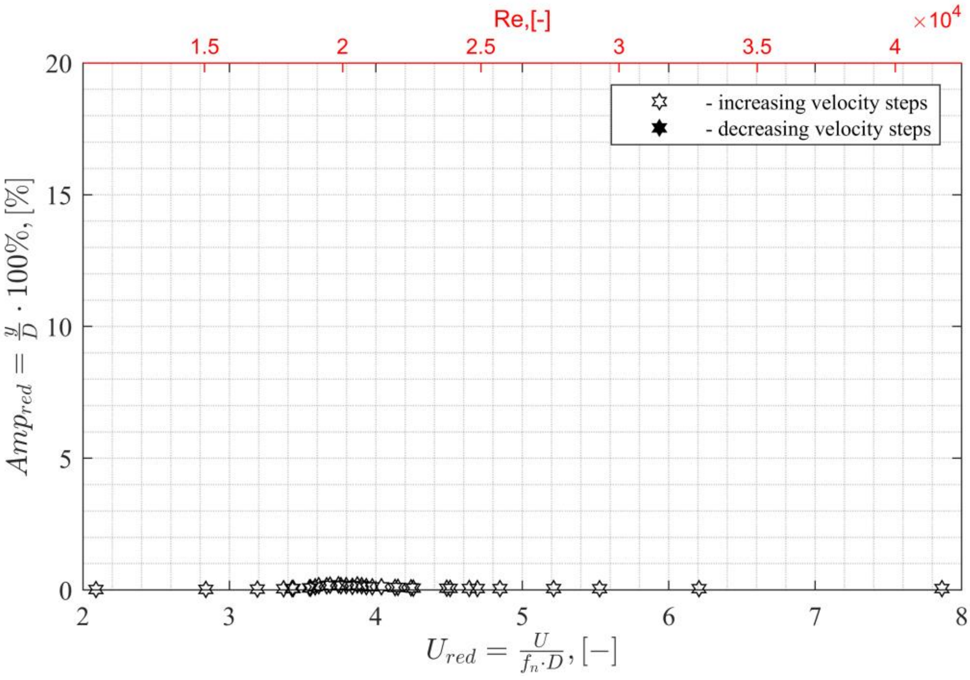

Figure 5.45 Amplitude response plot of helical cable 1x91-12 model in turbulent flow I_u*=6.5%*

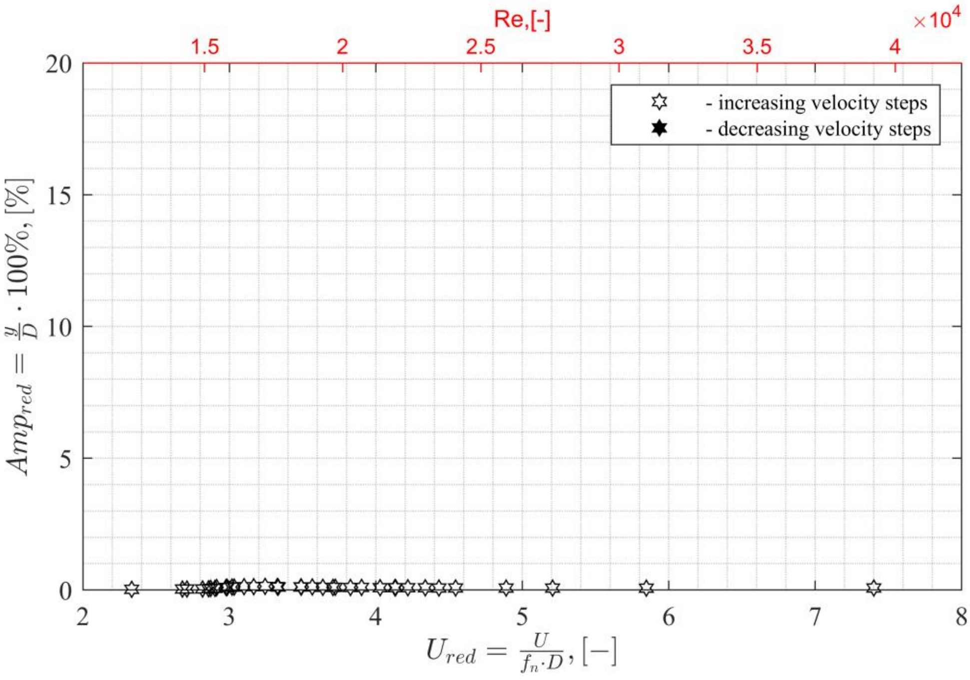

Figure 5.46 Amplitude response plot of helical cable 1x91-12 model in turbulent flow I_u*=12.3%*

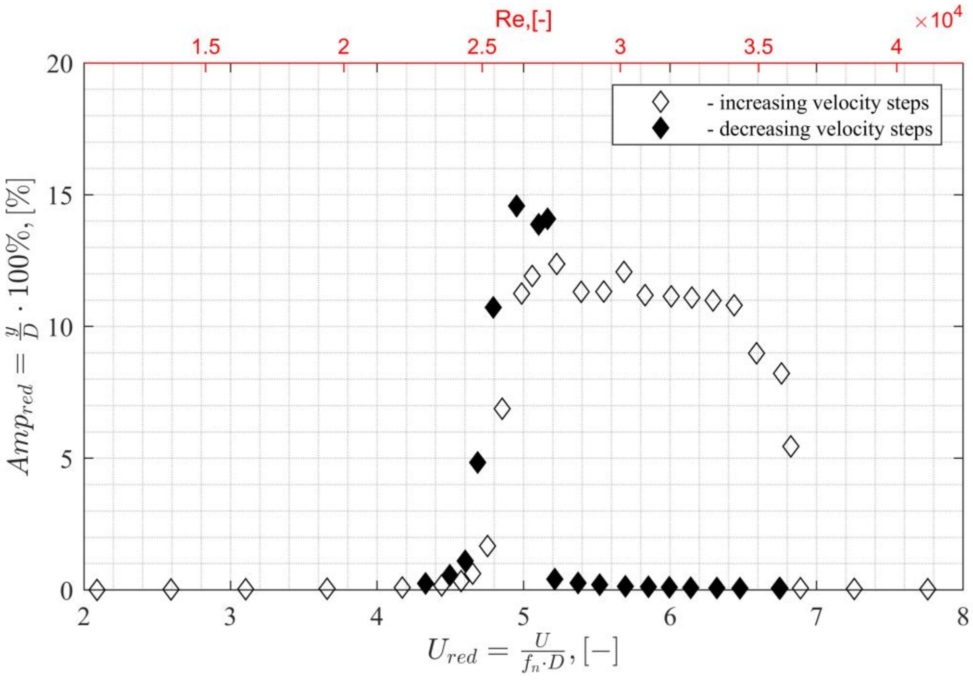

Figure 5.47 Amplitude response plot of helical cable 1x61-24 model in smooth flow I_u*=0.75%*

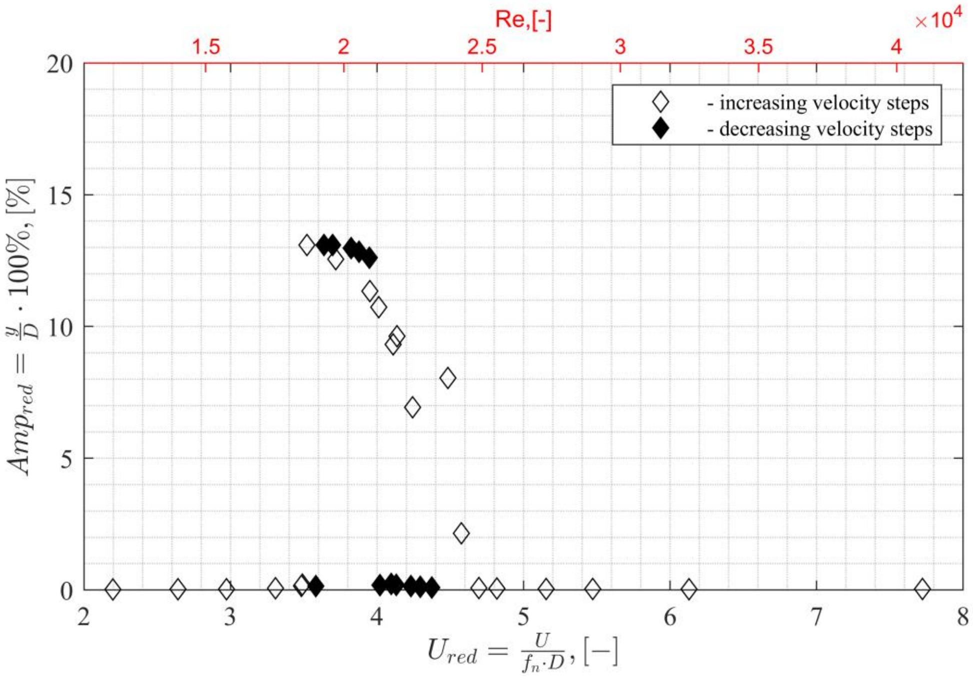

Figure 5.48 Amplitude response plot of helical cable 1x61-24 model in turbulent flow I_u*=4.5%*

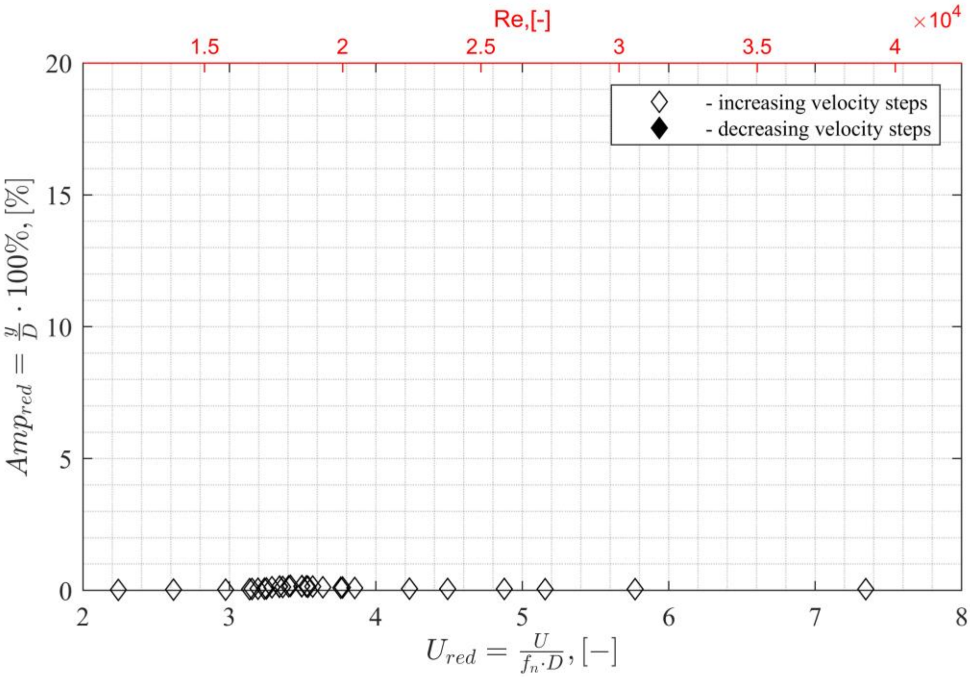

Figure 5.49 Amplitude response plot of helical cable 1x61-24 model in turbulent flow I_u*=6.5%*

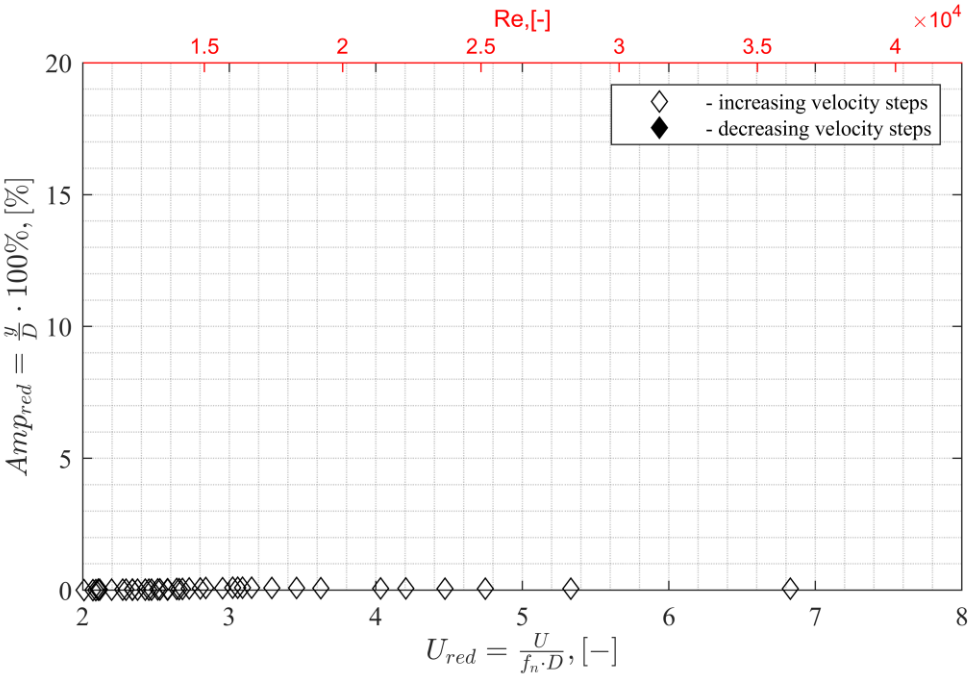

Figure 5.50 Amplitude response plot of helical cable 1x61-24 model in turbulent flow I_u*=12.3%*

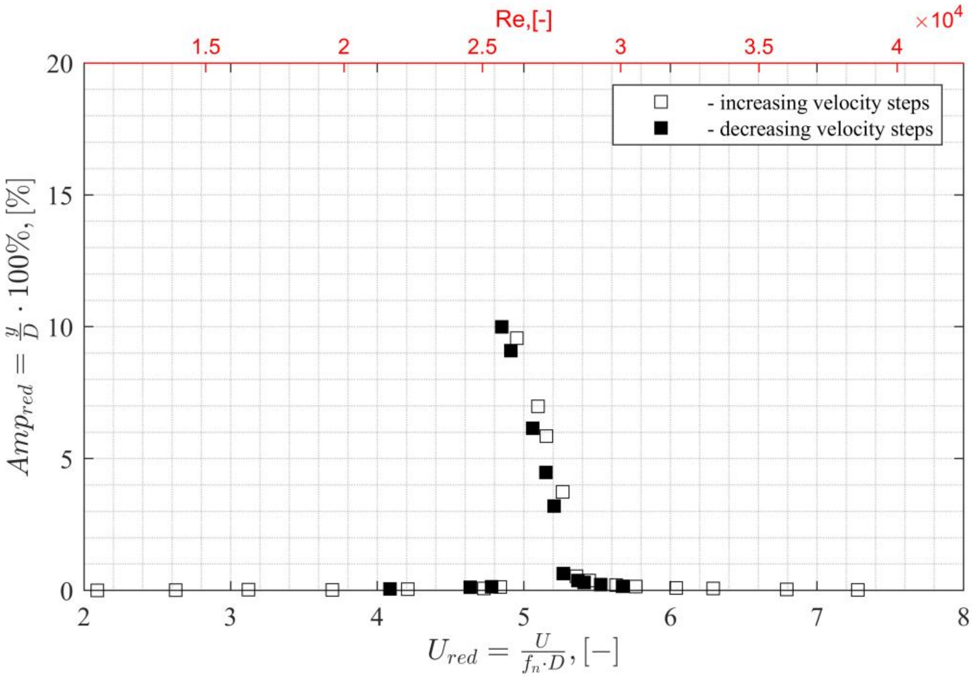

Figure 5.51 Amplitude response plot of helical cable 1x61-12 model in smooth flow I_u*=0.75%*

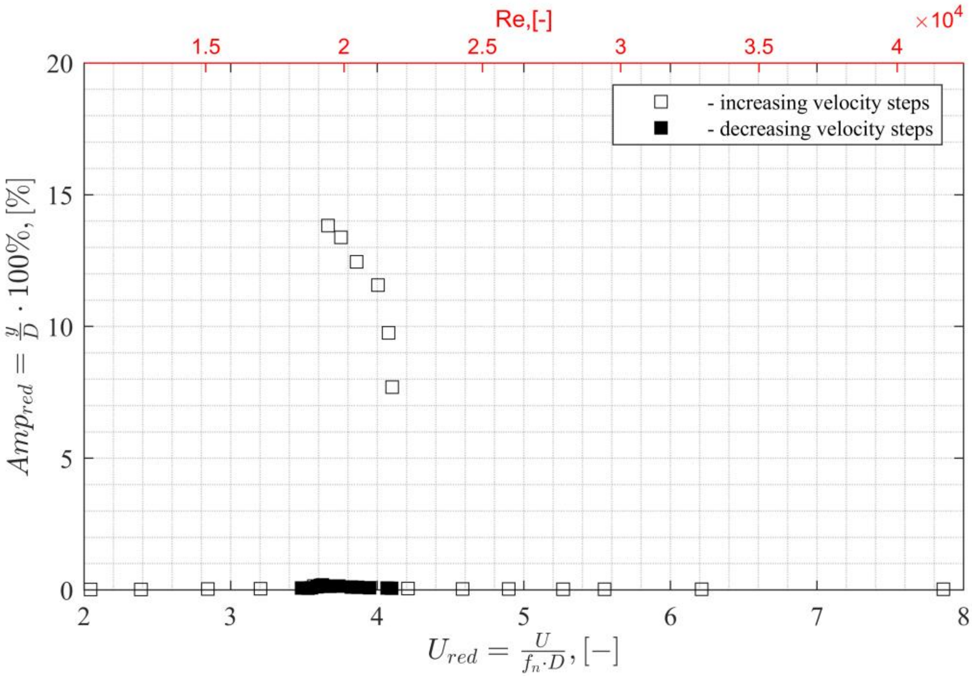

Figure 5.52 Amplitude response plot of helical cable 1x61-12 model in turbulent flow I_u*=4.5%*

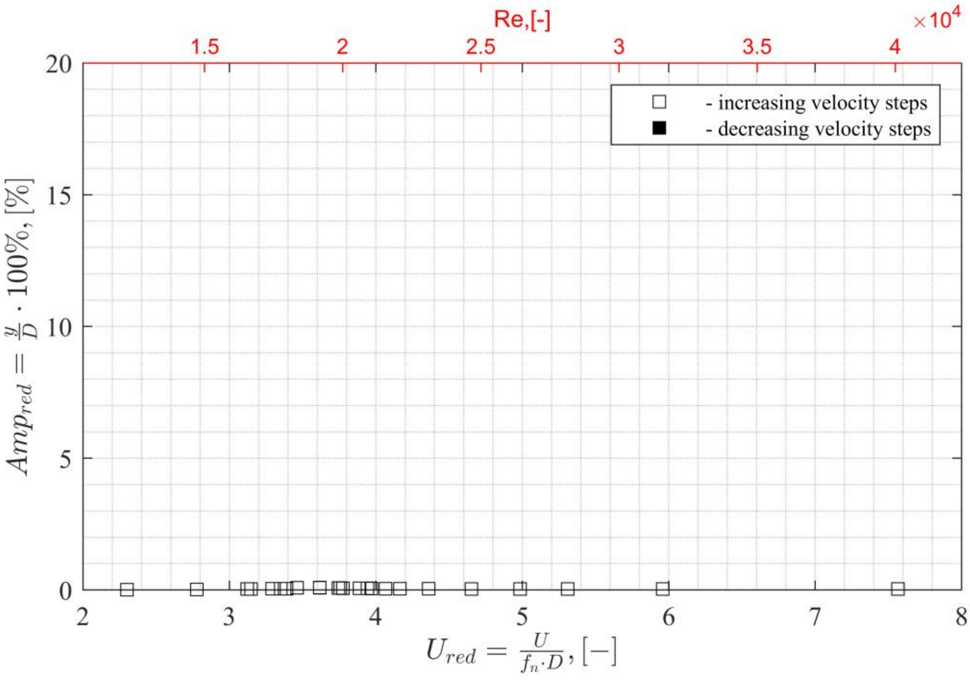

Figure 5.53 Amplitude response plot of helical cable 1x61-12 model in turbulent flow I_u=6.5%

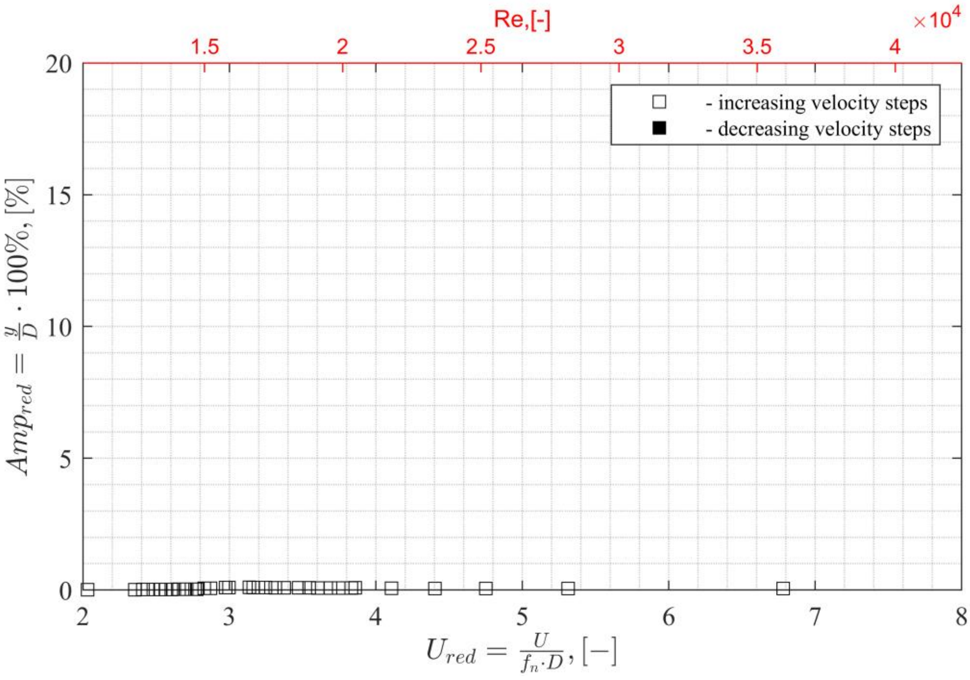

Figure 5.54 Amplitude response plot of helical cable 1x61-12 model in turbulent flow I_u=12.3%

As can be seen from the above graphs, the use of advanced settings with a more detailed step of velocity adjustment and stability of the steady flow in the wind tunnel during the second stage of the experiments, as well as along with improved model parameters allowed to achieve more reliable results. In particular, stable lock-in for iced model with ice on windward side in low turbulence flow and for smooth cylinder model in high turbulent flow. For all iced models no bifurcation in amplitude distribution were obtained.

The surface roughness of the helical strand cables reduces the lock-in range comparing to reference smooth model whereby the greatest impact is an increase of the lay angle. This trend remains valid in the turbulent flows with higher intensities and the vibrations starts at lover critical velocities as well, which indicates an increase of the Strouhal number. The hysteresis character of the response caused by the change in the wind attack angle is observed for all of models and the turbulence intensities. The most pronounced effect was observed for the case of model with higher values of the surface roughness and greater lay angle. For helical cable models no vibrations with dimensionless amplitude exceeding value of 2% in lock-in range were observed in turbulent flows with intensities 6.5% and 12.3%.

Flow-to-structure energy transfer

As previously mentioned, when a vortex is shed at the surface, there form the areas of high and low pressure which are located on opposite sides of the bluff body. We assume that these areas with pressure gradient generate an aerodynamic harmonically varying lift force, see the equation:

$$F_L = F_{L,max} \cdot sin(\omega t) \tag{5.4}$$

The steady-state amplitude of this type of aeroelastic oscillations depends on the one side of the characteristics of the oncoming wind flow (speed, intensity level and time/spatial scale of turbulence) and, on the other side, the dynamic (structural damping, mode shape) and aerodynamic (cross-sectional shape, surface roughness) design characteristics. The interaction of these factors is taken into account using the following coefficients: the mode shape factor K, the effective correlation length factor K_w, the Scruton number, lateral force coefficient c_{lat}.

During vortex shedding frequency lock-in the dynamic system draws energy to overcome the forces of constructive and aerodynamic damping from the flow.

Present vortex shedding models used in building codes provide the peak amplitude corresponds to condition of equality of actual wind flow velocity to critical velocity. Response the in lock-in range of velocities is taking into account using the so-called bandwidth coefficient. In this case, a conservative assumption is made that the oscillation amplitude remains constant, that does not match real behavior as seen from obtained response curves. Therefore, for further evaluation of response over full lock-in range will be used the comparison of the reduced amount of energy absorbed by the mechanical system (structure) from the stream. Similar method is widely used in evaluating the effectiveness of energy harvesters based on VIV, see [98] and [99].

To consider the energy transformations, let us turn to the equation of motion of a material point according to the second Newton law:

$$m_{tot}a + F_{damp.,tot} + F_{stiff.} = F_L \tag{5.5}$$

If we represent restoring elastic and damping forces as a function of position y, we get second order ordinary differential equation:

$$m_{tot}\ddot{y} + c_{tot}\dot{y} + ky = F_{L,max} \cdot sin(\omega t) \tag{5.6}$$

Where:

$m_{tot} = m_{strct} + m_{add}$. total mass consists of oscillated mass of structure and added mass of air

k- stiffness coefficient,

c- total damping coefficient consisting of structural and aerodynamical damping.

The position in this case is described by the equation:

$$y = y_{amp}\, cos(\omega t + \varphi) \tag{5.7}$$

Where:

φ – phase shift between driving force and displacement

The energy input into the system during one full cycle of oscillation is equal to the work of the resultant force applied to the body:

$$\mathrm{A} = \int_{0}^{\mathrm{T}} \mathrm{F} \cdot \dot{\mathrm{y}}\, \mathrm{dt} \tag{5.8}$$

The steady oscillation amplitude corresponds to the equilibrium point of energy input and energy dissipation, or in other words work of lift force is equal to work of damping forces. For this study to assess the risk of fatigue damage, the most interesting is the energy absorbed directly by the structure.

The elementary work of damping force is:

$$dA = Fdy \tag{5.9}$$

Where damping force F is:

$$F = C \cdot V = C \cdot \omega \cdot y_{amp}\, cos(\omega t + \varphi) \tag{5.10}$$

Where C - structural damping coefficient.

Substituting (5.10) and (5.7) in (5.9) we get:

$$dA = C \cdot \omega^2 \cdot y_{amp}^2 cos^2\ (\omega t + \varphi)\, dt \tag{5.11}$$

Then work over cycle is:

$$\mathrm{A} = \int_{0}^{\mathrm{T}} \mathrm{C} \cdot \omega^2 \cdot \mathrm{y}_{\mathrm{amp}}^2 \cdot \cos^2\ (\omega \mathrm{t} + \varphi)\, \mathrm{dt} \tag{5.12}$$

After trigonometric transformations and reductions we get:

$$A = \frac{1}{2} C \cdot \omega^2 \cdot y_{amp}^2 \cdot \left(t|_0^T + \frac{cos(2\varphi)}{2\omega} sin(2\omega t)\,|_0^T - \frac{sin(2\varphi)}{2\omega}\ cos(2\omega t)|_0^T \right) \tag{5.13}$$

Since:

$$\omega = \frac{2\,\pi}{T} \tag{5.14}$$

Then:

$$A = \frac{1}{2} C \cdot \left(\frac{2\,\pi}{T}\right)^2 \cdot y_{amp}^2 \cdot \left(T - 0 + \frac{cos(2\varphi)}{2\omega}(0-0) - \frac{sin(2\varphi)}{2\omega}\ (1-1)\right)$$
$$= \frac{1}{2} C \cdot \left(\frac{2\,\pi}{T}\right)^2 \cdot y_{amp}^2 \cdot T \tag{5.15}$$

$$A = \frac{2\pi^2 C y_{amp}^2}{T} \tag{5.16}$$

Further, when processing the experimental data as an amplitude value of displacement will be used value of root mean square value of amplitudes obtained experimentally:

$$y_{amp} = y_{rms} \tag{5.17}$$

After reducing the damping coefficient and period of oscillations which is identical for different sets and after reducing amplitude the equation (5.16) takes the form:

$$A_{red} = \frac{A \cdot T}{2\pi^2 C \left(\frac{y_{amp}}{D} \cdot 100\%\right)^2} \tag{5.18}$$

Dependence of the work on the reduced velocity was stepwise approximated in the next a way: the number of approximation steps corresponds to the number of discrete speeds at which response measurements were taken. Each stage takes the corresponding value $\mathrm{A_{red,j}}$, the width of sampling step is determined by the boundary values $\mathrm{u}_{j,\mathrm{min}}$ $\mathrm{u_{j,max}}$ calculated as the arithmetic average between the velocity for a given measurement and the nearest smaller or larger velocity value for other measurements, see:

$$\mathrm{u}_{j,\mathrm{min}} = \frac{\mathrm{u_i} + \mathrm{u_{i-1}}}{2} \tag{5.19}$$

$$\mathrm{u_{j,max}} = \frac{\mathrm{u_i} + \mathrm{u_{i+1}}}{2} \tag{5.20}$$

The calculation took into account measurements obtained in the velocity range corresponding to lock-in.

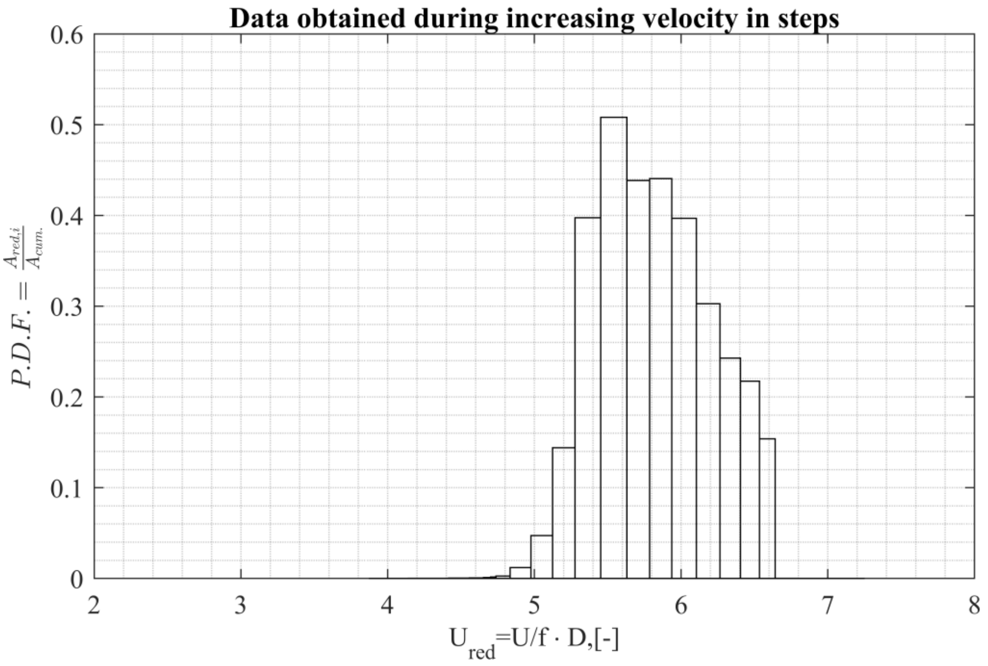

Figure 5.55 Work over lock-in, smooth surface cable, smooth flow I_u=0.75%, normalized to cumulative work over smooth cylinder, data obtained during increasing velocity in steps.

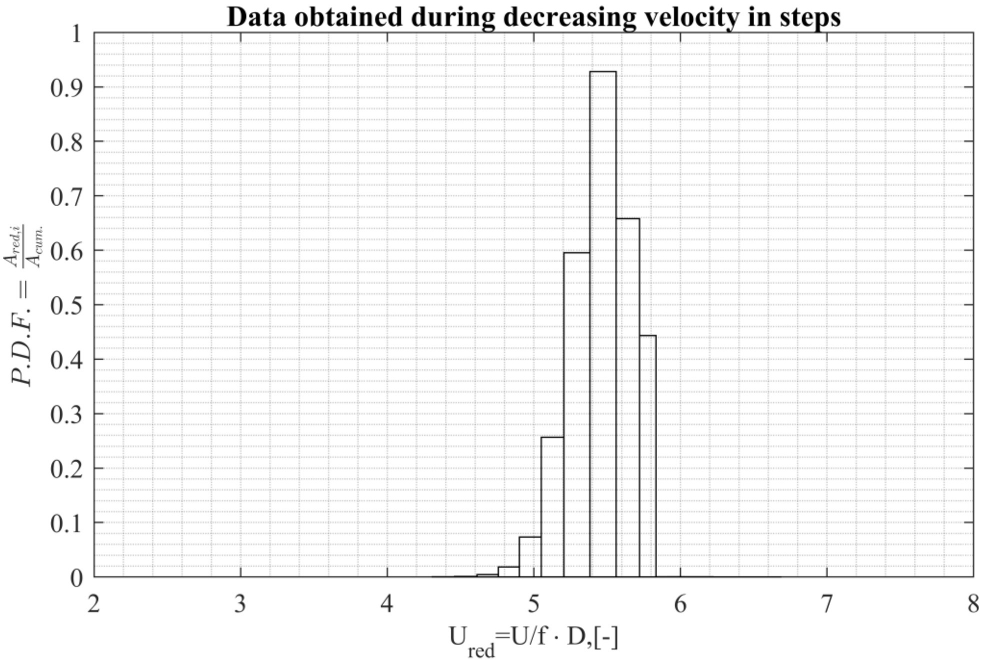

Figure 5.56 Work over lock-in, smooth surface cable, smooth flow I_u=0.75%, normalized to cumulative work over smooth cylinder, data obtained during decreasing velocity in steps.

Further on, the cumulative work A_{cum} over lock-in range was obtained as an integral of step-approximated function $A_{red}(u)$, being the sum of the area limited by approximation function:

$$\mathrm{A_{cum}} = \int_{\mathrm{u_{lock-in,min}}}^{\mathrm{u_{lock-in,max}}} \mathrm{A_{red}(u)du} = \sum_{\mathrm{i}} \mathrm{A_{red,i}} \cdot (\mathrm{u_{i,max}} - \mathrm{u_{i,min}}) \qquad (5.21)$$

The graphs of probability density function for individual sets apart for case $P.D.F. = A_{red,i,(in/dc)}/A_{cum}$ where A_{cum} was calculated as summary of both velocity increasing(*in*) and decreasing(*dc*) cases, are presented with examples of approximations in Figure 5.55 and Figure 5.56, full results are presented in Figure 10.57- Figure 10.96 of Appendix A.

Next value of cumulative work for each experimental set normalized to reference value of cumulative work for case of smooth cylinder response in nearly smooth flow is shown at Figure 5.57

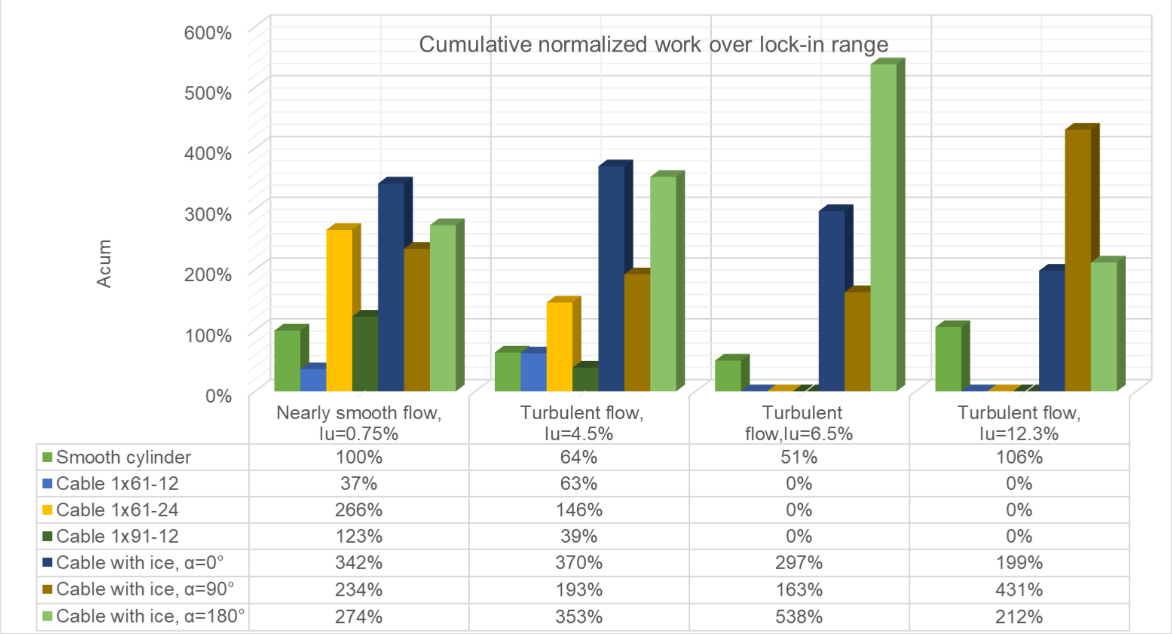

	Nearly smooth flow, Iu=0.75%	Turbulent flow, Iu=4.5%	Turbulent flow,Iu=6.5%	Turbulent flow, Iu=12.3%
Smooth cylinder	100%	64%	51%	106%
Cable 1x61-12	37%	63%	0%	0%
Cable 1x61-24	266%	146%	0%	0%
Cable 1x91-12	123%	39%	0%	0%
Cable with ice, α=0°	342%	370%	297%	199%
Cable with ice, α=90°	234%	193%	163%	431%
Cable with ice, α=180°	274%	353%	538%	212%

Figure 5.57 Cumulative work over lock-in range for all tested models normalized to cum. work over smooth cylinder in smooth flow

As can be seen from the presented graph the greatest amount of energy absorbed from the stream with all tested turbulence levels and as a result the greatest risk of fatigue damage was for model with ice accretions. During the construction in areas with high risk of icing anti-icing measures must be taken: the use of surface modification, hydrophobic coatings, etc.

The rationality of using cables with a smooth or spiral surface is determined by the turbulent conditions of ABL at the construction site and arrangement of structural elements. Smooth circular shape is optimal for single or widely spaced cable in open areas, where turbulence is lowest. Cables with helical shape are optimal for moderate to strong turbulence levels, while preference should be given to higher values of surface roughness and lower lay lengths.

Direct force measurement

The resulting force measured by force sensors in the direction of vibration perpendicular to the wind flow consists of two components:

$$F_{tot} = F_L + F_{inert.} \tag{5.22}$$

where
F_L – aerodynamic lift force;

F_{inert} – inertial force arising from the (nearly-) harmonic varying acceleration model during vibrations relative to force balance stand arms.

Knowing the mass of the model m_{model} and acceleration measured by accelerometer a the inertia force is:

$$F_{tot} = -m_{model} \cdot a \tag{5.23}$$

Thus, the lifting force will be equal to the difference between the resulting force measured by the sensors and the inertia force calculated according to the readings of the accelerometer.

Lift force coefficient is defined as:

$$C_L = \frac{F_L}{F_{press}} \tag{5.24}$$

Pressure force F_{press} was calculated from flow velocity obtained by CTA probe as

$$F_{press} = \frac{\rho \cdot U^2 \cdot D \cdot l}{2} \tag{5.25}$$

Where:

ρ – is air density

D–cylinder diameter

l– cylinder length

During the experiment the temperature in the working section increased due to the transition of the kinetic energy of the flow into heat during the flow around obstacles and changes in direction in the tunnel ring. The air density was calculated for actual temperature and humidity in each test.

Results of force measurements for smooth cylinder model in smooth flow with I_u=0.75% are presented in Figure 10.97- Figure 10.133. At the top part of figures presented measured and calculated forces, at the bottom of figures presented peak values of lift force coefficients.

As can be seen the most stable values were obtained for cases of VIV at the beginning of the lock-in range, i.e. resonant vibrations with maximum amplitude, as example see Figure 10.109. Lift force coefficient value in this case are comparable to values measured on fixed cylinder [100], [29]. In other cases, the value of the lifting force assumes extremely high or low values, while showing a strong correlation with inertial force. This fact may be caused by error introduced by the accelerometers or design features of the stand. Based assumption verification tests were conducted.

5.4 Additional testing

Additional verification tests were carried out in two stages.

In the first, two similar accelerometers Kistler 8302B2S1 were installed on the stand's arm. Readings were also monitored by Laser PDV-100 Portable Digital Vibrometer [101]. No difference in results was obtained in this case.

In the second stage, accelerometers were installed on both (left and right) arms of the stand. Below are the results obtained at a speed less than critical (see Figure 5.58) in the beginning of the lock-in range (see Figure 5.59), in the middle of it (see Figure 5.60) and in the postcritical regime (Figure 5.61).

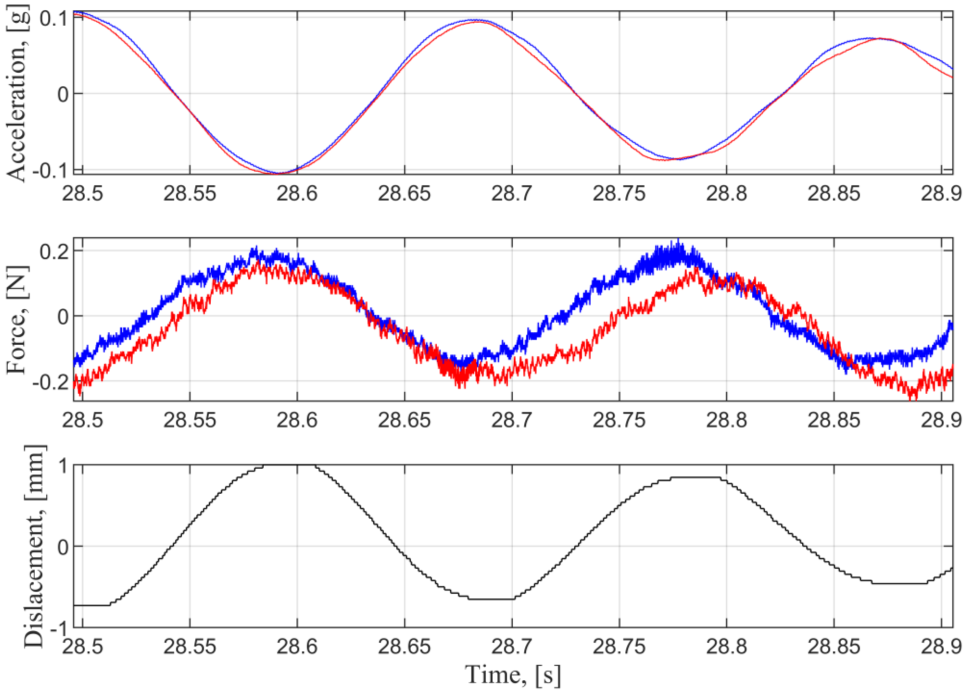

Figure 5.58 Difference in phase of balance stand arms, U=2.68 m/s

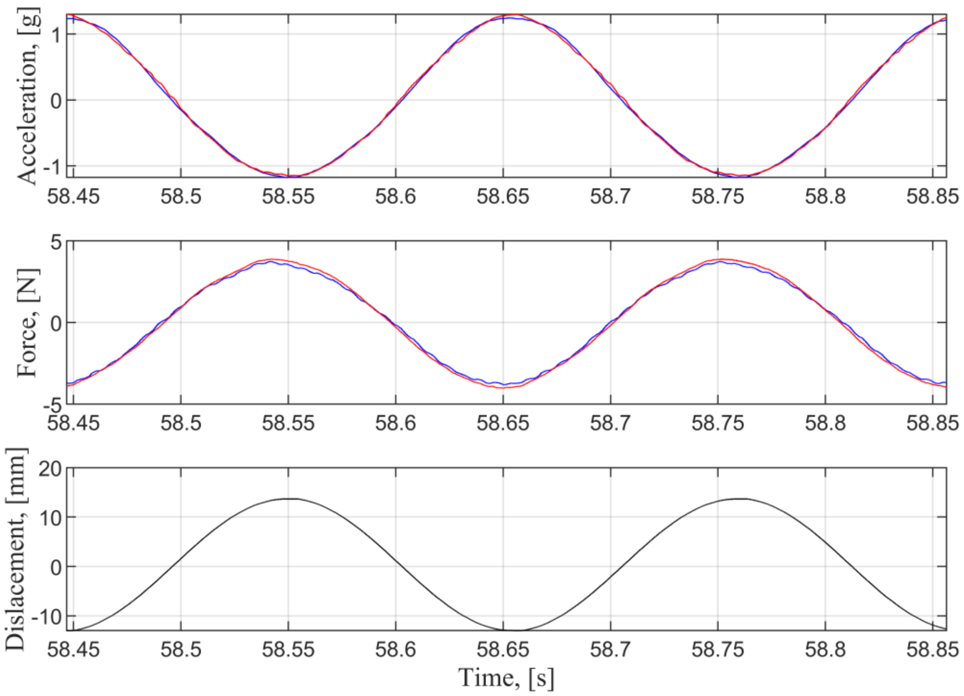

Figure 5.59 Difference in phase of balance stand arms, U=3.931 m/s

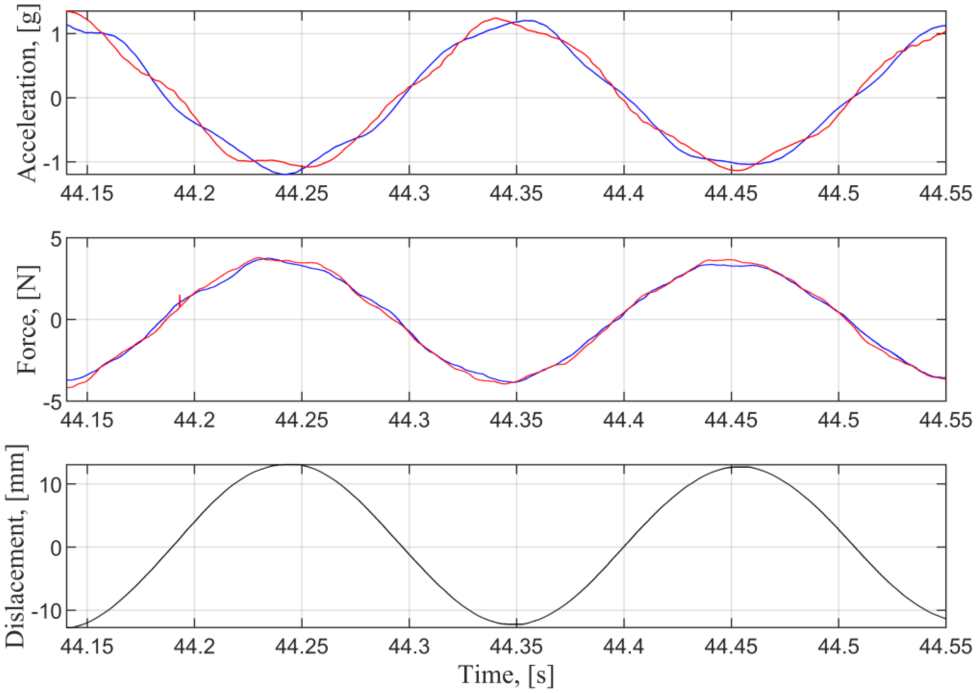

Figure 5.60 Difference in phase of balance stand arms, U=4.103 m/s

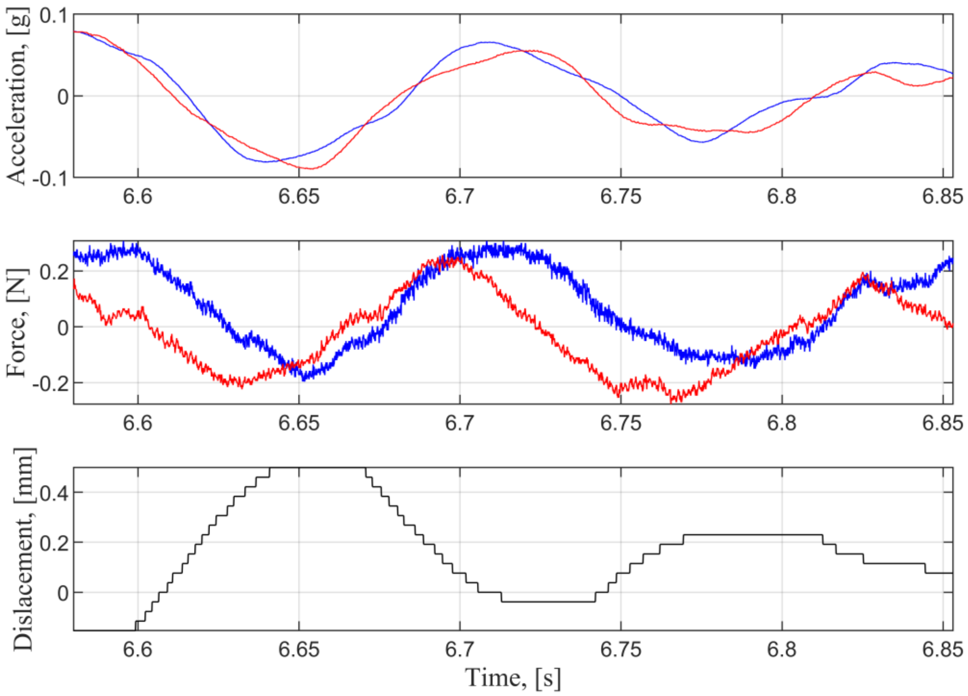

Figure 5.61 Difference in phase of balance stand arms, U=5.02 m/s

As seen from the above graphs, there is a difference between the acceleration data of the left and right fixing point, presumably due to insufficient structural rigidity and backlash in joints and bearings. Thus, since the main measurements were carried out with the accelerometer mounted on only one arm of the stand, this caused an erroneous calculation of inertial forces. Correction of errors caused by spurious vibrations is extremely difficult due to their unpredictability

The smallest difference between the readings of accelerometers was observed in the case of vibrations with maximum amplitude, as a result of which these data are the most reliable and are consistent with the literature [100].

6. Fatigue analysis based on the experimental data

The data obtained during testing were used for dynamic and the fatigue analysis of the first level of the cables of the mast Kojal. Cable fixing height 56 meters, tilt angle 23.4 degrees. The first level consists of single construction cables 1x61 with 4.25 mm wire diameter and 40 mm total outer diameter. Pre-tension force was F_{tens}=155700 N. To maintain the same outer diameter when calculating the cable with the structure 1x91 wire diameter was taken equal 3.5 mm. Logarithmical decrement δ=0.002 according to [102], [103].

High frequency dampers are installed on the cables, the influence of which is not considered in this calculation.

The natural frequencies of the cable were determined from the string formula:

$$f_{n,i} = \frac{i}{2L}\sqrt{\frac{F_{tens}}{m_l}} \tag{6.1}$$

m_l – is vibrating mass per unit length

The oscillation form in this case corresponds to the formula of a standing wave of harmonic oscillations with nodes at the attachment points:

$$y(x) = sin(k \cdot x) \tag{6.2}$$

Coefficient $k=2\pi/\lambda$ called the wave number or spatial frequency of the wave.

$\lambda=2L/i$ – is wavelength.

The wind speed in ABL depends on the height (between z_{min}=2m for II terrain category and z_{max}=200 m) according to the logarithmic law (function increment rate decreases with increasing argument) see Figure 6.1. Therefore, the length of the cable affected by the “lock-in” range of speeds of the corresponding mode number is maximum in the upper part of the cable. This is the most unfavorable case of vibrations.

The range of “lock-in” velocities was determined based on the data of the frequency of vortex disruption for the branch of increasing velocity, since it has the most broadband and strong response.

$$u_{mean}(z) = c_r(z) \cdot c_0(z) \cdot u_b \tag{6.3}$$

$$c_r(z) = k_r \cdot \ln\left(\frac{z}{z_0}\right) \tag{6.4}$$

Where:

$u_{mean}(z)$ – is wind velocity at z height;

u_b – is basic wind velocity;

$c_0(z)$ – is orphography factor;

$c_r(z)$ – is roughness factor;

z_0 =0.05 – is roughness height (II terrain category);

k_r – is terrain factor.

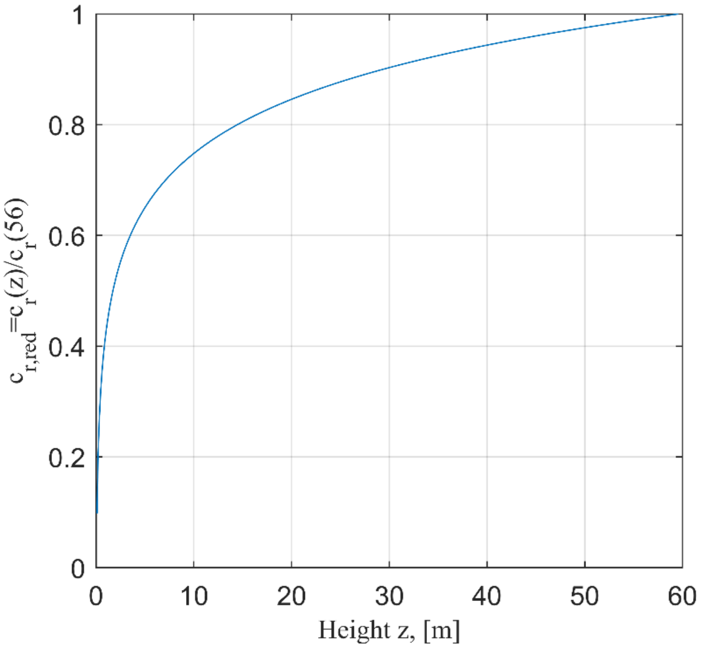

Figure 6.1 Roughness factor dependence on height

Thus, the height from which VIV synchronization zone starts for each mode I determined by the width of the lock-in range. For this height, the velocity of the peak of the Weibull velocity distribution is adjusted. For the corrected peak of velocity determined the number and frequency of eigenmode according to the Strouhal number. Eigenmode with two nearest higher and two lower frequencies were considered additionally.

Because of lift coefficient data from direct force measurement were corrupted for dynamic analysis further be used values of lift coefficient C_L calculated with modified equation (3.47) from Eurocode Vortex-resonance model:

$$C_L = \frac{y_{F,max} \cdot St^2 \cdot Sc}{b \cdot K \cdot K_w} \tag{6.5}$$

Calculation of the amplitude of the maximum displacement $y_{F,max}$ was carried out accordingly to the vortex-resonance model in iteration procedure. As the correlation length coefficient K_w depends on the effective correlation length (see Table 3.1) the initial calculation of $y_{F,max}$ was for relation $L_j=6 \cdot D$. Further, if the value $y_F(s_j)/b>0.1$ L_j, *the* K_w *and* $y_{F,max}$ recalculated until the difference between the value $y_{F,max}$ in the current and previous iteration did not exceed 1%.

The number of load cycles in Eurocode is calculated fora range of velocities with a certain bandwidth ε_0=0.1÷0.3. The standard maximum amplitude is used.

Loads from vibration (with corresponding number of load cycles) were calculated from experimental response data for each velocity (similar to the approximation for calculating of the amount of mechanical work in the section 5.3 Flow-to-structure energy transfer for the more detailed fatigue analysis.

The load obtained according to the formula (3.50) was applied on numerical cable model in Comsol Multyphisics, (see Appendix C: Matlab code for Comsol). Model is realized as polygon consists of 2 dimensional elastic material truss elements taking into account geometrical nonlinearity from prestressing. To prevent compression in the numerical model, the elastic modulus in compression was assigned as a negligible value.

Results of stress distribution along single wave for cases of maximal lift force values for corresponding model and flow properties are presented at Figure 10.134-Figure 10.138 of Appendix A: Figures.

For the obtained values of the stress ranges $\Delta\sigma$ the number of cycles during lifetime T=50 years= 50·365·24·60·60=1.5768·10^9 seconds:

$$N_{mode,i} = P_{WBL,i} \cdot f_{n,i} \cdot T \tag{6.6}$$

Where

P_{WBL} – is wind velocity probability:

$$P_{WBL} = \int_{u_{ij,min}}^{u_{ij,max}} WBL(u) \tag{6.7}$$

Where:
$WBL(u)$ – is Weibull wind velocity distribution

$u_{ij,min/max}$ – are corresponding minimal and maximal velocity of range approximated

tested reduced velocity j for considered mode number i.

According to the obtained number of cycles and stress ranges, fatigue damage was calculated according to [12], Figure 3.4. Overall results for 5 modes are presented at Table 6.1, detailed results for individual modes are presented at Table 11.1-Table 11.50 of Appendix B.

Table 6.1 Fatigue damage over 5 modes corresponding to maximal probability flow velocity

Cable type	Flow properties	Modes	D
smooth surface cable	smooth flow I_u=0.75%	93...97	8.88712E-06
helical cable 1x61-12	smooth flow I_u=0.75%	124...128	7.06916E-06
helical cable 1x61-24	smooth flow I_u=0.75%	91...95	0.003599426
helical cable 1x91-12	smooth flow $\mathrm{I_u}$=0.75%	108...112	0.000108714
smooth surface cable	turbulent flow I_u=4.5%	120...124	0.064315097
helical cable 1x61-12	turbulent flow $\mathrm{I_u}$=4.5%	165...169	8.305478555
helical cable 1x61-24	turbulent flow I_u=4.5%	146...150	283.5970586
helical cable 1x91-12	turbulent flow $\mathrm{I_u}$=4.5%	160...164	0.321835591
smooth surface cable	turbulent flow I_u=6.5%	131...135	0.373698878
smooth surface cable	turbulent flow I_u=12.3%	126...130	140.6001337

Highest risk of damage over 5 modes for most probability wind velocity ranges was determined for helical cable 1x61-24, 1x61-12 and smooth surface cable and in turbulent flows with turbulence intensities I_u=4.5% and I_u=12.3%. This fact is associated with an increase of the Strouhal number in turbulent flows. At higher Strouhal number the considered velocity range corresponds to higher natural modes of vibration. This factor increases the resulting loads and according to the Vortex Resonance model given in the Eurocode. In addition, with an increase in the number of the eigenmode, the wavelength decreases and approaches the value of the effective correlation length L_j from the Table 3.1, which contradicts the physical principle: the breakdown of the vortex must be synchronized along the effective correlation length L_j but to have the opposite direction on adjacent half-waves of the oscillating structure. Thus, decrease in the wave length should lead to the reduction of the correlation length due to air viscosity. This is not provided for in the Eurocode procedure, however.

The attention should be paid also to the fact, that as bandwidth range (both experimentally obtained and the bandwidth ε_0 used in Eurocode) exceeds the difference between the critical speeds of the nearest eigenmodes, see Table 11.1-Table 11.50. Considering the above facts, the applicability of standard models for the high number eigenmodes is controversial.

7. Conclusions

Improvement of testing technology and verification of dynamic loads on slender structures has a significant economic effect in the design of new structures, reconstruction and evaluation of the remaining lifetime of building structures, increases reliability and serviceability. Aerodynamic and climatic loads on the cable elements and structures are directly related to their design and production technology.

Due to its inherent physical and mathematical complexity, the description of the turbulence wind loading cannot be fully resolved without experiments, which are usually carried out in situ or in the modern wind tunnels. This research is based primarily on such an experimental and large experimental campaign. A particular focus is on the effects of surface roughness and ice accretion of structural supporting cables and hangers with nominally circular cross-sections, as well as on the influence of flow turbulence and the analysis of the contribution to the fatigue analysis of the cables.

The experiments were carried out in two steps. An initial step was conducted in a wind tunnel laboratory of the Department of Building aerodynamics at the of Ruhr University in Bochum, Germany. It was focused upon the determination of the dependence of the response on the position of the rough surface relative to the flow direction. It has been found, that VIV of structural cables proved to considerably modify due to changes in flow turbulence and surface roughness of structural cables. In particular, increasing the turbulence intensity of the incoming flow causes a reduction in the amplitude of VIV of ice-accreted structural cables. The ice accretion causes the peak amplitude to change (increase or decrease) depending on the ice orientation for each studied level of flow turbulence. The ice-accretion at the leeward cable surface is the most critical case, as the amplitudes of the VIV are enhanced the most in this configuration, particularly for the low-turbulent flow. Smaller vibration amplitudes along with lower critical velocity for the lock-in occurrence were observed for the cylinder with the helical strand in comparison with the smooth cylinder, which is exhibited for the low-turbulent flow. An increase in flow turbulence along with a simultaneous reduction of turbulence length scales causes a decrease in response and a contraction of the lock-in domain for all test cases.

At the same time, some of the results were difficult to interpret, as an example:

- Lack of “lock-in” range of iced cable model with ice formation on wind ward side in nearly smooth flow I_u =1.5% and smooth cylinder model in turbulent flow I_u =10.2%;
- The presence of two peaks in the distribution of amplitudes of iced cable models.

Based on the experience gained, a second experimental set was prepared in domestic Climatic Wind Tunnel “Vincenc Strouhal” in Institute of Theoretical and Applied Mechanics of the Czech Academy of Sciences:

- The parameters of the models were changed for increasing the length of the model and reducing its diameter to obtain a length-to-diameter ratio close to 10. This allowed us to achieve optimal two-dimensional flow conditions, reduce the influence of end effects, while maintaining a low wind tunnel blockage ratio and the required Reynolds number range. Models were also made with parameters allowing separately assess the effect of lay angle end effective surface roughness on response of helical strand models.
- The intensity and integral length scale of the turbulence were measured over a wide range of speeds and with a detailed step along the model axis at its current height. Has been added the CTA-probe in wake of models for direct measurement of vortex shedding frequency and Strouhal number.
- The existing dynamic stand was redesigned and modernized in such a way as to measure not only the frequency and amplitude characteristics of the vortex induced response but also the aerodynamic forces. The use of the lever-hinged system of balance stand is optimal for this purpose, since it has a number of advantages over classical model locking schemes:
- The lever-joint scheme is more compact and does not require sensors with high longitudinal bearing capacity or additional frame constructions that perceive tensile force when attached to stretched strings, which is important for the relatively small wind tunnel testing cross section.
- The absence of the need for stabilization in the plane perpendicular to the plane of vibration characteristic to the system with suspended springs.
- In contrast to systems with mechanically (engine) driven oscillations, the concept proposed in this paper allows one to measure the aerodynamic forces arising directly during the aeroelastic interaction of an oscillating object and air flow without intermediate iterations and errors introduced by recalculating the parameters of driven system.

The concept proved to be workable, however, to obtain reliable results, it is necessary to build a new stand with higher manufacturing accuracy and out of plain stiffness to get rid of spurious vibrations.

According to the results surface roughness of helical strand cables reduces the lock-in range comparing to reference smooth model whereby the greatest impact is an increase of lay angle. This trend remains in turbulent flows with higher intensities, also vibrations starts at lover critical velocities which indicates an increase of Strouhal number. The hysteresis character of amplitude response caused by the direction of velocity change observed for all of models and turbulence intensities. The most pronounced effect was for the case of model with higher values of surface roughness and lay angle.

The impact of the study results lies both in the field of theory of physical mechanisms and the practical application.

The most valuable findings are obtained dependencies of amplitude response, Strouhal number values and amount of energy absorbed from flow by cylinders. An additional benefit is using of obtained extensive experimental data sets to validate future numerical simulations.

Work has practical results which will improve the knowledge of the complex wind loading at the bridge cables, cables of the mast towers as well as the loading on the broadcast towers with tubular members. Experimental data from wind tunnel testing were used for obtaining the loads characteristics under different turbulent conditions and further for dynamic analysis and fatigue risks evaluation. The limited applicability of Eurocode dynamic analysis procedures were found for high eigenmodes. Possible solutions could be the further development of multy-mode vibration models. The practical significance of the proposed project is in application of obtained experimental results in the design in terms of wind loading and structural serviceability, in design and codification, in rethinking architecture of traffic and industrial infrastructure in regard to minimize adverse cost effects of wind and climatic loading.

The reported results provide some important findings for bridge designers, as flow turbulence and cable surface roughness clearly prove to considerably influence VIV of structural cables, which in turn may considerably alter the dynamic characteristics and lifetime of cable-supported bridges.

The further research objectives are aimed to:

- Improving the design of a dynamic balance stand
- Separate studies of the effects of turbulence intensity and integral length scale: when varying changing of one parameter with stable value of the second. This is planned to be achieved by using sets of grids with various sizes of cells and rods. The preliminary tests for grids with bar width 100 mm and 200 mm were carried out.
- Improving the method of generating turbulence in a wind tunnel to obtain large values of integral length scale.
- Study of influence of inclination, wind incidence angle, ice and cable surface patterns.

8. References

[1] K. Mahmoud, "Fracture strength for a high strength steel bridge cable wire with a surface crack," *Theoretical and Applied Fracture Mechanics,* vol. 48, no. 2, pp. 152-160, 2007.

[2] M. Gu and S. Ren, "Parametric vibration of stay cables under axial narrow-band stochastic excitation," *International Journal of Structural Stability and Dynamics,* vol. 13, no. 8, 2013.

[3] C. Li, G. Xiang and X. Tang, "Fatigue crack growth of cable steel wires in a suspension bridge: Multiscaling and mesoscopic fracture mechanics," *Theoretical and Applied Fracture Mechanics,* vol. 53, no. 2, pp. 113-126, 2010.

[4] K. Gjerding-Smith, R. Johnsen, H. Lange, B. Leinum, G. Gundersen, B. Isaksen and G. Naerum, "Wire fractures in locked coil cables," *Bridge Structures,* vol. 2, no. 2, 2006.

[5] R. Haight, D. Billington and D. Khazem, "Cable Safety Factors for Four Suspension Bridge," *Journal of Bridge Engineering,* vol. 2, no. 4, 1997.

[6] G. Fu, F. Moses and K. D.A., "Strength of parallel wire cables for suspension bridges," in *Proceedings 8th ASCE special conference on probabilistic mechanics and structural reliability*, Notre Dame, 2000.

[7] Bridge Technology Consulting, "Main Cable Investigation at the Mid-Hudson Suspension Bridge – Fracture Toughness Identification of Main Cable Wire. Technical Report prepared for the New York State Bridge Authority," New York, 2007.

[8] C. H. K. Williamson and R. Govardhan, "Vortex-induced vibration," *Annual Review of Fluid Mechanics,* vol. 36, no. 1, pp. 413-455, 2004.

[9] F. Cluni, V. Gusella and F. Ubertini, "A parametric investigation of wind-induced cable fatigue," *Engineering Structures,* vol. 29, no. 11, pp. 3094-3105, 2007.

[10] M. Miner, "Cumulative damage in fatigue," *Journal of Applied Mechanics,* vol. 12, no. 3, 1945.

[11] D. Zhang, H. Geng, Z. Zhang, D. Wang, S. Wang and S. Ge, "Investigation on the fretting fatigue behaviors of steel wires under different strain ratios," *Wear,* vol. 303, no. 1-2, pp. 334-342, 2013.

[12] EN 1993-1-11:2006, *Eurocode 3: design of steel structures, Part 1–11: Design of structures with tension components,* Brussels: CEN, 2007.

[13] M. Pirner and O. Fischer, Zatížení staveb větrem, Praha: ČKAIT, 2003.

[14] E. Simiu and R. Scanlan, Wind Effects on Structures, New York: John Wiley & Sons, 1996.

[15] J. Counihan, "A review and analysis of data from the period 1880-1972," *Atmospheric Environment,* 1979.

[16] Q. Yang, Y. Tian, B. Li and B. Chen, "Statistical spectrum model of wind velocity at Beijing Meteorological Tower," in *In proceedings of 7th International Colloquium on Bluff Body Aerodynamics and Applications (BBAA7)*, Shanghai, China, 2012.

[17] H. Sockell, Aerodynamik der Bauwerke, Braunschweig, Wiesbaden: Vieweg & Sohn, Vieweg & Sohn, 1984.

[18] R. Hill, "Corrections to Taylor's frozen turbulence approximation," *Atmospheric Research,* vol. 40, no. 2-4, pp. 153-175, 1996.

[19] G. Batchelor, The theory of homogeneous turbulence, London: Cambridge University Press, 1953.

[20] P. Moin, "Revisiting Taylor's hypothesis," *Journal of Fluid Mechanics,* vol. 640, 2009.

[21] T. Von Karman, "Progress on the statical theory of turbulence," *Journal of Maritime Research,* vol. 7, 1948.

[22] AS/NZS 1170.2-2002, *Structural design actions - Wind actions,* 2002.

[23] AIJ-RLB, *Recommendations on Loads for Buildings,* Japan: Architectural Institute of Japan, 2004.

[24] NBC, Ottawa, Canada: Associate Committee on the National Building Code, National Research Council, 2005.

[25] EN 1991-1-4:2005, *Eurocode 1: Actions on structures – Part 1-4: General actions – Wind actions,* Brussels: CEN, 2005.

[26] ANSI/ASCE 7-10, *Minimum Design Loads for Buildings and Other Structures,* Reston, U.S.A.: American Society of Civil Engineers, 2010.

[27] G. H. Fichtl and G. McVehil, "Longitudinal and lateral spectra of turbulence in the atmospheric boundary layer at the Kennedy Space Center," *Journal of Applied Meteorology,* vol. 9, pp. 51-63, 1970.

[28] R. Flay and D. Stevenson, "Integral length scales in atmospheric Boundary-Layer near theGround," in *In Proc. 9th Australasian Fluid Mechanics Conference*, Aucland, 1986.

[29] M. Zdravkovich, Flow around circular cylinders, 1 ed., Oxford, UK: Oxford University Press, 1997.

[30] J. Gerrard, "The wakes of cylindrical bluff bodies at low Reynolds number," *Philosophical Transactions of the Royal Society of London,* vol. 288, pp. 351-382, 1978.

[31] J. Dowd, M. Poser, K. Frank, S. Wood and E. Williamson, "Bending Fatigue of Cable Stays," *Journal of Bridge Engineering,* vol. 6, pp. 639-644, 2001.

[32] K. Gjerding Smith, R. Johnsen, H. Lange, B. Leinum, G. Gundersen, B. Isaksen and G. Naerum, "Wire fractures in locked coil cables," *Bridge Structures ,* vol. 2, no. 2, 2006.

[33] H. Li, W. Chen, F. Xu, F. Li and J. Ou, "A numerical and experimental hybrid approach for the investigation of aerodynamic forces on stay cables suffering from rain-wind induced vibration," *Journal of Fluids and Structures,* vol. 26, no. 7-8, pp. 1195-1215, 2010.

[34] D. Dan, W. Cheng, L. Sun and Y. Guo, "Fatigue durability study of high density polyethylene stay cable sheathing," *Construction and Building Materials,* vol. 111, pp. 474-481, 2016.

[35] T. Sarpkaya, "A critical review of the intrinsic nature of vortex-induced vibrations," *Journal of Fluids and Structures,* vol. 19, no. 4, p. 389–447, 2004.

[36] M. Matsumoto, T. Yagi, Y. Shigemura and D. Tsushima, "Vortex-induced cable vibration of cable-stayed bridges at high reduced wind velocity," *Journal of Wind Engineering and Industrial Aerodynamics,* vol. 89, no. 7-8, pp. 633-647, 2001.

[37] I. Goswami, R. Scanlan and N. Jones, "Vortex-Induced Vibration of Circular Cylinders. I: Experimental Data," *Journal of Engineering Mechanics,* vol. 119, no. 11, 1993.

[38] D’Asdia and S. Noe, "Vortex induced vibration of reinforced concrete chimneys: in situ experimentation and numerical previsions," *Journal of Wind Engineering & Industrial Aerodynamics.*

[39] C. Demartino and F. Ricciardelli, "Aerodynamic stability of ice-accreted bridge cables.," *Journal of Fluids and Structures,* vol. 52, pp. 81-100, 2015.

[40] M. Matsumoto, T. Yagi, M. Goto and S. Sakai, "Rainwind-induced vibration of inclined cables at limited high reduced wind velocity region," *Journal of Wind Engineering and Industrial Aerodynamics,* vol. 91, no. 1-2, pp. 1-12, 2003.

[41] N. J. Gimsing and C. T. Georgakis, Cable supported bridges: Concept and design, Chichester, United Kingdom: Wiley, 2012.

[42] J. Macdonald and G. Larose, "A unified approach to aerodynamic damping and drag/lift instabilities, and its application to dry inclined cable galloping," *The Journal of Fluids and Structures ,* vol. 22, no. 2, pp. 229-252, 2006.

[43] J. J.B., T. Andersen, J. Macdonald, N. Nikitas, G. Larose, M. Savage and B. McAuliffe, "Wind-induced response and excitation characteristics of an inclined cable model in the critical Reynolds number range," *Journal of Wind Engineering & Industrial Aerodynamics,* vol. 110, 2012.

[44] Y. Xu, Wind effects on cable-supported bridges, Singapore: John Wiley & Sons,, 2013.

[45] J. P. D. Hartog, "Transmission-line vibration due to sleet," *American Institute of Electrical Engineers,* vol. 51, pp. 1074-1086, 1932.

[46] H. Gjelstrup, C. T. Georgakis and A. Larsen, "An evaluation of iced bridge hanger vibrations through wind tunnel testing and quasi-steady theory," *Wind and Structures,* vol. 15, pp. 385-407, 2012.

[47] R. Zdero and O. Turan, "The effect of surface strands, angle of attack, and ice accretion on the flow field around electrical power cables," *Journal of Wind Engineering and Industrial Aerodynamics,* vol. 98, pp. 672-678, 2010.

[48] C. Gurung, H. Yamaguchi and T. Yukino, "Identification of large amplitude wind-induced vibration of ice-accreted transmission lines based on field observed data," *Engineering Structures,* vol. 24, pp. 179-188, 2002.

[49] L. Makkonen, T. Laakso, M. Marjaniemi and K. J. Finstad, "Modelling and prevention of ice accretion on wind turbines," *Wind Engineering,* vol. 25, pp. 3-21, 2001.

[50] C. K. H. G. C. a. R. F. Demartino, "Effects of ice accretion on the aerodynamics of bridge cables," *Journal of Wind Engineering and Industrial Aerodynamics,* vol. 138, pp. 98-119, 2015.

[51] C. Dyrbye and S. O. Hansen, Wind load on structures, Chichester, United Kingdom: Wiley,, 1997.

[52] G. Buresti, "The effect of surface roughness on the flow regime around circular cylinders.," *Journal of Wind Engineering & Industrial Aerodynamics,* vol. 8, no. 1-2, pp. 105-114, 1981.

[53] G. Schewe, "On the force fluctuations acting on a circular cylinder in crossflow from subcritical up to transcritical Reynolds numbers," *Journal of Fluid Mechanics,* vol. 133, no. 1, pp. 265-285, 1983.

[54] M. Kiya, Y. Suzuki, M. Arie and M. Hagino, "A contribution to the free-stream turbulence effect on the flow past a circular cylinder," *Journal on Fluid Mechanics,* pp. 151-164, 1982.

[55] J. Howell and M. Novak, "Vortex shedding from circular cylinders in turbulent flow," in *In: Wind engineering, Proceedings of the Fifth International Conference, Fort Collins, Colorado, USA, July 1979.*, Oxford, 1980.

[56] T. Miyata and M. Miyazaki, "Turbulence effects on aerodynamic response of rectangular bluff cylinders," in *In: Wind Engineering, Proceedings of the Fifth International Conference, Fort Collins, Colorado, USA, July 1979.*, Oxford, 1980.

[57] A. Kareem and T. Wu, "Wind induced effects on bluff bodies in turbulent flows: nonstationary, non/Gaussian and nonlinear features," in *The seventh International Colloquium on Bluff Body Aerodynamics and its Application (BBAA7)*, Shanghai, 2012.

[58] G. Solari, "Mathematical Model to Predict 3-D Wind Loading on Buildings," *Journal of Engineering Mechanics,* vol. 111, no. 2, January 1985.

[59] G. Piccardo and G. Solari, "Closed Form Prediction of 3D Wind-excited response of slender structures," *Journal of Wind Engineering in Industrial Aerodynamics,* Vols. 74-76, pp. 697-708, 1998.

[60] G. Piccardo and G. Solari, "3D wind-excited response of slender structures: Closed form solution," *Journal of Structural Engineering,* vol. 126, no. 8, 2000.

[61] G. Piccardo and G. Solari, "Generalized equivalent spectrum technique," *Wind and Structures Journal,* 1998.

[62] S. Krenk and S. R. K. Nielsen, "Energy-balanced double oscillator model for vortex-induced vibrations," *Journal of Engineering Mechanics,* vol. 125, no. 3, 1999.

[63] S. O. Hansen, *Vortex-induced vibrations of line-like structures,* vol. 15 , 1999, pp. 15-23.

[64] S. O. Hansen, "Vortex-induced vibrations of structures," in *In Proceedings of Structural Engineers World Congress, November 2-7, 2007*, Bangalore, India, 2007.

[65] H. Niemann and N. Hölscher, "A review of recent experiments on the flow past circular cylinders," *Journal of Wind Engineering & Industrial Aerodynamics,* vol. 33, no. 1-2, pp. 197-209, 1990.

[66] G. Schewe, "Reynolds-number effects in flow around more-or-less bluff bodies," *Journal of Wind Engineering & Industrial Aerodynamics,* vol. 89, pp. 1267-1289, 2001.

[67] G. Matteoni and C. T. Georgakis, "Effects of surface roughness and cross-sectional distortion on the windinduced response of bridge cables in dry conditions," *Journal of Wind Engineering and Industrial Aerodynamics,* vol. 136, pp. 89-100, 2015.

[68] J. Ribeiro, "Effects of Surface Roughness on the two dimensional flow past circular cylinders 1: mean forces and pressures.," *Journal of Wind Engineering & Industrial Aerodynamics,* vol. 37, pp. 299-309, 1991.

[69] A. Fage and J. Warsap, "The effects of turbulence and surface roughness on the drag of a circular cylinder," *British Aeronautical Research Council,* vol. 1179, pp. 248-255, 1929.

[70] E. Achenbach, "Influence of surface roughness on the cross-flow around a circular cylinder," *Journal of Fluid Mechanics,* vol. 46, pp. 321-335, 1971.

[71] O. Guven, C. Farell and V. C. Patel, "Surface-roughness effects on the mean flow past circular cylinders," *Journal of Fluid Mechanics,* vol. 98, pp. 673-701, 1980.

[72] Y. Nakamura and Y. Tomonari, "The effects of surface roughness on the flow past circular cylinders at high Reynolds numbers," *Journal of Fluid Mechanics,* vol. 124, pp. 363-378, 1982.

[73] G. Diana, M. Belloli, S. Giappino and S. Muggiasca, "Vortex induced vibrations at high reynolds numbers," in *In Proceedings of 6th. International Colloquiumon Bluff Bodies Aerodynamics and Applications*, Milano, Italy, 2008.

[74] F. J. Huera-Huarte and P. Bearman, "Wake structures and vortex-induced vibrations of a long flexible cylinder. Part 1: dynamic response," *Journal of Fluid Mechanics,* vol. 25, no. 6, pp. 969-990, 2009.

[75] W.-L. Chen, Q.-Q. Zhang, H. Li and H. Hu, "An experimental investigation on vortex induced vibration of a flexible inclined cable under a shear flow," *Journal of Fluids and Structures,* vol. 54, pp. 297-311, 2015.

[76] M. Matsumoto, N. Shiraishi and H. Shirato, "Rain-wind induced vibration of cables of cable-stayed bridges," *Journal of Wind Engineering & Industrial Aerodynamics,* vol. 43, no. 1-3, pp. 2011-2022, 1992.

[77] H. Gjelstrup, C. Georgakis and A. Larsen, "A preliminary investigation of the hanger vibrations on the Great Belt East Bridge," in *In Proc. 7th International Symposium on Cable Dynamics*, Vienna, 2007.

[78] R. Král, "n experimental investigation of unsteady thermal processes on a pre-cooled circular cylinder of porous material in the wind," *International Journal of Heat and Mass Transfer,* vol. 77, pp. 906-914, 2014.

[79] L. Makkonen, "Modeling of Ice Accretion on Wires," *Journal of Applied Meteorology and Climatology,* vol. 23, pp. 929-939, 1984.

[80] R. Zdero and O. Turan, "The effect of surface strands, angle of attack, and ice accretion on the flow field around electrical power cables," *Journal of Wind Engineering & Industrial Aerodynamics,* vol. 98, pp. 672-678, 2010.

[81] A. K. H. H. M. L. O. Hudecz, "Ice Accretion on Wind Turbine Blades," *In Proceedings of the 15th International Workshop on Atmospheric Icing of Structures (IWAIS XV).,* 2013.

[82] R. Hartlen and I. Currie, "Lift-oscillator model of vortex induced vibration," *Journal of the Engineering Mechanics Division,* vol. 96, no. 5, pp. 577-591, 1970.

[83] W. Iwan and R. Blewins, "A model for vortex induced oscillation of structures," *Journal of Applied Mechanics,* vol. 41, 1974.

[84] R. Skop and O. Griffin, "A model for the vortex excited resonant response of bluff cylinders," *Journal of Sound and Vibration,* vol. 27, no. 2, pp. 225-233, 1973.

[85] P. Gorski, S. Pospısil, S. Kuznetsov, M. Tatara and A. Marusic, "Strouhal number of bridge cables with ice accretion at low flow turbulence," *Wind and Structures,* vol. 22, pp. 253-272, 2016.

[86] ISO 12494, *Atmospheric icing of structures,* The International Organization for Standardization, 2001.

[87] P. Górski, S. Pospíšil, S. Kuznetsov, M. Tatara and A. Marušić, "Investigation of Strouhal number of iced cable model of cable-supported bridges with respect to angle of wind attack," in *7th International Symposium on Environmental Effects on Buildings and People: Actions, Influences, Interactions, Discomfor*, Lublin, 2014.

[88] G. S. West and C. J. Apelt, "The effects of tunnel blockage and aspect ratio on the mean flow past a circular cylinder with Reynolds numbers between 10^4 and 10^5," *Journal of Fluid Mechanics,* vol. 114, pp. 361-377, 1982.

[89] A. Zasso, M. Belloli, S. Giappino and S. Muggiasca, "Energy input by the flow on a vibrating smooth circular cylinder in cross flow at Re = 5 · 10^4.," in *In Proceedings of 6-th International Simposium on Cable Dynamics*, Liege, Belgium, 2005.

[90] A. Zasso, M. Belloli, S. Giappino and S. Muggiasca, "Pressure field analysis on oscillating circular cylinder," *Journal of Fluids and Structures,* vol. 24, no. 5, pp. 628-650, 2008.

[91] R. Kral, S. Pospíšil and J. Náprstek, "Experimental set-up for advanced aeroelastic tests on sectional models," *Experimental Techniques,* vol. 40, no. 1, pp. 3-13, 2016.

[92] P. Roach, "The generation of nearly isotropic turbulence by means of grids," *International Journal of Heat and Fluid Flow,* vol. 8, no. 2, 1987.

[93] B. Silverman, Density estimation for statistics and data analysis, London, U.K.: Chapman and Hall, 1986.

[94] A. Trush, S. Pospíšil, S. Kuznetsov and H. Kozmar, "Wind-Tunnel Experiments on Vortex-Induced Vibration of Rough Bridge Cables," *Journal of Bridge Engineering,* vol. 22, no. 10, 2017.

[95] A. I. Automation, "https://www.ati-ia.com/products/ft/ft_models.aspx?id=Nano25," [Online].

[96] H. Moritz, "Geodetic Reference System 1980," *Journal of Geodesy,* vol. 74, no. 1, 2000.

[97] W. Telford, L. Geldart and R. Sheriff, Applied Geophysics, 2nd ed., Cambridge: Cambridge University Press, 1990.

[98] M. M. Bernitsas, K. Raghavan, Y. Ben-Simon and E. .. Garcia, "VIVACE (Vortex Induced Vibration Aquatic Clean Energy): A New Concept in Generation of Clean and Renewable Energy From Fluid Flow," *Journal of Offshore Mechanics and Arctic Engineering,* vol. 130, no. 4, 2008.

[99] M. Bernitsas, "The VIVACE Converter: Model Tests at High Damping and Reynolds Number Around 10^5," *Journal of Offshore Mechanics and Arctic Engineering,* vol. 12, 2009.

[100] M. Morkovin, "Flow around circular cylinders: a kaleidoscope of challenging fluid phenomena," in *in Proceedings ASME Symposium on Fully Separated Flow*, Philadelphia, 1968.

[101] Polytec GmbH, "Portable digital vibrometer," [Online]. Available: https://www.polytec.com/eu/vibrometry/products/single-point-vibrometers/pdv-100-portable-digital-vibrometer/.

[102] U.S. Department of transportation, Federal Highway Administration Research and Technology, *Wind-Induced Vibration of Stay Cables,* McLean, U.S.A.: Research, Development, and Technology Turner-Fairbank Highway Research Center, 2007.

[103] Y. Fujino, K. Kimura and H. Tanaka, Wind Resistant Design of Bridges in Japan: Developments and practices, Tokyo, Japan: Springer Japan, 2012.

[104] M. Efimova and V. Tsipenko, : Fundamenals of aerodynamics and aircraft performance characteristics (in rus.), vol. 1, Moscow: Moscow State Technical University of Civil Aviation, 2009.

[105] C. Cremona, "A short note on cable fatigue," in *In: Proc. 5th international symposium on cable dynamics*, Santa Margherita Ligure, Genoa, 2003.

[106] J. Garratt, The atmospheric boundary layer,, Cambridge: Cambridge University Press, 1992.

[107] C. Votaw and O. Griffin, "Vortex shedding from smooth cylinder and stranded cables," *Journal of Basic Engineering,* vol. 93, no. 3, pp. 457-460, 1971.

[108] R. Wardaw and K. Cooper, "A wind tunnel investigation of the steady aerodynamic forces on smooth and strangled twin bundled power conductors for the aluminum company in America," Natural Resources Council, Canada, 1973.

[109] G. Bartoli, F. Cluni, V. Gusella and L. Procino, "Dynamics of cable under wind action: Wind tunnel experimental analysis," *Journall of Wind Engineering and Industrial Aerodynamics,* vol. 94, pp. 259-273.

[110] H. Jing, Y. Xia, H. Li, Y. Xu and Y. Li, "Excitation mechanism of rainwind induced cable vibration in a wind tunnel," *Journal of Fluid Mechanics,* vol. 68, pp. 32-47, 2017.

[111] H. Koss and M. S. M. Lund, "Experimental investigation of aerodynamic instability of iced bridge cable sections," in *In Proceedings of 6th European and African Conference on Wind Engineering, IAWE*, Cambridge, UK., 2013.

[112] T. Wagner and U. Peil, "Ice formation on transmission line cables in tandem arrangement," in *In Proceedings of 13th International Conference on Wind Engineering*, Amsterdam, Netherlands, 2011.

[113] M. J. Walsh and L. M. Weinstein, "Drag and heat-transfer characteristics of small longitudinally ribbed surfaces," *AIAA Journal,* vol. 17, pp. 770-771, 1979.

[114] W.-L. Chen, H. Li, J.-P. Ou and F.-C. Li, "Numerical simulation of vortex-induced vibrations of inclined cables under different wind profiles," *Journal of Bridge Engineering,* vol. 18, no. 1, pp. 42-53, 2013.

[115] X. Wu, F. Ge and Y. Hong, "A review of recent studies on vortex-induced vibrations of long slender cylinders," *Journal of Fluids and Structures,* vol. 28, pp. 292-308, 2012.

[116] D. Zuo, N. Jones and J. Main, "Field observation of vortex- and rainwind induced stay-cable vibrations in a three-dimensional environment," *Journal of Wind Engineering and Industrial Aerodynamics,* vol. 96, no. 6-7, pp. 1124-1133, 2008.

[117] S. Pastò, "Vortex-induced vibration of a circular cylinder in laminar and turbulent flow," *Journal of Fluids and Structures,* vol. 24, pp. 977-993, 2008.

[118] Couniah J., *Lift and drag measurements on stranded cables,* vol. 117, London: Imperial College, 1963.

[119] A. E. Gill, Atmosphere-Ocean Dynamics, vol. Appendix Two, New York: Academic Press, 1982.

9. List of publications by the dissertant related to the dissertation

Journal articles:

[1]. Trush, A.; Pospíšil, S.; Kuznetsov, S.; Kozmar, H., “Wind-Tunnel Experiments on Vortex-Induced Vibration of Rough Bridge Cables”, *ASCE Journal of Bridge Engineering*, vol. 22, no.10, October 2017, DOI: 10.1061/(ASCE)BE.1943-5592.0001104.

[2]. Kuznetsov, S., Ribičić, M., Pospíšil, S., Plut, M., Trush, A., Kozmar, H., “Flow and Turbulence Control in a Boundary Layer Wind Tunnel Using Passive Hardware Devices”, *Experimental Techniques*, vol. 41,no. 6, pp 643–661, 2017. DOI: 10.1007/s40799-017-0196-z.

[3]. Górski, P, Pospíšil, S., Tatara, M., Trush, A., “PIV analysis of near-wake flow patterns of an ice-accreted bridge cable in low and moderately turbulent wind”, *Journal of Wind Engineering and Industrial Aerodynamics*, vol. 191, 297-311, 2019, DOI: 10.1016/j.jweia.2019.06.011.

Conference articles:

[4]. Trush, A., “Turbulence Effects on Wind-induced Fatigue of Slender Steel Structures”, *Sborník semináře doktorandů katedry ocelových a dřevěných konstrukcí* 20.5. a 22.9. 2015, Praha, 2015, ISBN (978-80-01-05741-4).

[5]. Trush, A., Pospíšil, S., Kuznetsov, “Aeroelasticity of cables with ice accretion”, *In Proc*. *HELIX 2015: Fluid-Structure Interactions and Vortex Dynamics in Aerodynamics*; Porquerolles Island, Hyeres, France; 29.06.2015 - 04.07.2015.

[6]. Pospíšil, S., Trush, A., Kuznetsov, S. “Influence of wind angle of attack and isotropic turbulence on wind-induced vibrations of ice accreted bridge cables”, *In Proc. 8th International Colloquium on Bluff Body Aerodynamics and Applications. Boston*, 2016.

[7]. Kuznetsov, S., Ribičić, M., Pospíšil, S., Plut, M., Trush, A., Kozmar, H., “Flow and turbulence in the boundary layer wind tunnel controlled using various hardware devices”, *In Proc. 8th International Colloquium on Bluff Body Aerodynamics and Applications. Boston*, 2016.

[8]. Trush, A., “Turbulence Effects on Wind-induced Fatigue of Slender Steel Structures”, *Sborník semináře doktorandů katedry ocelových a dřevěných konstrukcí* 18.2. a 22.9. 2016, Praha, 2016, ISBN (978-80-01-05963-0).

[9]. Trush, A., Pospíšil, S., Kuznetsov, S.: “Study of Strouhal number of bridge cables in turbulent flows”, *in Proc. of the International Workshop on Wind Effects on Buildings and Urban Environment*, 10-12.03.2019, Tokyo Polytechnic University, Japan.

[10]. Trush, A., Pospíšil, S., Kuznetsov, S.:Wind tunnel tests for lifetime estimation of bridge and mast cables exposed to vortex induced vibrations, *17th Youth Symposium on Experimental Solid Mechanics*, 6-8.06.2019, Telč, Czech Republic.

[11]. Trush, A., Pospíšil, S., Kuznetsov, S., “Vortex induced response of bridge cables in turbulent flow”, *in Proc. The 15th International Conference on Wind Engineering*, 1-6.09.2019, Beijing, China.

10. Appendix A: Figures

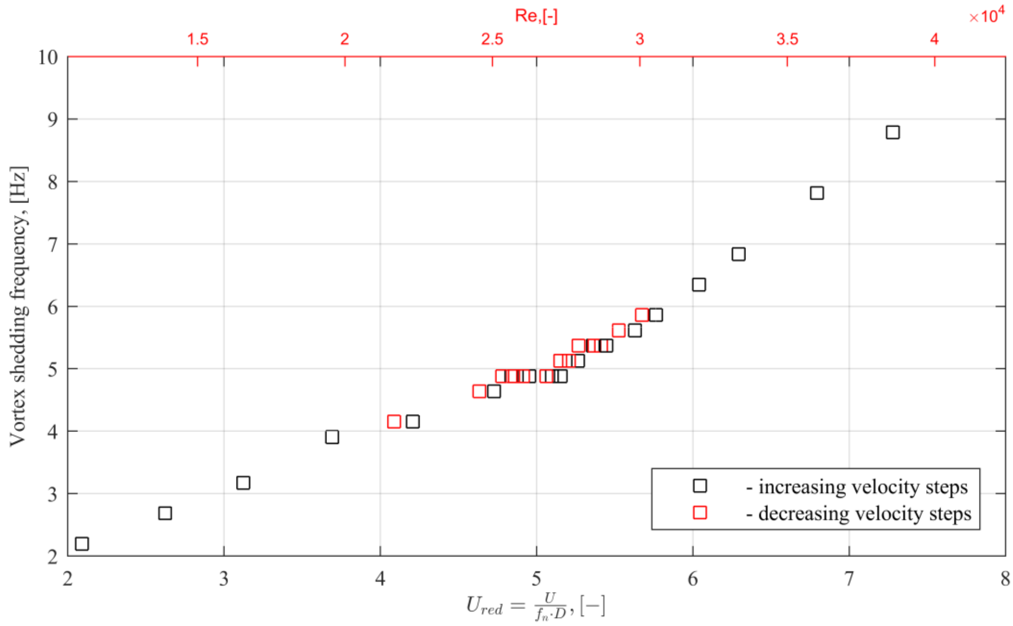

Figure 10.1 Lock-in range of helical cable 1x61-12 model in flow with I_u=0.75%

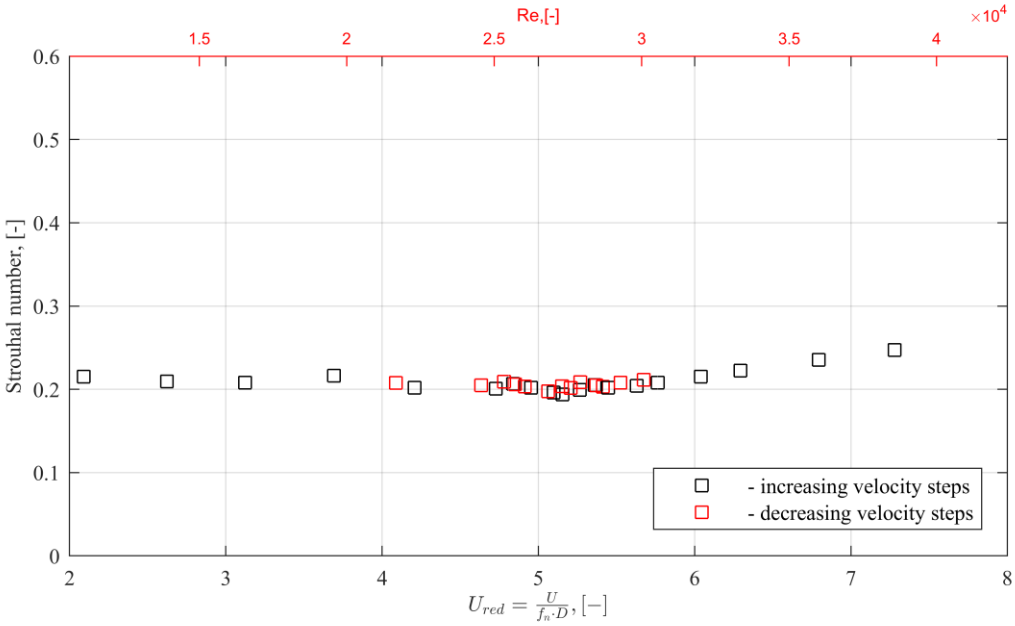

Figure 10.2 Strouhal number of helical cable 1x61-12 model in flow with I_u=0.75%

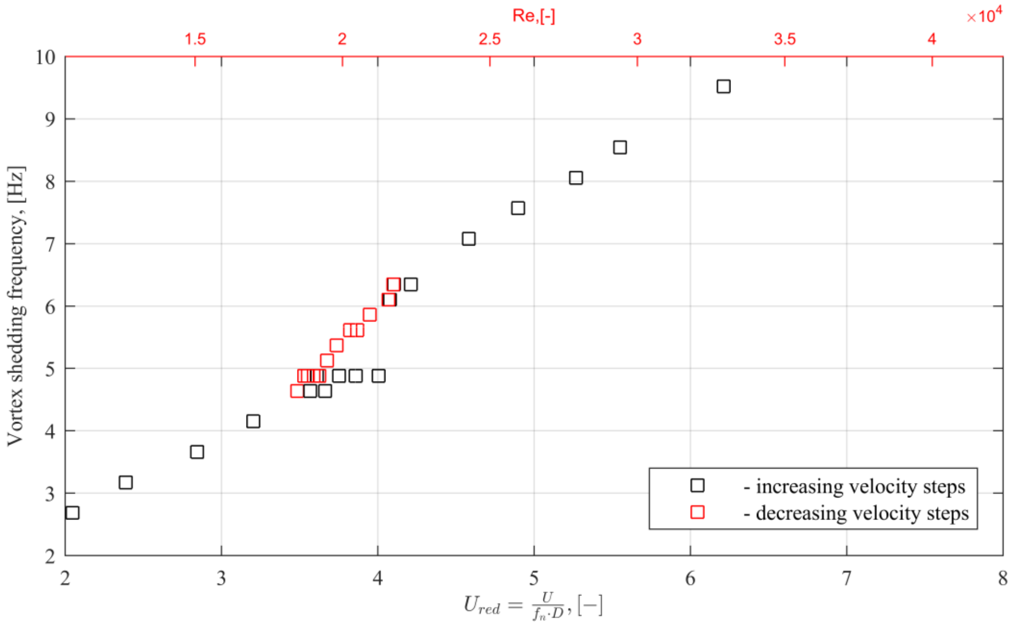

Figure 10.3 Lock-in range of helical cable 1x61-12 model in flow with I_u=4.5%

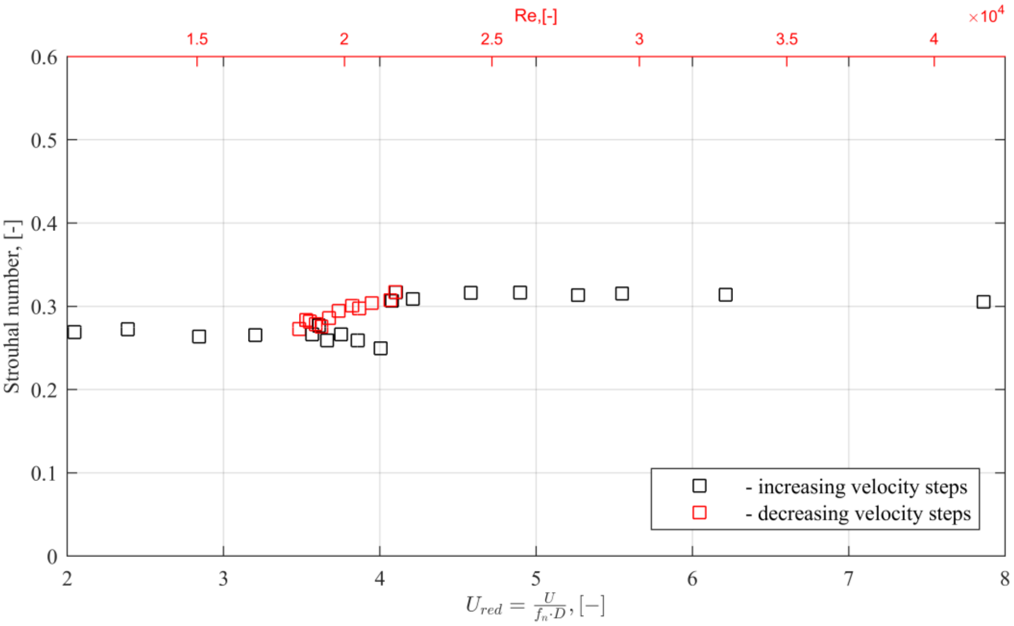

Figure 10.4 Strouhal number of helical cable 1x61-12 model in flow with I_u=4.5%

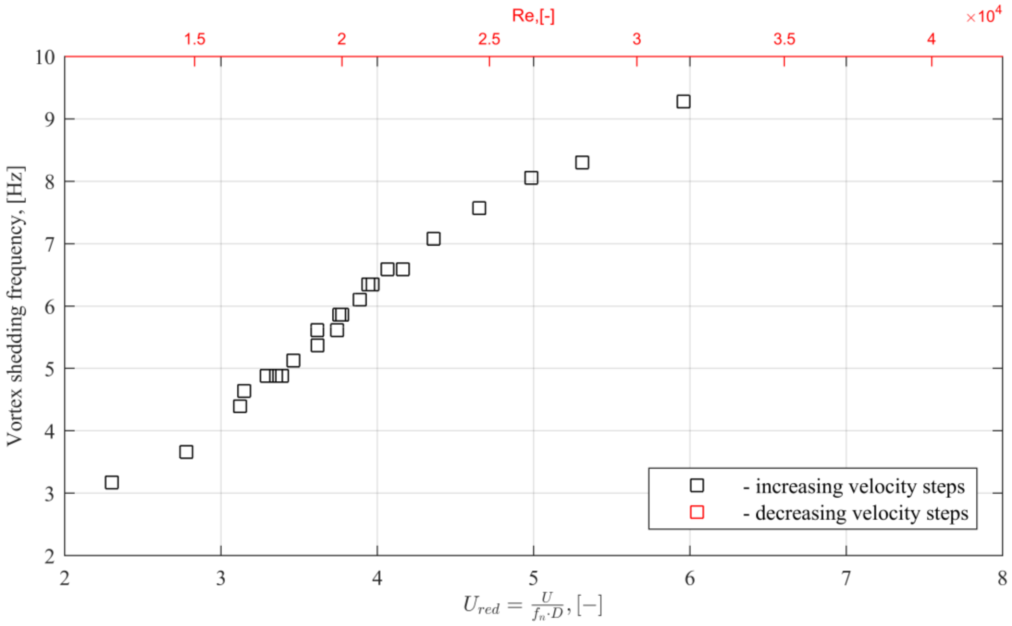

Figure 10.5 Lock-in range of helical cable 1x61-12 model in flow with I_u=6.5%

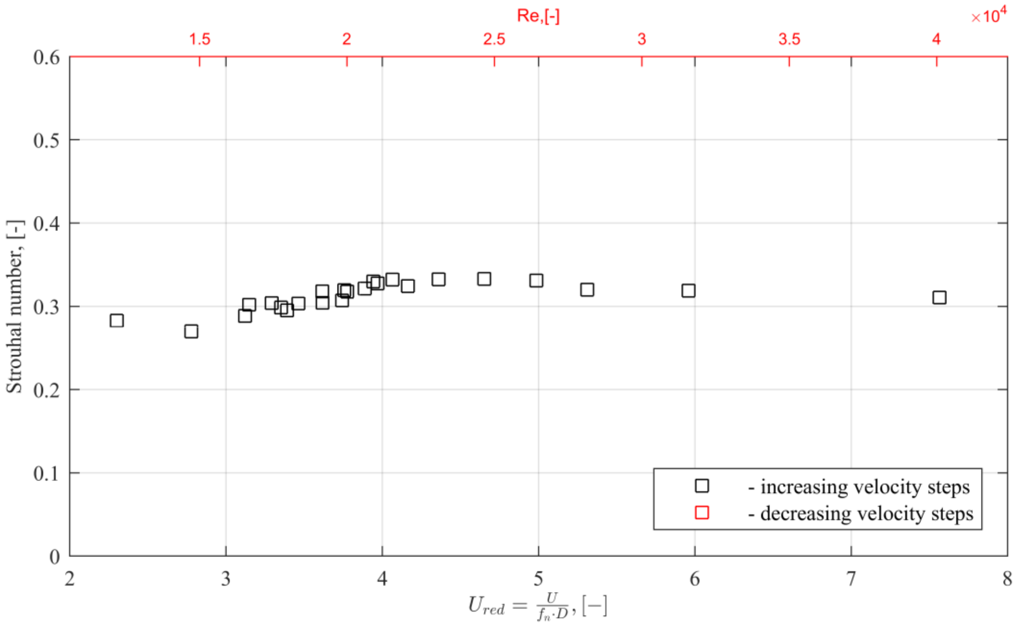

Figure 10.6 Strouhal number of helical cable 1x61-12 model in flow with I_u=6.5%

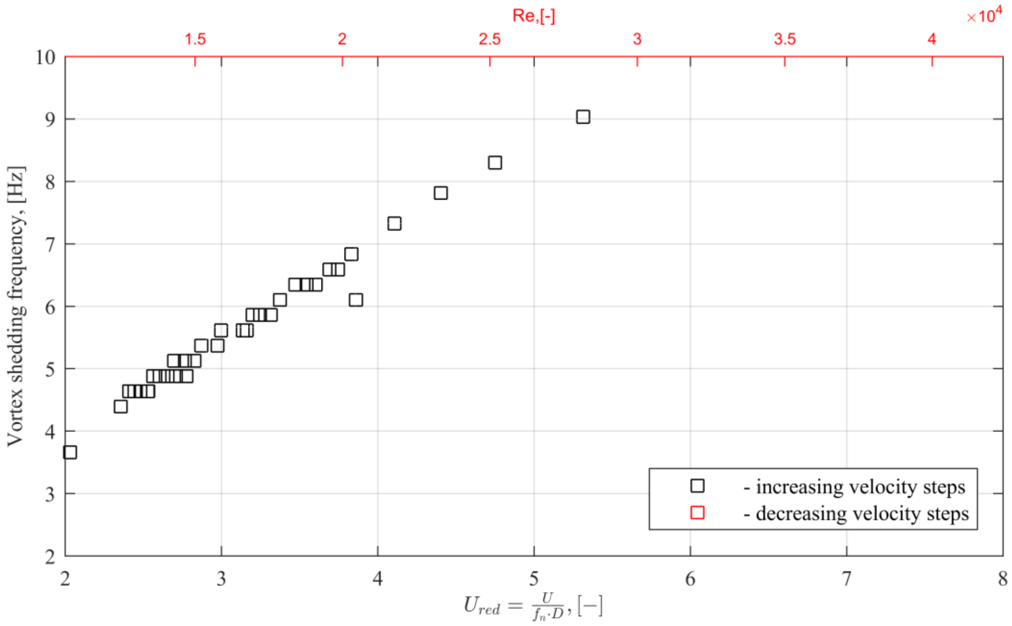

Figure 10.7 Lock-in range of helical cable 1x61-12 model in flow with I_u=12.3%

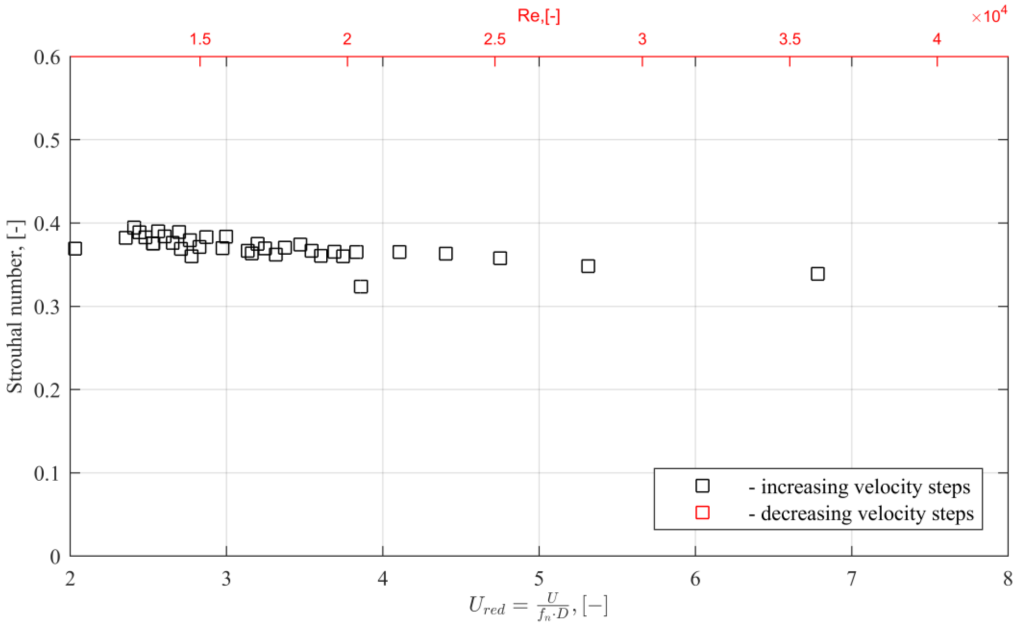

Figure 10.8 Strouhal number of helical cable 1x61-12 model in flow with I_u=12.3%

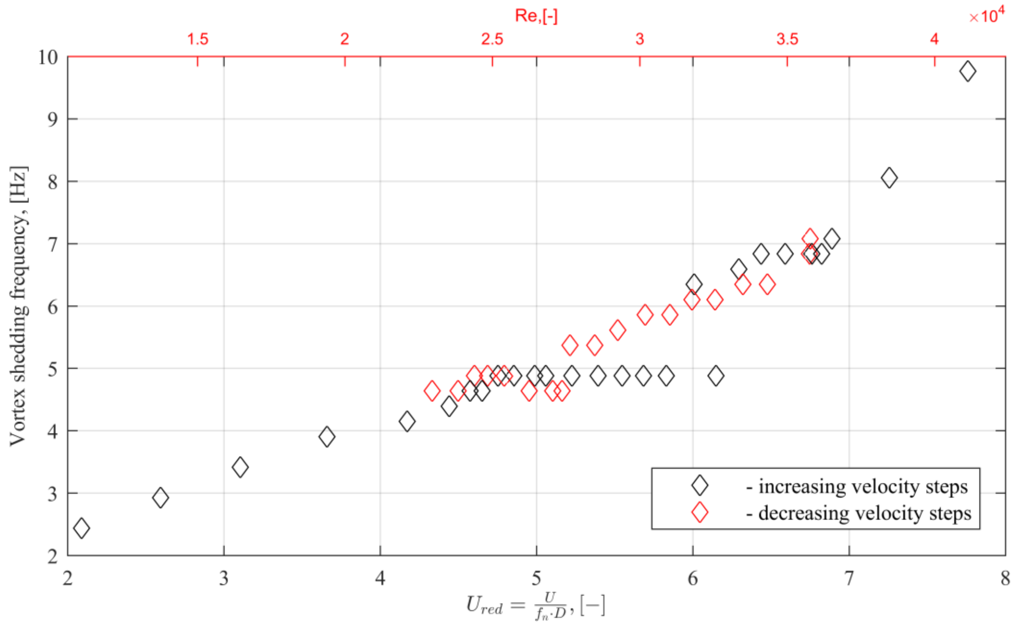

Figure 10.9 Lock-in range of helical cable 1x61-24 model in flow with I_u=0.75%

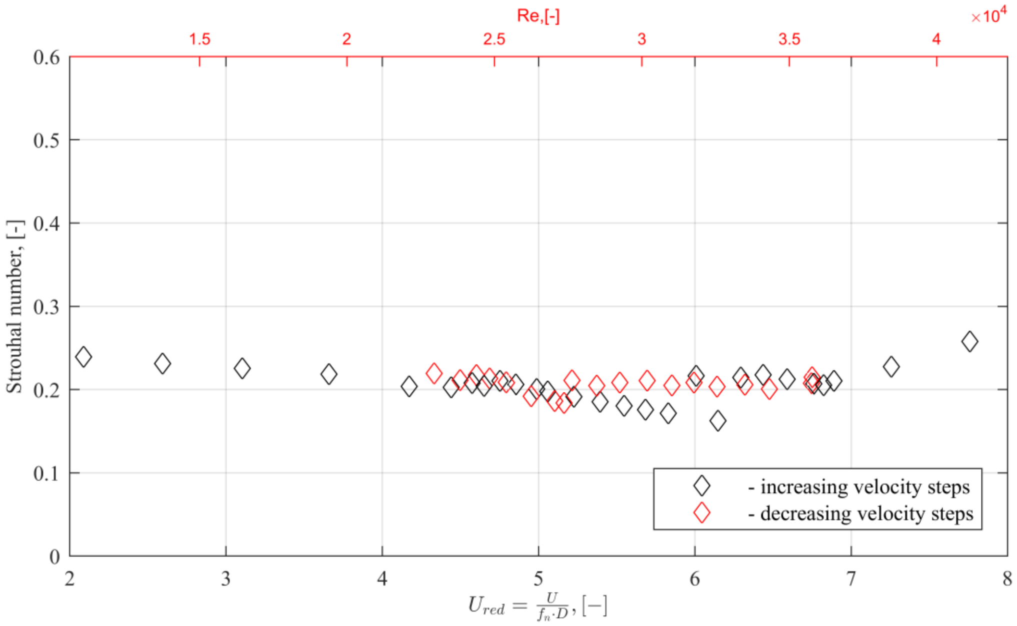

Figure 10.10 Strouhal number of helical cable 1x61-24 model in flow with I_u=0.75%

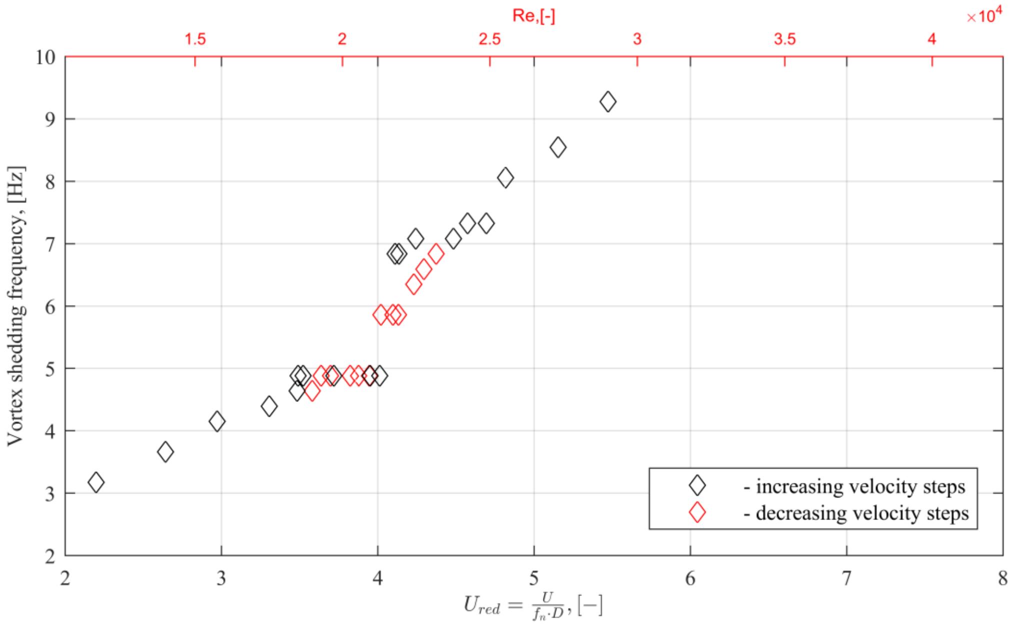

Figure 10.11 Lock-in range of helical cable 1x61-24 model in flow with I_u=4.5%

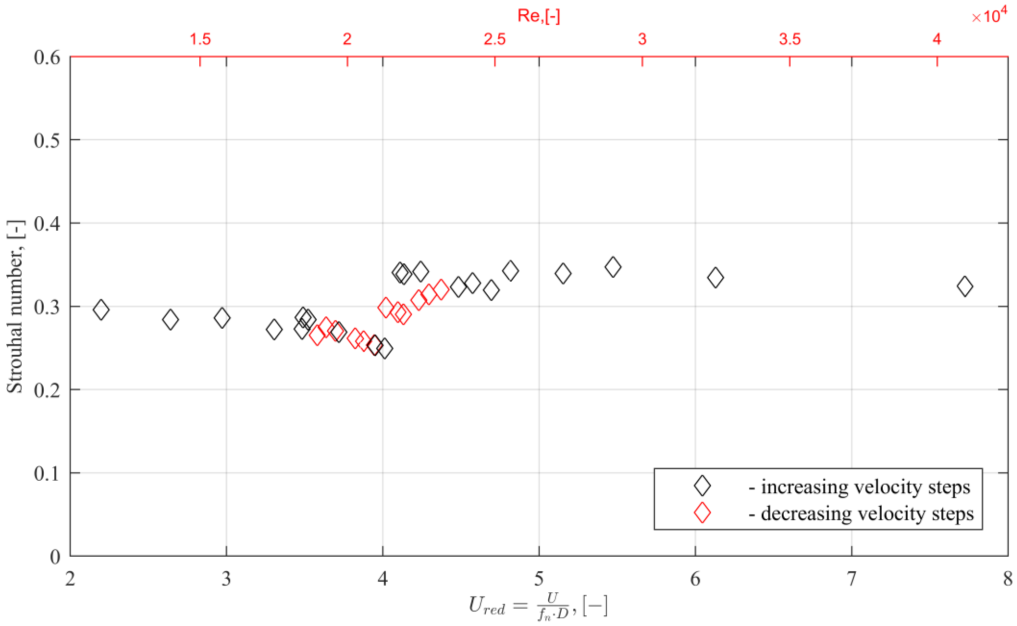

Figure 10.12 Strouhal number of helical cable 1x61-24 model in flow with I_u=4.5%

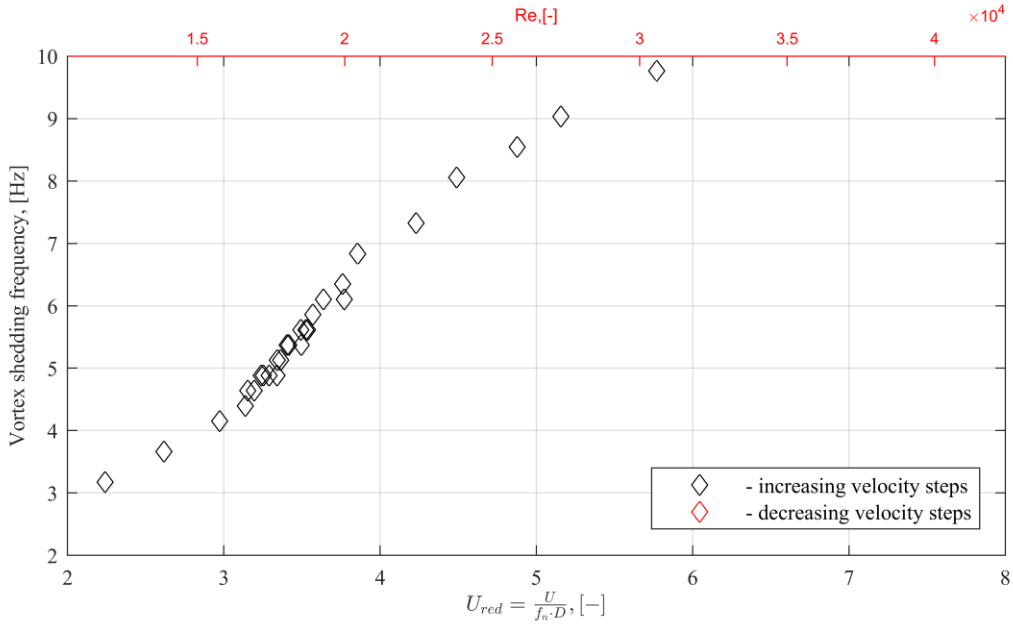

Figure 10.13 Lock-in range of helical cable 1x61-24 model in flow with I_u=6.5%

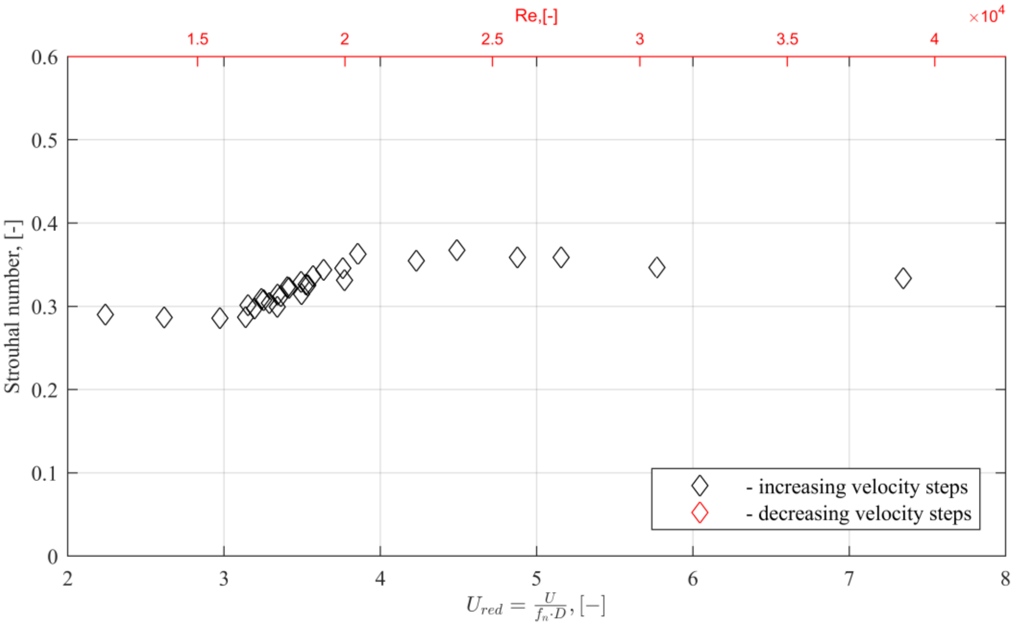

Figure 10.14 Strouhal number of helical cable 1x61-24 model in flow with I_u=6.5%

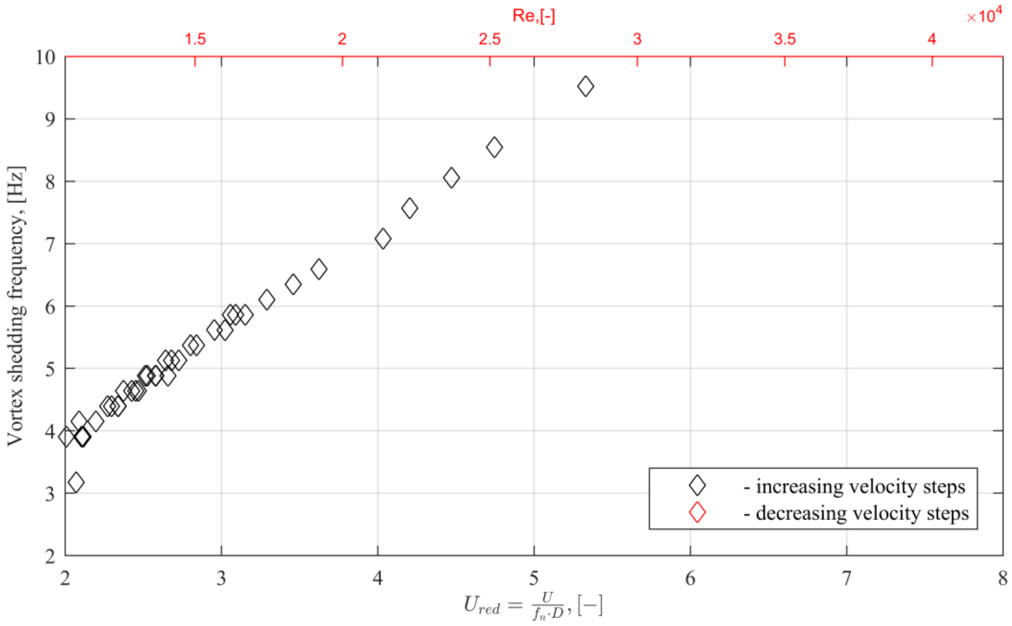

Figure 10.15 Lock-in range of helical cable 1x61-24 model in flow with I_u=12.3%

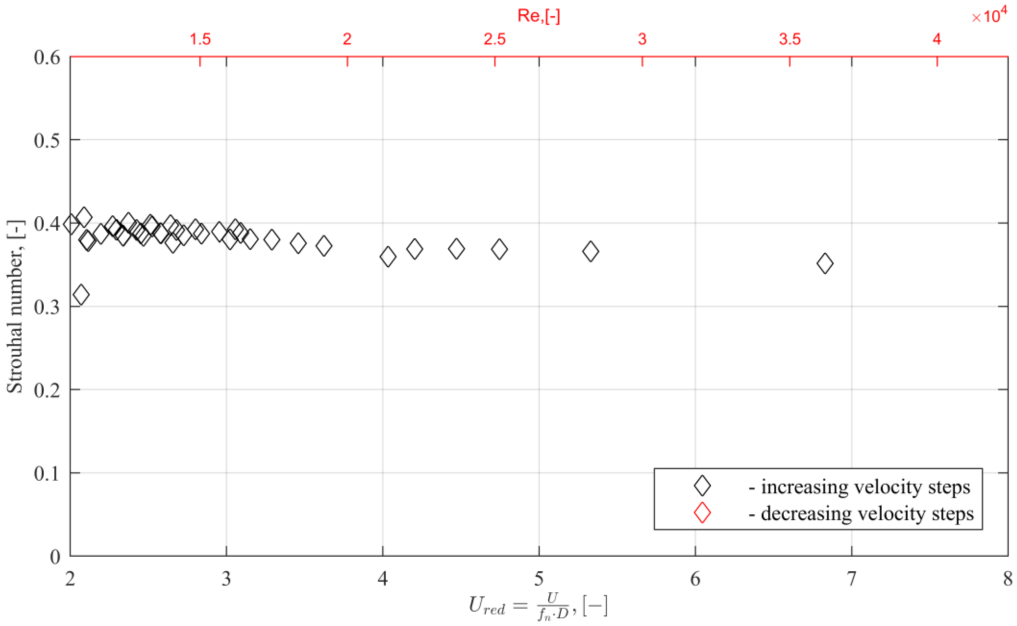

Figure 10.16 Strouhal number of helical cable 1x61-24 model in flow with I_u=12.3%

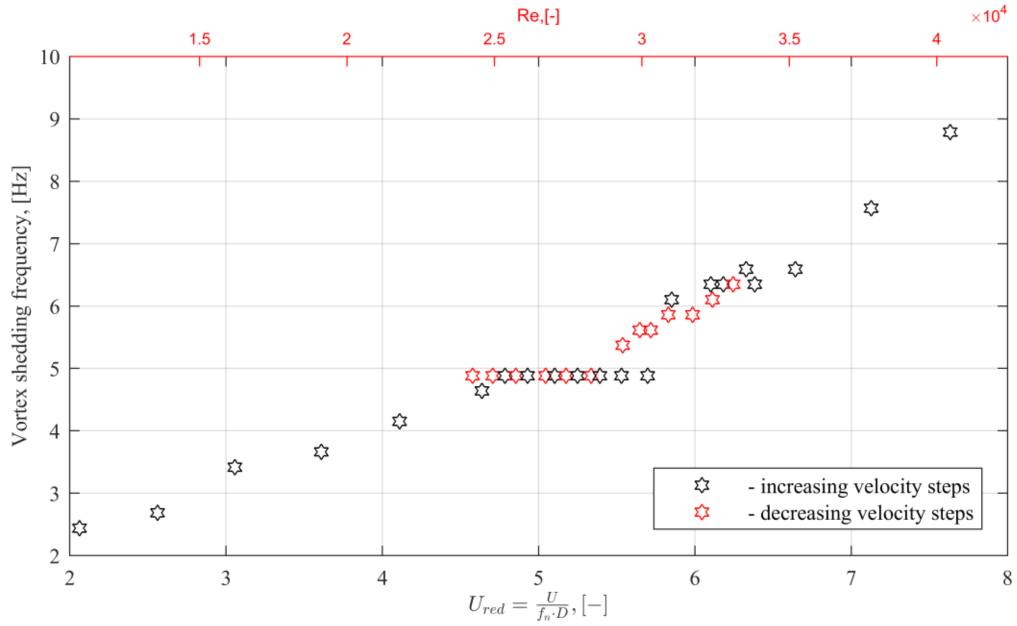

Figure 10.17 Lock-in range of helical cable 1x91-12 model in flow with I_u=0.75%

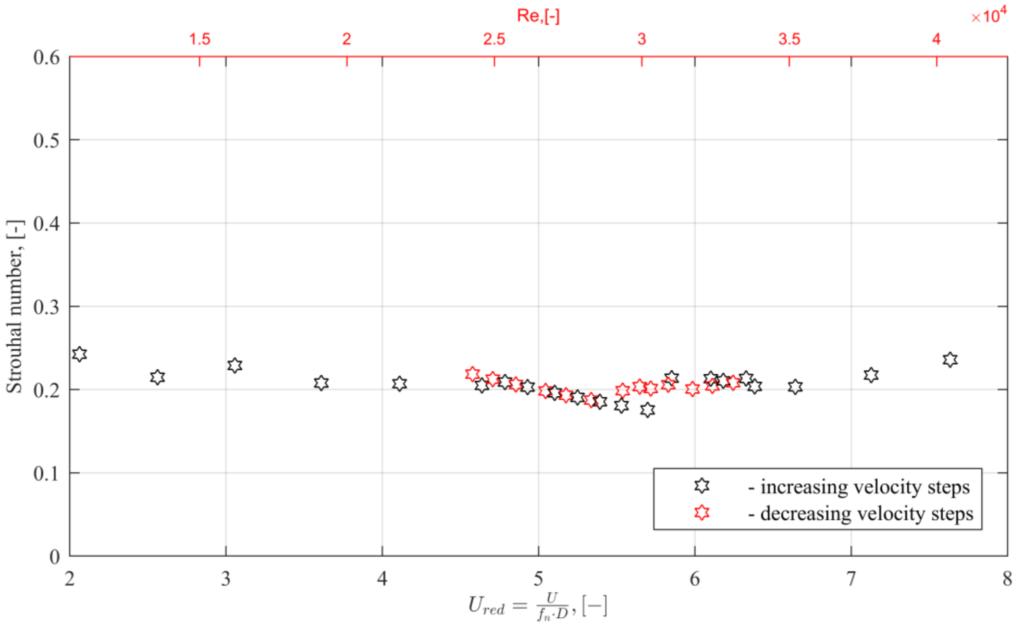

Figure 10.18 Strouhal number of helical cable 1x91-12 model in flow with I_u=0.75%

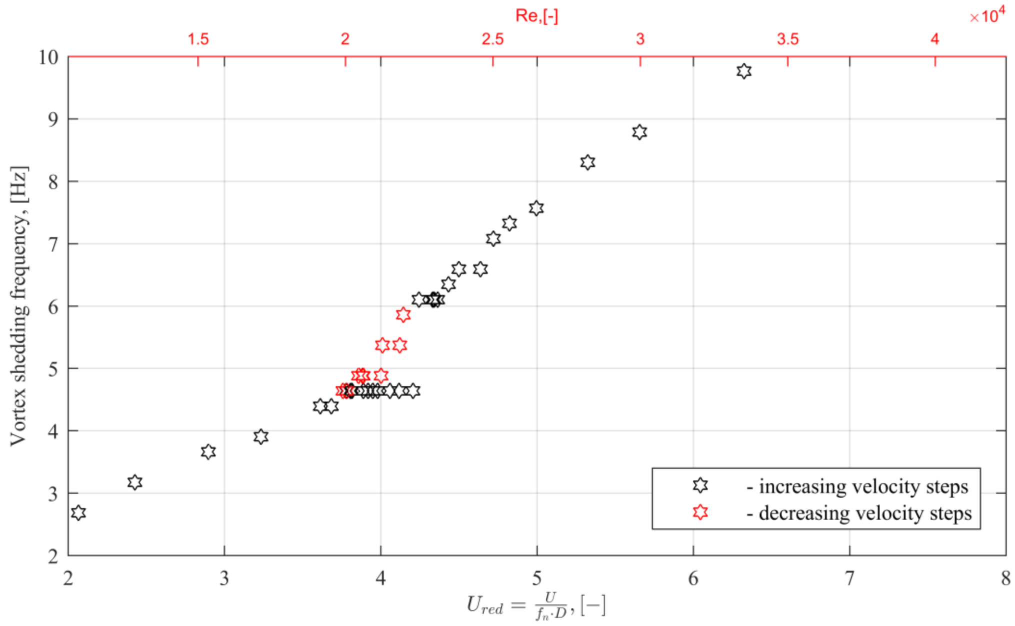

Figure 10.19 Lock-in range of helical cable 1x91-12 model in flow with I_u=4.5%

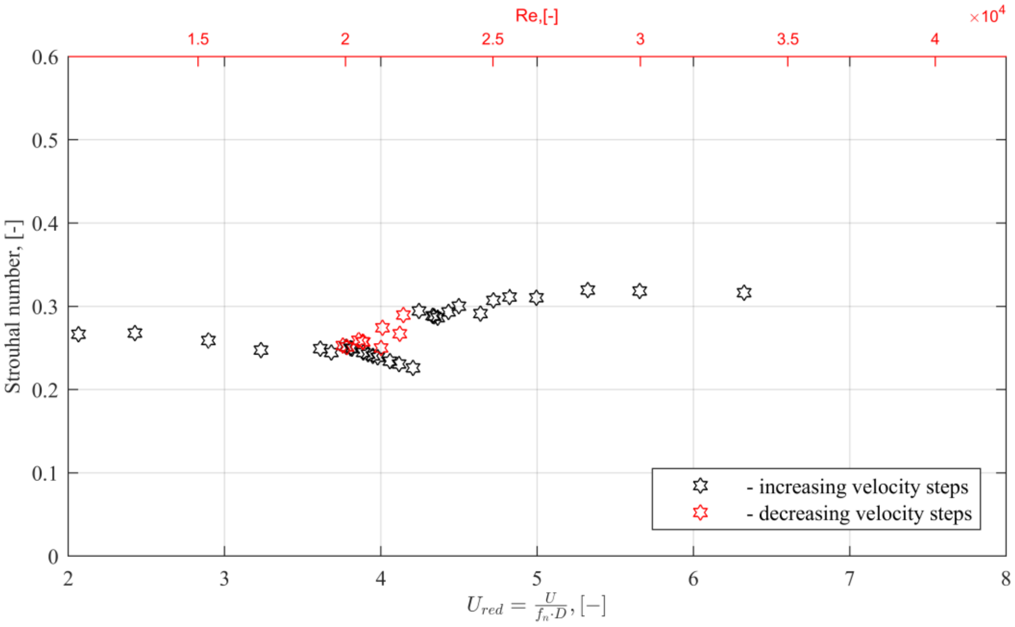

Figure 10.20 Strouhal number of helical cable 1x91-12 model in flow with I_u=4.5%

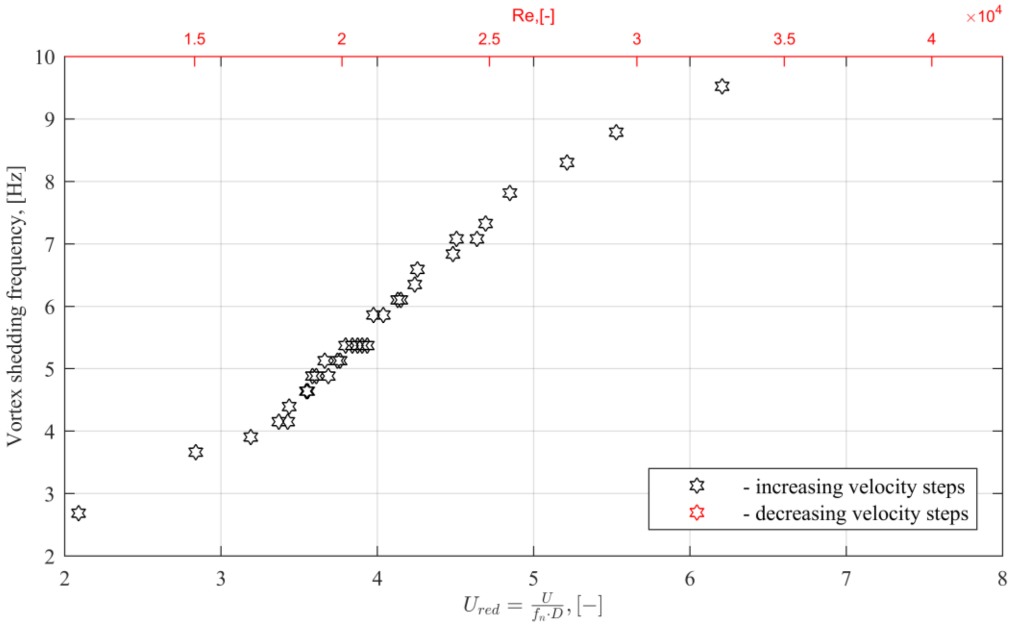

Figure 10.21 Lock-in range of helical cable 1x91-12 model in flow with I_u=6.5%

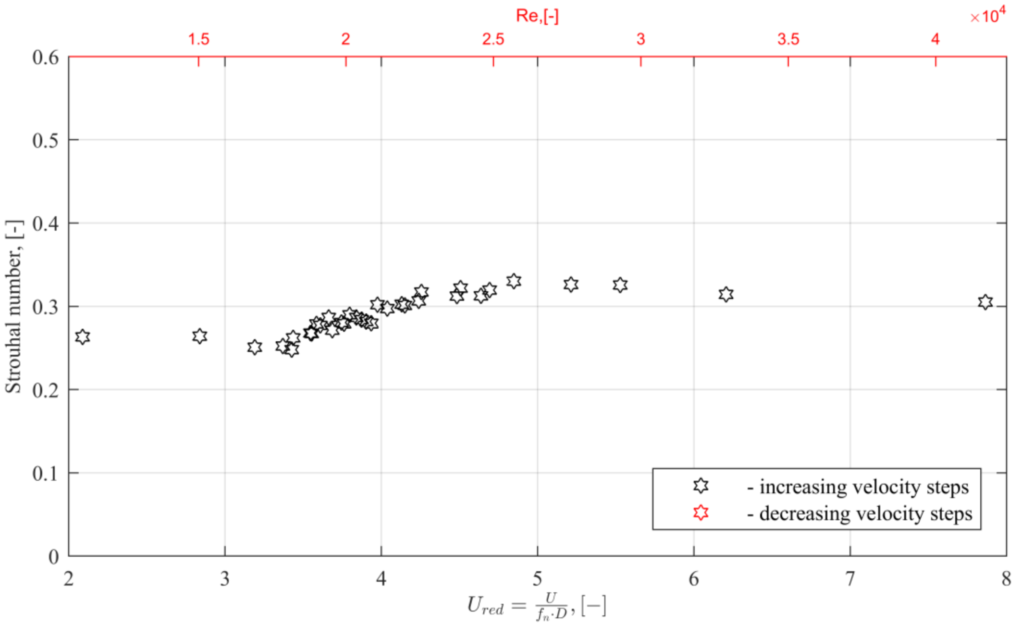

Figure 10.22 Strouhal number of helical cable 1x91-12 model in flow with I_u=6.5%

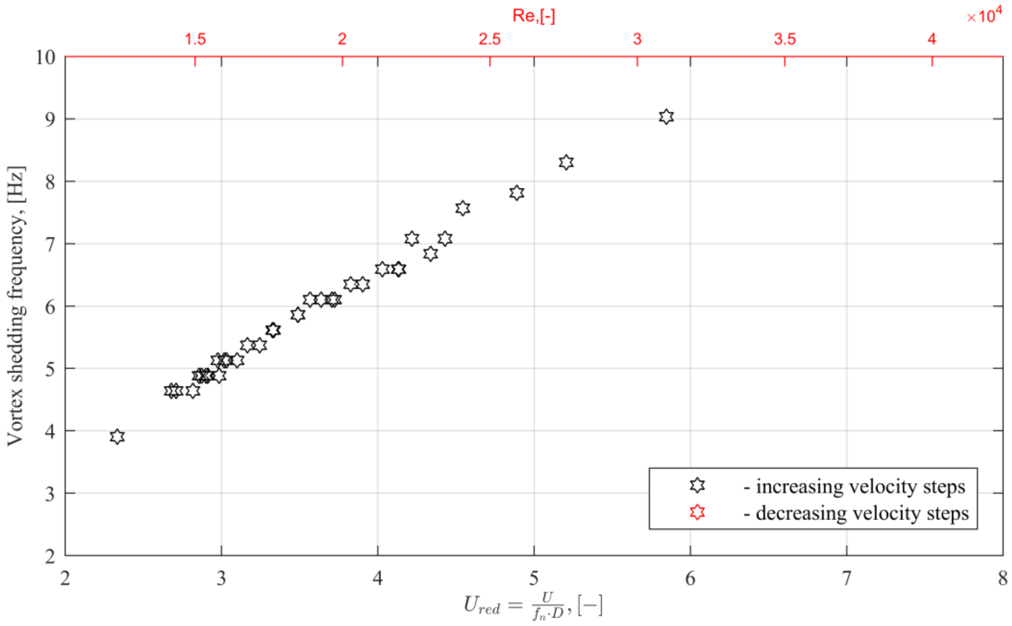

Figure 10.23 Lock-in range of helical cable 1x91-12 model in flow with I_u=12.3%

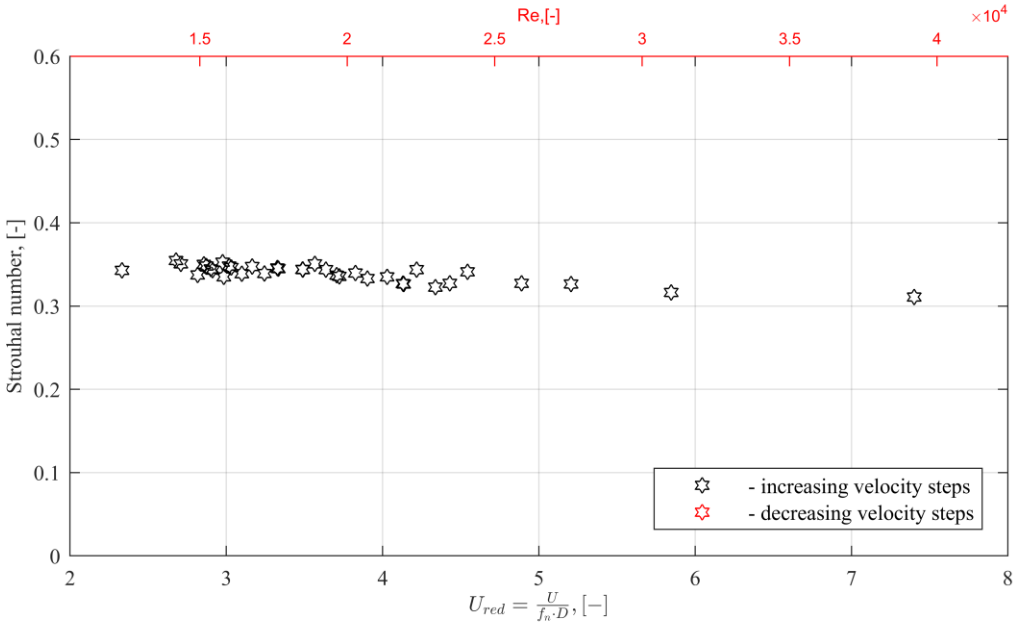

Figure 10.24 Strouhal number of helical cable 1x91-12 model in flow with I_u=12.3%

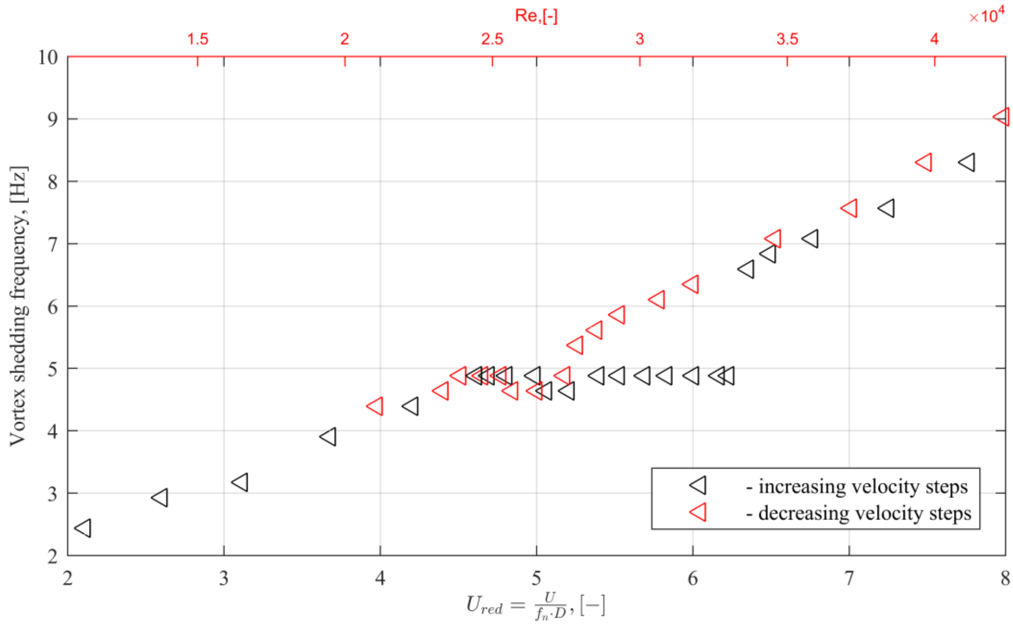

Figure 10.25 Lock-in range of iced cable model, α=0° in flow with I_u=0.75%

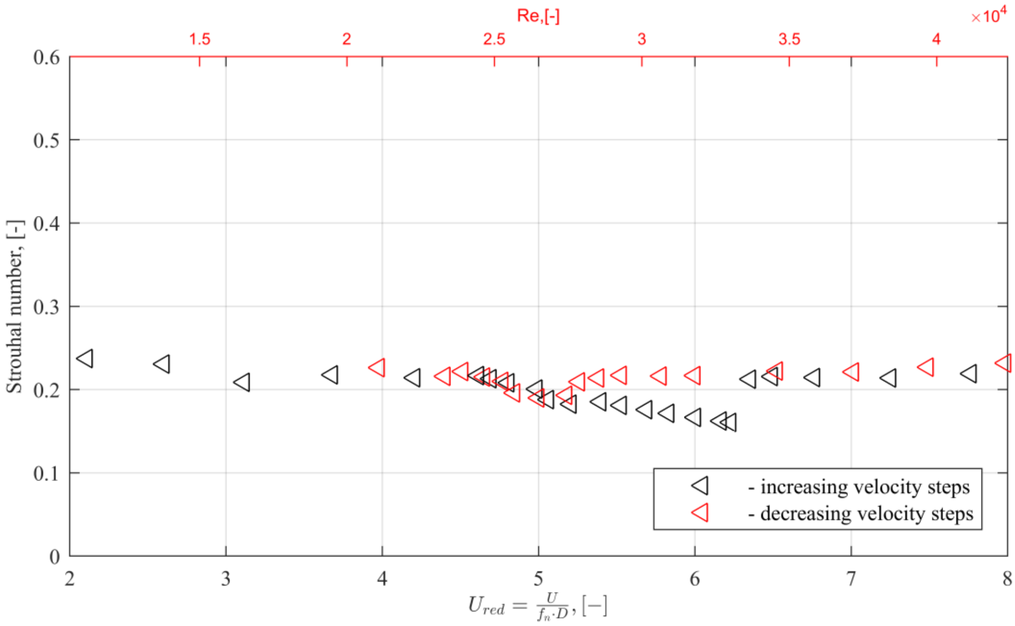

Figure 10.26 Strouhal number of iced cable model, α=0° in flow with I_u=0.75%

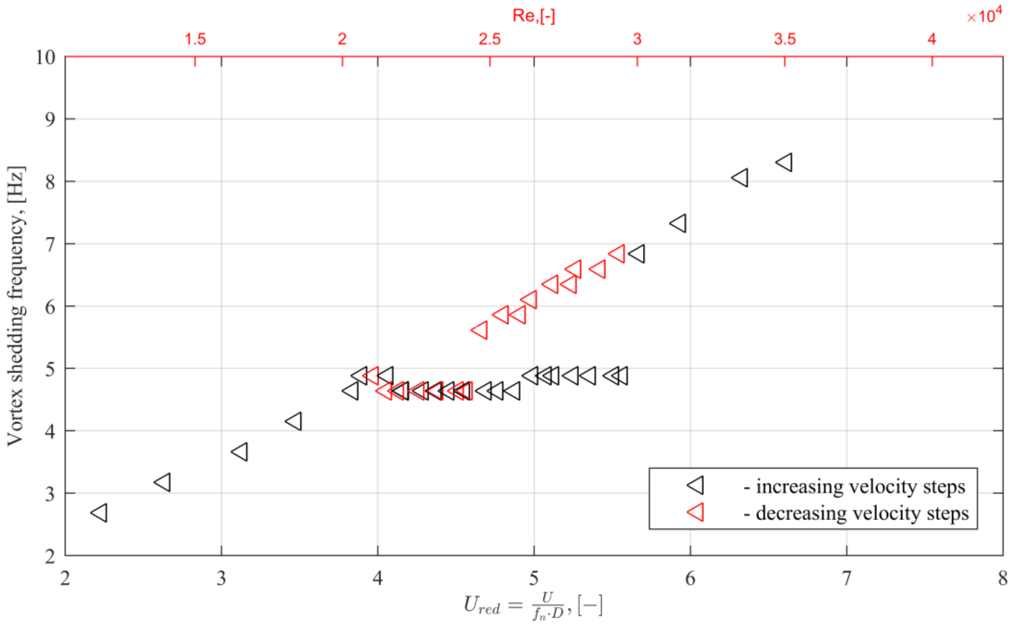

Figure 10.27 Lock-in range of iced cable model, α=0° in flow with I_u=4.5%

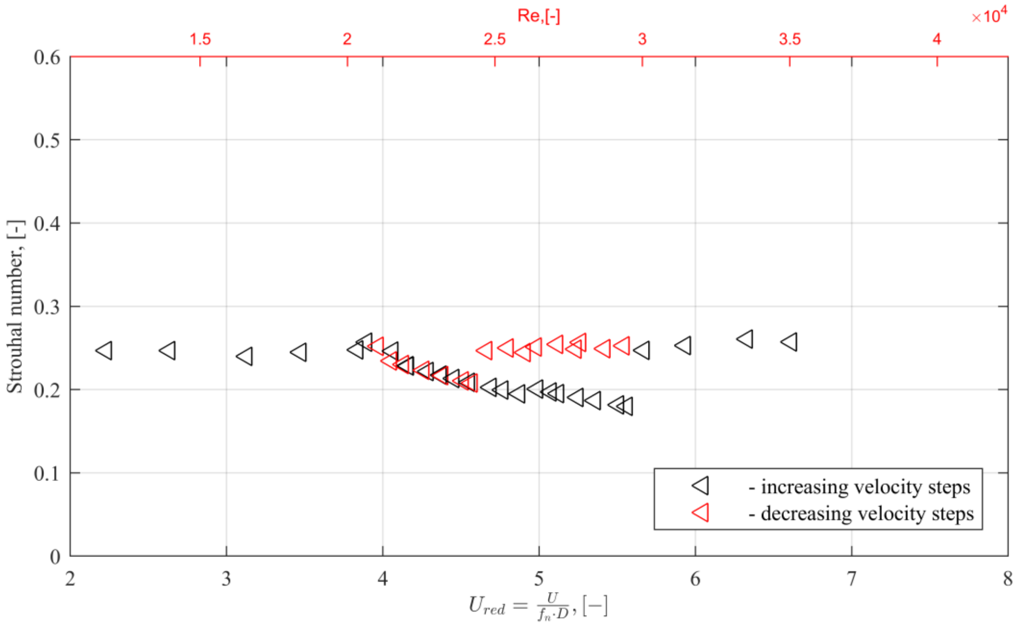

Figure 10.28 Strouhal number of iced cable model, α=0° in flow with I_u=4.5%

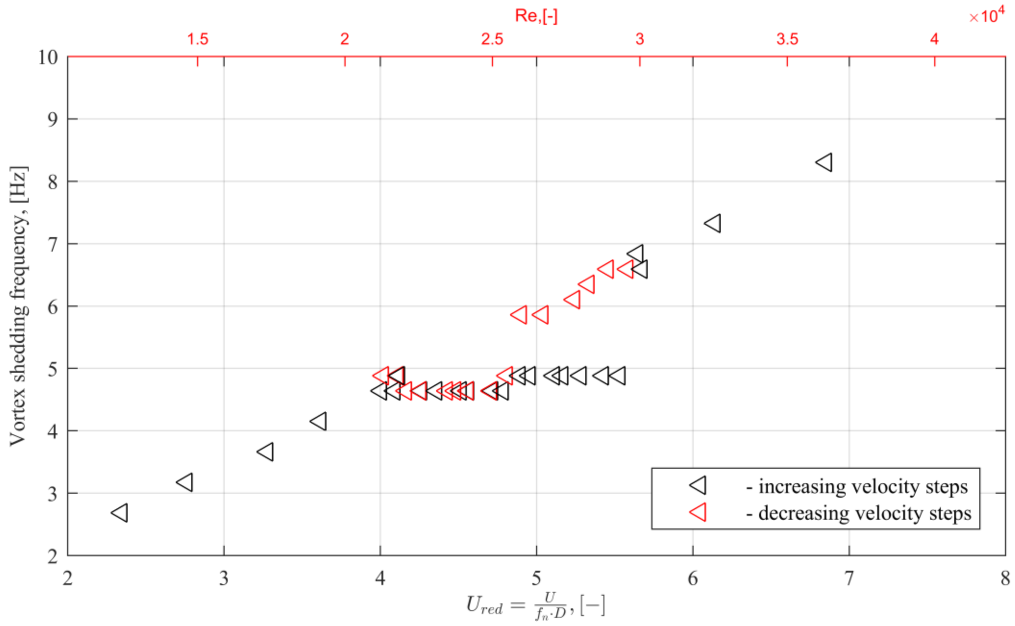

Figure 10.29 Lock-in range of iced cable model, α=0° in flow with I_u=6.5%

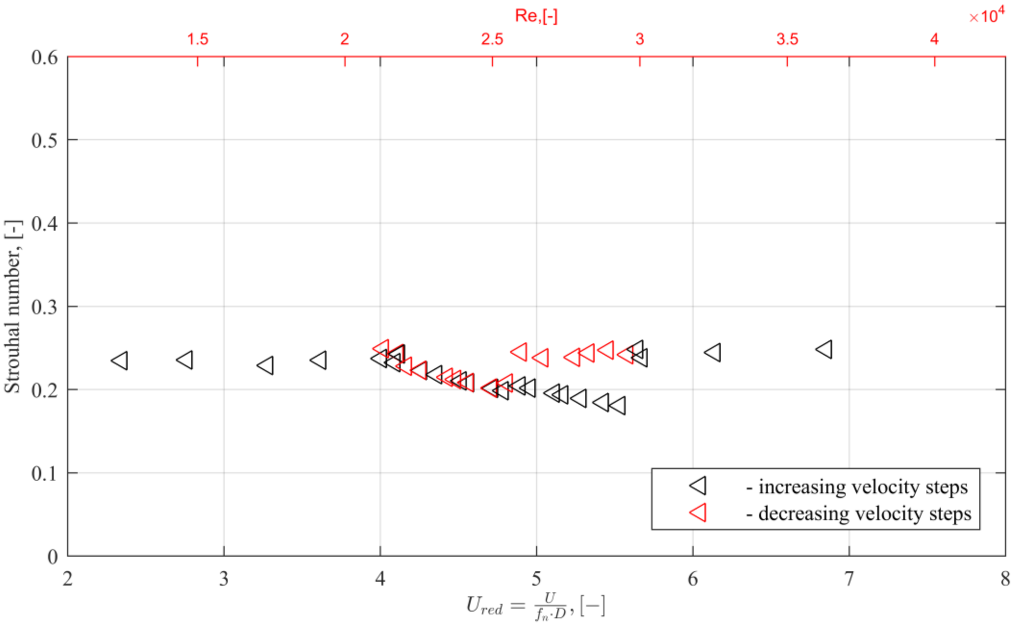

Figure 10.30 Strouhal number of iced cable model, α=0° in flow with I_u=6.5%

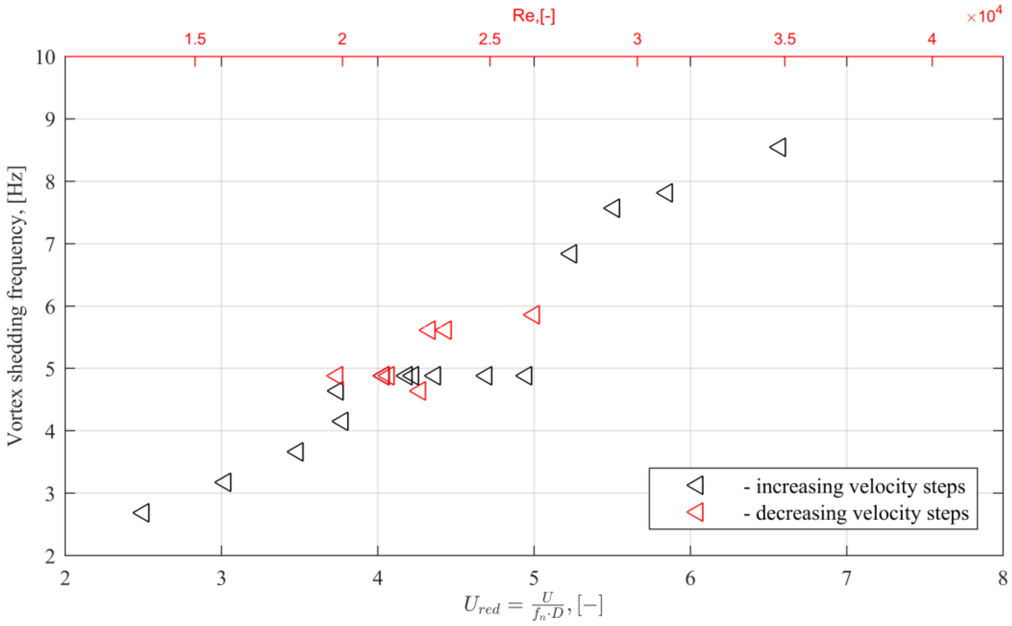

Figure 10.31 Lock-in range of iced cable model, α=0° in flow with I_u=12.3%

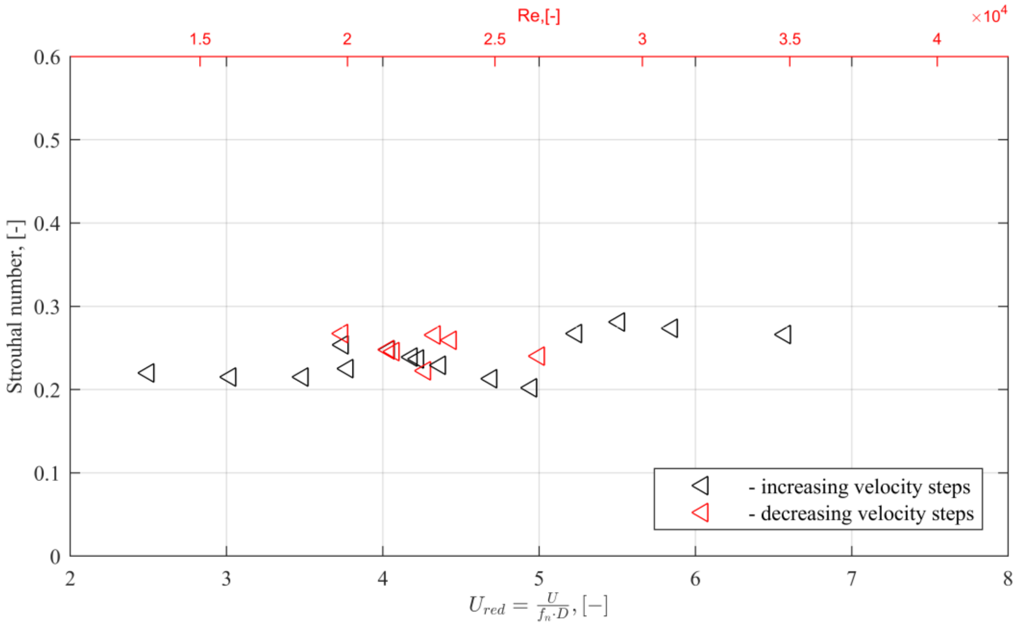

Figure 10.32 Strouhal number of iced cable model, α=0° in flow with I_u=12.3%

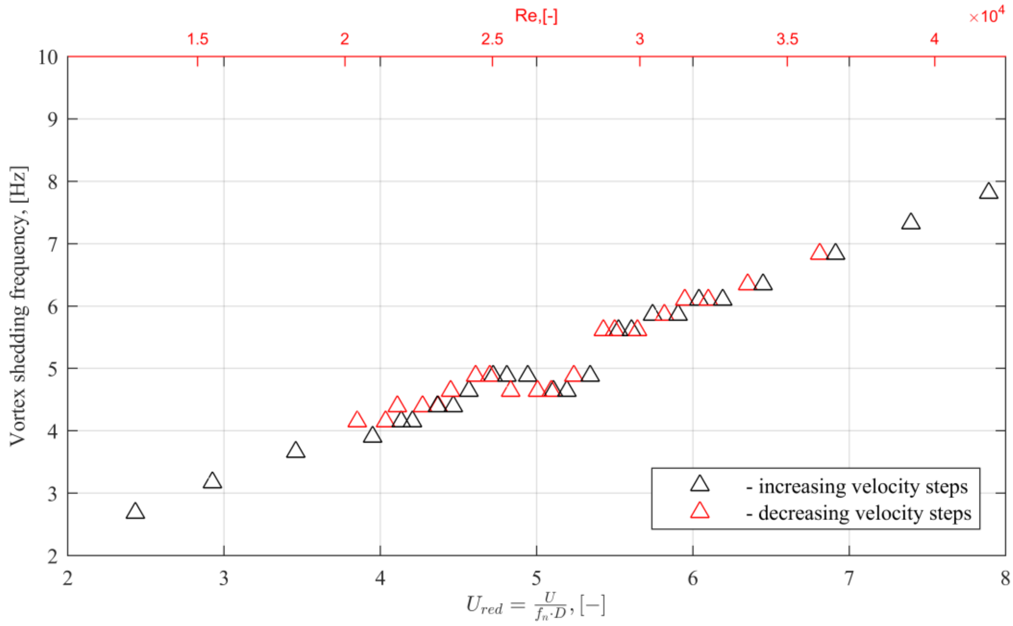

Figure 10.33 Lock-in range of iced cable model, α=90° in flow with I_u=0.75%

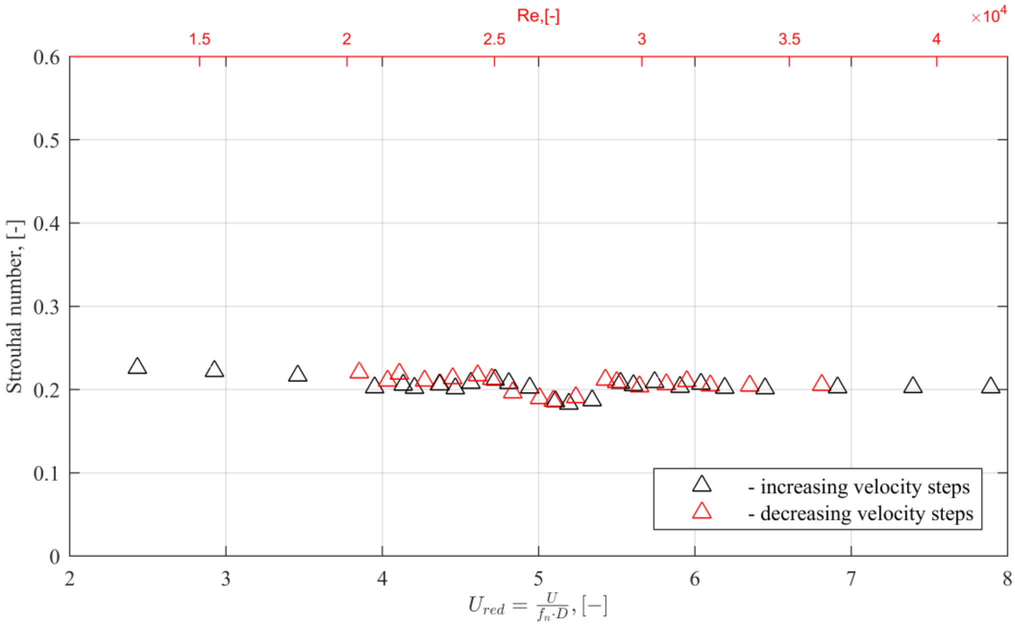

Figure 10.34 Strouhal number of iced cable model, α=90° in flow with I_u=0.75%

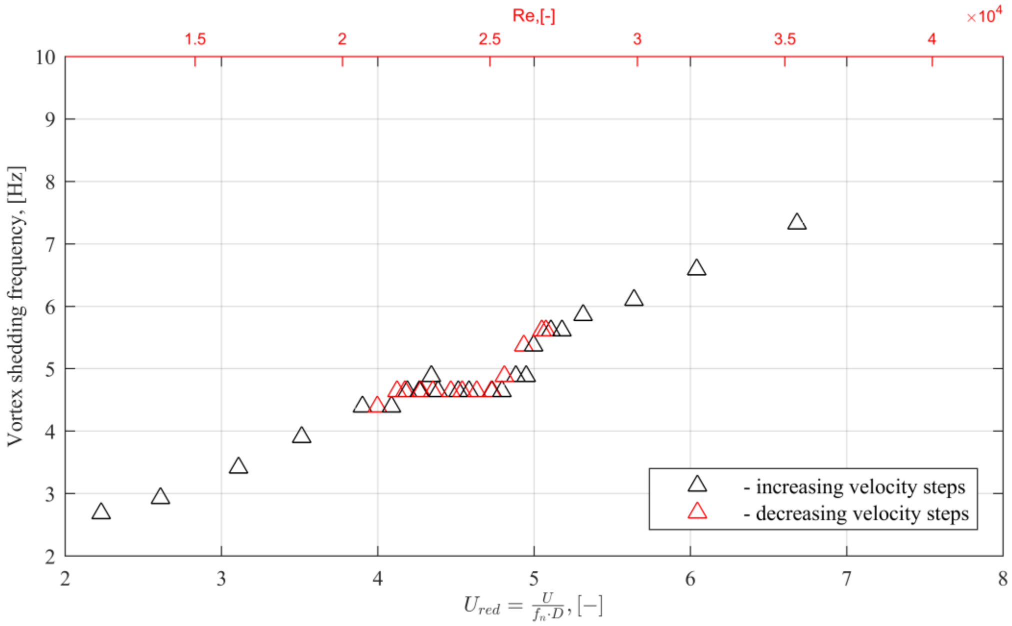

Figure 10.35 Lock-in range of iced cable model, α=90° in flow with I_u=4.5%

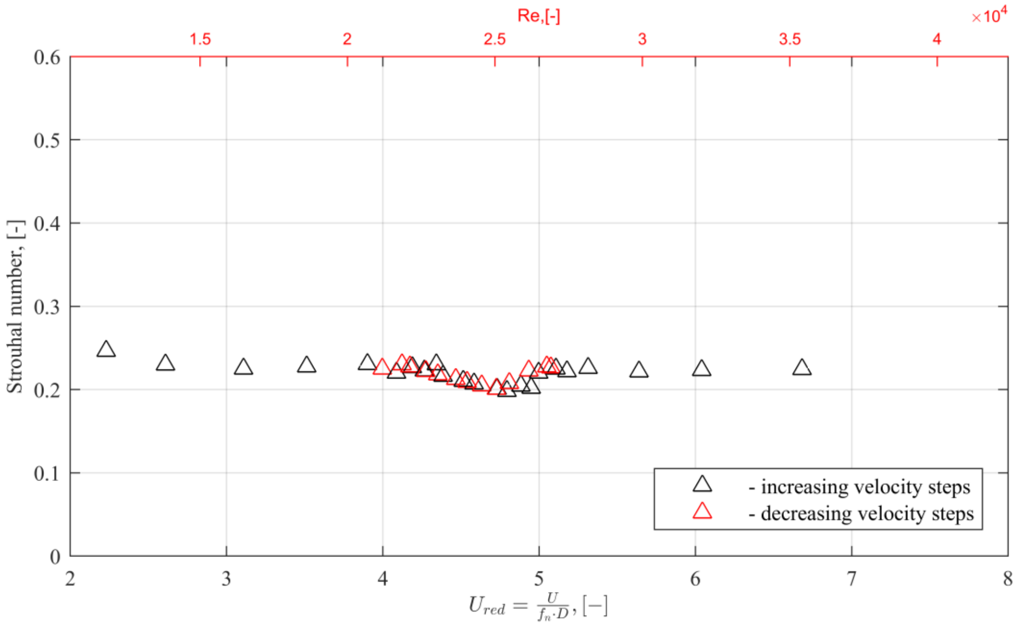

Figure 10.36 Strouhal number of iced cable model, α=90° in flow with I_u=4.5%

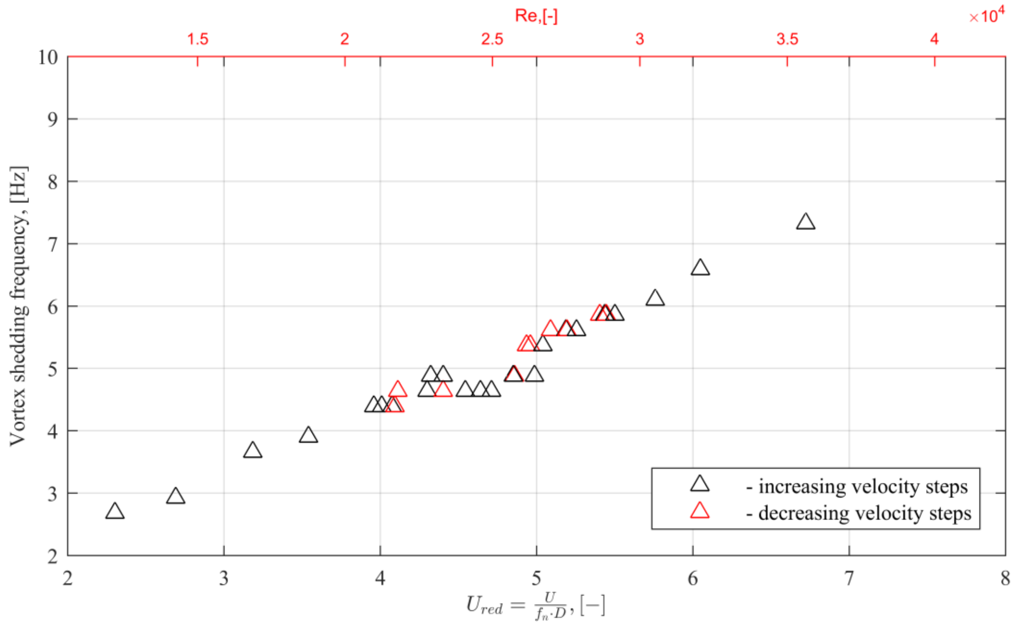

Figure 10.37 Lock-in range of iced cable model, α=90° in flow with I_u=6.5%

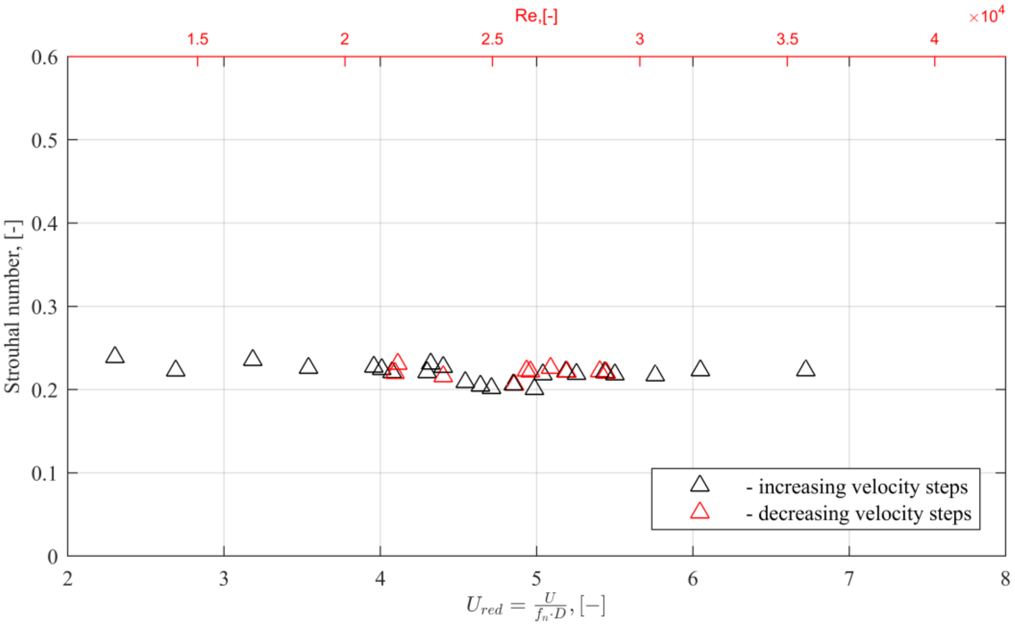

Figure 10.38 Strouhal number of iced cable model, α=90° in flow with I_u=6.5%

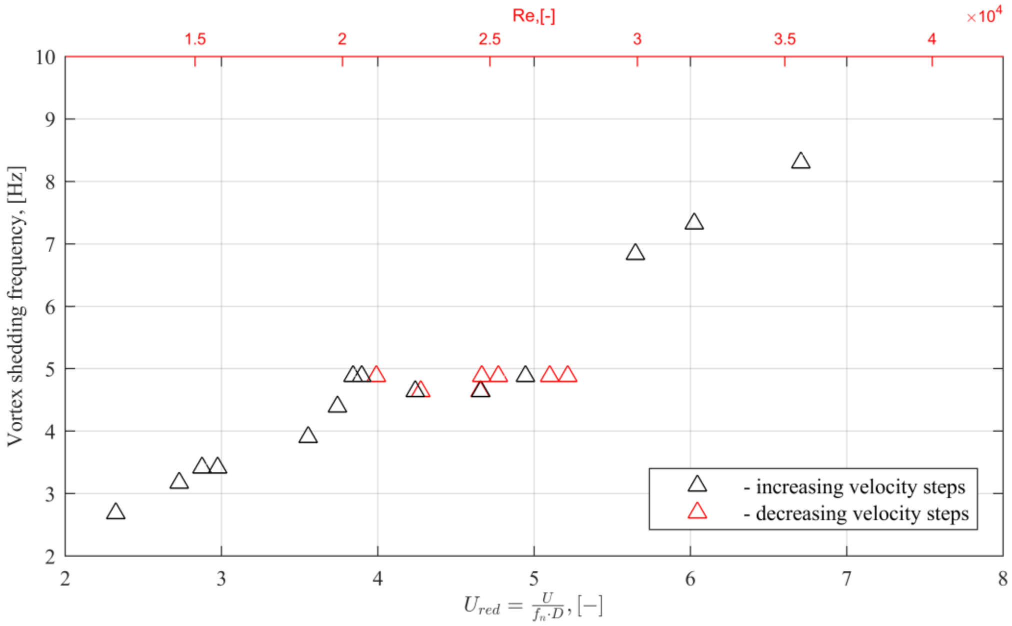

Figure 10.39 Lock-in range of iced cable model, α=90° in flow with I_u=12.3%

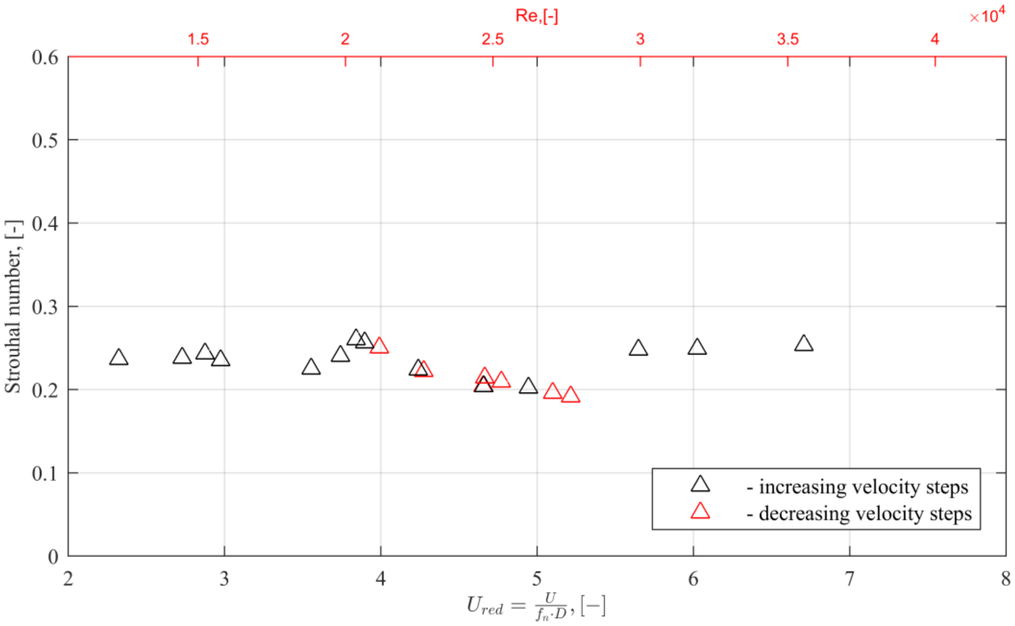

Figure 10.40 Strouhal number of iced cable model, α=90° in flow with I_u=12.3%

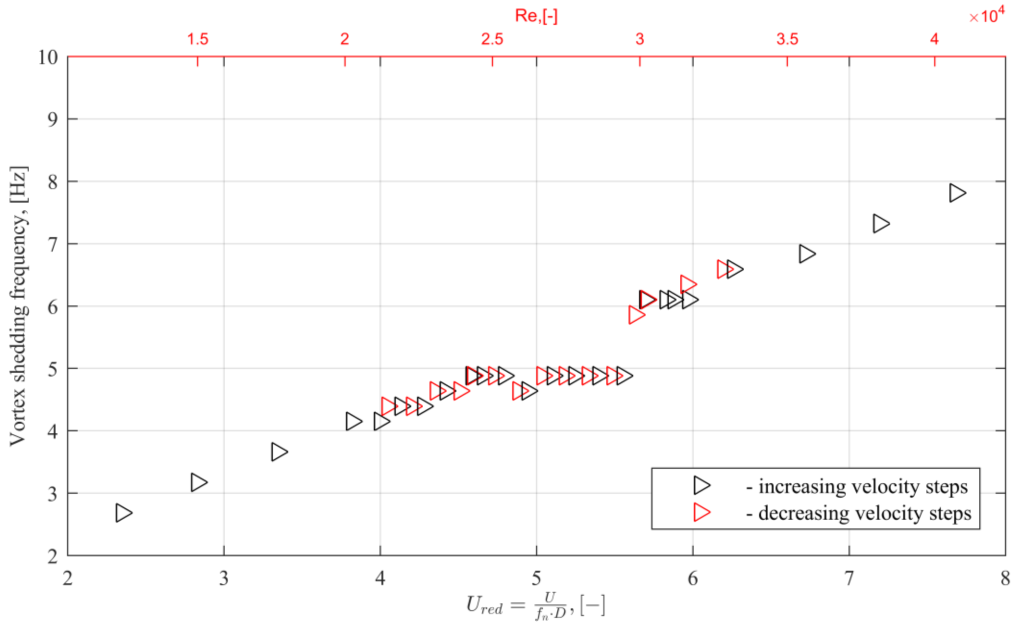

Figure 10.41 Lock-in range of iced cable model, α=180° in flow with I_u=0.75%

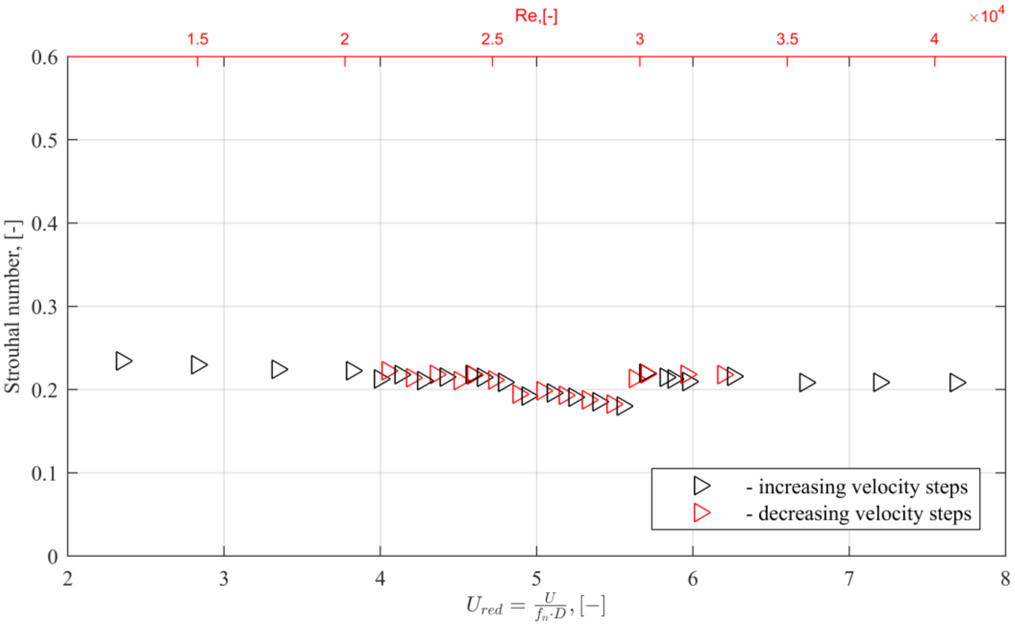

Figure 10.42 Strouhal number of iced cable model, α=180° in flow with I_u=0.75%

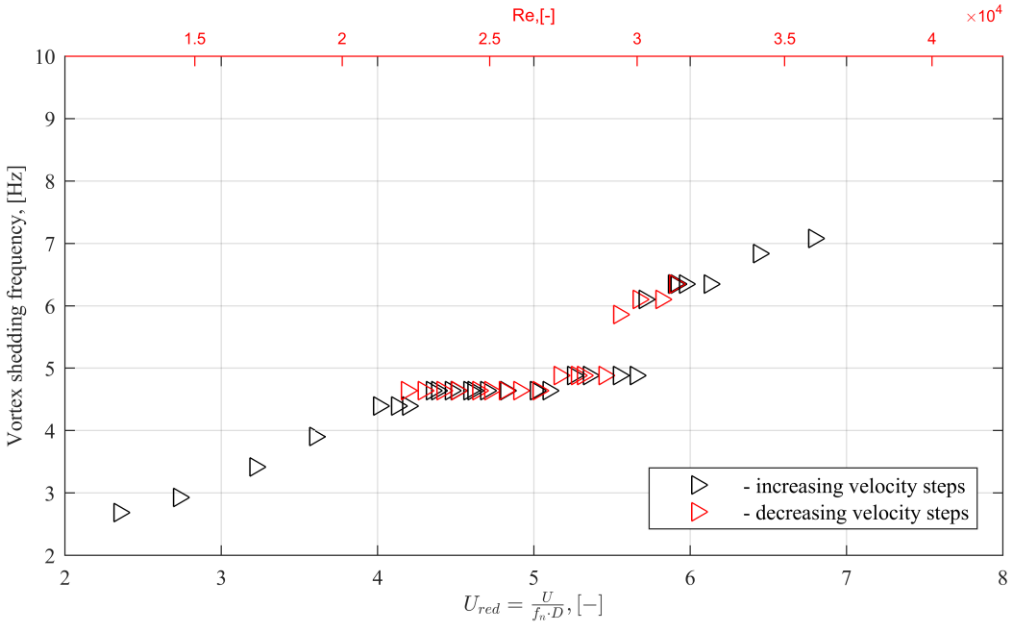

Figure 10.43 Lock-in range of iced cable model, α=180° in flow with I_u=4.5%

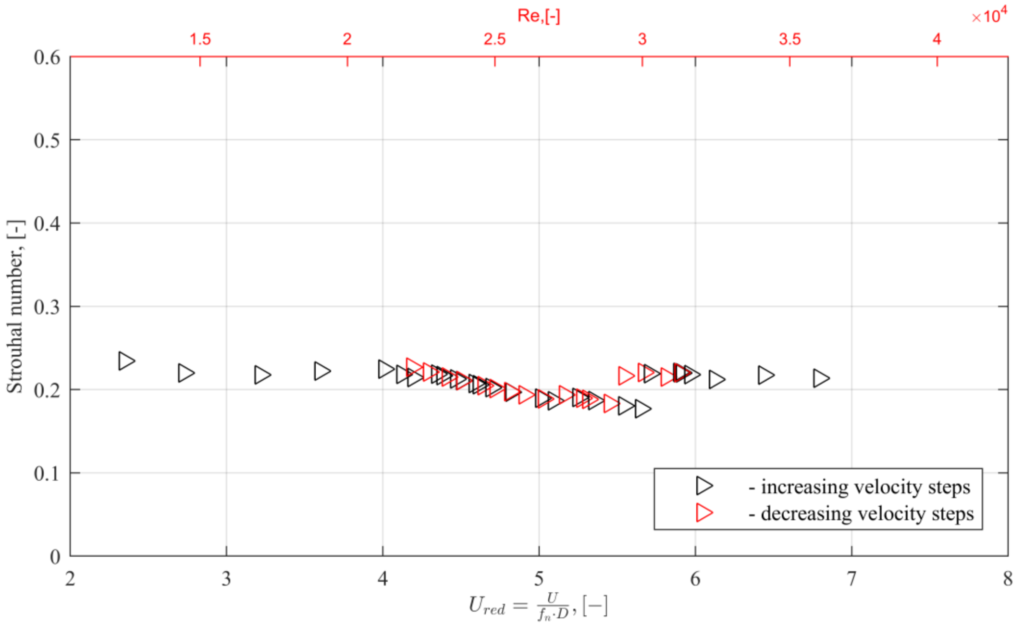

Figure 10.44 Strouhal number of iced cable model, α=180° in flow with I_u=4.5%

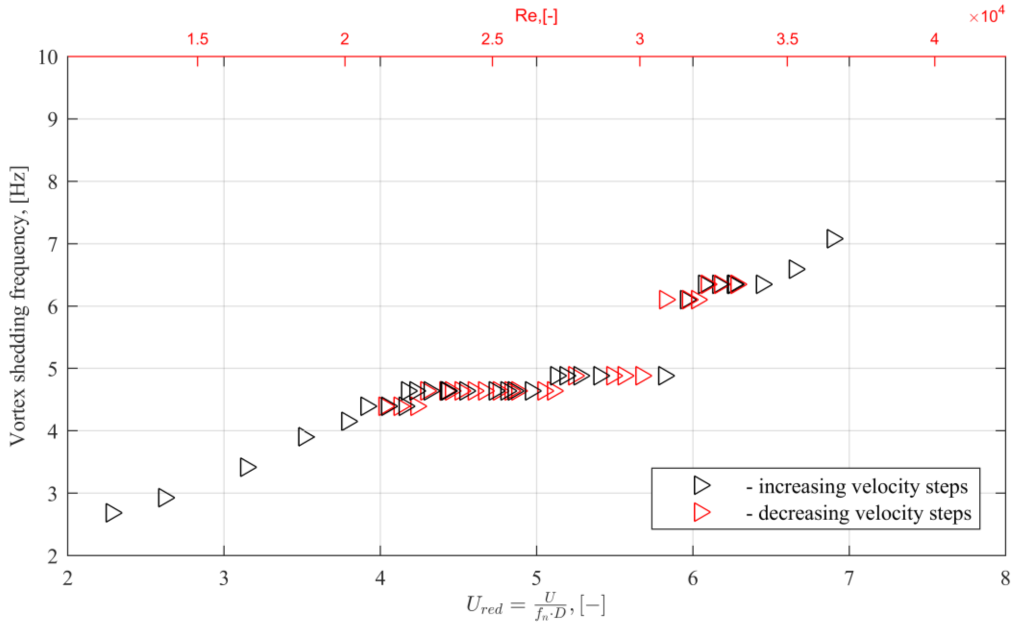

Figure 10.45 Lock-in range of iced cable model, α=180° in flow with I_u=6.5%

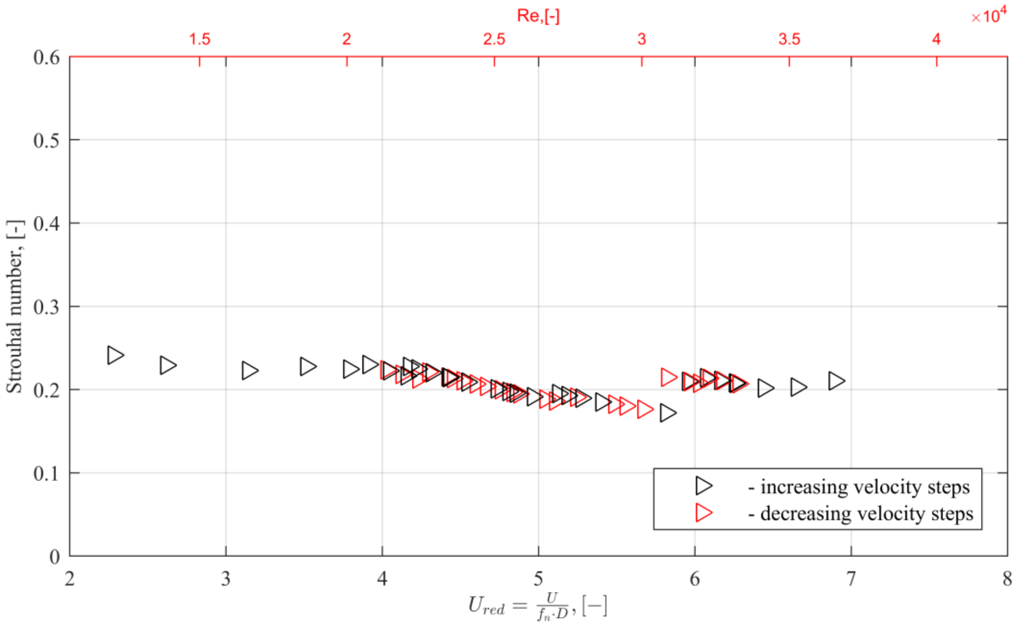

Figure 10.46 Strouhal number of iced cable model, α=180° in flow with I_u=6.5%

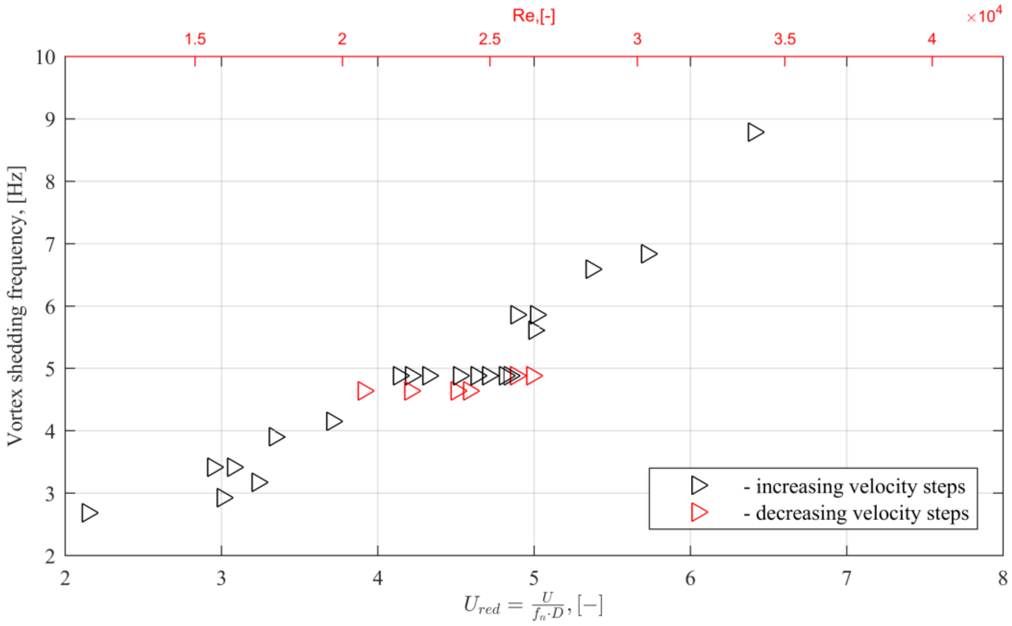

Figure 10.47 Lock-in range of iced cable model, α=180° in flow with I_u=12.3%

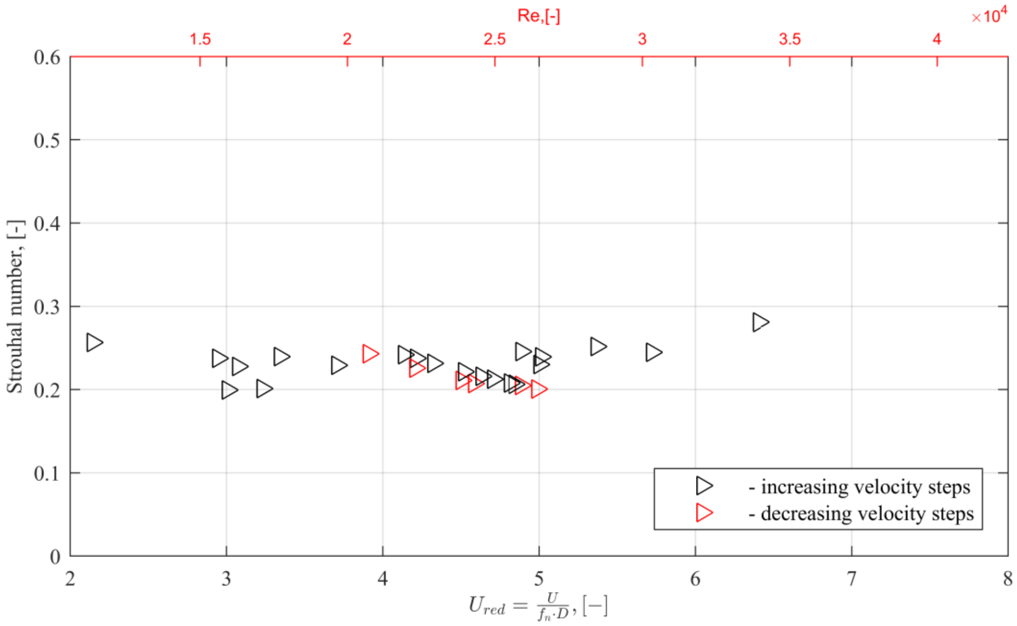

Figure 10.48 Strouhal number of iced cable model, α=180° in flow with I_u=12.3%

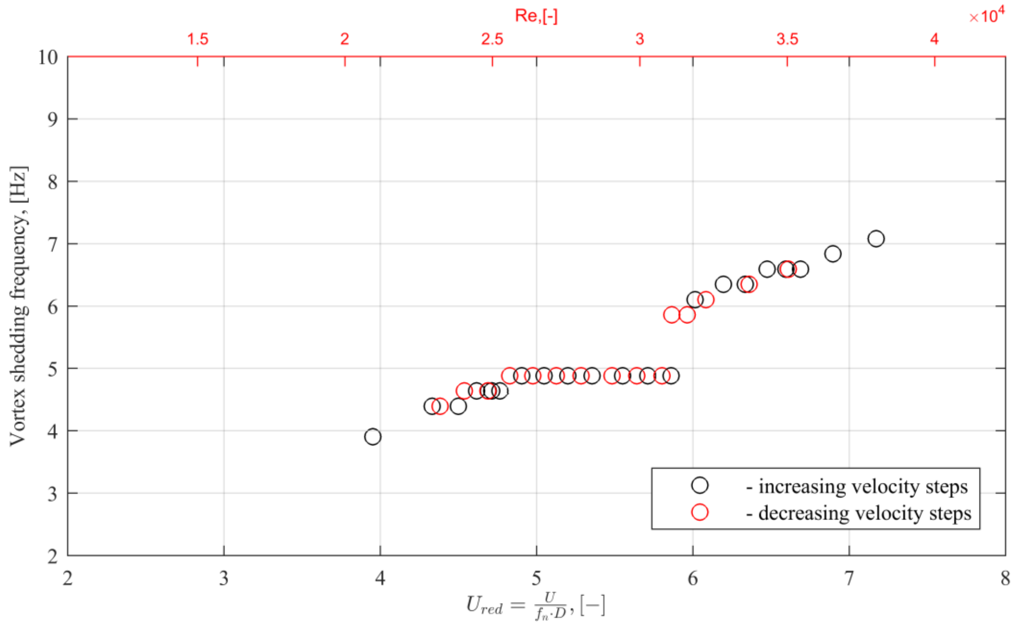

Figure 10.49 Lock-in range of smooth cable model in flow with I_u=0.75%

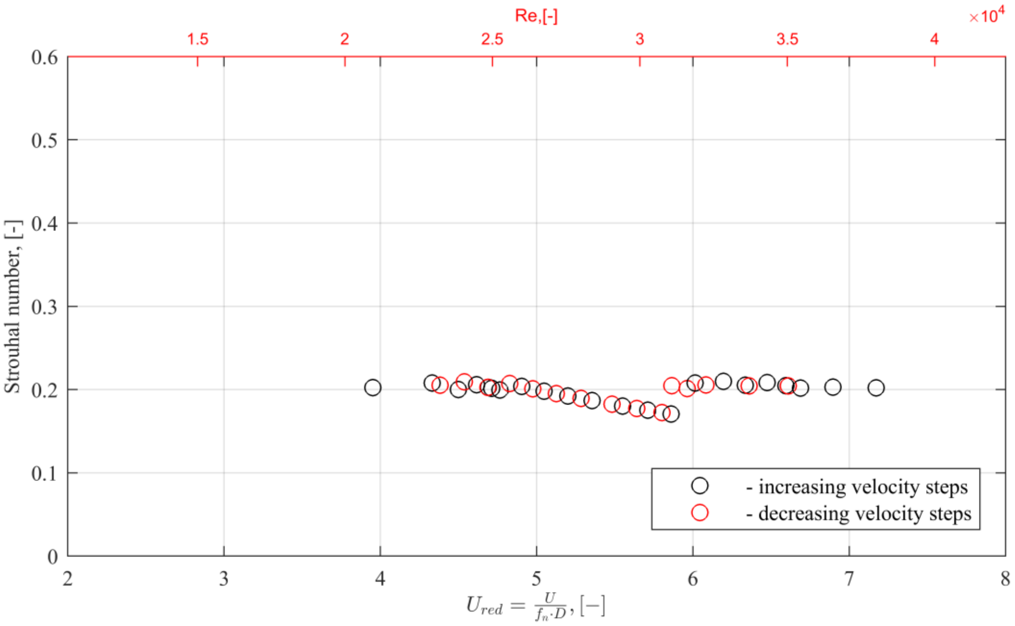

Figure 10.50 Strouhal number of smooth cable model in flow with I_u=0.75%

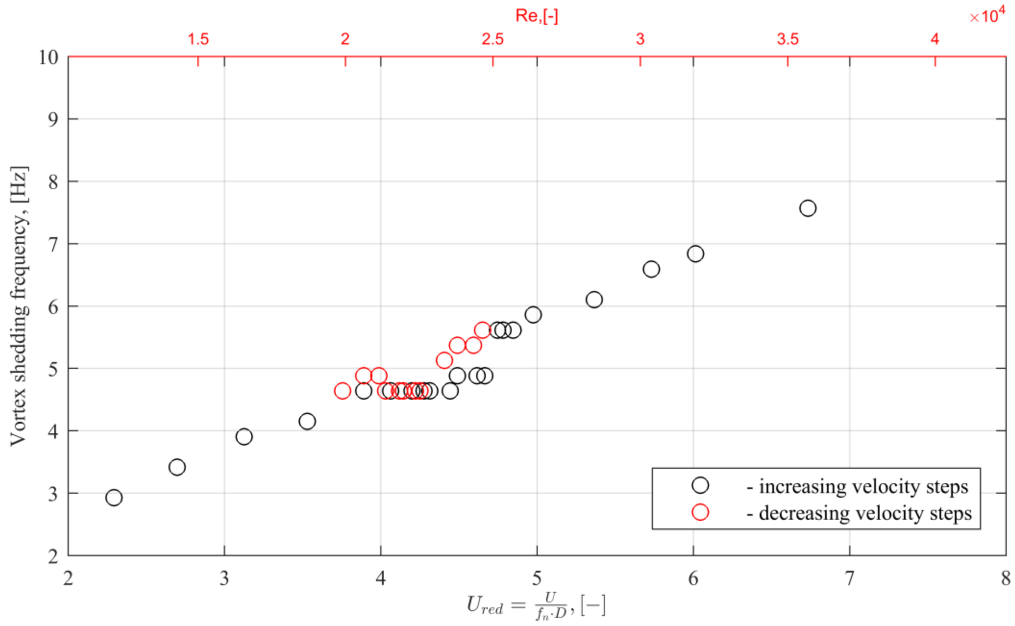

Figure 10.51 Lock-in range of smooth cable model in flow with I_u=4.5%

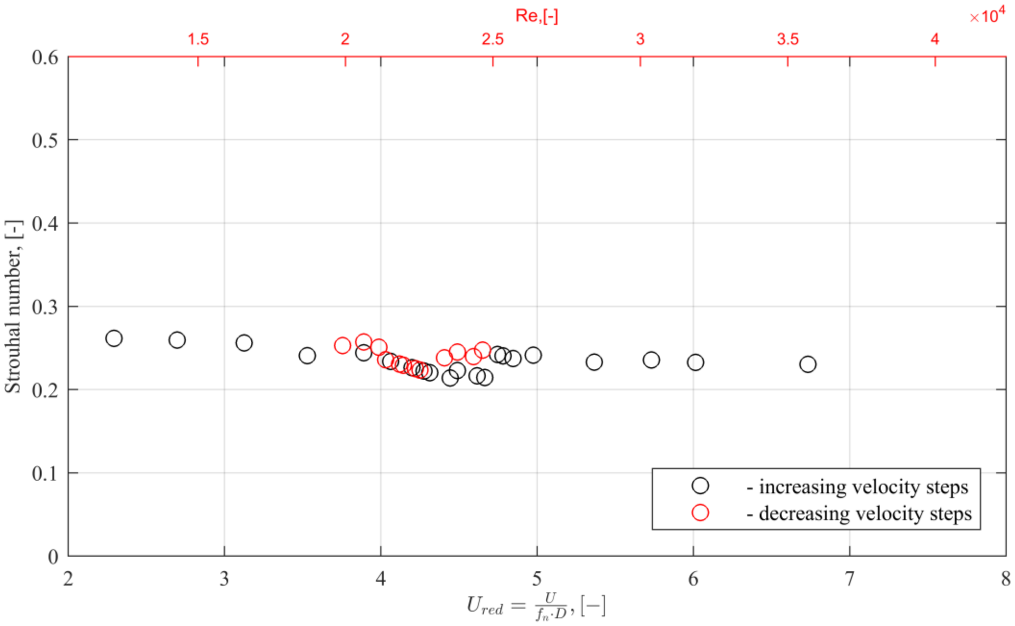

Figure 10.52 Strouhal number of smooth cable model in flow with I_u=4.5%

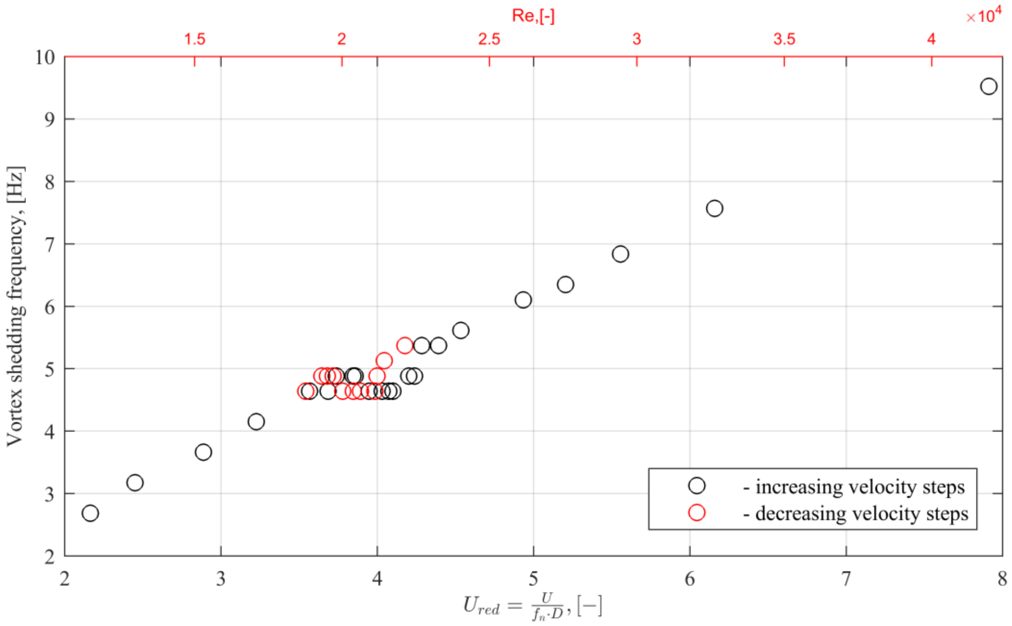

Figure 10.53 Lock-in range of smooth cable model in flow with I_u=6.5%

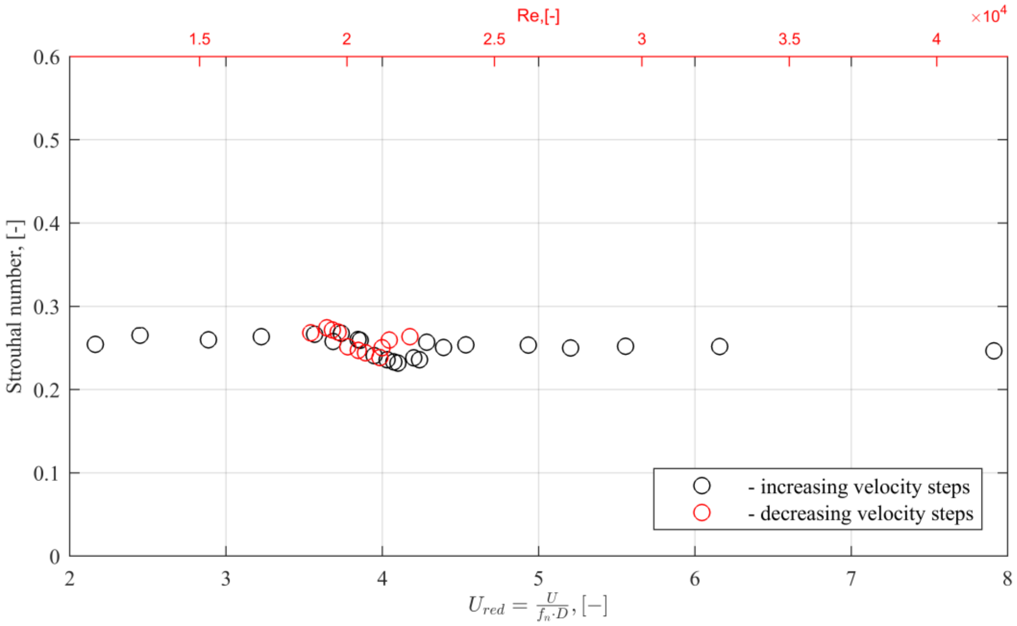

Figure 10.54 Strouhal number of smooth cable model in flow with I_u=6.5%

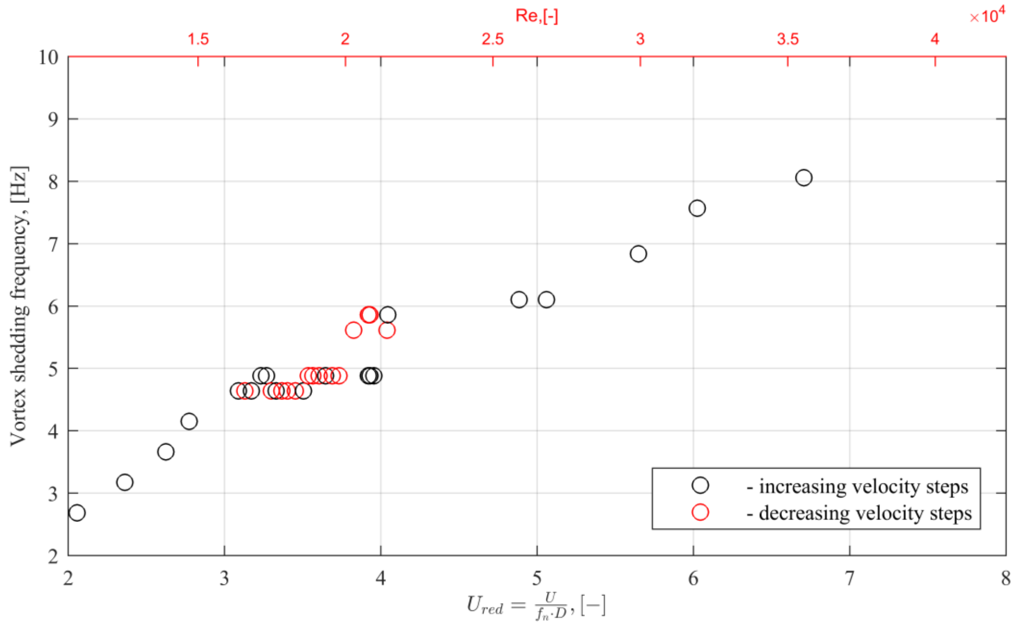

Figure 10.55 Lock-in range of smooth cable model in flow with I_u=12.3%

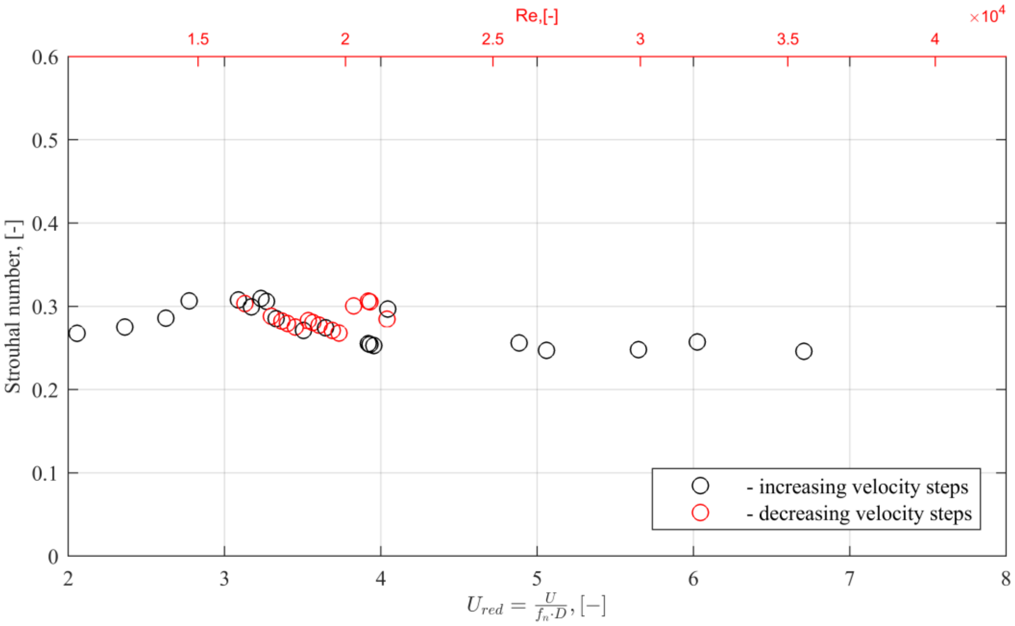

Figure 10.56 Strouhal number of smooth cable model in flow with I_u=12.3%

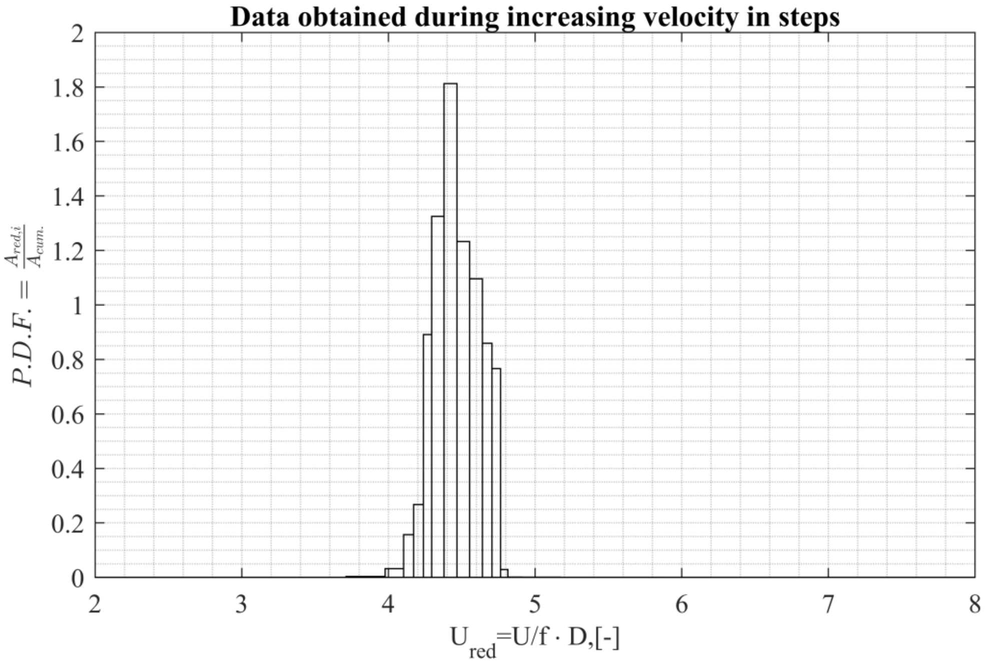

Figure 10.57 Work over lock-in, smooth surface cable, turbulent flow I_u=4.5%, normalized to cumulative work over smooth cylinder, data obtained during increasing velocity in steps.

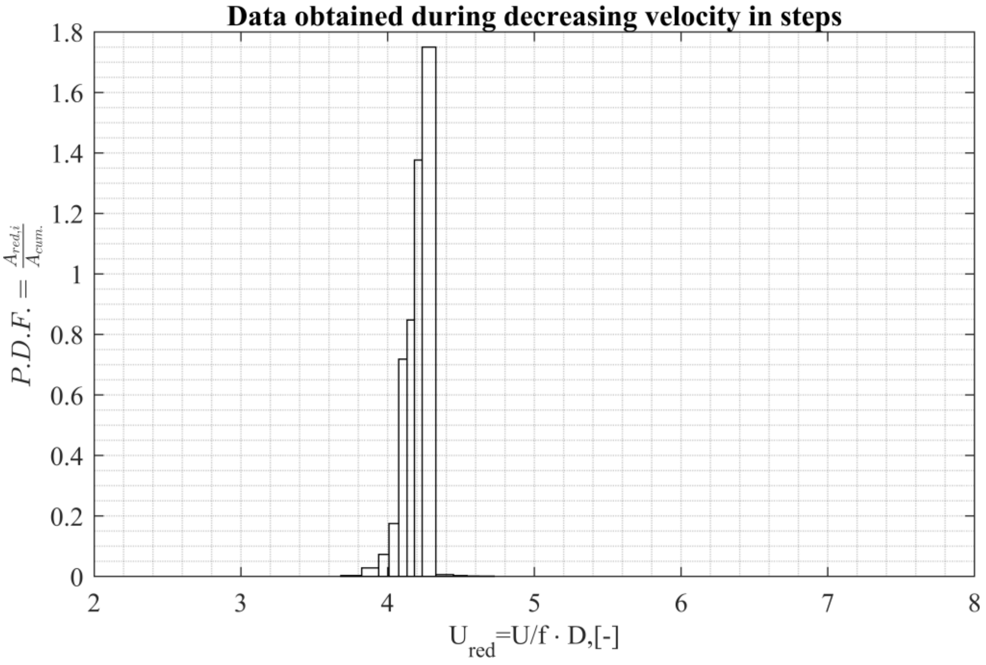

Figure 10.58 Work over lock-in, smooth surface cable, turbulent flow I_u=4.5%, normalized to cumulative work over smooth cylinder, data obtained during decreasing velocity in steps.

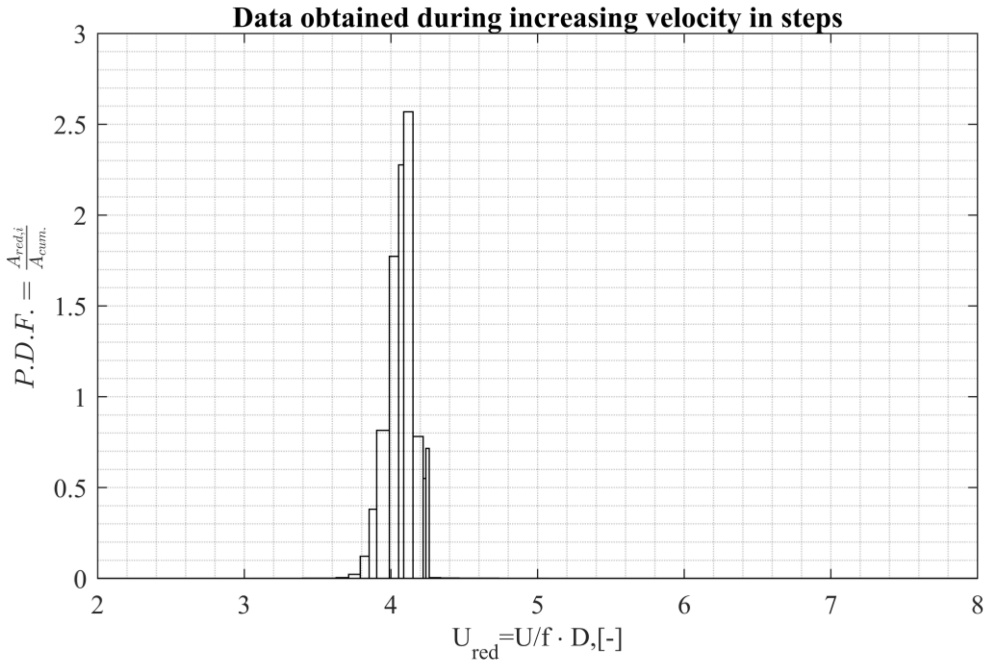

Figure 10.59 Work over lock-in, smooth surface cable, turbulent flow I_u=6.5%, normalized to cumulative work over smooth cylinder, data obtained during increasing velocity in steps.

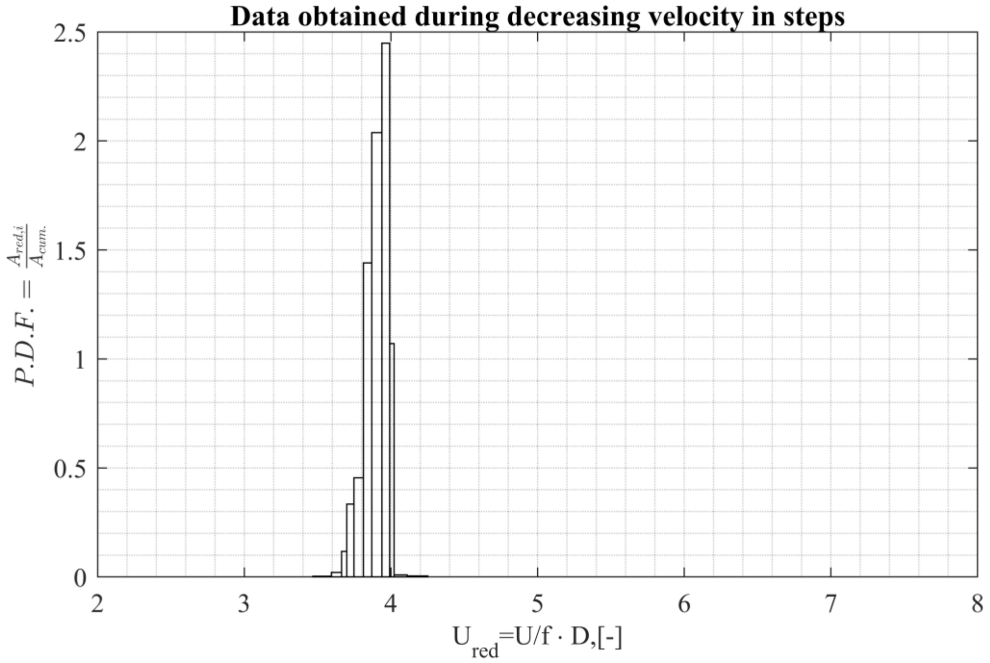

Figure 10.60 Work over lock-in, smooth surface cable, turbulent flow I_u=6.5%, normalized to cumulative work over smooth cylinder, data obtained during decreasing velocity in steps.

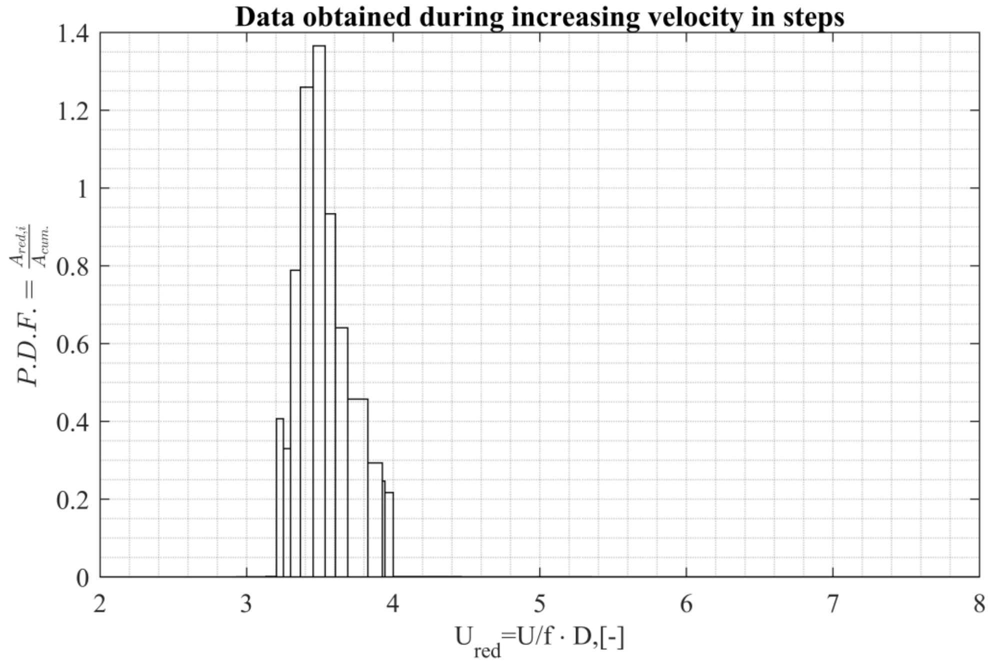

Figure 10.61 Work over lock-in, smooth surface cable, turbulent flow I_u=12.3%, normalized to cumulative work over smooth cylinder, data obtained during increasing velocity in steps.

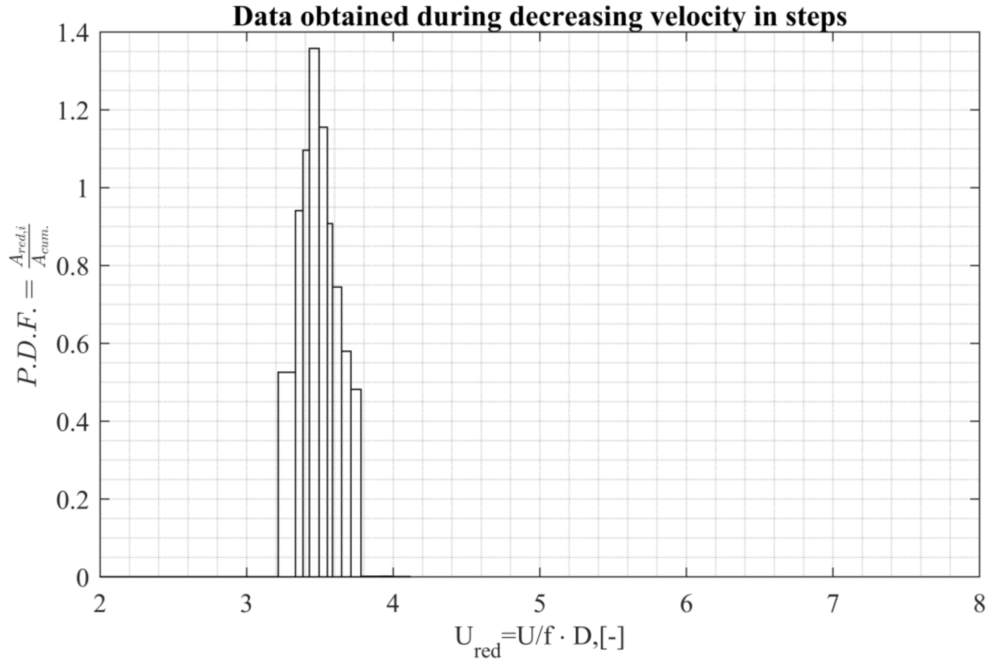

Figure 10.62 Work over lock-in, smooth surface cable, turbulent flow I_u=12.3%, normalized to cumulative work over smooth cylinder, data obtained during decreasing velocity in steps.

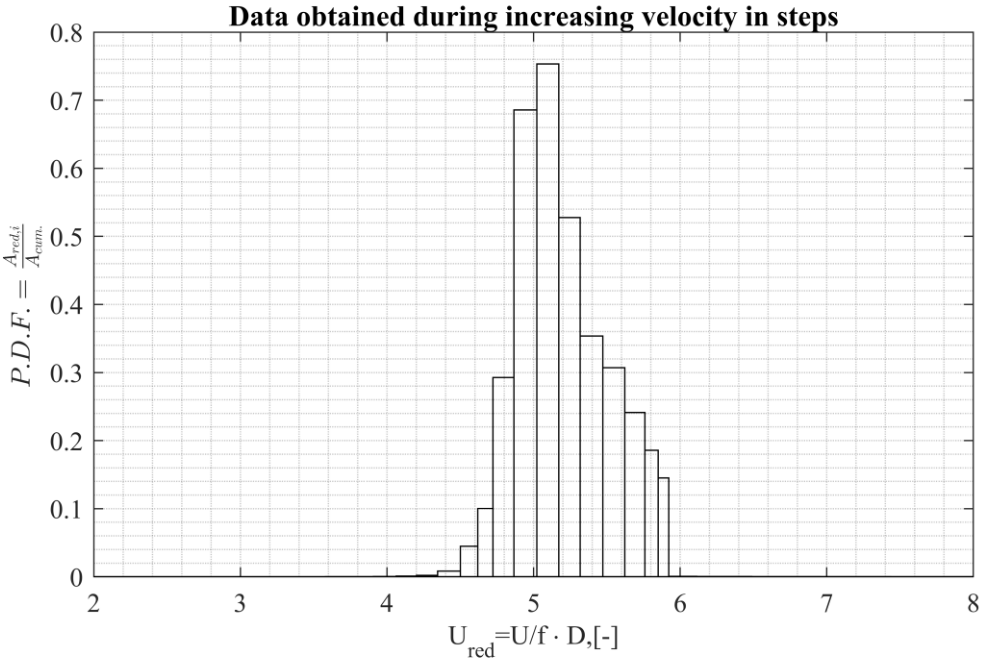

Figure 10.63 Work over lock-in, iced cable, α=180°, smooth flow I_u=0.75%, normalized to cumulative work over smooth cylinder, data obtained during increasing velocity in steps.

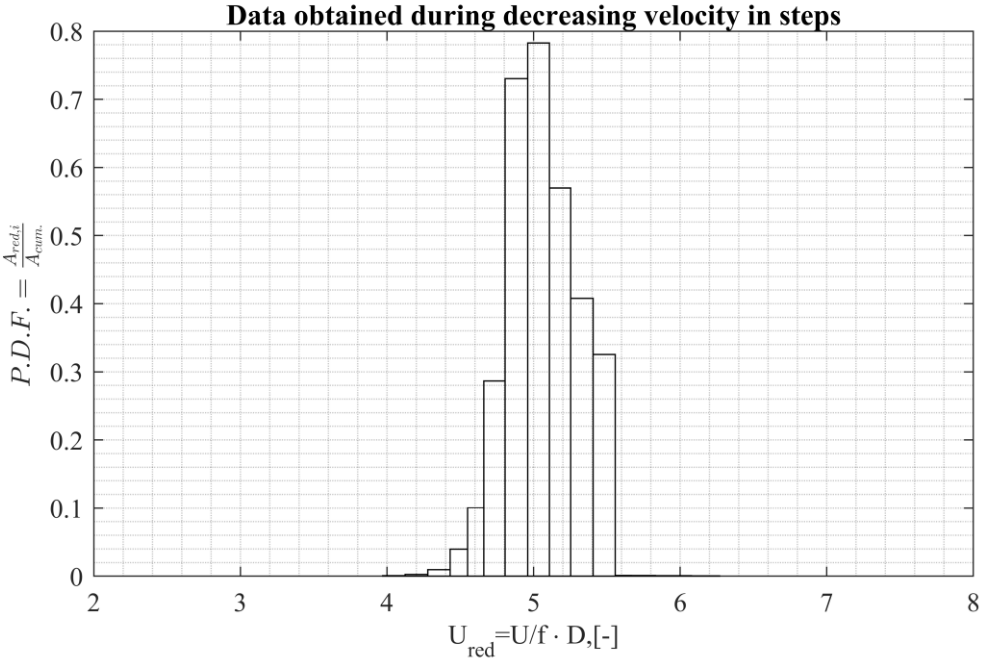

Figure 10.64 Work over lock-in, iced cable, α=180°, smooth flow I_u=0.75%, normalized to cumulative work over smooth cylinder, data obtained during decreasing velocity in steps.

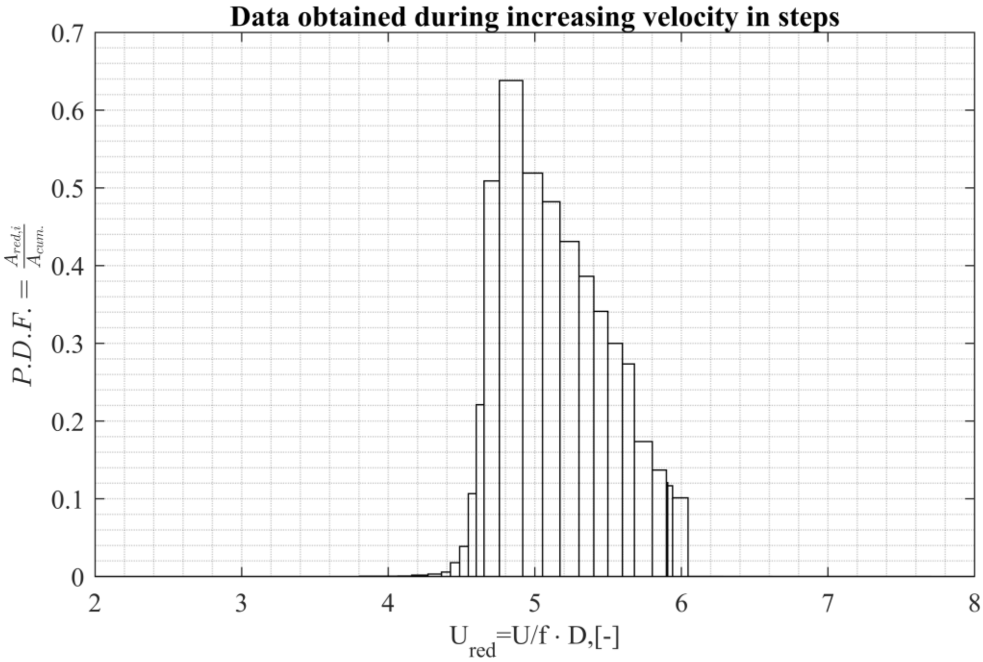

Figure 10.65 Work over lock-in, iced cable, α=180°, turbulent flow I_u=4.5%, normalized to cumulative work over smooth cylinder, data obtained during increasing velocity in steps.

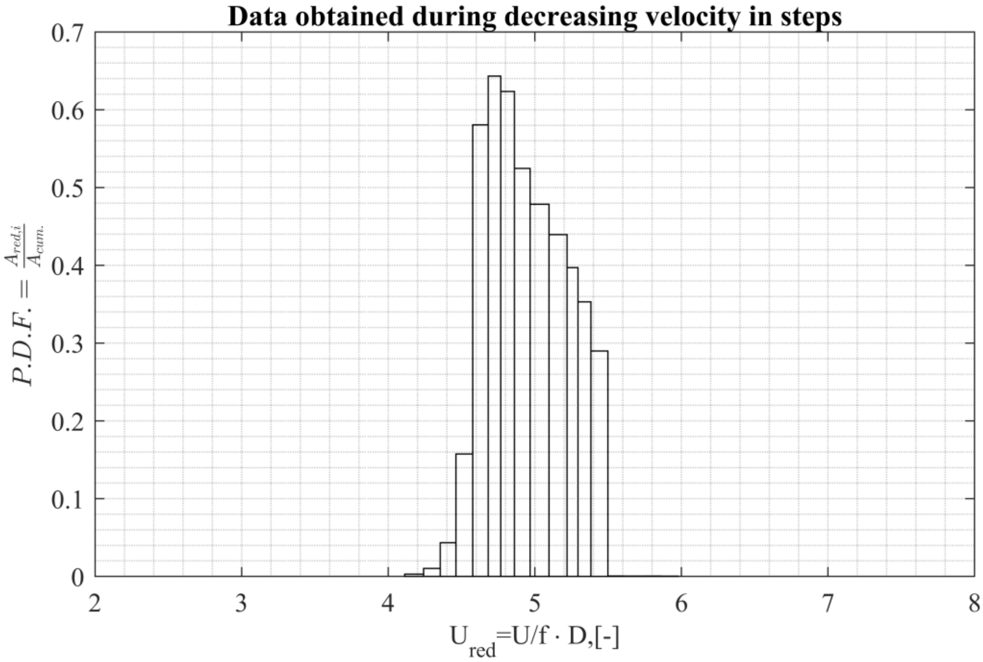

Figure 10.66 Work over lock-in, iced cable, α=180°, turbulent flow I_u=4.5%, normalized to cumulative work over smooth cylinder, data obtained during decreasing velocity in steps.

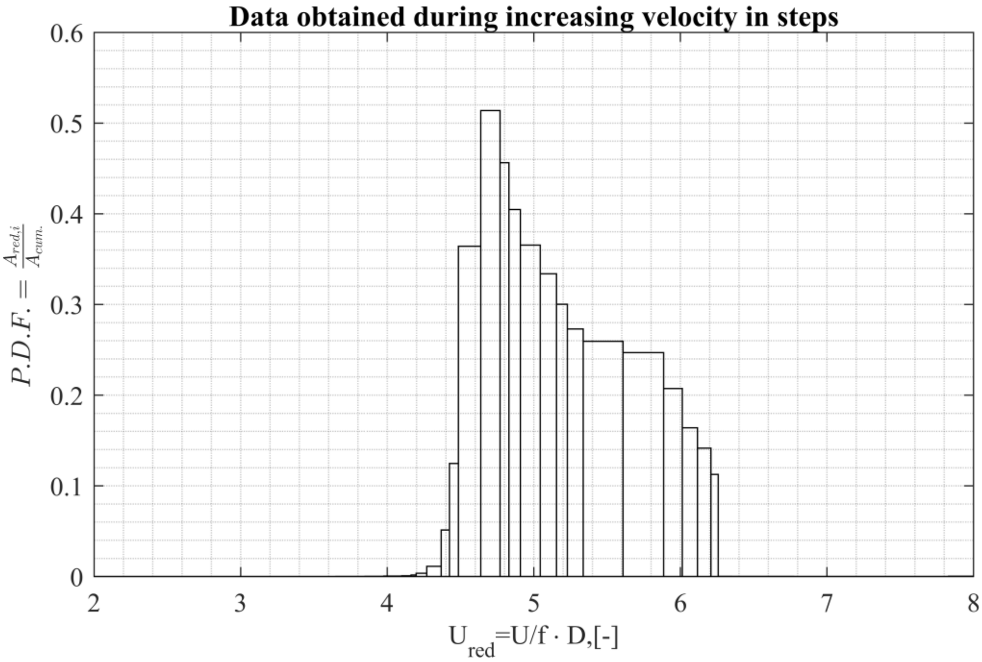

Figure 10.67 Work over lock-in, iced cable, α=180°, turbulent flow I_u=6.5%, normalized to cumulative work over smooth cylinder, data obtained during increasing velocity in steps.

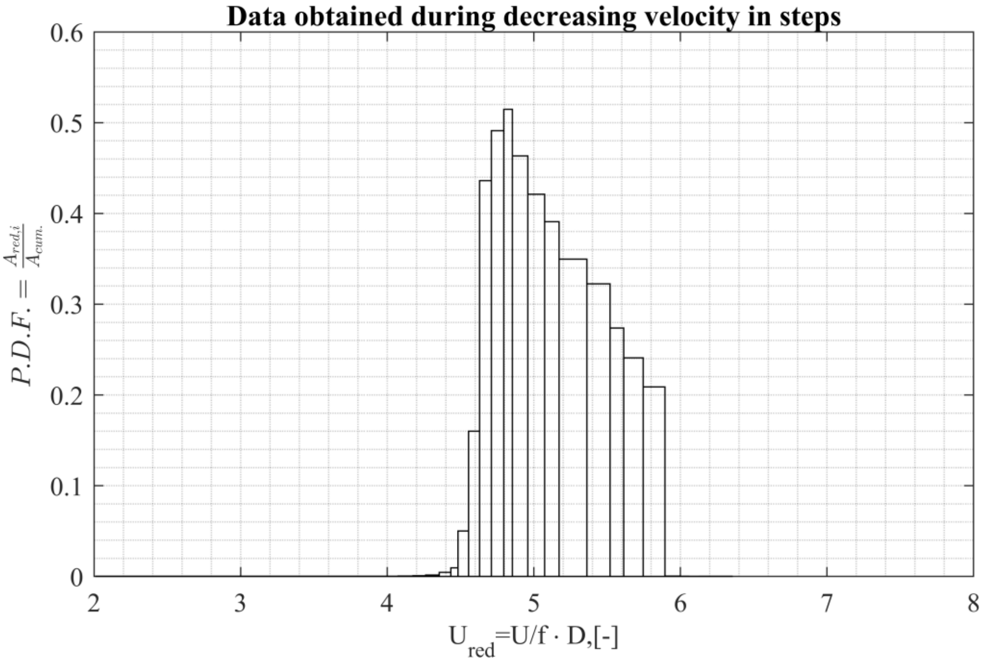

Figure 10.68 Work over lock-in, iced cable, α=180°, turbulent flow I_u=6.5%, normalized to cumulative work over smooth cylinder, data obtained during decreasing velocity in steps.

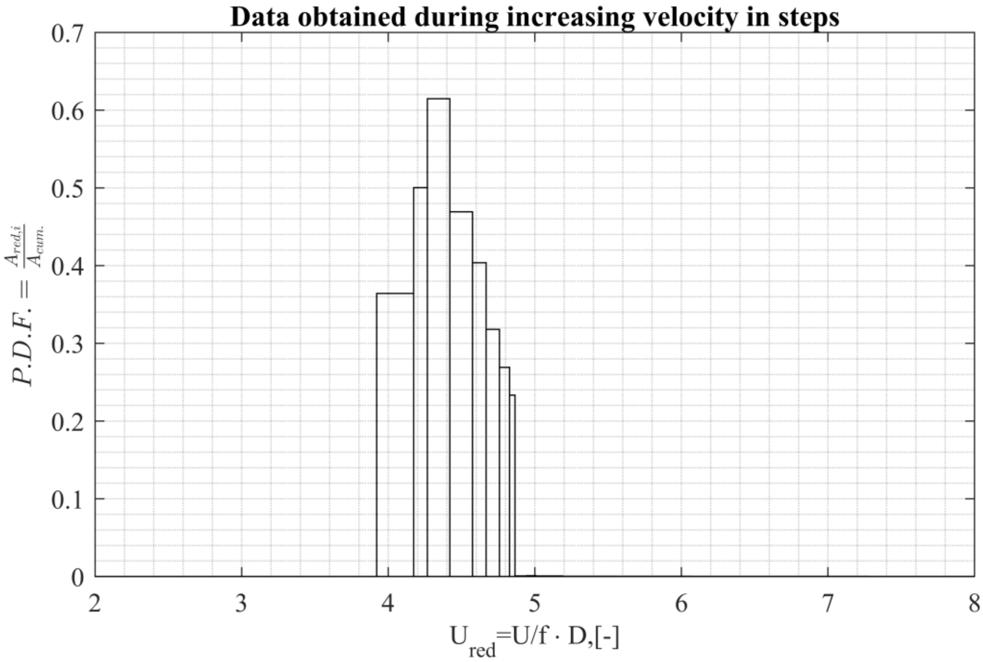

Figure 10.69 Work over lock-in, iced cable, α=180°, turbulent flow I_u=12.3%, normalized to cumulative work over smooth cylinder, data obtained during increasing velocity in steps.

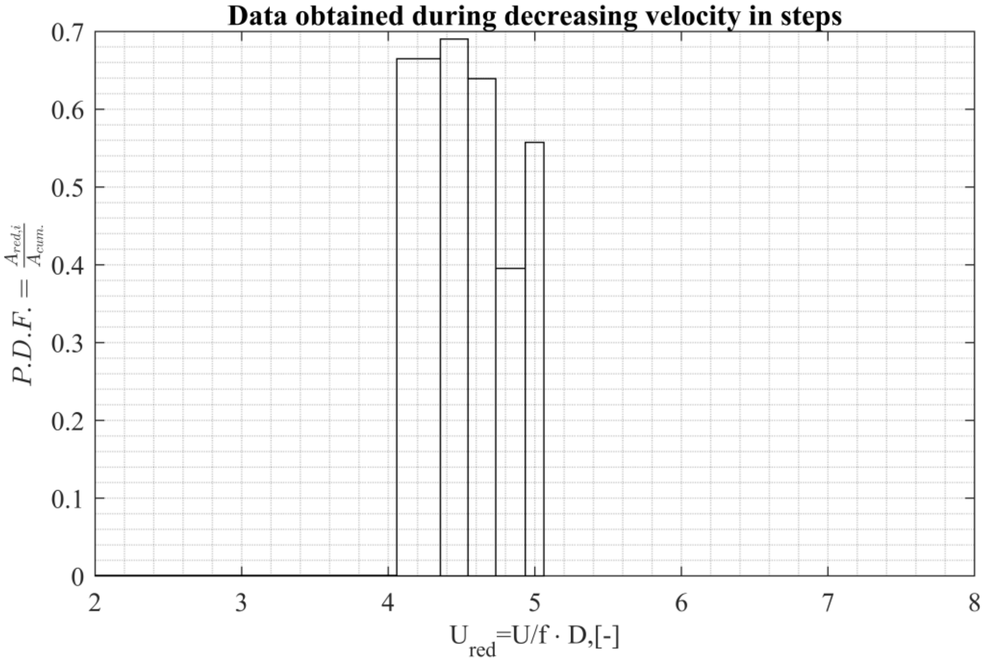

Figure 10.70 Work over lock-in, iced cable, α=180°, turbulent flow I_u=12.3%, normalized to cumulative work over smooth cylinder, data obtained during decreasing velocity in steps.

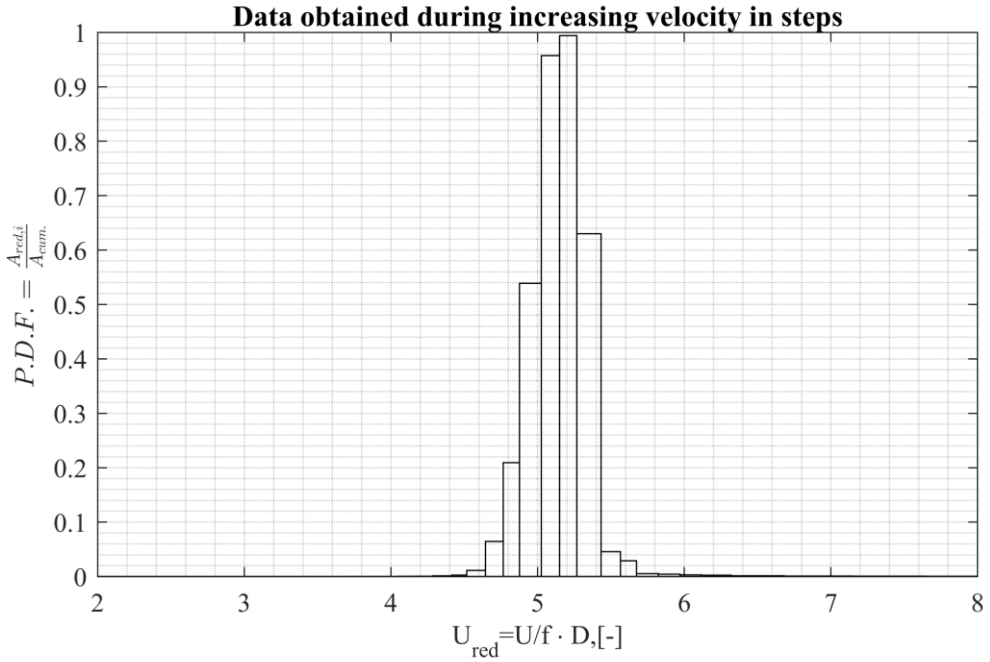

Figure 10.71 Work over lock-in, iced cable, α=90°, smooth flow I_u=0.75%, normalized to cumulative work over smooth cylinder, data obtained during increasing velocity in steps.

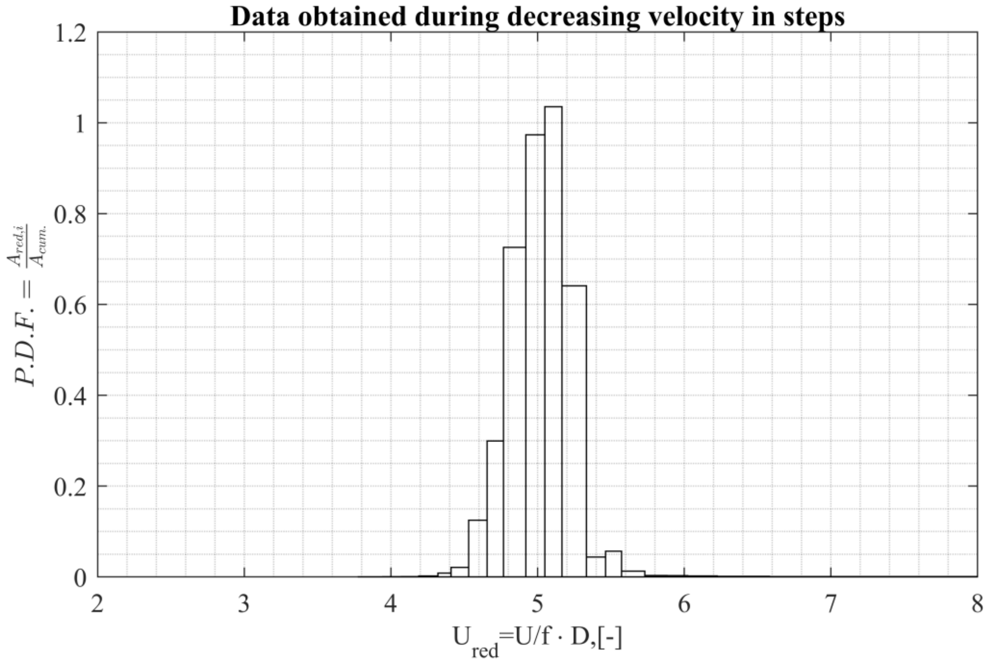

Figure 10.72 Work over lock-in, iced cable, α=90°, smooth flow I_u=0.75%, normalized to cumulative work over smooth cylinder, data obtained during decreasing velocity in steps.

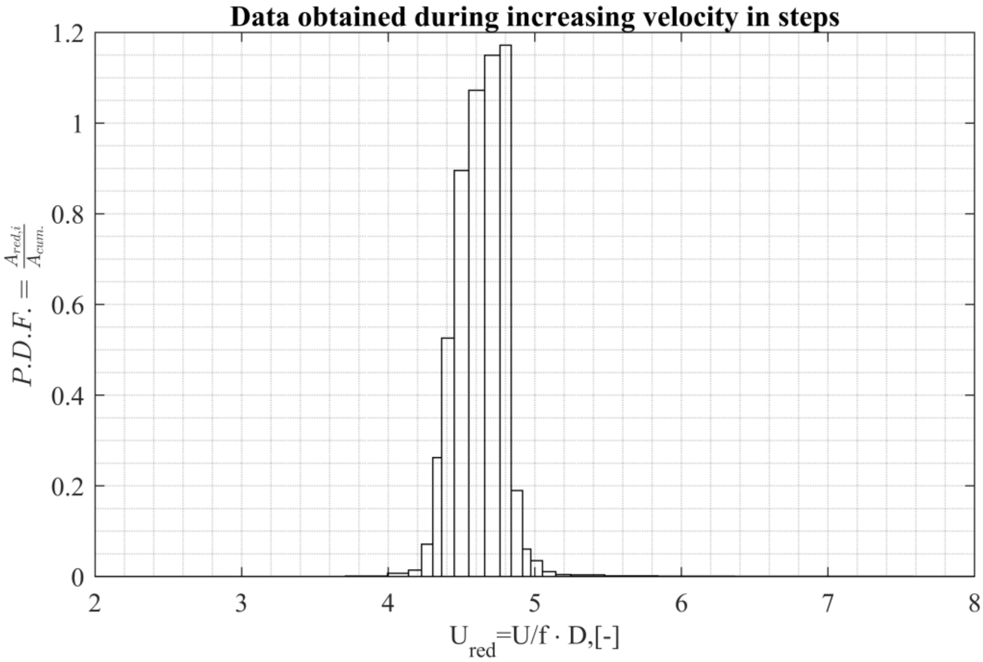

Figure 10.73 Work over lock-in, iced cable, α=90°, turbulent flow I_u=4.5%, normalized to cumulative work over smooth cylinder, data obtained during increasing velocity in steps.

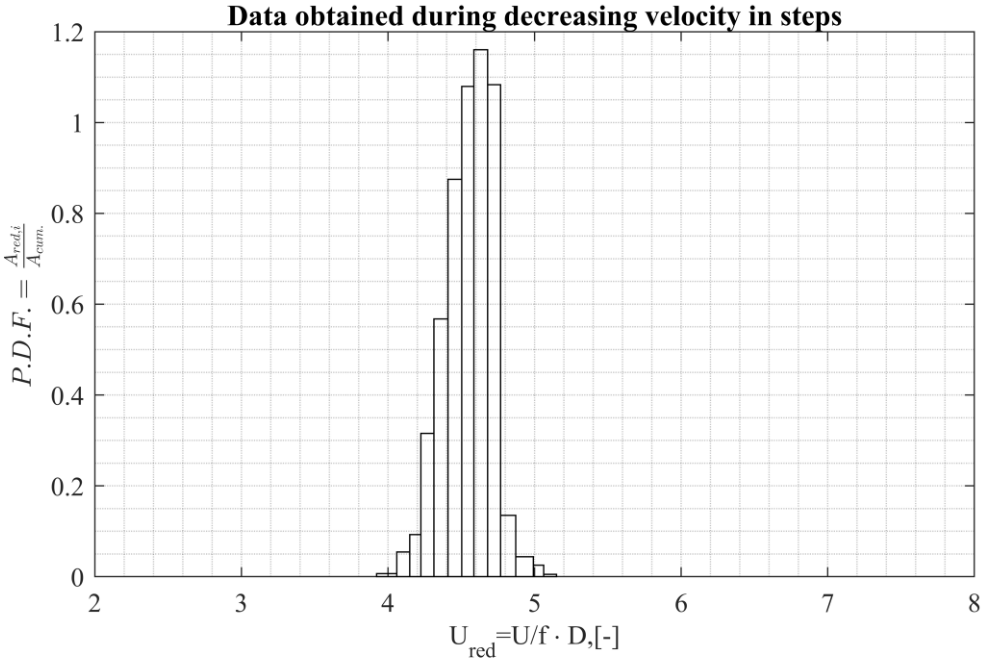

Figure 10.74 Work over lock-in, iced cable, α=90°, turbulent flow I_u=4.5%, normalized to cumulative work over smooth cylinder, data obtained during decreasing velocity in steps.

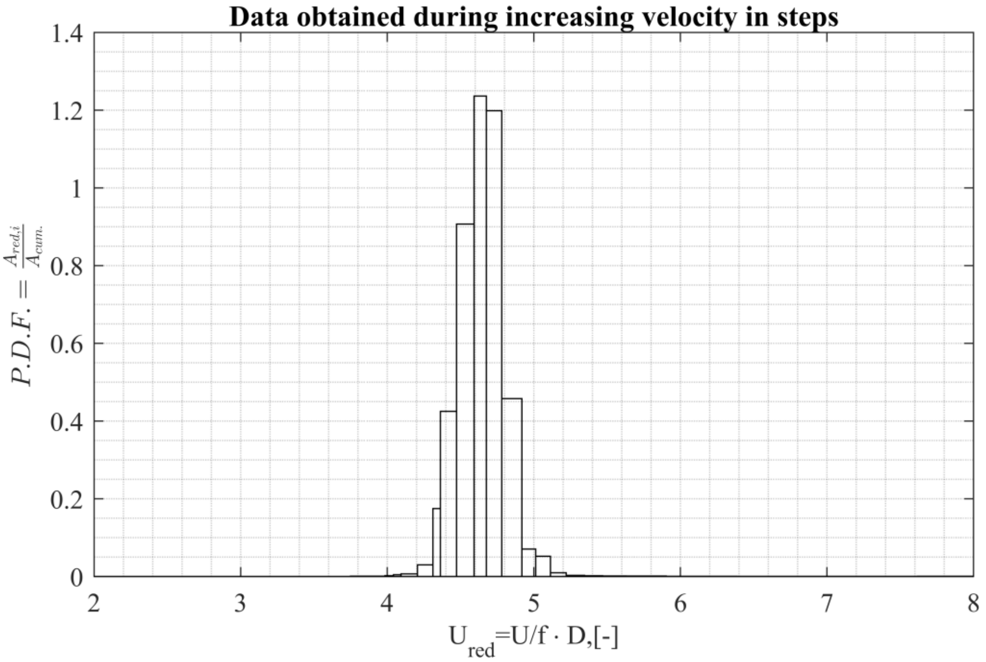

Figure 10.75 Work over lock-in, iced cable, α=90°, turbulent flow I_u=6.5%, normalized to cumulative work over smooth cylinder, data obtained during increasing velocity in steps.

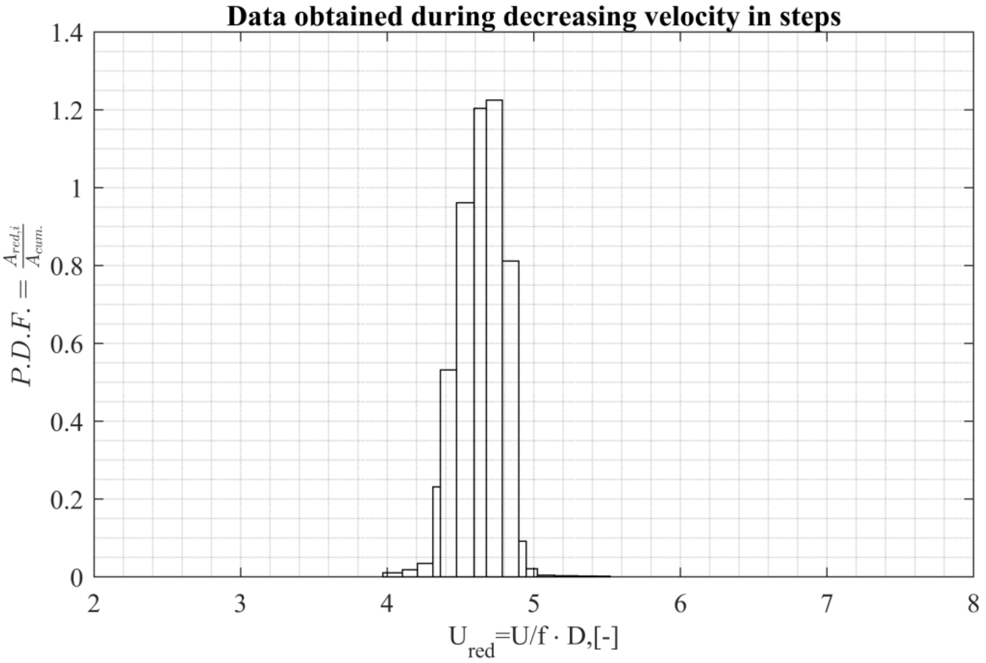

Figure 10.76 Work over lock-in, iced cable, α=90°, turbulent flow I_u=6.5%, normalized to cumulative work over smooth cylinder, data obtained during decreasing velocity in steps.

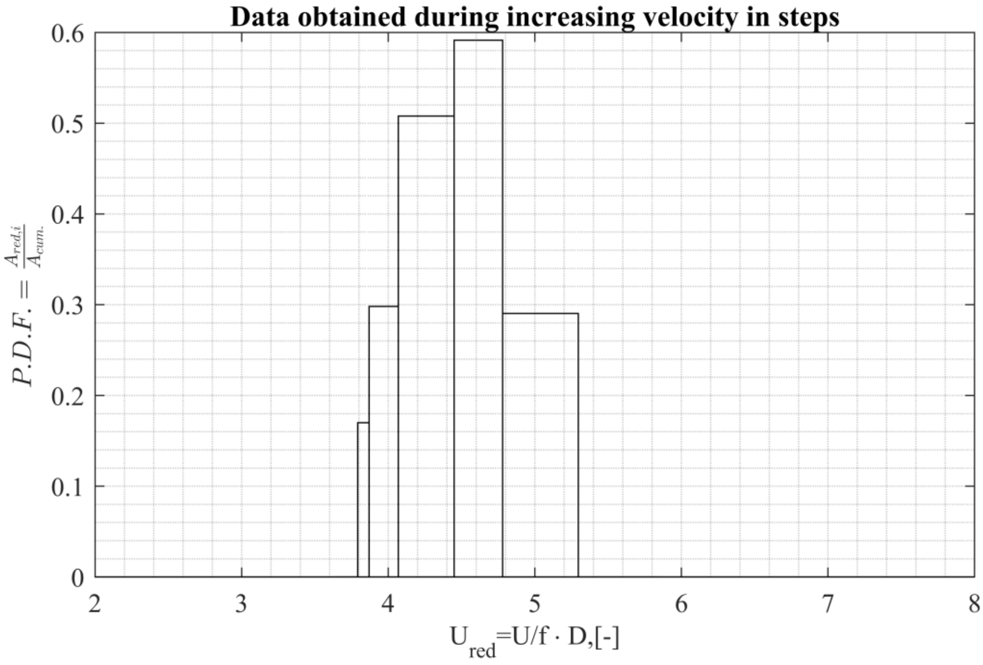

Work over lock-in, iced cable, α=90°, turbulent flow I_u=12.3%, normalized to cumulative work over smooth cylinder, data obtained during increasing velocity in steps.

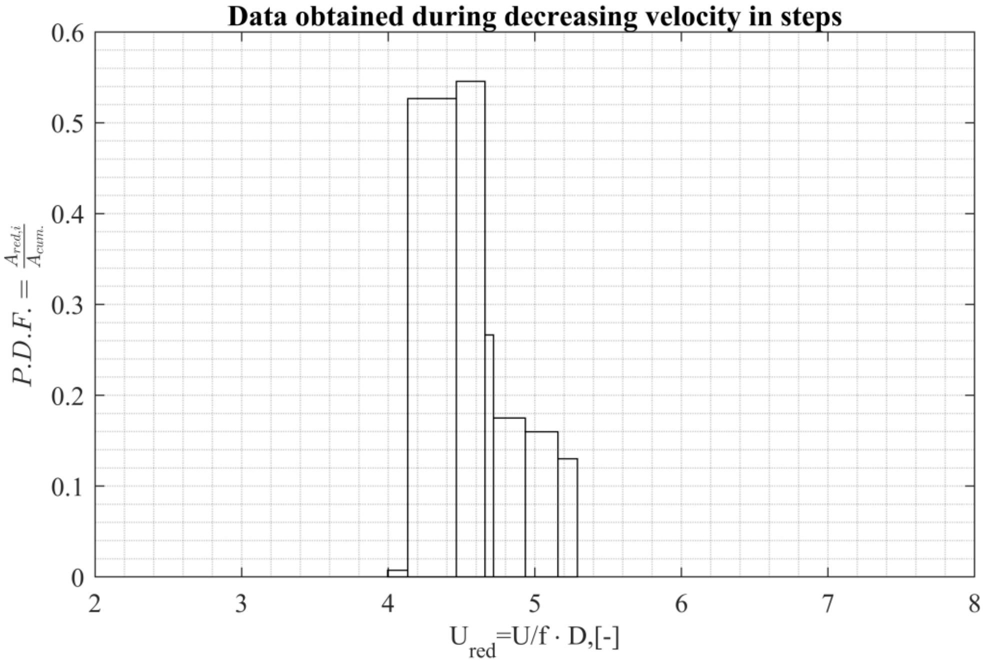

Work over lock-in, iced cable, α=90°, turbulent flow I_u=12.3%, normalized to cumulative work over smooth cylinder, data obtained during decreasing velocity in steps.

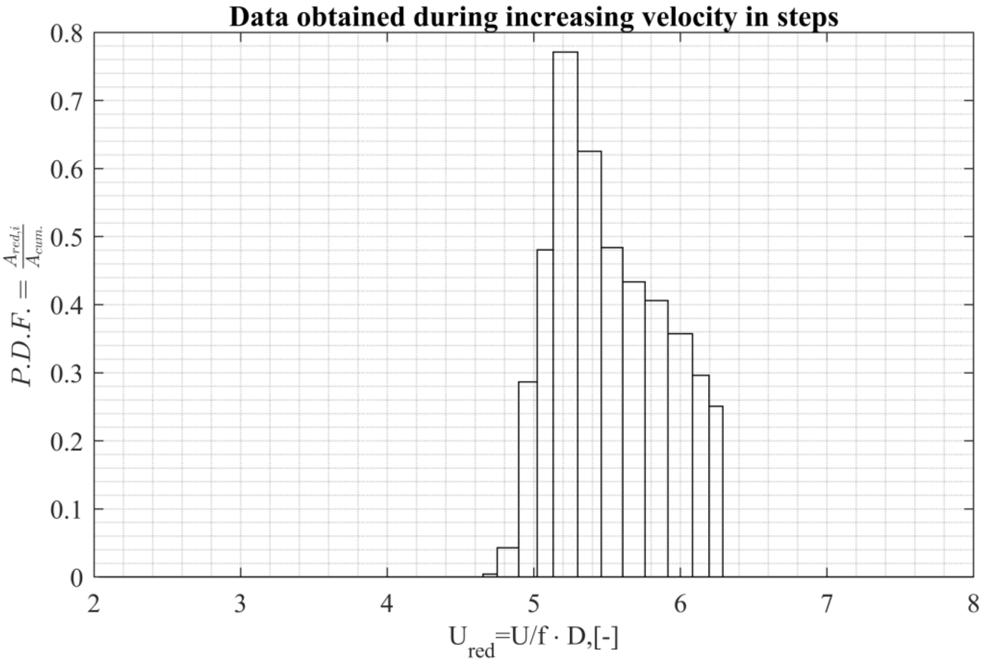

Figure 10.77 Work over lock-in, iced cable, α=0°, smooth flow I_u=0.75%, normalized to cumulative work over smooth cylinder, data obtained during increasing velocity in steps.

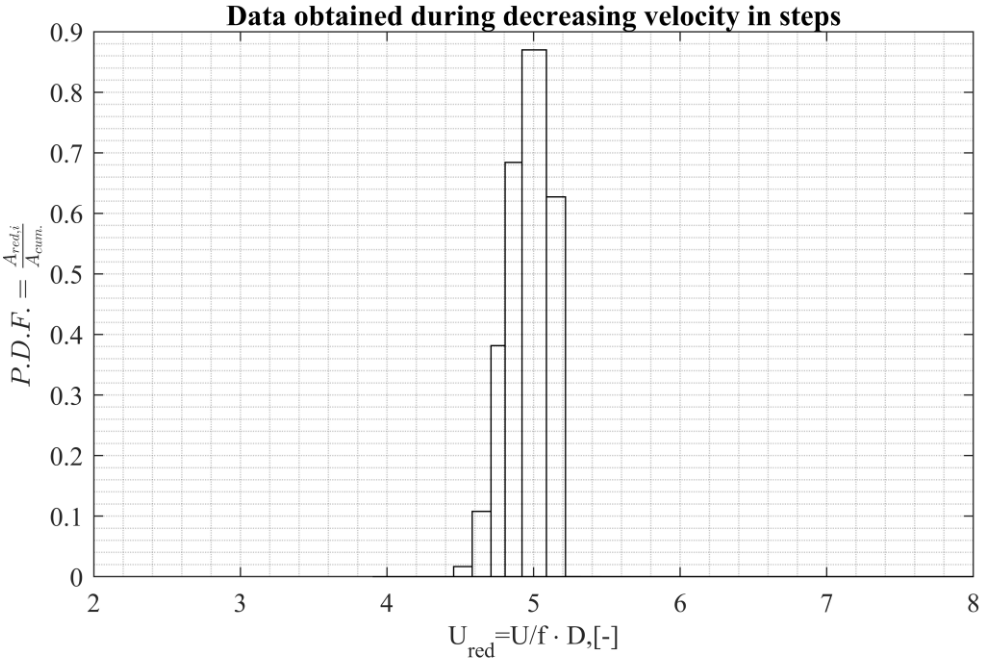

Figure 10.78 Work over lock-in, iced cable, α=0°, smooth flow I_u=0.75%, normalized to cumulative work over smooth cylinder, data obtained during decreasing velocity in steps.

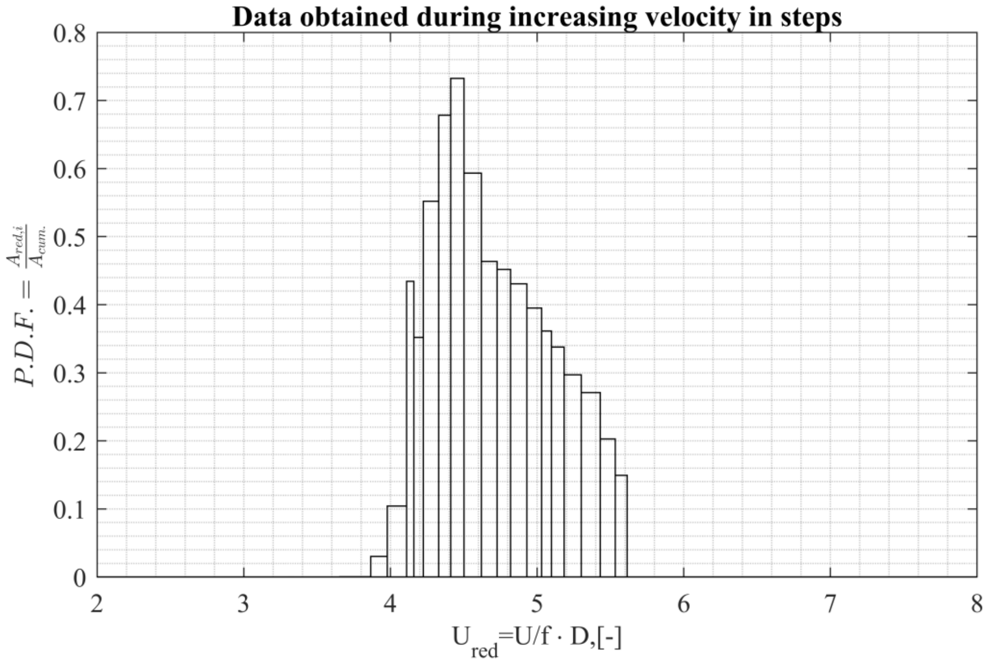

Figure 10.79 Work over lock-in, iced cable, α=0°, turbulent flow I_u=4.5%, normalized to cumulative work over smooth cylinder, data obtained during increasing velocity in steps.

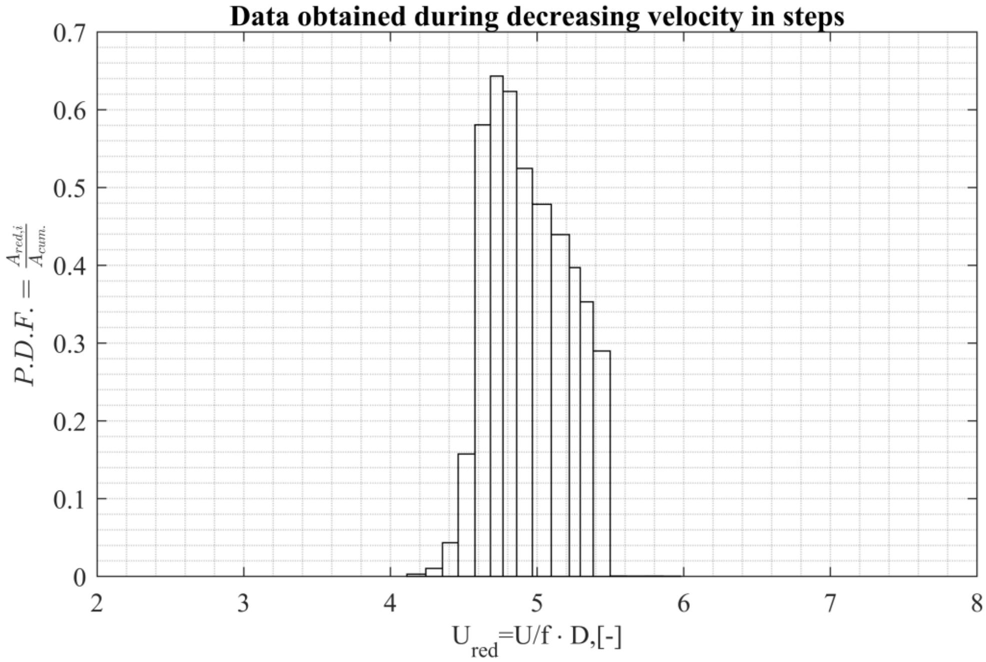

Figure 10.80 Work over lock-in, iced cable, α=180°, turbulent flow I_u=4.5%, normalized to cumulative work over smooth cylinder, data obtained during decreasing velocity in steps.

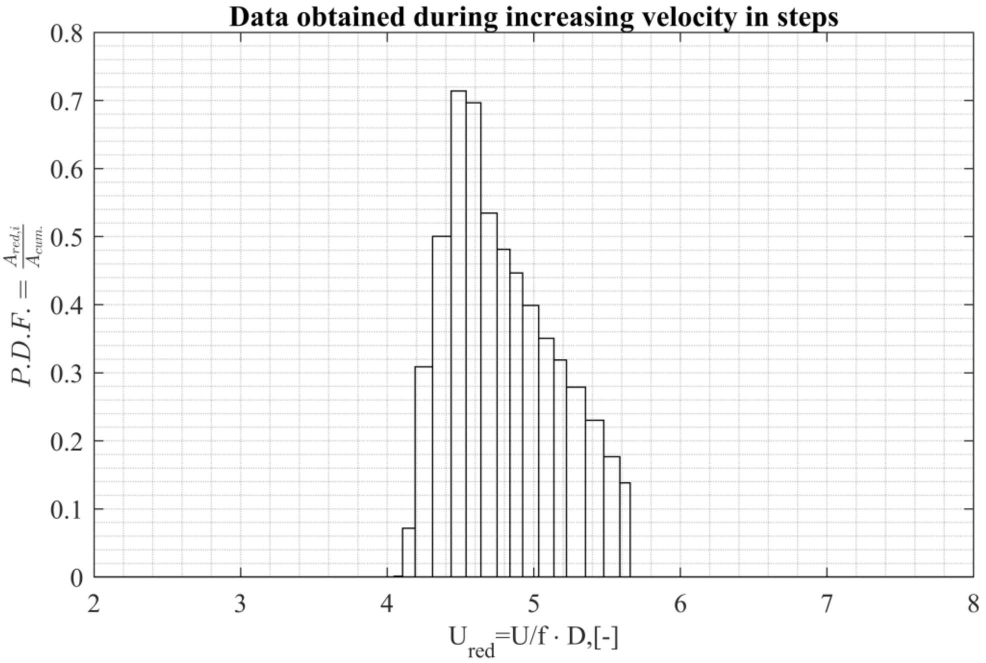

Figure 10.81 Work over lock-in, iced cable, α=0°, turbulent flow I_u=6.5%, normalized to cumulative work over smooth cylinder, data obtained during increasing velocity in steps.

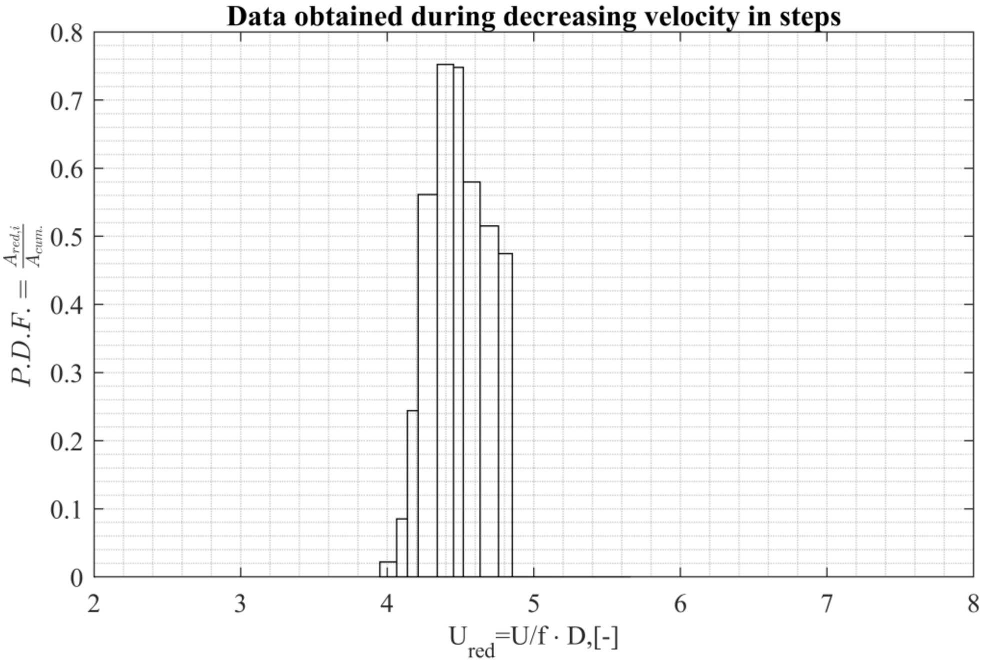

Figure 10.82 Work over lock-in, iced cable, α=0°, turbulent flow I_u=6.5%, normalized to cumulative work over smooth cylinder, data obtained during decreasing velocity in steps.

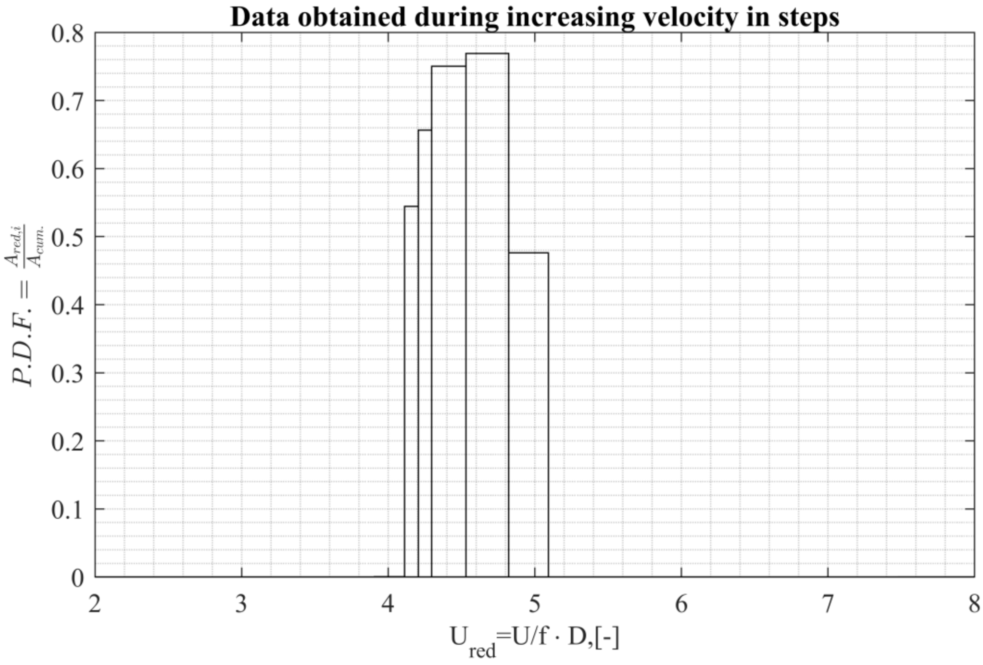

Figure 10.83 Work over lock-in, iced cable, α=0°, turbulent flow I_u=12.3%, normalized to cumulative work over smooth cylinder, data obtained during increasing velocity in steps.

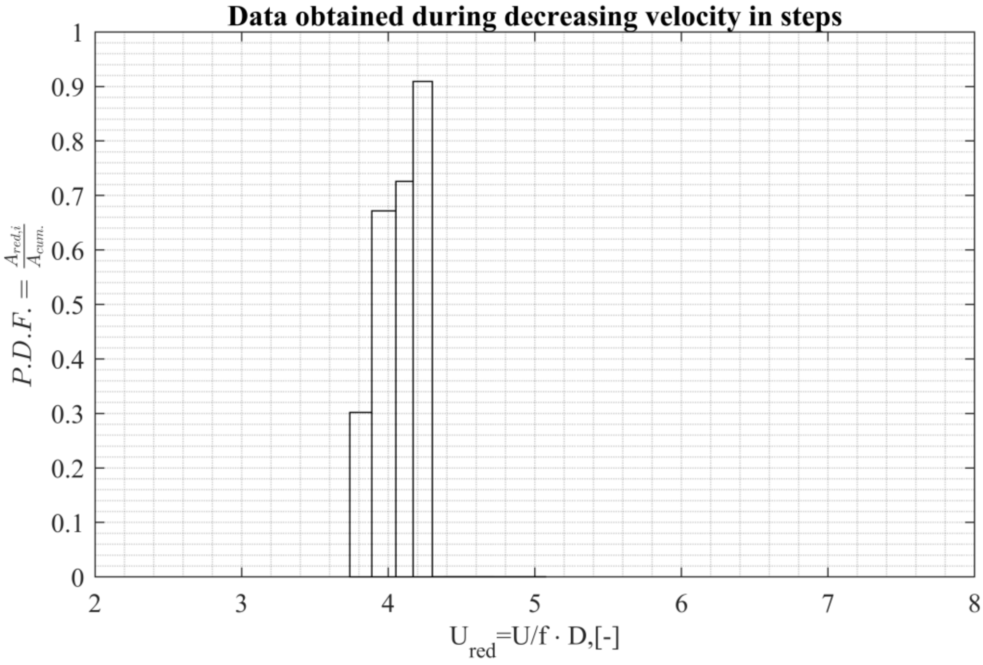

Figure 10.84 Work over lock-in, iced cable, α=0°, turbulent flow I_u=12.3%, normalized to cumulative work over smooth cylinder, data obtained during decreasing velocity in steps.

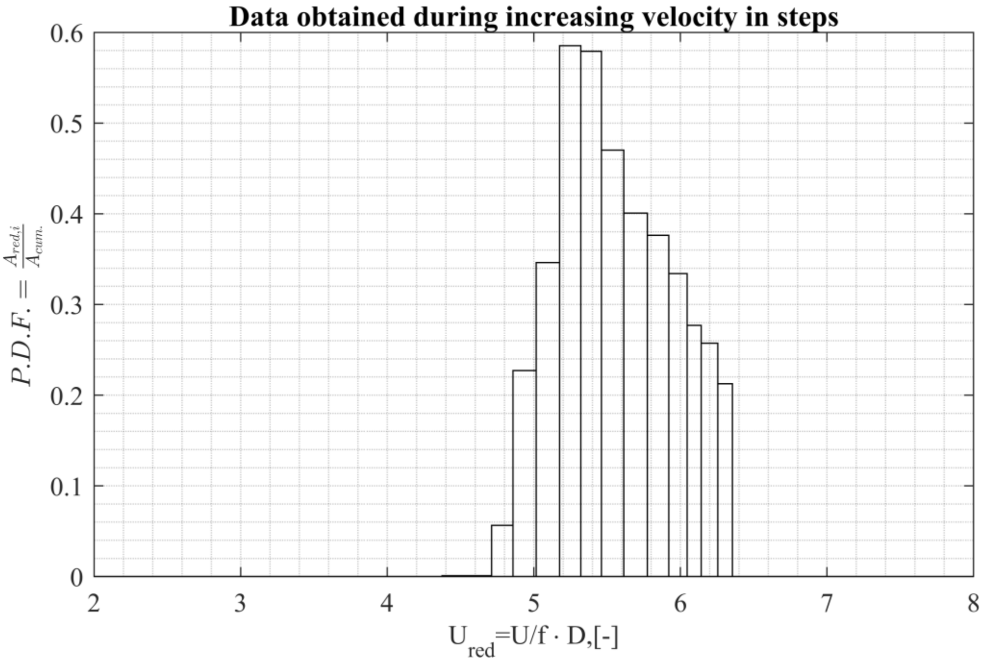

Figure 10.85 Work over lock-in, helical cable 1x91-12, smooth flow I_u=0.75%, normalized to cumulative work over smooth cylinder, data obtained during increasing velocity in steps.

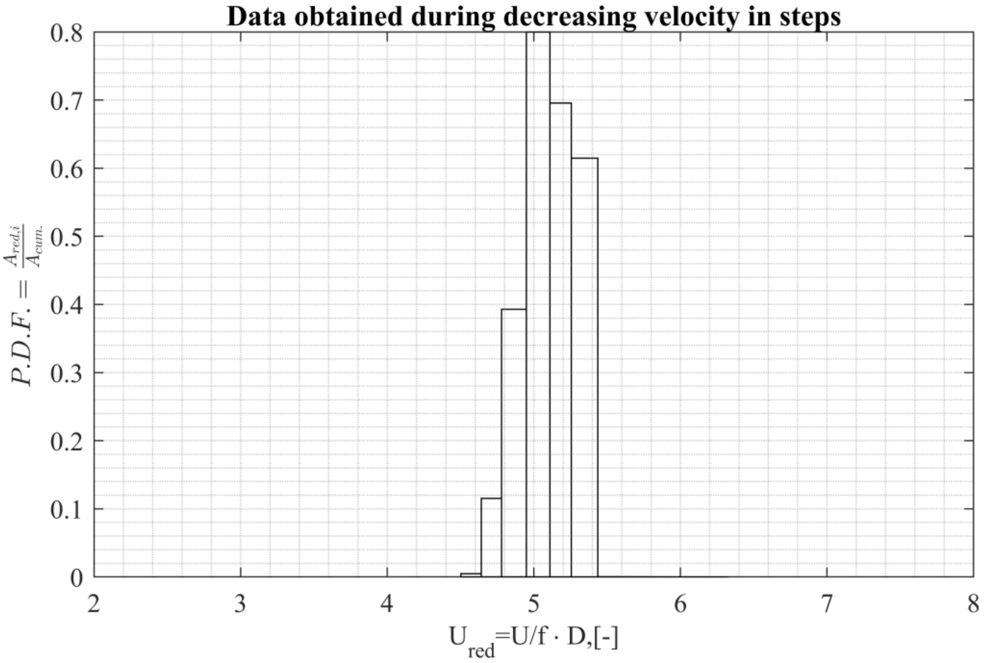

Figure 10.86 Work over lock-in, helical cable 1x91-12, smooth flow I_u=0.75%, normalized to cumulative work over smooth cylinder, data obtained during decreasing velocity in steps.

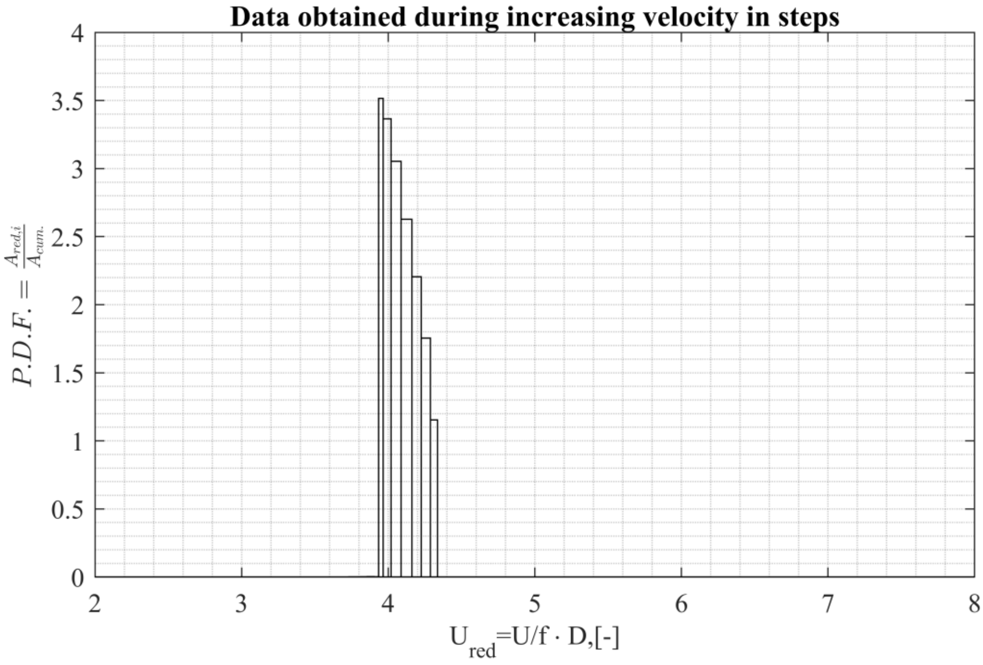

Figure 10.87 Work over lock-in, helical cable 1x91-12, turbulent flow I_u=4.5%, normalized to cumulative work over smooth cylinder, data obtained during increasing velocity in steps.

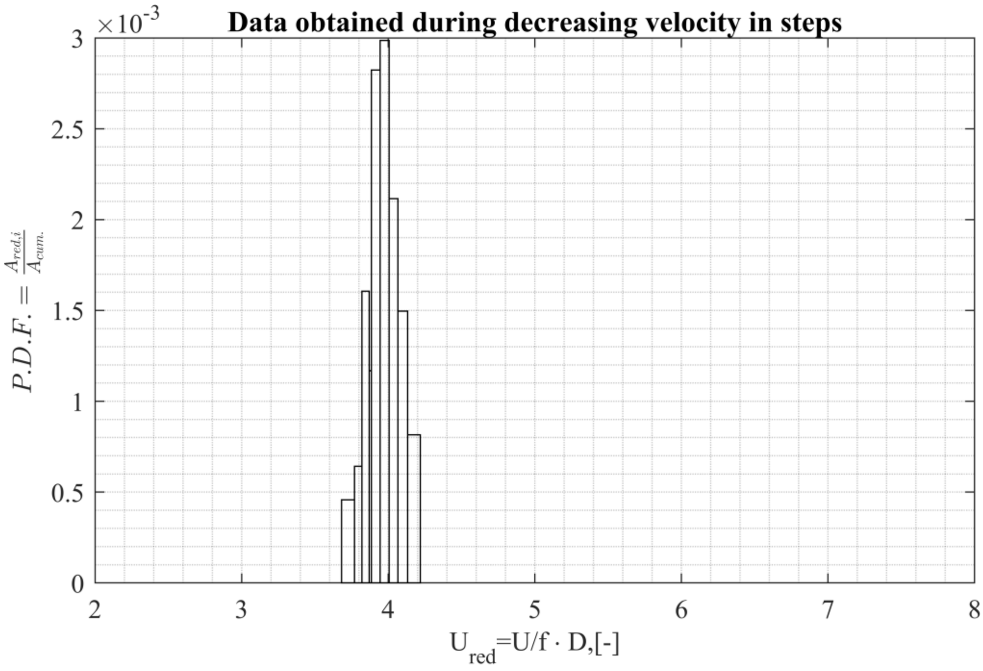

Figure 10.88 Work over lock-in, helical cable 1x91-12, turbulent flow I_u=4.5%, normalized to cumulative work over smooth cylinder, data obtained during decreasing velocity in steps.

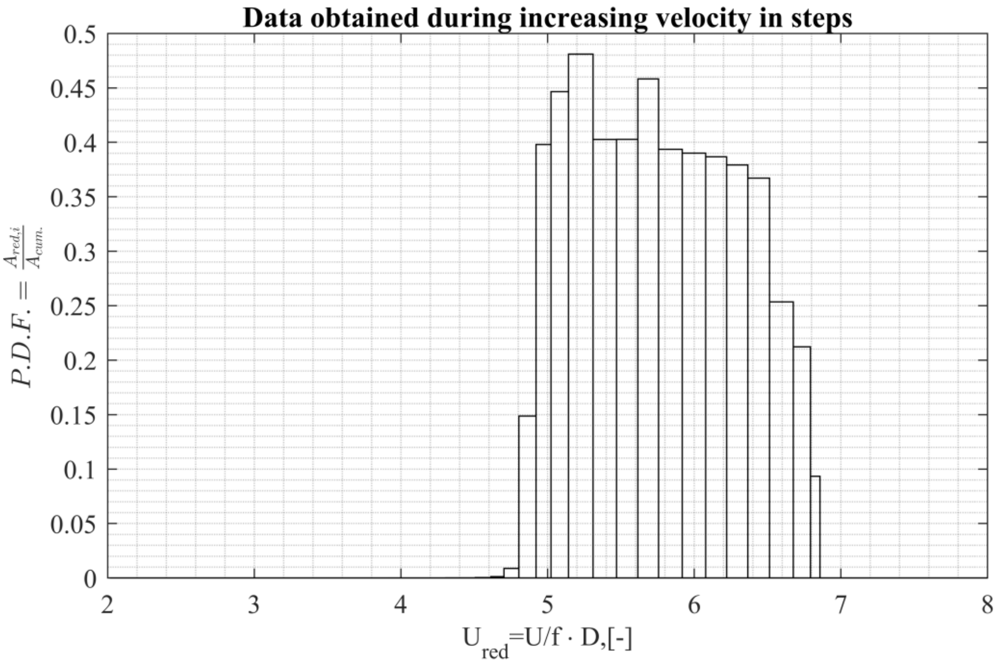

Figure 10.89 Work over lock-in, helical cable 1x61-24, smooth flow I_u=0.75%, normalized to cumulative work over smooth cylinder, data obtained during increasing velocity in steps.

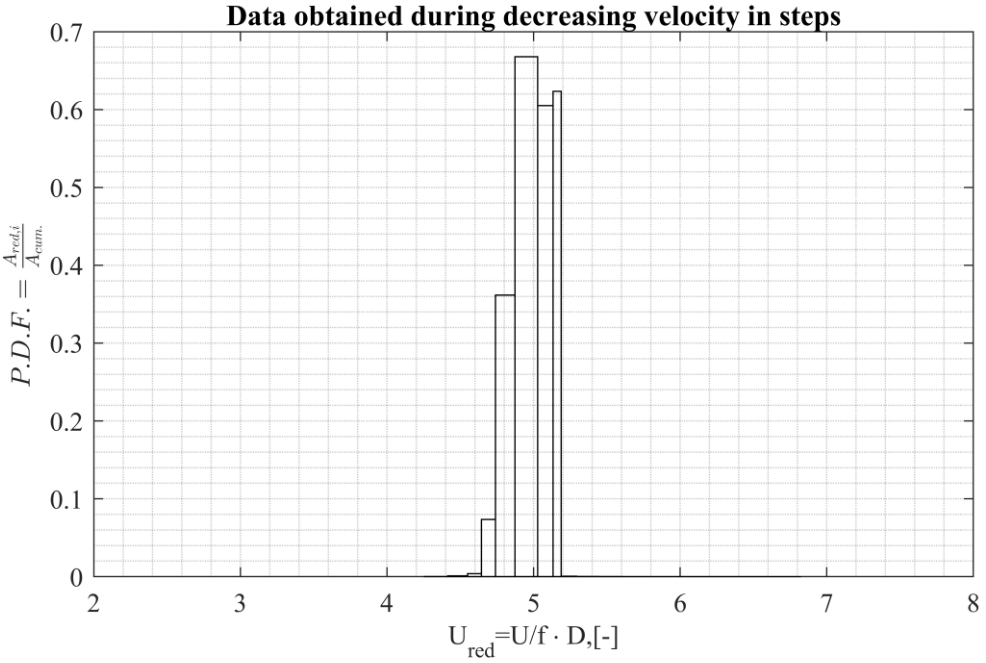

Figure 10.90 Work over lock-in, helical cable 1x61-24, smooth flow I_u=0.75%, normalized to cumulative work over smooth cylinder, data obtained during decreasing velocity in steps.

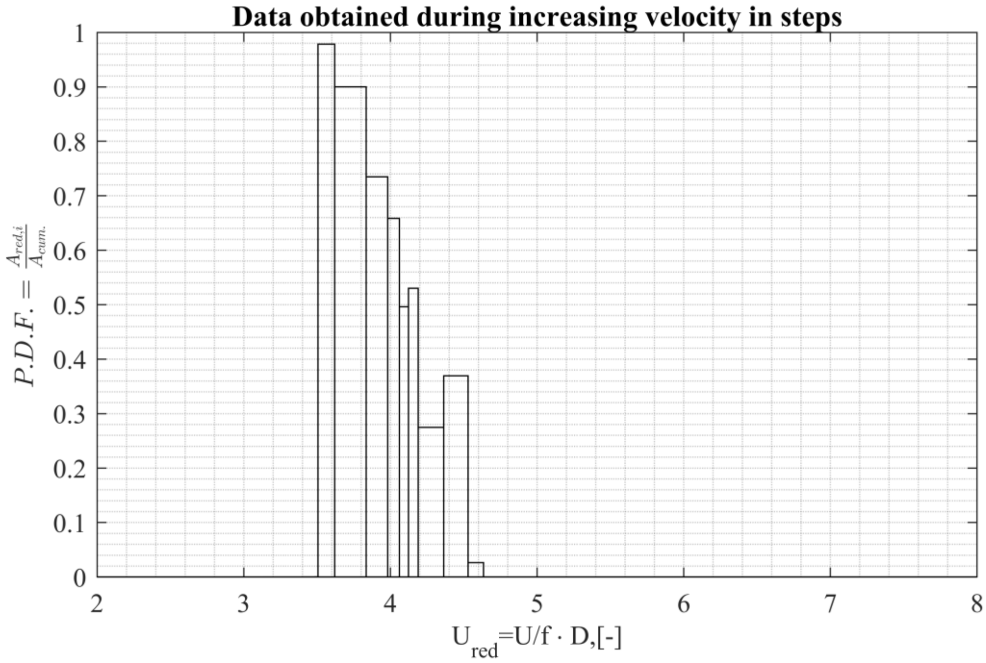

Figure 10.91 Work over lock-in, helical cable 1x61-24, turbulent flow I_u=4.5%, normalized to cumulative work over smooth cylinder, data obtained during increasing velocity in steps.

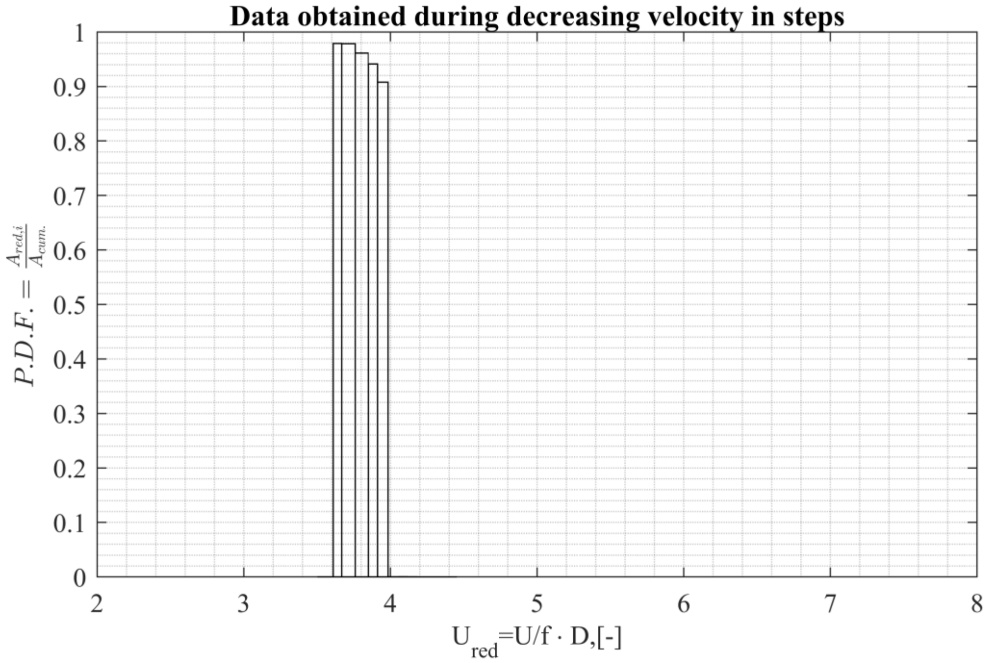

Figure 10.92 Work over lock-in, helical cable 1x61-24, turbulent flow I_u=4.5%, normalized to cumulative work over smooth cylinder, data obtained during decreasing velocity in steps.

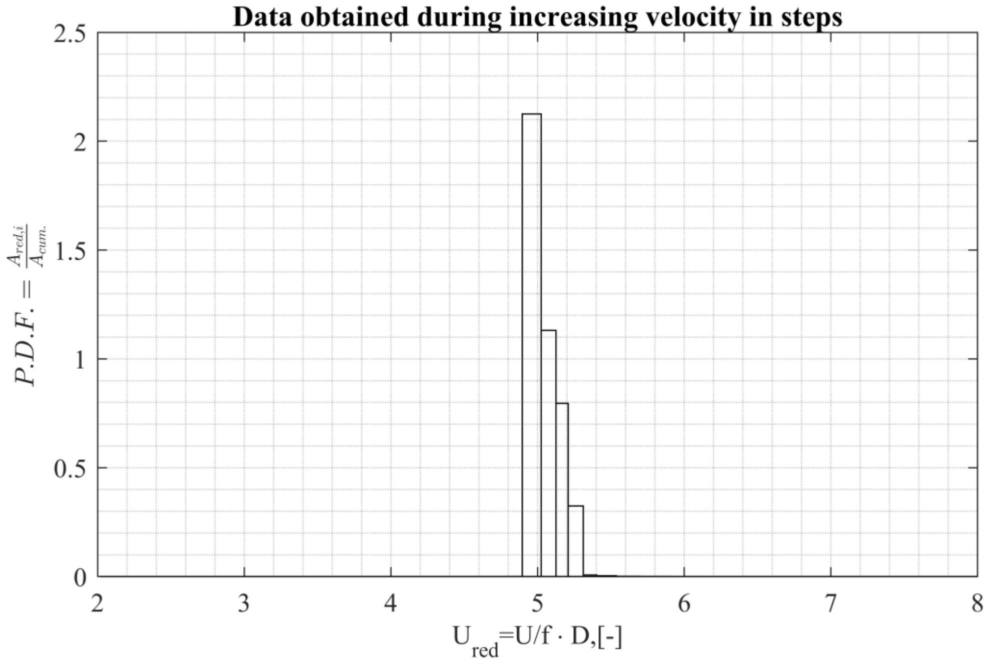

Figure 10.93 Work over lock-in, helical cable 1x61-12, smooth flow I_u=0.75%, normalized to cumulative work over smooth cylinder, data obtained during increasing velocity in steps.

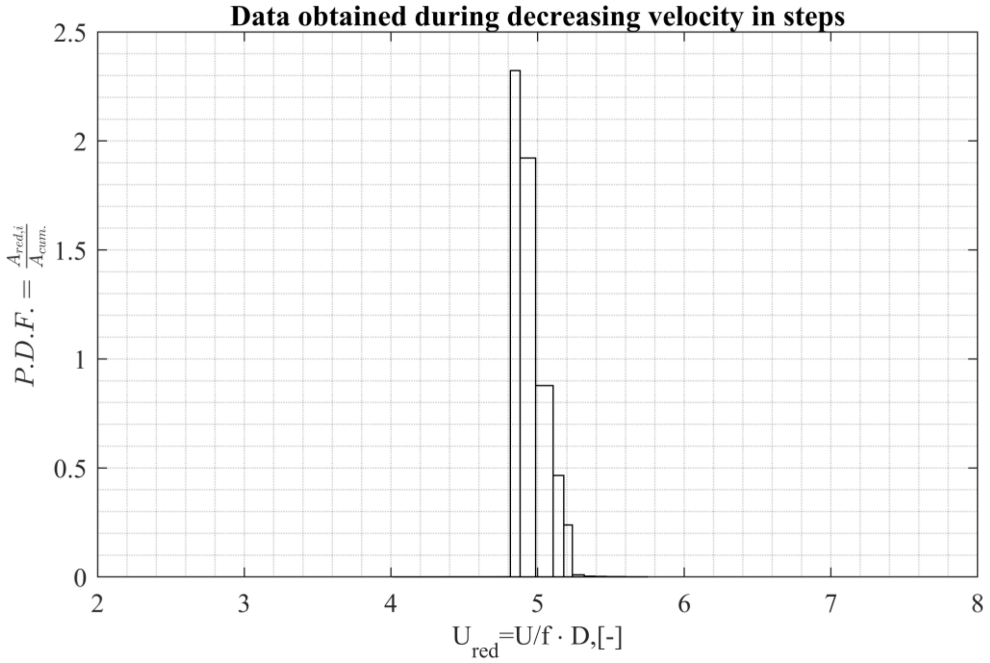

Figure 10.94 Work over lock-in, helical cable 1x61-12, smooth flow I_u=0.75%, normalized to cumulative work over smooth cylinder, data obtained during decreasing velocity in steps.

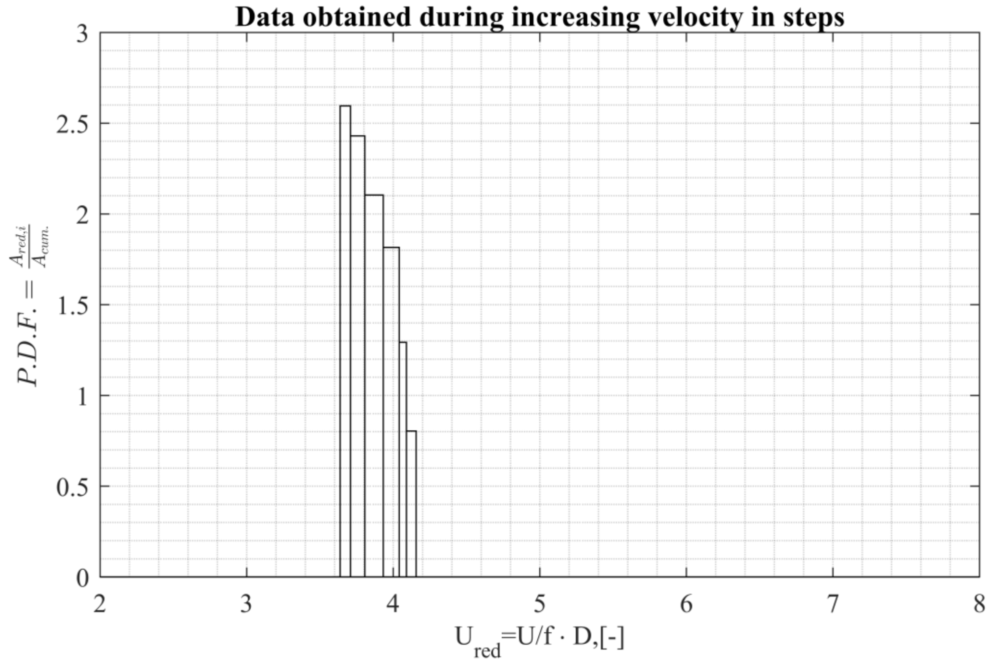

Figure 10.95 Work over lock-in, helical cable 1x61-12, turbulent flow I_u=4.5%, normalized to cumulative work over smooth cylinder, data obtained during increasing velocity in steps.

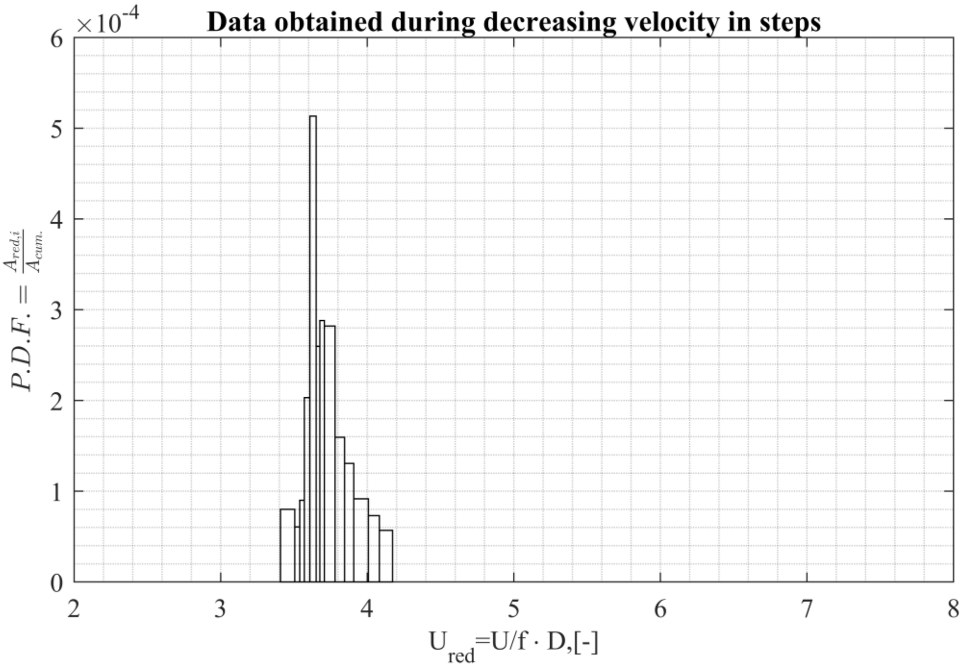

Figure 10.96 Work over lock-in, helical cable 1x61-12, turbulent flow I_u=4.5%, normalized to cumulative work over smooth cylinder, data obtained during decreasing velocity in steps.

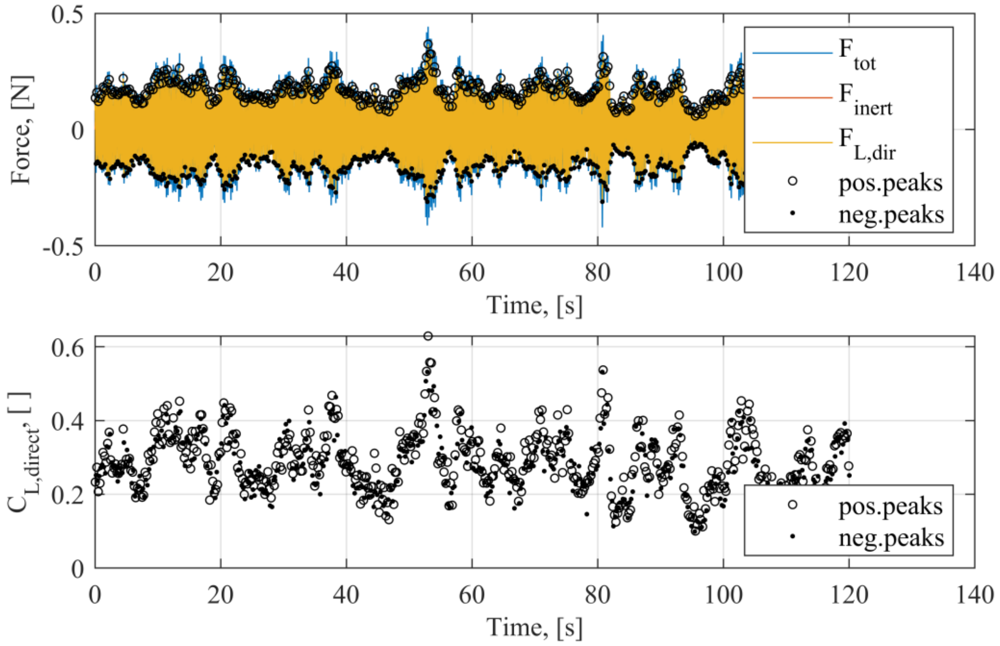

Figure 10.97 Forces (top) and lift coefficients (bottom) for smooth cylinder model in nearly smooth flow, U=2.509 m/s, data obtained during increasing velocity in steps

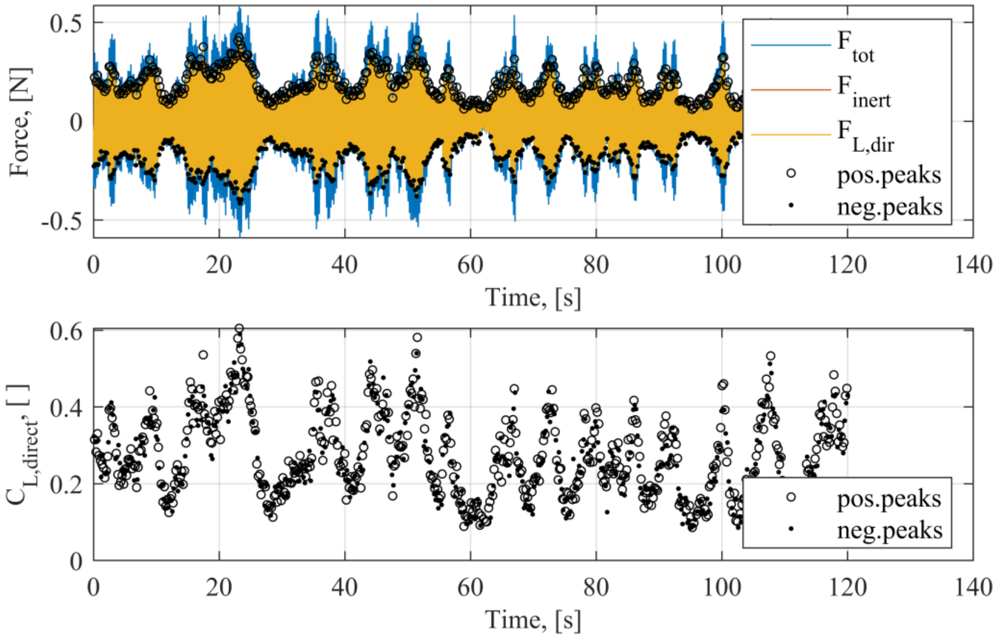

Figure 10.98 Forces (top) and lift coefficients (bottom) for smooth cylinder model in nearly smooth flow, U=2.749 m/s, data obtained during increasing velocity in steps

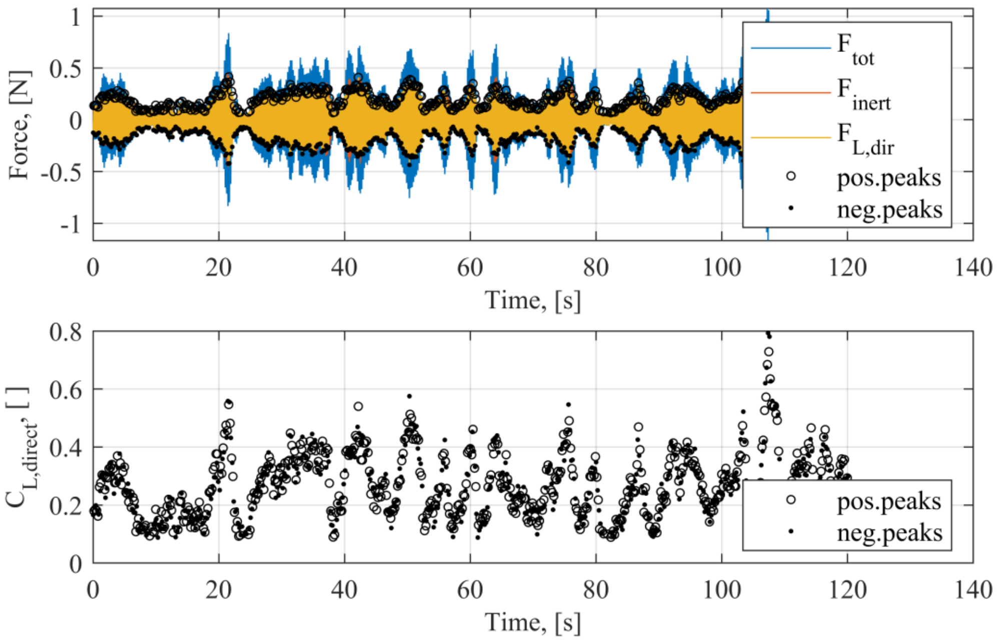

Figure 10.99 Forces (top) and lift coefficients (bottom) for smooth cylinder model in nearly smooth flow, U=2.856 m/s, data obtained during increasing velocity in steps

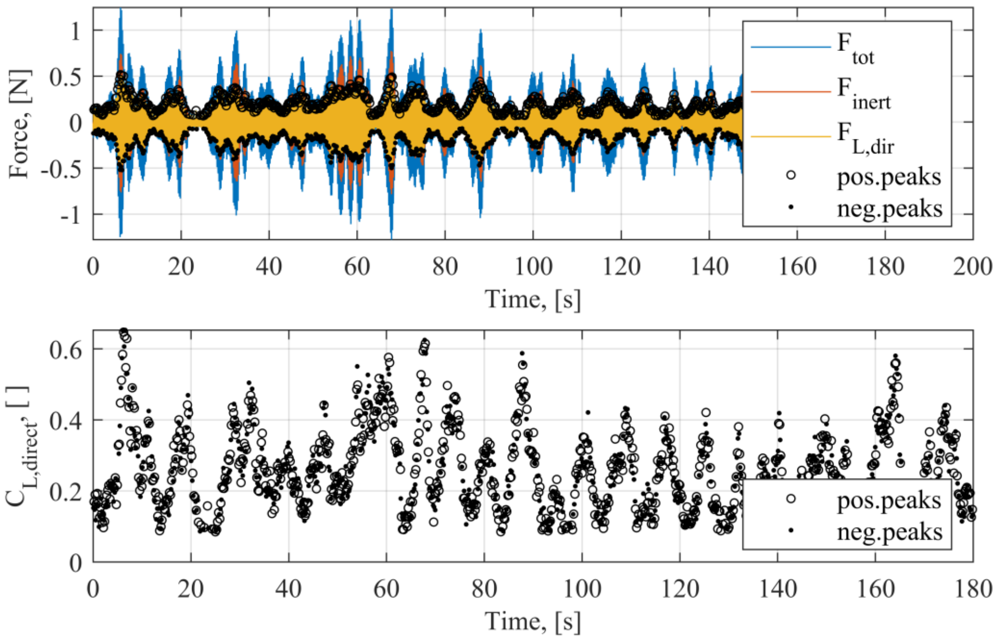

Figure 10.100 Forces (top) and lift coefficients (bottom) for smooth cylinder model in nearly smooth flow, U=2.930 m/s, data obtained during increasing velocity in steps

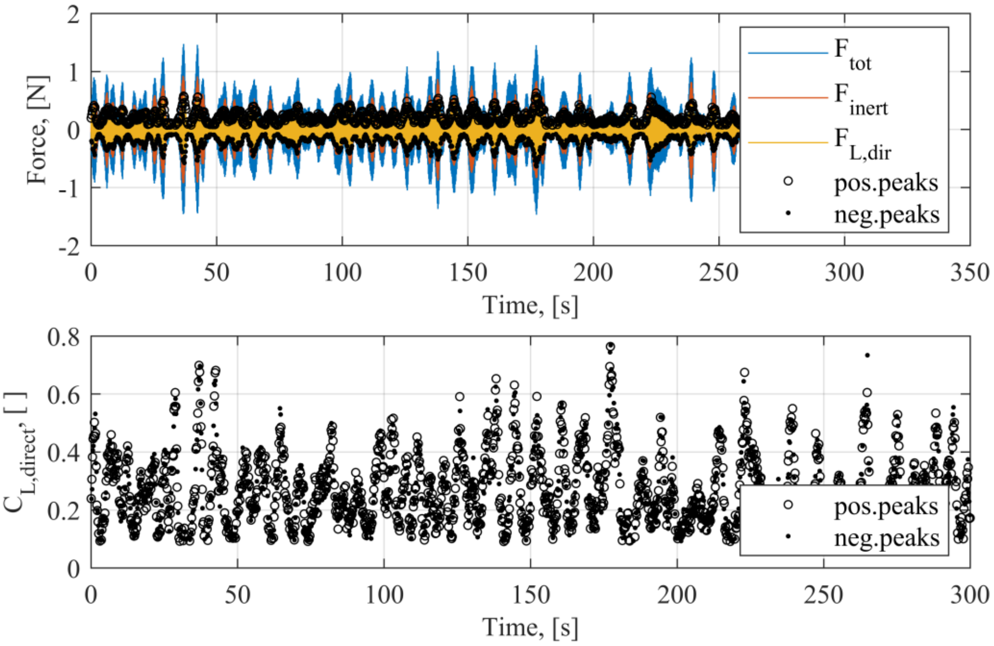

Figure 10.101 Forces (top) and lift coefficients (bottom) for smooth cylinder model in nearly smooth flow, U=2.978 m/s, data obtained during increasing velocity in steps

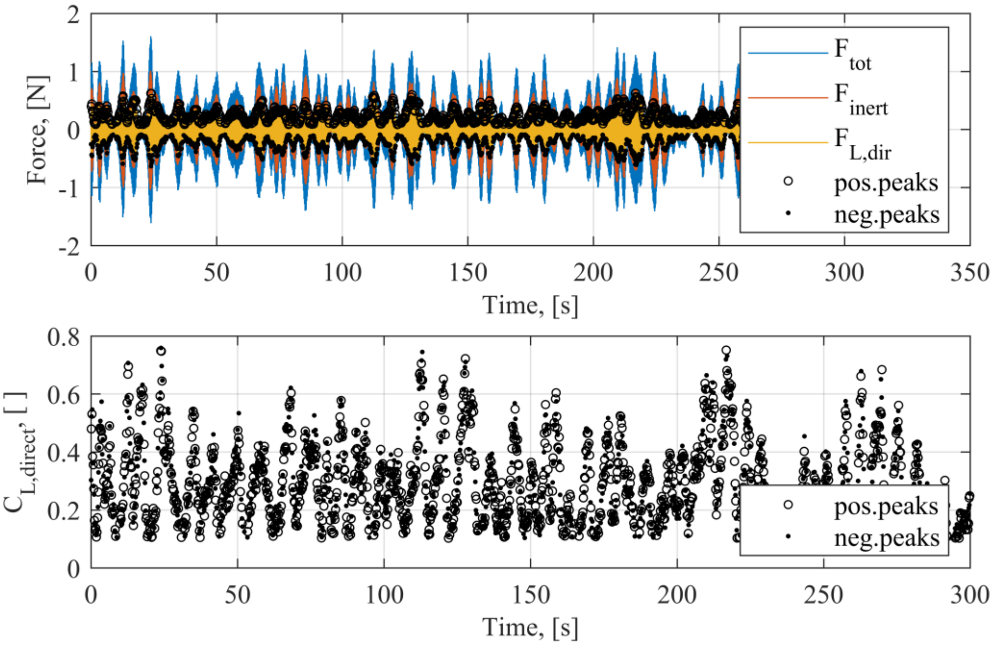

Figure 10.102 Forces (top) and lift coefficients (bottom) for smooth cylinder model in nearly smooth flow, U=2.991 m/s, data obtained during increasing velocity in steps

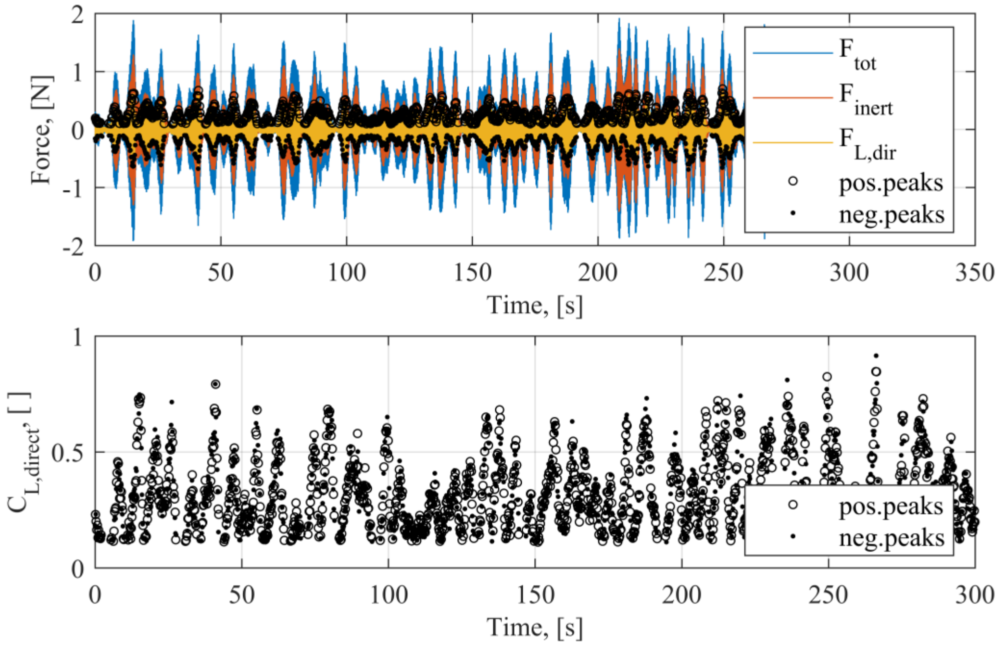

Figure 10.103 Forces (top) and lift coefficients (bottom) for smooth cylinder model in nearly smooth flow, U=3.024 m/s, data obtained during increasing velocity in steps

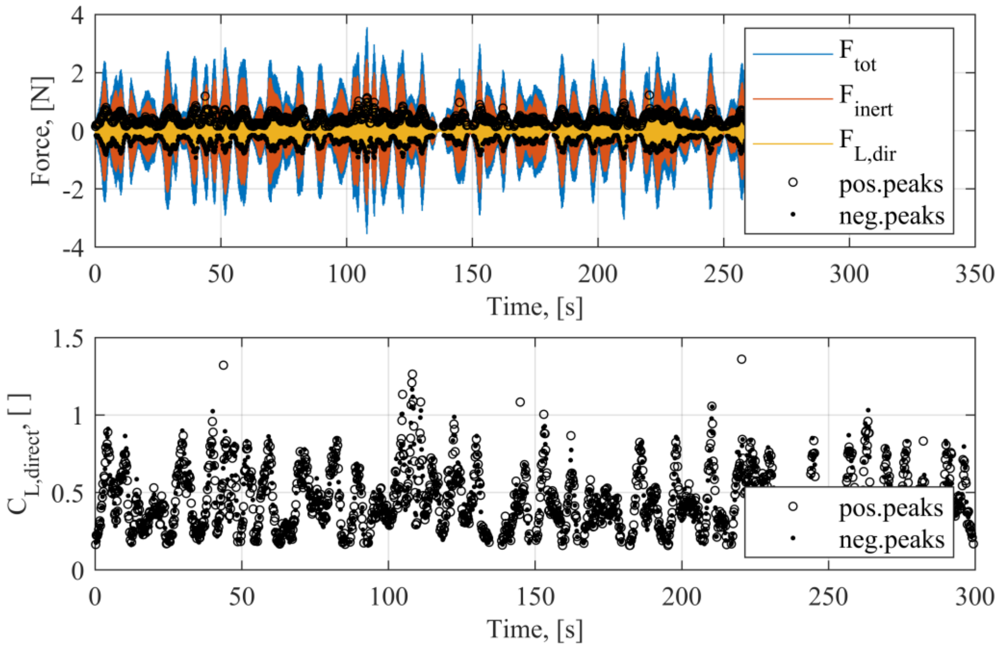

Figure 10.104 Forces (top) and lift coefficients (bottom) for smooth cylinder model in nearly smooth flow, U=3.113 m/s, data obtained during increasing velocity in steps

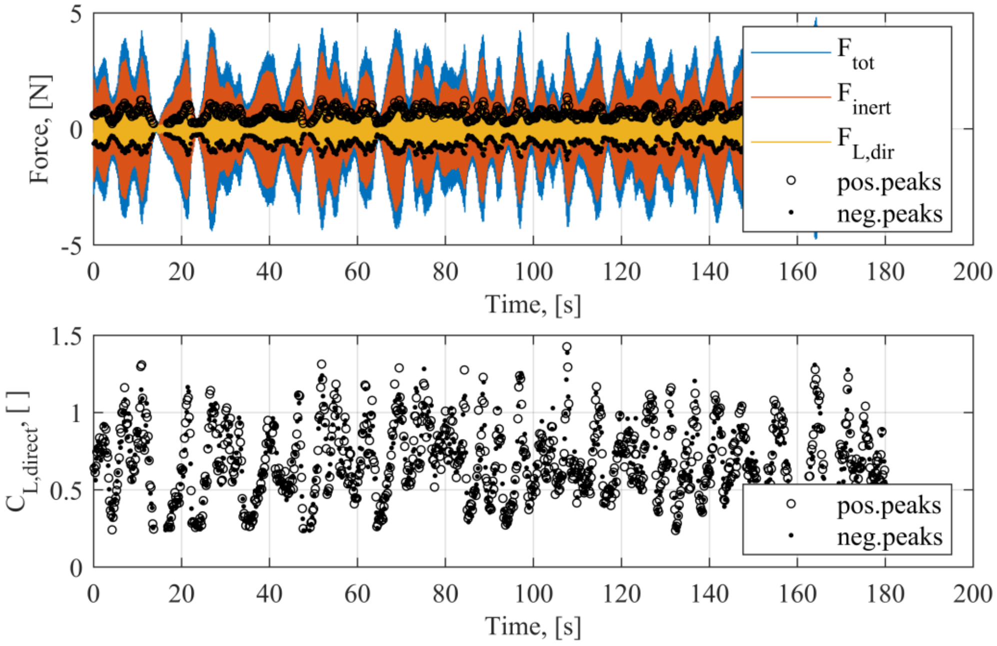

Figure 10.105 Forces (top) and lift coefficients (bottom) for smooth cylinder model in nearly smooth flow, U=3.205 m/s, data obtained during increasing velocity in steps

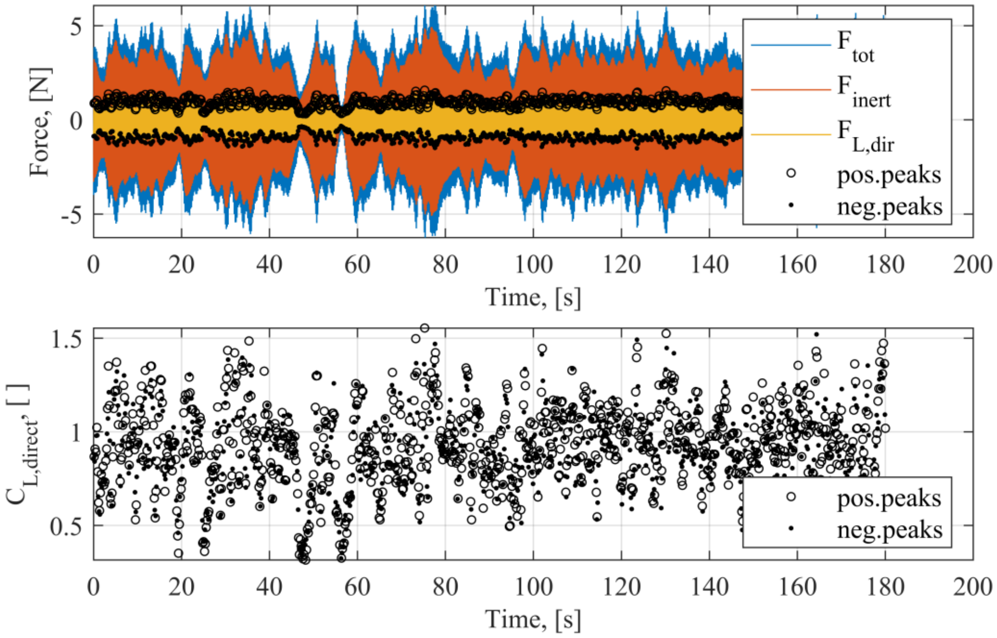

Figure 10.106 Forces (top) and lift coefficients (bottom) for smooth cylinder model in nearly smooth flow, U=3.301 m/s, data obtained during increasing velocity in steps

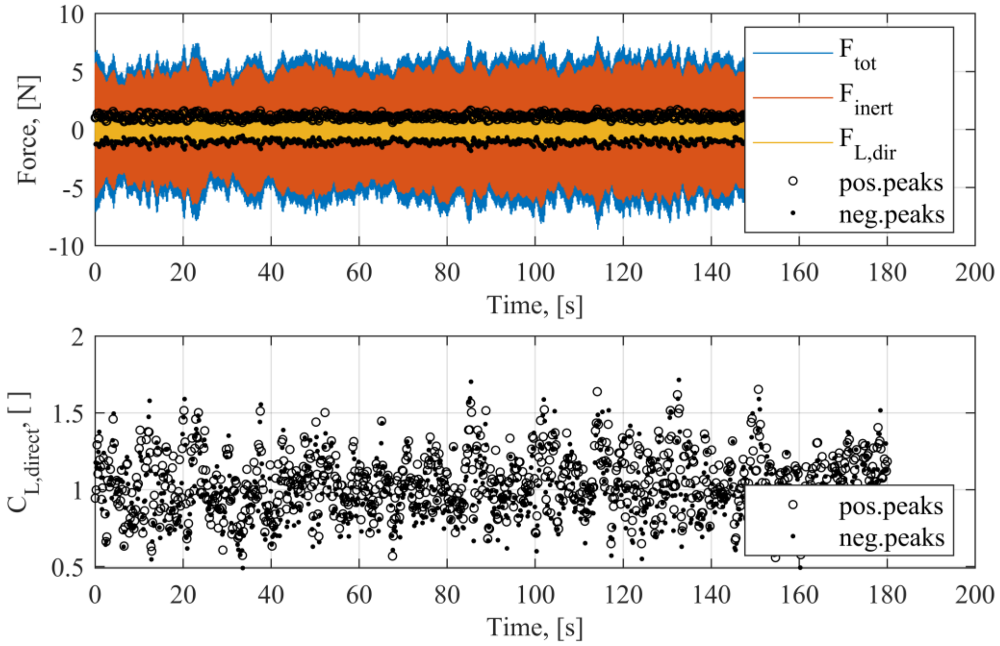

Figure 10.107 Forces (top) and lift coefficients (bottom) for smooth cylinder model in nearly smooth flow, U=3.399 m/s, data obtained during increasing velocity in steps

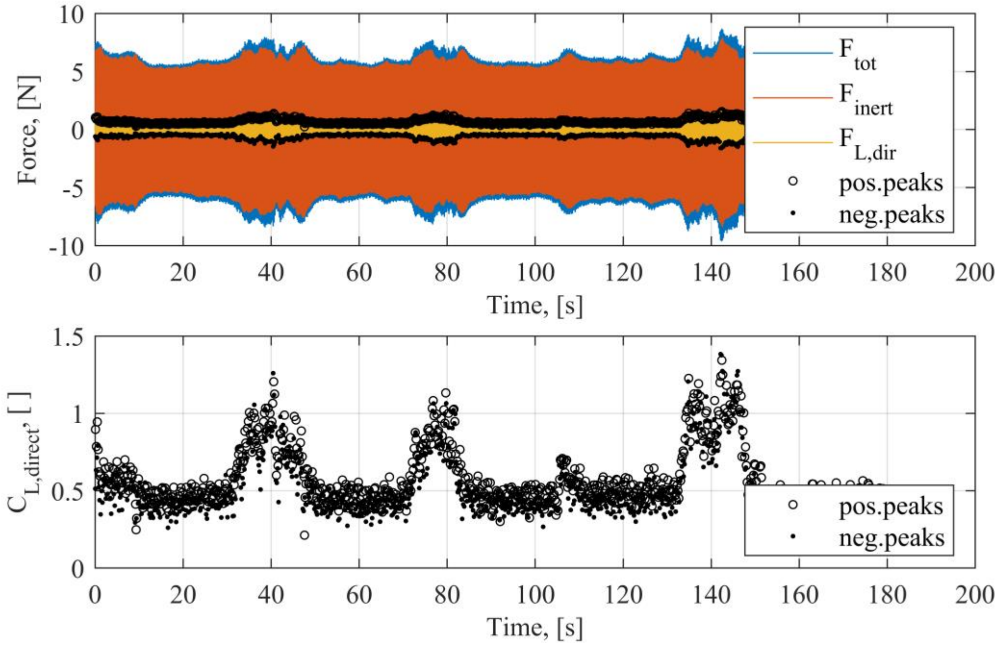

Figure 10.108 Forces (top) and lift coefficients (bottom) for smooth cylinder model in nearly smooth flow, U=3.523 m/s, data obtained during increasing velocity in steps

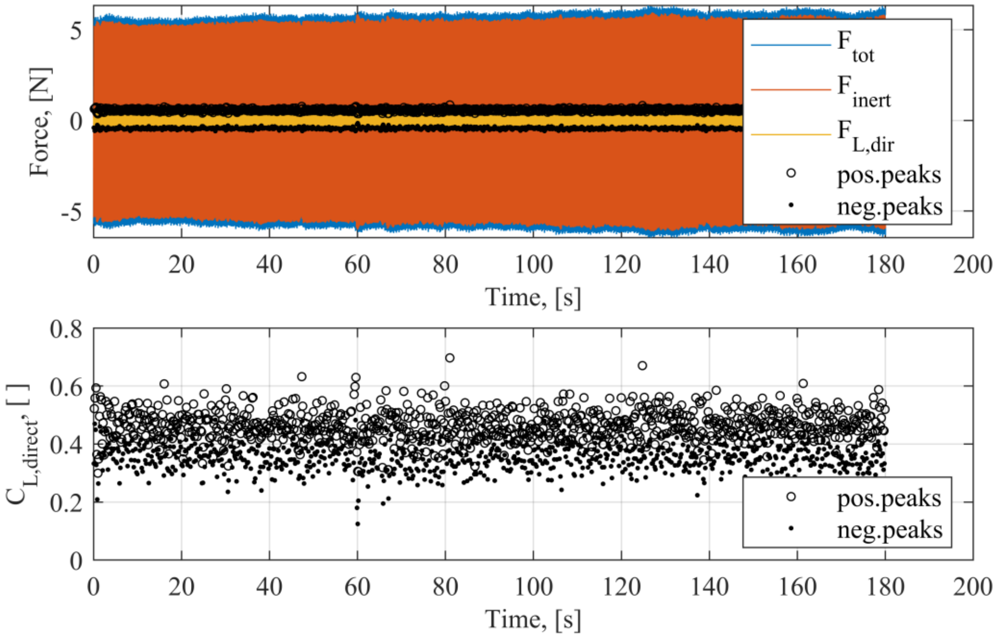

Figure 10.109 Forces (top) and lift coefficients (bottom) for smooth cylinder model in nearly smooth flow, U=3.925 m/s, data obtained during increasing velocity in steps

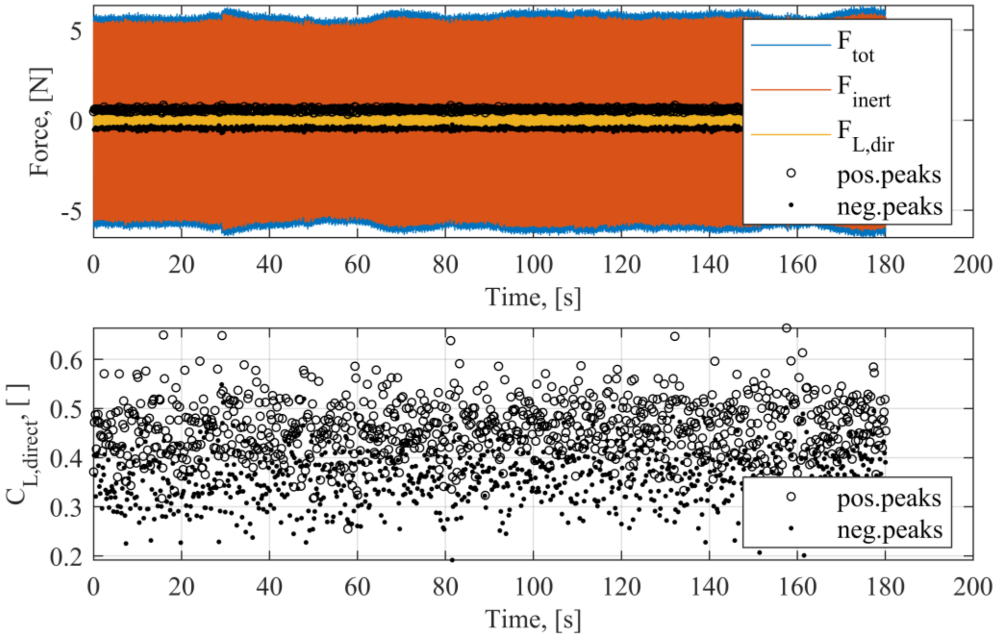

Figure 10.110 Forces (top) and lift coefficients (bottom) for smooth cylinder model in nearly smooth flow, U=3.720 m/s, data obtained during increasing velocity in steps

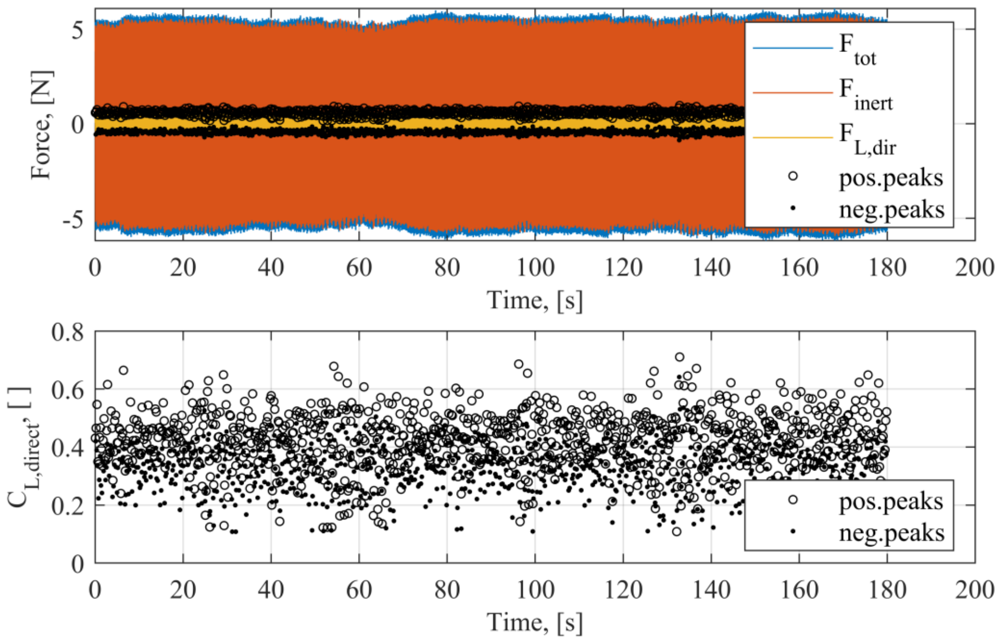

Figure 10.111 Forces (top) and lift coefficients (bottom) for smooth cylinder model in nearly smooth flow, U=3.817 m/s, data obtained during increasing velocity in steps

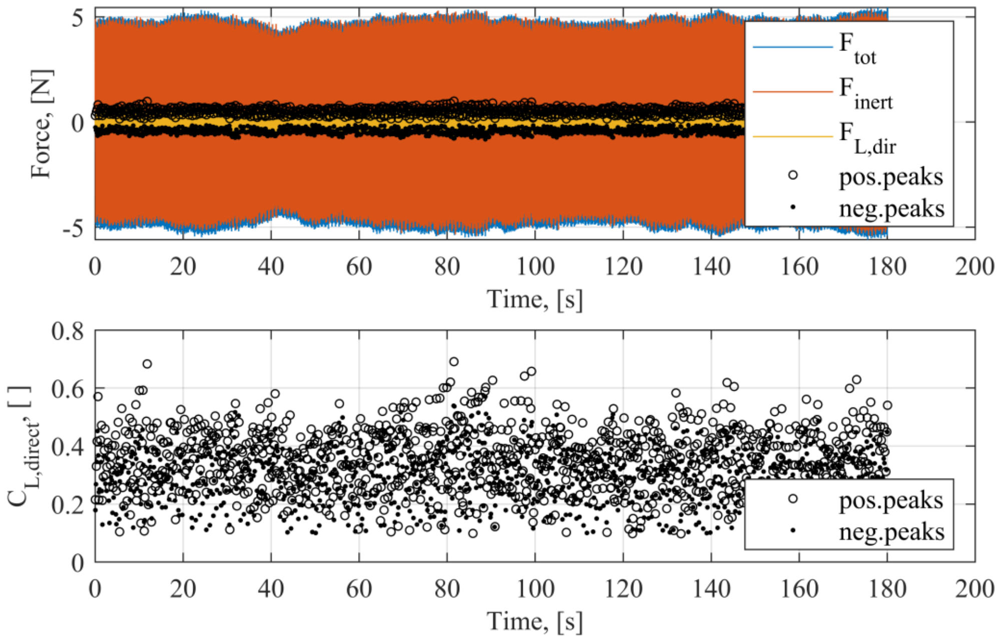

Figure 10.112 Forces (top) and lift coefficients (bottom) for smooth cylinder model in nearly smooth flow, U=3.933 m/s, data obtained during increasing velocity in steps

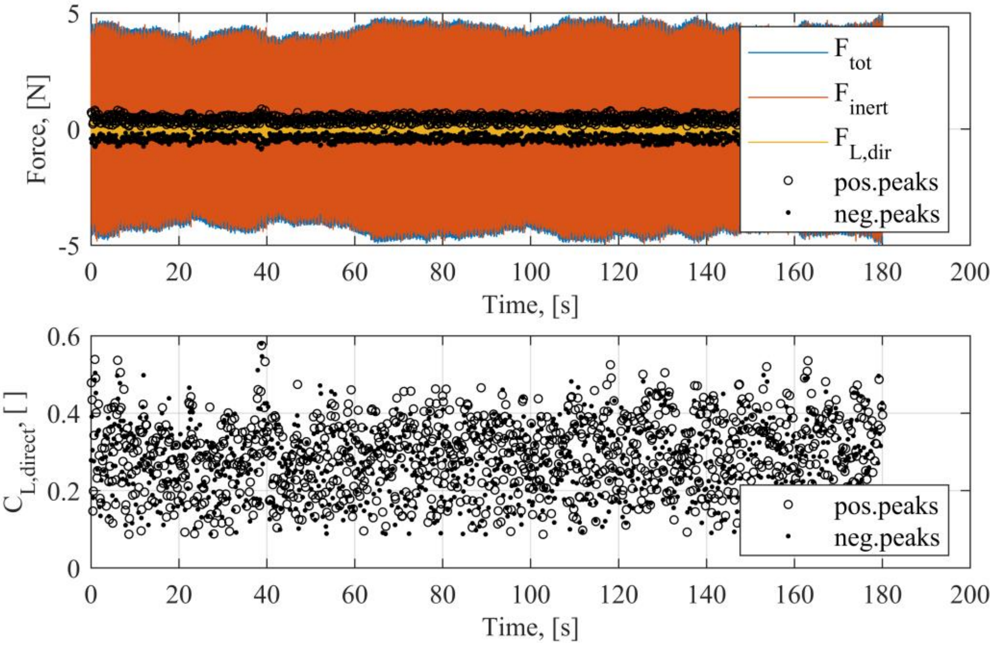

Figure 10.113 Forces (top) and lift coefficients (bottom) for smooth cylinder model in nearly smooth flow, U=4.012 m/s, data obtained during increasing velocity in steps

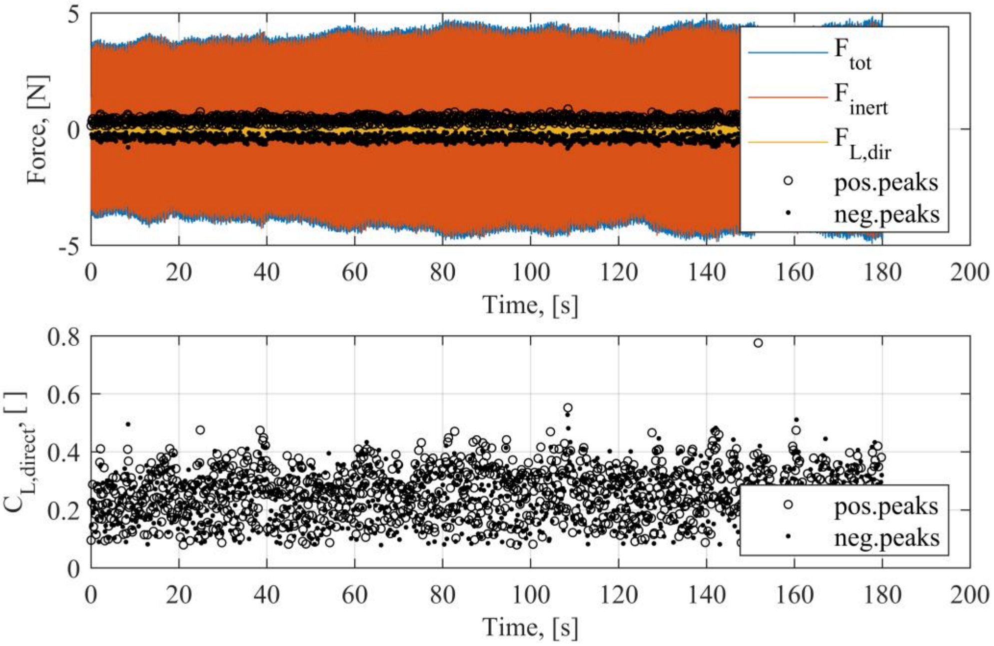

Figure 10.114 Forces (top) and lift coefficients (bottom) for smooth cylinder model in nearly smooth flow, U=4.110 m/s, data obtained during increasing velocity in steps

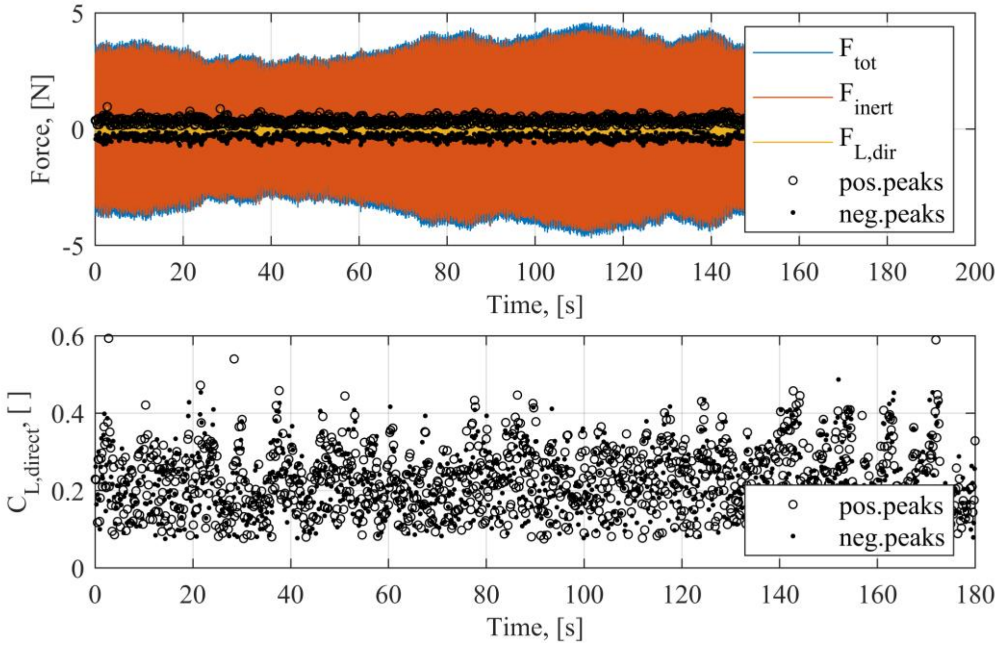

Figure 10.115 Forces (top) and lift coefficients (bottom) for smooth cylinder model in nearly smooth flow, U=4.186 m/s, data obtained during increasing velocity in steps

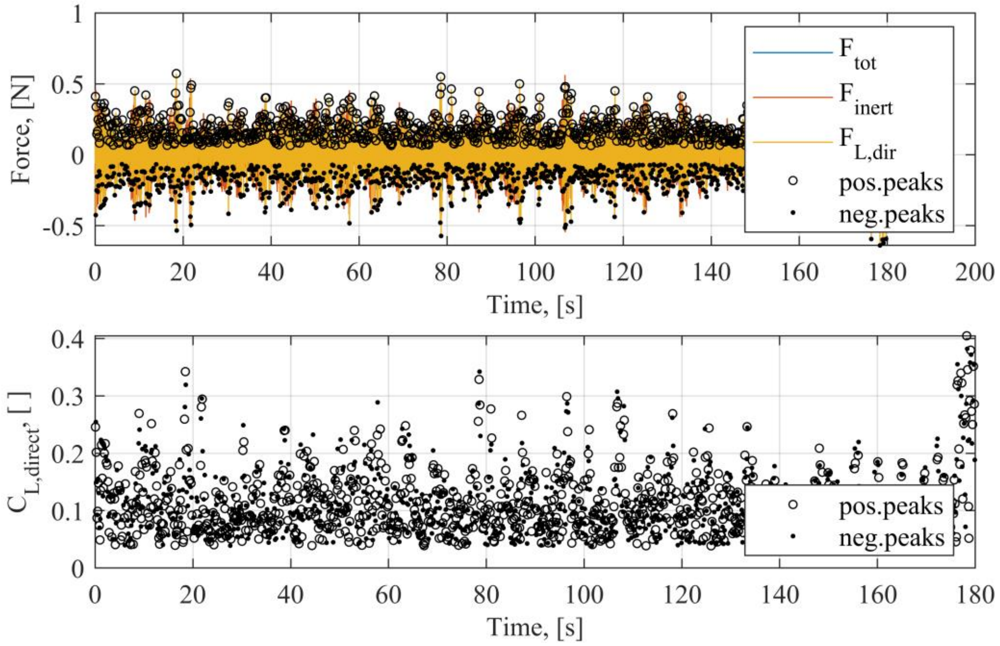

Figure 10.116 Forces (top) and lift coefficients (bottom) for smooth cylinder model in nearly smooth flow, U=4.246 m/s, data obtained during increasing velocity in steps

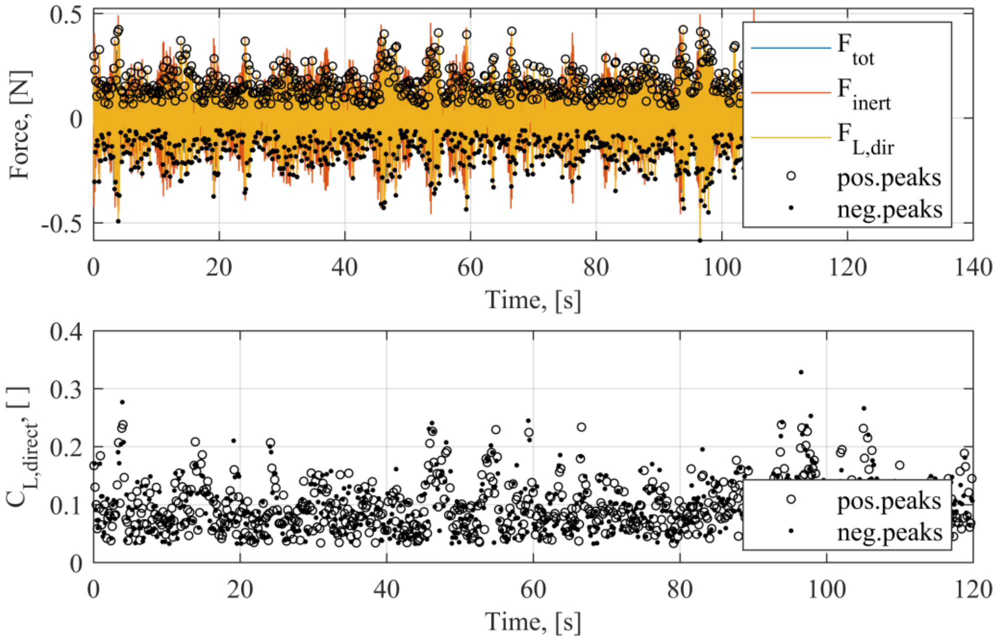

Figure 10.117 Forces (top) and lift coefficients (bottom) for smooth cylinder model in nearly smooth flow, U=4.377 m/s, data obtained during increasing velocity in steps

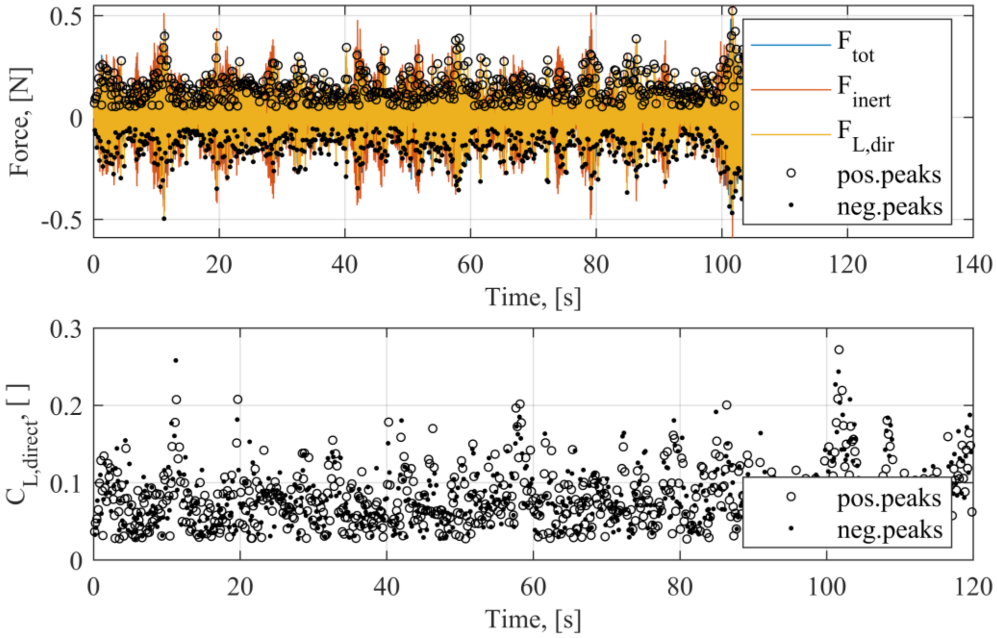

Figure 10.118 Forces (top) and lift coefficients (bottom) for smooth cylinder model in nearly smooth flow, U=4.522 m/s, data obtained during increasing velocity in steps

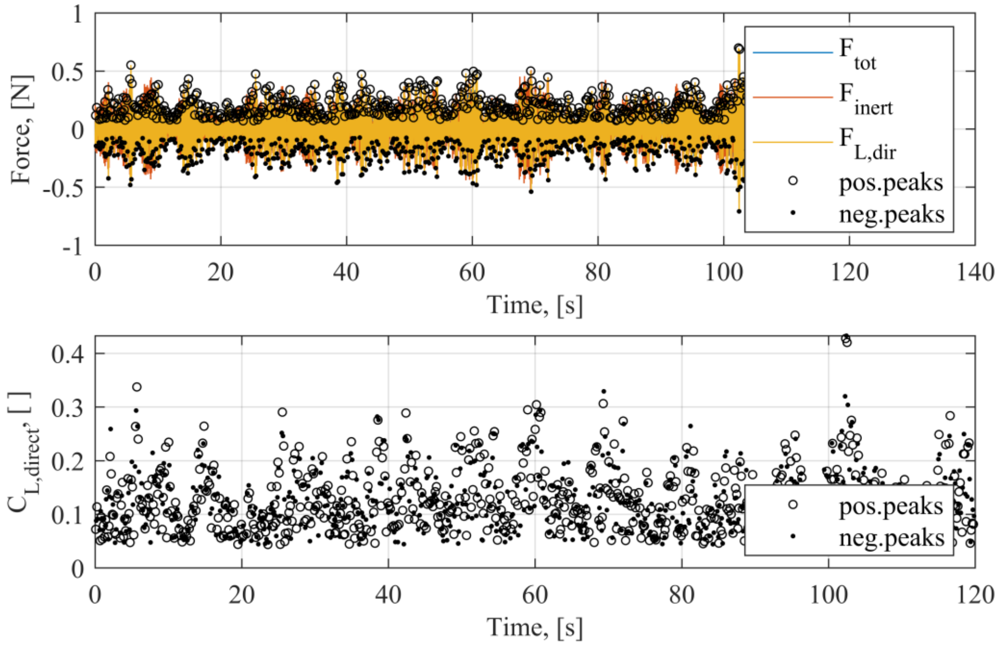

Figure 10.119 Forces (top) and lift coefficients (bottom) for smooth cylinder model in nearly smooth flow, U=4.195 m/s, data obtained during decreasing velocity in steps

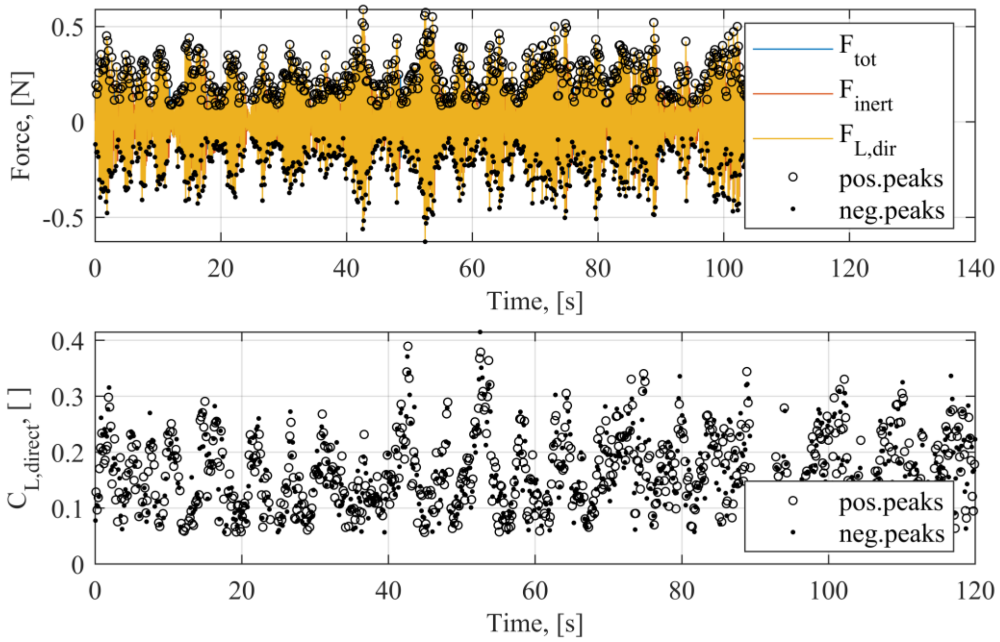

Figure 10.120 Forces (top) and lift coefficients (bottom) for smooth cylinder model in nearly smooth flow, U=4.037 m/s, data obtained during decreasing velocity in steps

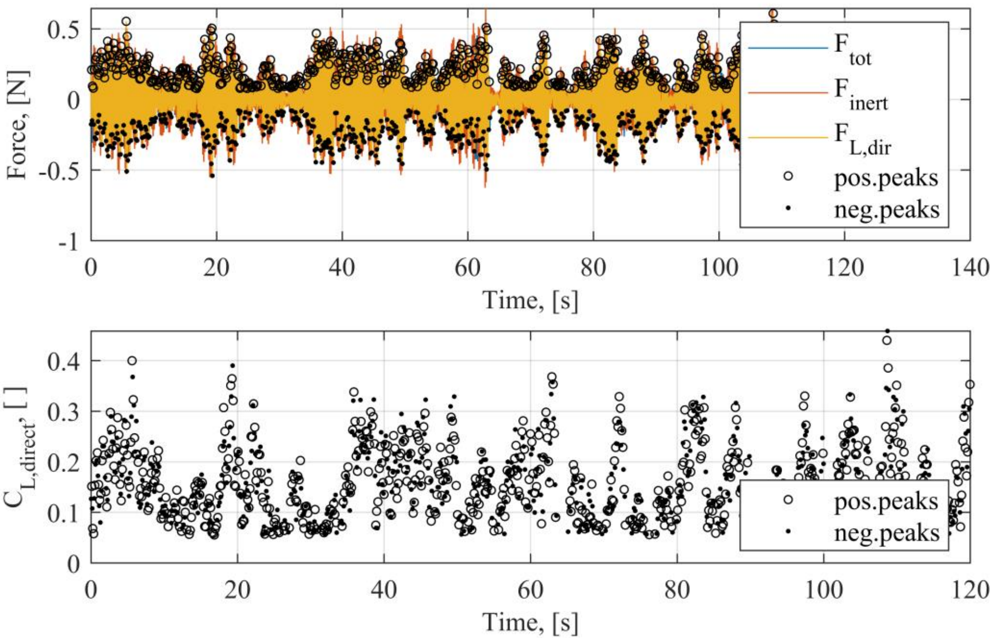

Figure 10.121 Forces (top) and lift coefficients (bottom) for smooth cylinder model in nearly smooth flow, U=3.862 m/s, data obtained during decreasing velocity in steps

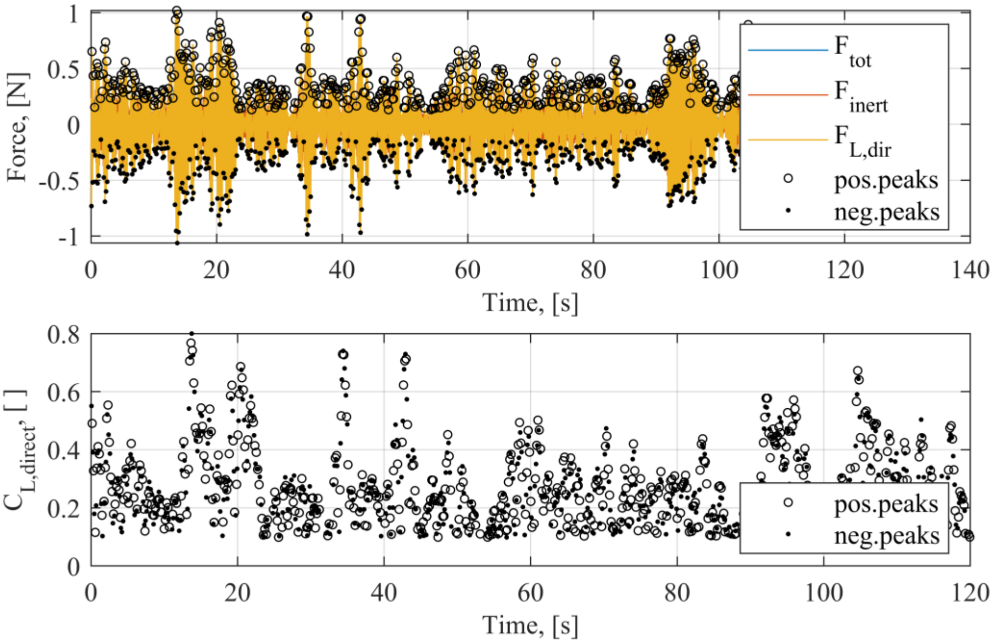

Figure 10.122 Forces (top) and lift coefficients (bottom) for smooth cylinder model in nearly smooth flow, U=3.785 m/s, data obtained during decreasing velocity in steps

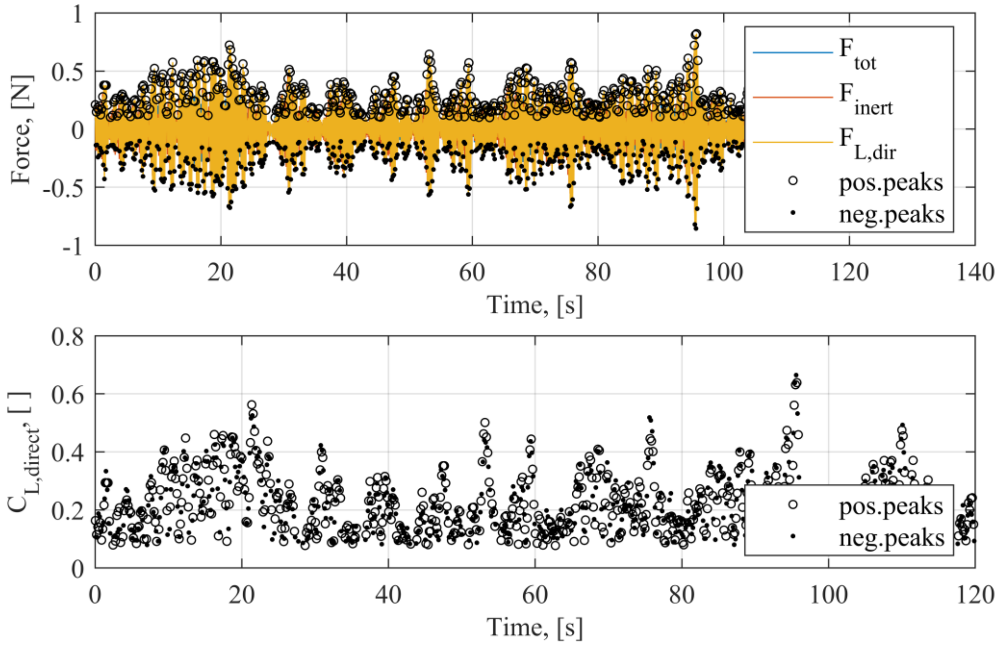

Figure 10.123 Forces (top) and lift coefficients (bottom) for smooth cylinder model in nearly smooth flow, U=3.723 m/s, data obtained during decreasing velocity in steps

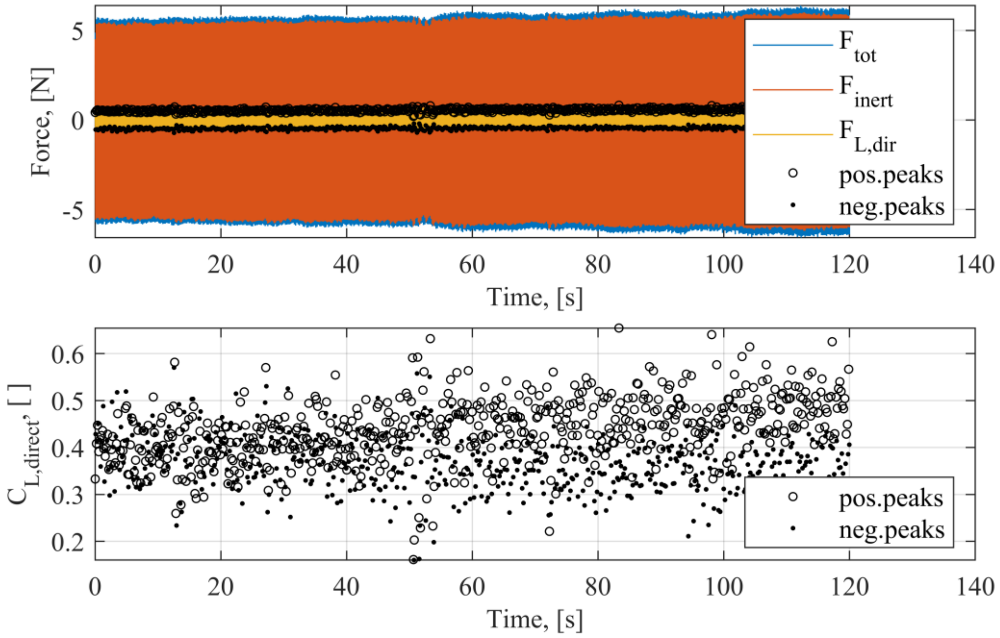

Figure 10.124 Forces (top) and lift coefficients (bottom) for smooth cylinder model in nearly smooth flow, U=3.683 m/s, data obtained during decreasing velocity in steps

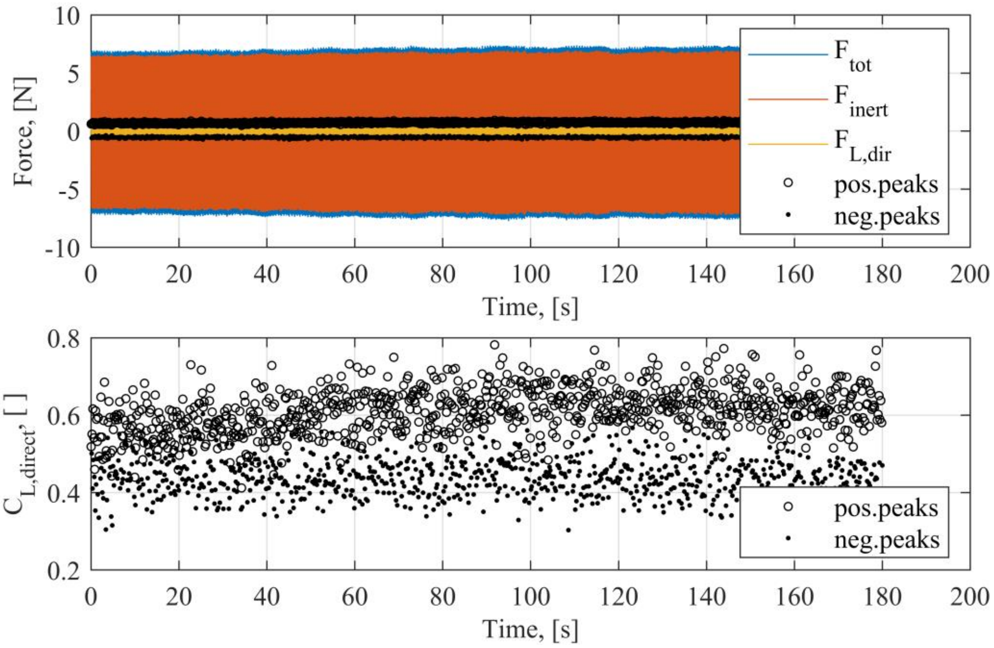

Figure 10.125 Forces (top) and lift coefficients (bottom) for smooth cylinder model in nearly smooth flow, U=3.581 m/s, data obtained during decreasing velocity in steps

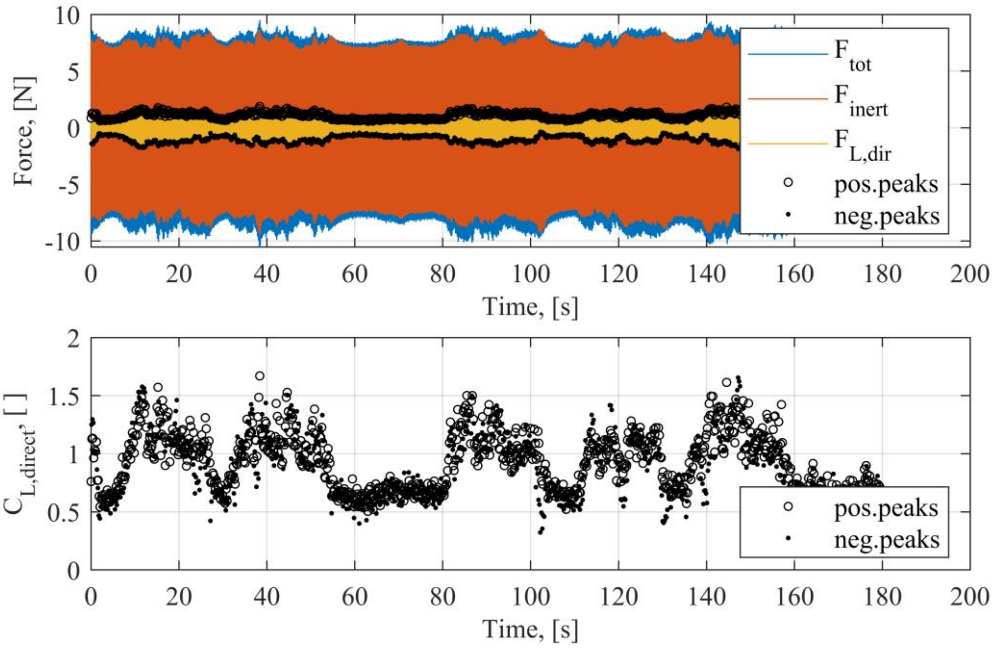

Figure 10.126 Forces (top) and lift coefficients (bottom) for smooth cylinder model in nearly smooth flow, U=3.480 m/s, data obtained during decreasing velocity in steps

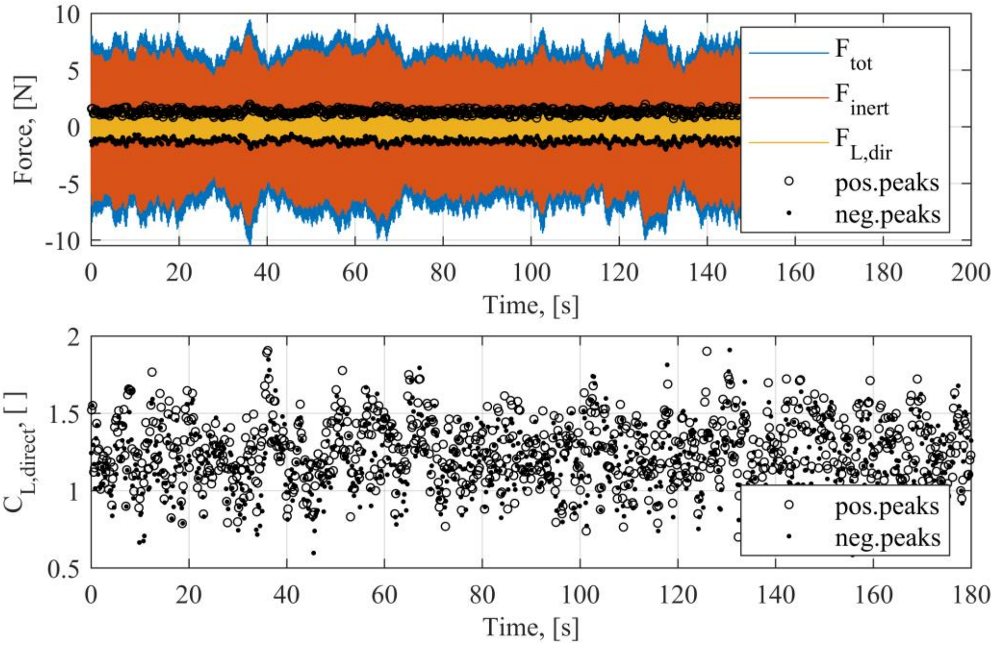

Figure 10.127 Forces (top) and lift coefficients (bottom) for smooth cylinder model in nearly smooth flow, U=3.354 m/s, data obtained during decreasing velocity in steps

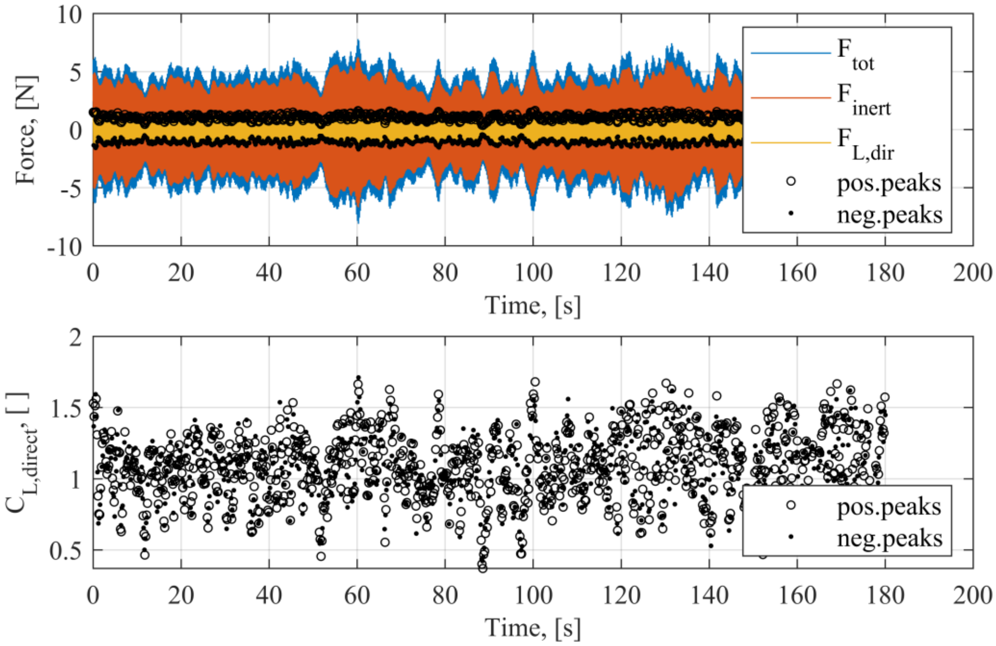

Figure 10.128 Forces (top) and lift coefficients (bottom) for smooth cylinder model in nearly smooth flow, U=3.254 m/s, data obtained during decreasing velocity in steps

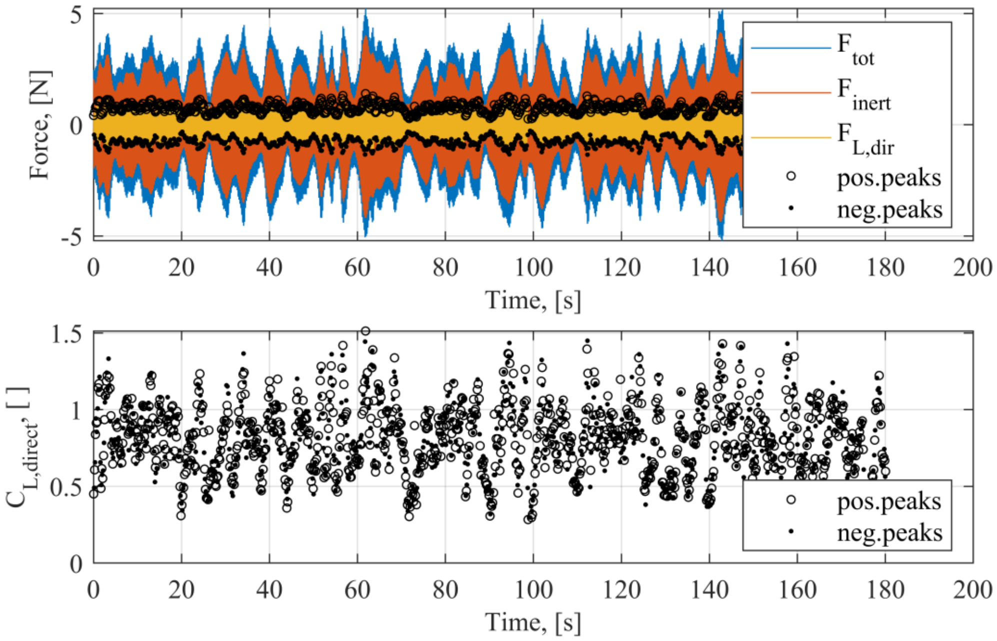

Figure 10.129 Forces (top) and lift coefficients (bottom) for smooth cylinder model in nearly smooth flow, U=3.158 m/s, data obtained during decreasing velocity in steps

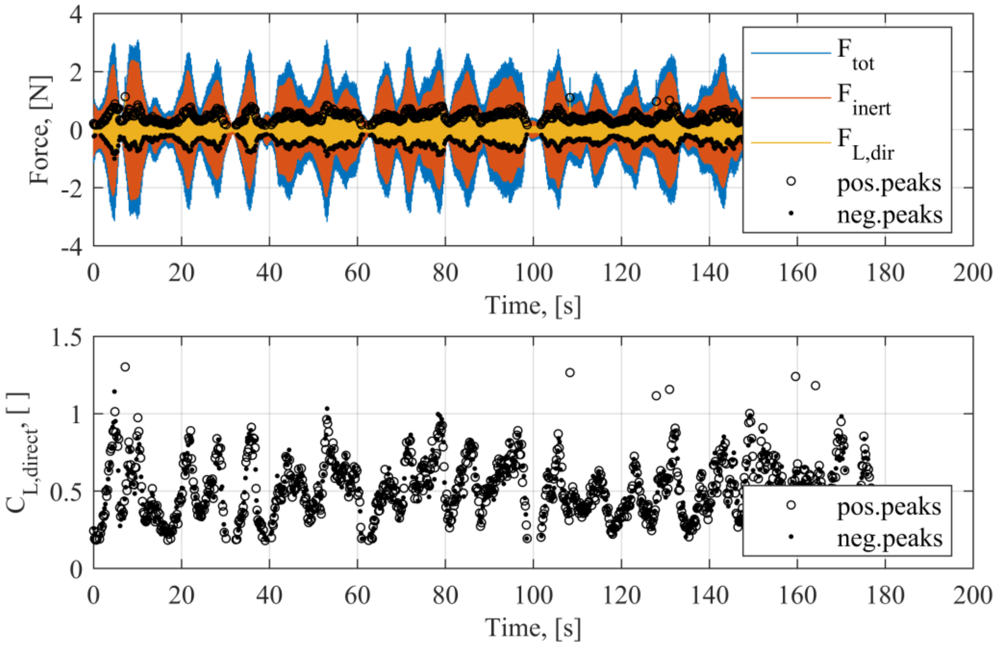

Figure 10.130 Forces (top) and lift coefficients (bottom) for smooth cylinder model in nearly smooth flow, U=3.065 m/s, data obtained during decreasing velocity in steps

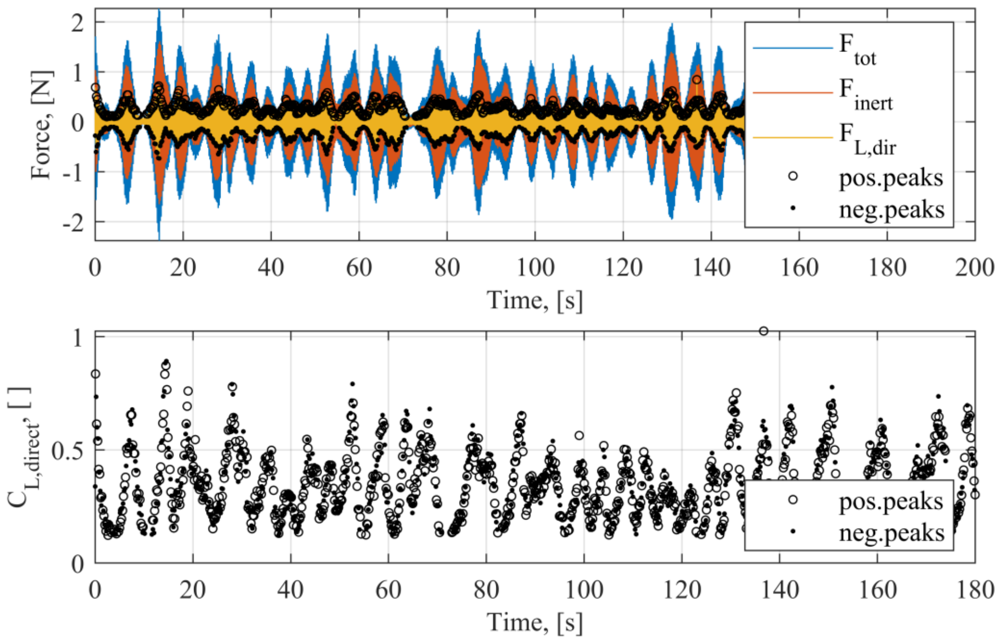

Figure 10.131 Forces (top) and lift coefficients (bottom) for smooth cylinder model in nearly smooth flow, U=2.976 m/s, data obtained during decreasing velocity in steps

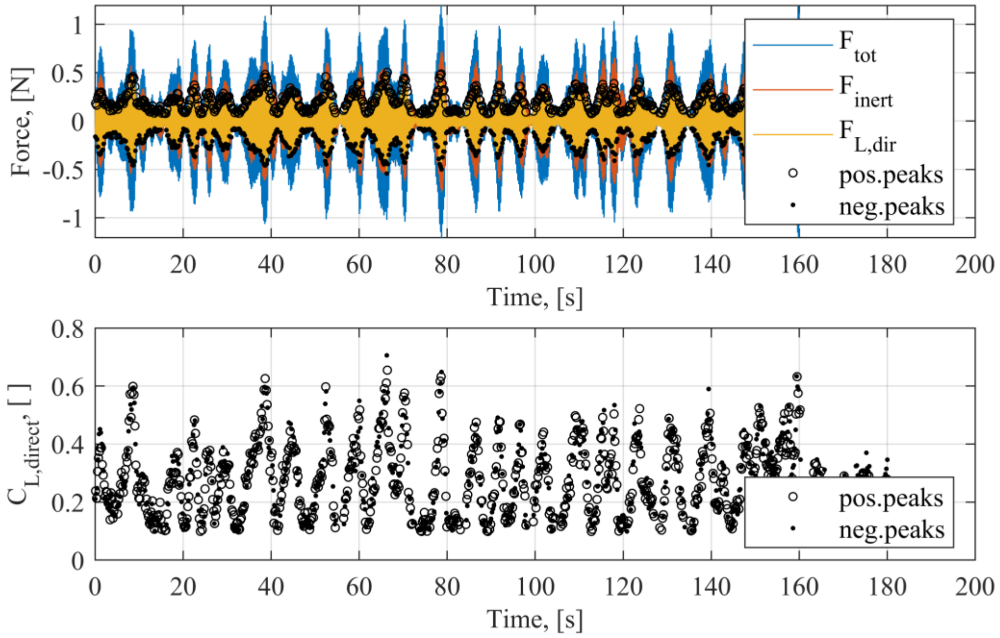

Figure 10.132 Forces (top) and lift coefficients (bottom) for smooth cylinder model in nearly smooth flow, U=2.880 m/s, data obtained during decreasing velocity in steps

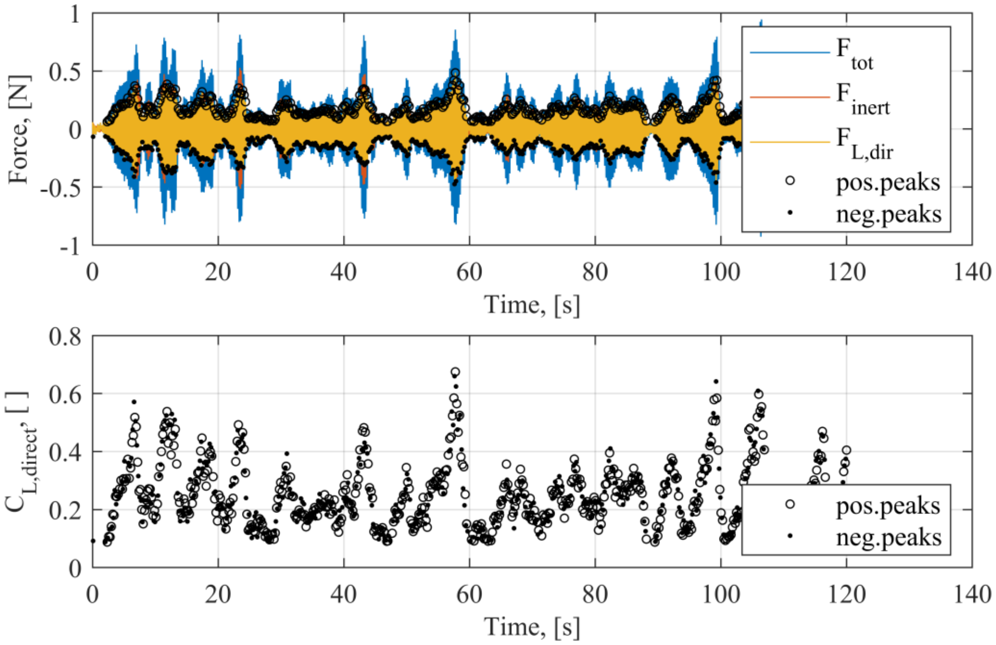

Figure 10.133 Forces (top) and lift coefficients (bottom) for smooth cylinder model in nearly smooth flow, U=2.782 m/s, data obtained during decreasing velocity in steps

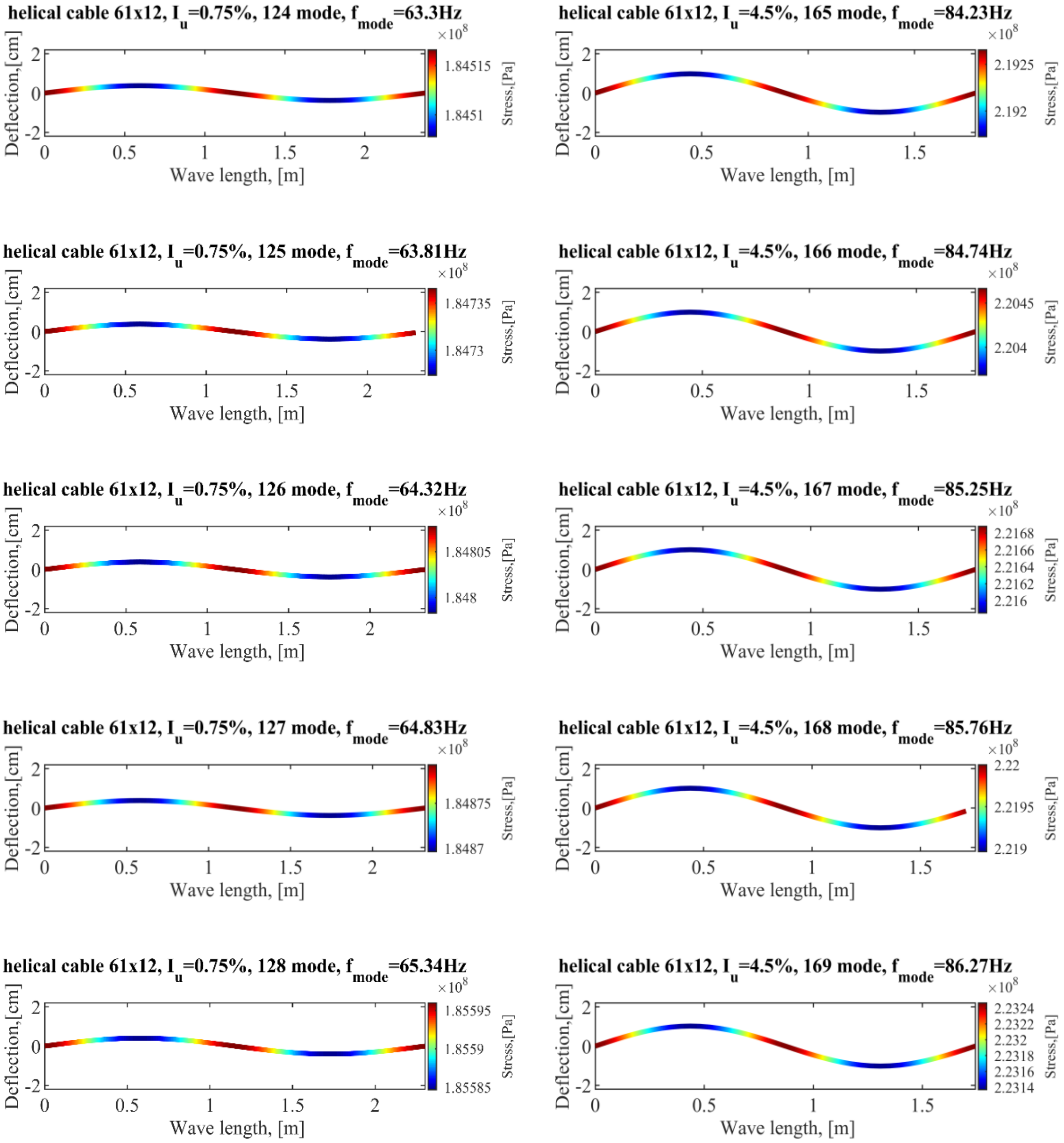

Figure 10.134 Stress distribution along wave, helical cable 1x61-12 in smooth flow I_u=0.75% (left), and in turbulent flow I_u=4.5% (right)

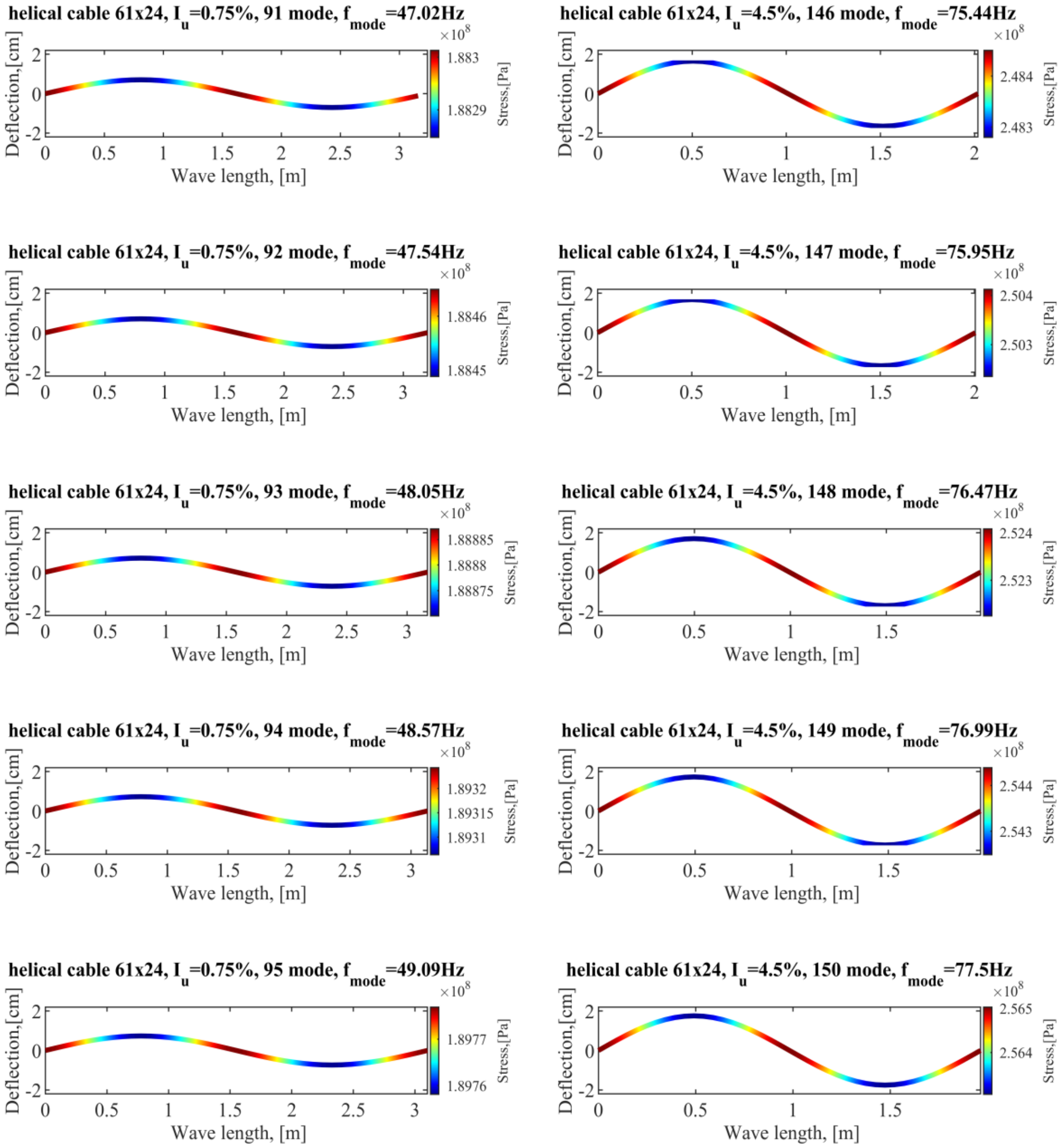

Figure 10.135 Stress distribution along wave, helical cable 1x61-24 in smooth flow I_u=0.75% (left), and in turbulent flow I_u=4.5% (right)

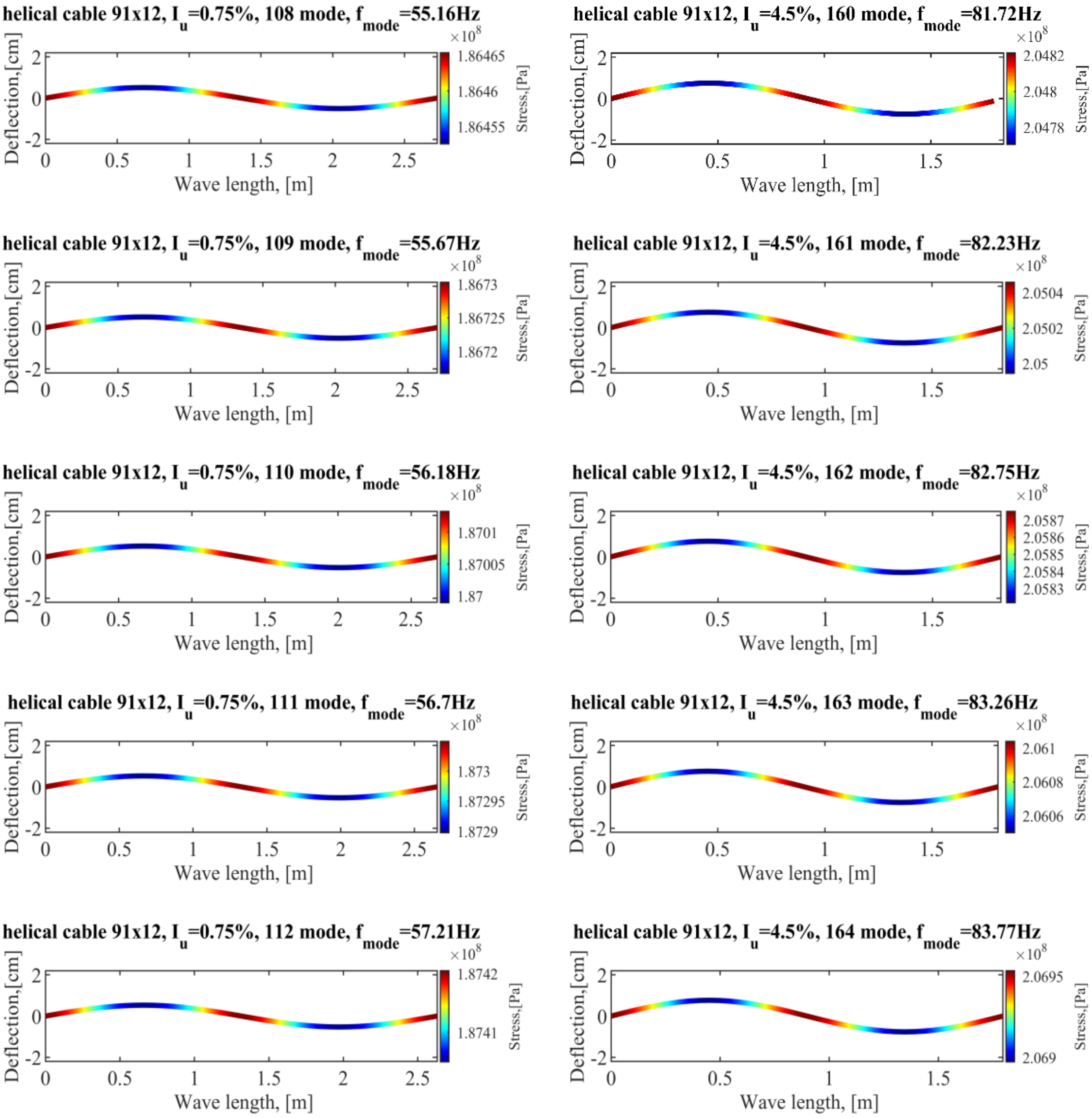

Figure 10.136 Stress distribution along wave, helical cable 91x24 in smooth flow I_u=0.75% (left), and in turbulent flow I_u=4.5% (right)

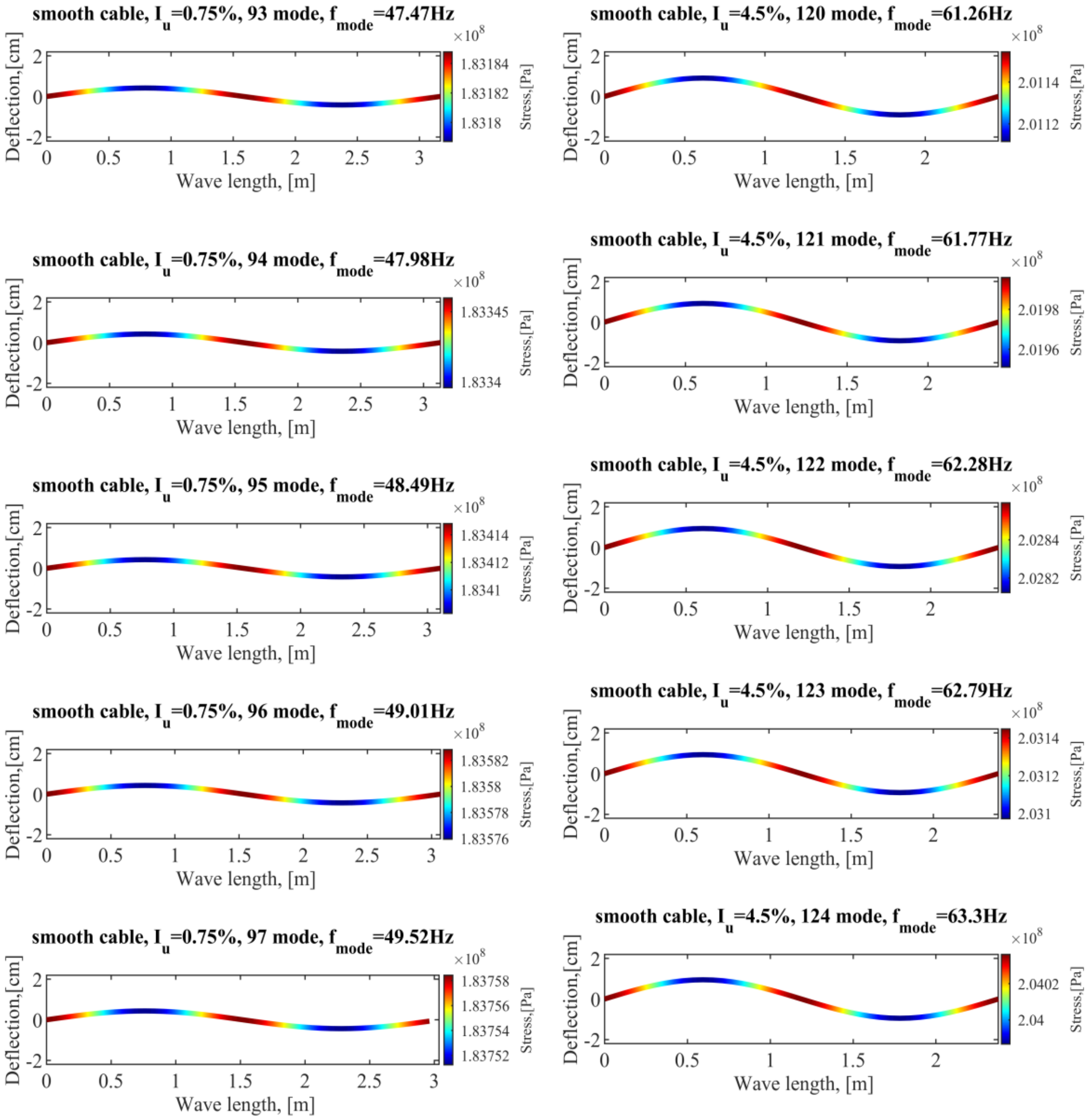

Figure 10.137 Stress distribution along wave, smooth surface cable in smooth flow I_u=0.75% (left), and in turbulent flow I_u=4.5% (right)

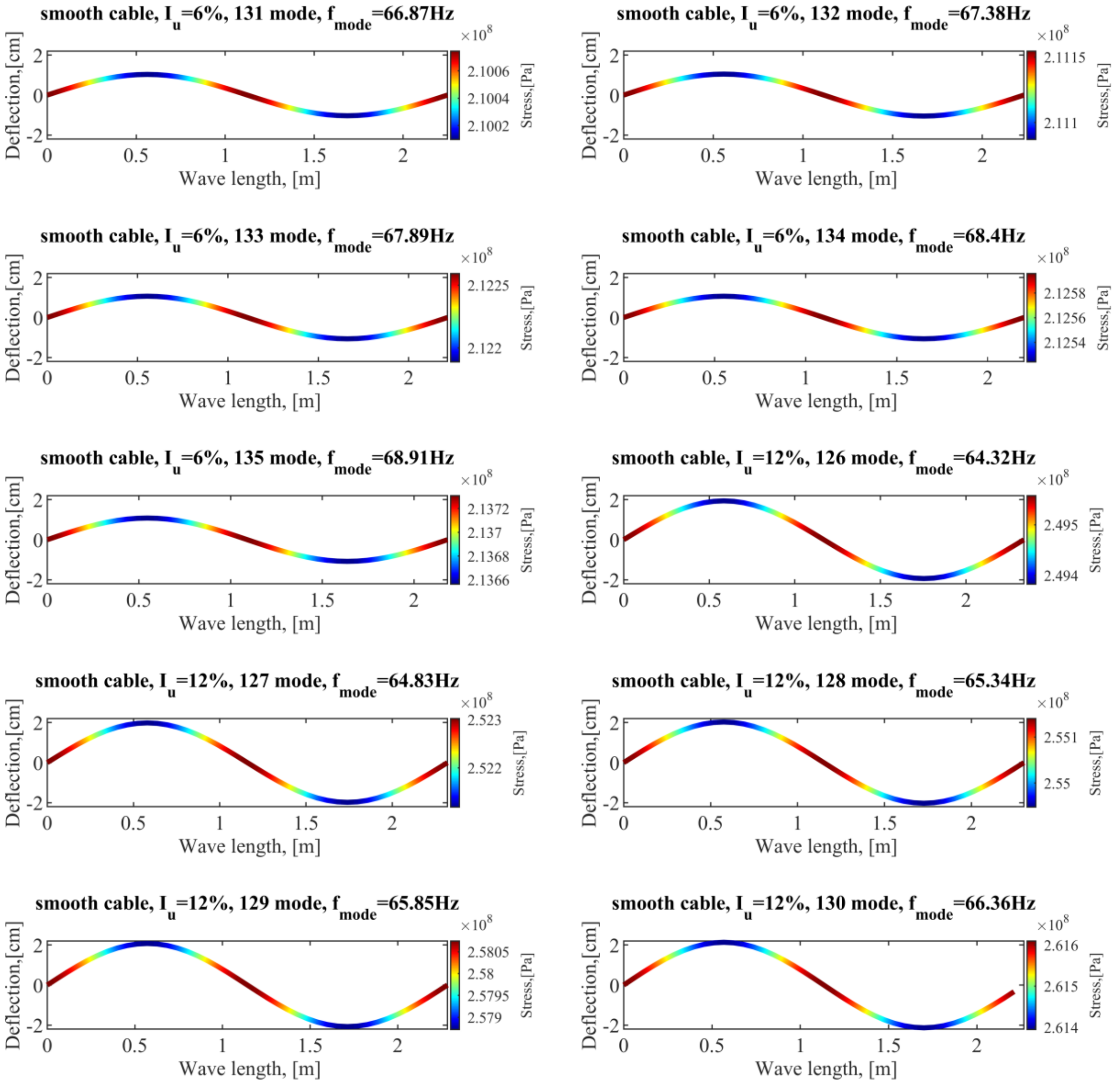

smooth cable, I_u=6%, 131 mode, f_{mode}=66.87Hz

smooth cable, I_u=6%, 132 mode, f_{mode}=67.38Hz

smooth cable, I_u=6%, 133 mode, f_{mode}=67.89Hz

smooth cable, I_u=6%, 134 mode, f_{mode}=68.4Hz

smooth cable, I_u=6%, 135 mode, f_{mode}=68.91Hz

smooth cable, I_u=12%, 126 mode, f_{mode}=64.32Hz

smooth cable, I_u=12%, 127 mode, f_{mode}=64.83Hz

smooth cable, I_u=12%, 128 mode, f_{mode}=65.34Hz

smooth cable, I_u=12%, 129 mode, f_{mode}=65.85Hz

smooth cable, I_u=12%, 130 mode, f_{mode}=66.36Hz

Figure 10.138 Stress distribution along wave, smooth surface cable in turbulent flow I_u=6.5% (left), and in turbulent flow I_u=12.3% (right)

11. Appendix B: Tables

Table 11.1 Fatigue damage for smooth surface cable, smooth flow Iu=0.75%, mode 93, fn=47.4738 Hz, Dmode=9.9858e-07

U_{red}	U, [m/s]	$U_{i,min}$	$U_{i,max}$	C_L	$y_{f,max}$, [m]	Stress range, [N/mm^2]	Probability	D_i
4.90	8.91	8.78	9.04	0.0676554	0.0008317	0.1337394	0.0160874	3.0248E-16
5.05	9.17	9.04	9.30	0.1268870	0.0014610	0.4114407	0.0168028	2.67841E-13
5.20	9.44	9.30	9.58	0.2088248	0.0024045	1.1058844	0.0174551	1.04914E-10
5.35	9.72	9.58	9.90	0.3271477	0.0037669	2.6680876	0.0199704	2.36723E-08
5.55	10.08	9.90	10.22	0.3443017	0.0041773	3.2599935	0.0203185	8.01394E-08
5.71	10.37	10.22	10.51	0.3020319	0.0036645	2.5287228	0.0175958	1.51171E-08
5.86	10.64	10.51	10.78	0.2875814	0.0034891	2.2983166	0.0170521	8.25829E-09
6.01	10.92	10.78	11.08	0.4049872	0.0050749	4.7353954	0.0188173	6.97186E-07
6.20	11.25	11.08	11.38	0.3603977	0.0044305	3.6515939	0.0178750	1.39249E-07
6.33	11.50	11.38	11.63	0.3087627	0.0037957	2.7078291	0.0153841	1.99275E-08
6.47	11.76	11.63	11.87	0.3015651	0.0037072	2.5864750	0.0141784	1.39486E-08
6.59	11.97	11.87	12.06	0.2445826	0.0030067	1.7176106	0.0115664	9.75887E-10

Table 11.2 Fatigue damage for smooth surface cable, smooth flow Iu=0.75%, mode 94, fn=47.9843 Hz, Dmode=1.3483e-06

U_{red}	U, [m/s]	$U_{i,min}$	$U_{i,max}$	C_L	$y_{f,max}$, [m]	Stress range, [N/mm^2]	Probability	D_i
4.90	9.00	8.87	9.13	0.067655385	0.000822091	0.133489674	0.016284604	3.06028E-16
5.05	9.27	9.13	9.40	0.126887017	0.001479027	0.430657755	0.016999331	3.60183E-13
5.20	9.54	9.40	9.69	0.208824782	0.002434114	1.157129302	0.017648839	1.40704E-10
5.35	9.83	9.69	10.01	0.327147721	0.003813316	2.789600591	0.020178758	3.15824E-08
5.55	10.19	10.01	10.33	0.34430171	0.004237503	3.421172283	0.020515344	1.09251E-07
5.71	10.48	10.33	10.62	0.3020319	0.003717266	2.65474065	0.017753479	2.06402E-08
5.86	10.76	10.62	10.90	0.287581393	0.003539416	2.413141493	0.017193274	1.1276E-08
6.01	11.04	10.90	11.20	0.404987215	0.005151003	4.971370789	0.018959384	9.50559E-07
6.20	11.37	11.20	11.50	0.360397747	0.004495809	3.833801367	0.017996094	1.89782E-07
6.33	11.63	11.50	11.76	0.308762723	0.003751824	2.702909432	0.015477214	2.00438E-08
6.47	11.88	11.76	11.99	0.301565082	0.003664364	2.581770169	0.014254828	1.40206E-08
6.59	12.10	11.99	12.19	0.244582563	0.002971961	1.71445804	0.011621859	9.80245E-10

Table 11.3 Fatigue damage for smooth surface cable, smooth flow Iu=0.75%, mode 95, fn=48.4948 Hz, Dmode=1.5444e-06

U_{red}	U, [m/s]	$U_{i,min}$	$U_{i,max}$	C_L	$y_{f,max}$, [m]	Stress range, [N/mm^2]	Probability	D_i
4.90	9.10	8.97	9.23	0.067655385	0.000821892	0.13627455	0.016478836	3.54249E-16
5.05	9.36	9.23	9.50	0.126887017	0.001478747	0.439659357	0.017192504	4.16803E-13
5.20	9.65	9.50	9.79	0.208824782	0.002433653	1.181121263	0.017838758	1.62564E-10
5.35	9.93	9.79	10.11	0.327147721	0.003812594	2.846429277	0.020382233	3.63871E-08
5.55	10.29	10.11	10.44	0.34430171	0.004236456	3.490017763	0.020706776	1.25595E-07
5.71	10.59	10.44	10.73	0.3020319	0.003716347	2.708594937	0.017906152	2.37334E-08
5.86	10.87	10.73	11.01	0.287581393	0.003538541	2.462221814	0.017329265	1.2961E-08
6.01	11.15	11.01	11.32	0.404987215	0.005149583	5.069571876	0.019095357	1.08805E-06
6.20	11.49	11.32	11.62	0.360397747	0.004494628	3.910504431	0.018111118	2.17388E-07
6.33	11.75	11.62	11.88	0.308762723	0.003750914	2.757738847	0.015564822	2.29804E-08
6.47	12.01	11.88	12.12	0.301565082	0.003663476	2.634209168	0.014325956	1.60664E-08
6.59	12.23	12.12	12.32	0.244582563	0.00297124	1.749606787	0.011672868	1.12386E-09

Table 11.4 Fatigue damage for smooth surface cable, smooth flow Iu=0.75%, mode 96, fn=49.0052 Hz, Dmode=2.1266e-06

U_{red}	U, [m/s]	$U_{i,min}$	$U_{i,max}$	C_L	$y_{f,max}$, [m]	Stress range, [N/mm^2]	Probability	D_i
4.90	9.19	9.06	9.33	0.067655385	0.000833543	0.143121395	0.016670049	4.85966E-16
5.05	9.46	9.33	9.61	0.126887017	0.001496717	0.45983904	0.017382205	5.57418E-13
5.20	9.75	9.61	9.89	0.208824782	0.002463227	1.234878828	0.018024731	2.16799E-10
5.35	10.04	9.89	10.22	0.327147721	0.004047519	3.261172827	0.020580774	8.39742E-08
5.55	10.40	10.22	10.55	0.34430171	0.004295955	3.658023702	0.020892738	1.69791E-07
5.71	10.71	10.55	10.85	0.3020319	0.003768542	2.840085044	0.01805373	3.21363E-08
5.86	10.98	10.85	11.13	0.287581393	0.003588239	2.582073449	0.017460006	1.75508E-08
6.01	11.27	11.13	11.44	0.404987215	0.005225992	5.317493255	0.019225193	1.47419E-06
6.20	11.61	11.44	11.74	0.360397747	0.004560211	4.102149767	0.018219987	2.94482E-07
6.33	11.87	11.74	12.01	0.308762723	0.003804089	2.892271989	0.015646887	3.10674E-08
6.47	12.14	12.01	12.25	0.301565082	0.003715411	2.76288941	0.014391784	2.17139E-08
6.59	12.36	12.25	12.45	0.244582563	0.003013362	1.835912023	0.011719422	1.52215E-09

Table 11.5 Fatigue damage for smooth surface cable, smooth flow Iu=0.75%, mode 97, fn=49.5157 Hz, Dmode=2.8692e-06

U_{red}	U, [m/s]	$U_{i,min}$	$U_{i,max}$	C_L	$y_{f,max}$, [m]	Stress range, [N/mm^2]	Probability	D_i
4.90	9.29	9.16	9.43	0.067655385	0.000845239	0.150237903	0.01685816	6.64399E-16
5.05	9.56	9.43	9.71	0.126887017	0.001514676	0.480699079	0.017568352	7.4287E-13
5.20	9.85	9.71	9.99	0.208824782	0.002492784	1.290406194	0.018206675	2.88092E-10
5.35	10.14	9.99	10.33	0.327147721	0.004104084	3.417400227	0.020774293	1.13408E-07
5.55	10.51	10.33	10.66	0.34430171	0.004356683	3.833678295	0.021073147	2.2928E-07
5.71	10.82	10.66	10.96	0.3020319	0.003821814	2.977681282	0.018196148	4.34701E-08
5.86	11.10	10.96	11.24	0.287581393	0.003638962	2.707524064	0.017585445	2.37427E-08
6.01	11.39	11.24	11.56	0.404987215	0.005302825	5.57383794	0.019348841	1.98849E-06
6.20	11.73	11.56	11.87	0.360397747	0.004626103	4.300731175	0.018322665	3.9736E-07
6.33	12.00	11.87	12.13	0.308762723	0.003857464	3.03170844	0.01572339	4.1842E-08
6.47	12.26	12.13	12.38	0.301565082	0.003767542	2.896276846	0.014452301	2.92361E-08
6.59	12.49	12.38	12.58	0.244582563	0.003055642	1.925460142	0.011761519	2.05406E-09

Table 11.6 Fatigue damage for smooth surface cable, turbulent flow Iu=4.5%, mode 120, fn=61.2565 Hz, Dmode=0.0080306

U_{red}	U, [m/s]	$U_{i,min}$	$U_{i,max}$	C_L	$y_{f,max}$, [m]	Stress range, [N/mm^2]	Probability	D_i
4.06	9.52	9.32	9.61	0.122521081	0.001156461	0.429097742	0.01856532	4.9135E-13
4.14	9.71	9.61	9.77	0.260532813	0.002459136	1.908916799	0.010057351	2.06327E-09
4.20	9.84	9.77	9.93	0.331071866	0.003124946	3.044550016	0.009787448	3.30491E-08
4.28	10.02	9.93	10.06	0.582897123	0.006229152	11.10154566	0.008327096	6.60915E-05
4.31	10.11	10.06	10.26	0.698767308	0.007926818	16.93173818	0.012323797	0.001231134
4.44	10.41	10.26	10.47	0.769631227	0.009069143	21.22973801	0.012964337	0.005032336
4.49	10.52	10.47	10.67	0.68907605	0.007877102	16.75070402	0.012555493	0.001175936
4.62	10.82	10.67	10.87	0.614644187	0.006761749	12.84618377	0.012686545	0.000241735
4.66	10.93	10.87	11.03	0.533065877	0.00562925	9.244487967	0.009400248	2.48764E-05
4.75	11.12	11.03	11.16	0.643041263	0.007071548	13.89863732	0.008456686	0.000258455
4.78	11.21	11.16	11.28	0.122804488	0.001350485	0.584157467	0.00718617	1.21068E-12

Table 11.7 Fatigue damage for smooth surface cable, turbulent flow Iu=4.5%, mode 121, fn=61.767 Hz, Dmode=0.010306

U_{red}	U, [m/s]	$U_{i,min}$	$U_{i,max}$	C_L	$y_{f,max}$, [m]	Stress range, [N/mm^2]	Probability	D_i
4.06	9.60	9.40	9.69	0.122521081	0.001168887	0.445623318	0.01872467	6.2687E-13
4.14	9.79	9.69	9.86	0.260532813	0.002485558	1.981226325	0.010139704	2.62171E-09
4.20	9.92	9.86	10.01	0.331071866	0.003158521	3.158466689	0.009864855	4.18701E-08
4.28	10.10	10.01	10.15	0.582897123	0.006314142	11.54408648	0.008390795	8.49016E-05
4.31	10.19	10.15	10.35	0.698767308	0.008043459	17.60523673	0.012414366	0.00158027
4.44	10.50	10.35	10.55	0.769631227	0.009208912	22.07115585	0.013054749	0.006451707
4.49	10.61	10.55	10.76	0.68907605	0.007995722	17.42802918	0.012638195	0.001514016
4.62	10.91	10.76	10.96	0.614644187	0.006859215	13.36818548	0.012765141	0.00031147
4.66	11.02	10.96	11.12	0.533065877	0.005706342	9.620283831	0.009455194	3.20445E-05
4.75	11.21	11.12	11.26	0.643041263	0.007171512	14.45134918	0.008503678	0.000331141
4.78	11.30	11.26	11.37	0.122804488	0.001369576	0.61066593	0.007224258	1.60166E-12

Table 11.8 Fatigue damage for smooth surface cable, turbulent flow Iu=4.5%, mode 122, fn=62.2775 Hz, Dmode=0.013182

U_{red}	U, [m/s]	$U_{i,min}$	$U_{i,max}$	C_L	$y_{f,max}$, [m]	Stress range, [N/mm^2]	Probability	D_i
4.06	9.68	9.47	9.78	0.122521081	0.001181304	0.462608637	0.018881546	7.97719E-13
4.14	9.87	9.78	9.94	0.260532813	0.002511962	2.055455551	0.010220618	3.32243E-09
4.20	10.00	9.94	10.10	0.331071866	0.003192074	3.275309081	0.009940796	5.29011E-08
4.28	10.19	10.10	10.23	0.582897123	0.006399572	11.99856805	0.008453196	0.000108725
4.31	10.27	10.23	10.43	0.698767308	0.008161004	18.2965238	0.01250293	0.002021871
4.44	10.59	10.43	10.64	0.769631227	0.009349986	22.93447567	0.013142944	0.008244335
4.49	10.70	10.64	10.85	0.68907605	0.008115405	18.12404524	0.012718645	0.001943129
4.62	11.00	10.85	11.05	0.614644187	0.00695743	13.90496179	0.012841359	0.000400092
4.66	11.11	11.05	11.21	0.533065877	0.005783898	10.00687595	0.009508313	4.11552E-05
4.75	11.31	11.21	11.35	0.643041263	0.00727212	15.01878144	0.008548979	0.000422914
4.78	11.39	11.35	11.47	0.122804488	0.001388789	0.638147677	0.007260874	2.11371E-12

Table 11.9 Fatigue damage for smooth surface cable, turbulent flow Iu=4.5%, mode 123, fn=62.7879 Hz, Dmode=0.014428

U_{red}	U, [m/s]	$U_{i,min}$	$U_{i,max}$	C_L	$y_{f,max}$, [m]	Stress range, [N/mm^2]	Probability	D_i
4.06	9.76	9.55	9.86	0.122521081	0.001181013	0.46995368	0.019035906	8.91208E-13
4.14	9.95	9.86	10.02	0.260532813	0.002511344	2.087529809	0.010300072	3.70435E-09
4.20	10.09	10.02	10.18	0.331071866	0.003191289	3.325762712	0.010015251	5.88959E-08
4.28	10.27	10.18	10.31	0.582897123	0.00639694	12.16500797	0.008514283	0.000119922
4.31	10.36	10.31	10.52	0.698767308	0.008156858	18.53444934	0.012589464	0.002217996
4.44	10.67	10.52	10.73	0.769631227	0.009344595	23.21997067	0.013228898	0.009010918
4.49	10.78	10.73	10.94	0.68907605	0.008111004	18.35898103	0.012796822	0.002129457
4.62	11.09	10.94	11.15	0.614644187	0.006954081	14.09298572	0.01291518	0.000439738
4.66	11.20	11.15	11.30	0.533065877	0.005781487	10.14807767	0.009559591	4.53751E-05
4.75	11.40	11.30	11.44	0.643041263	0.007268816	15.22070092	0.008592578	0.000464309
4.78	11.49	11.44	11.56	0.122804488	0.001388159	0.647992827	0.00729601	2.34737E-12

Table 11.10 Fatigue damage for smooth surface cable, turbulent flow Iu=4.5%, mode 124, fn=63.2984 Hz, Dmode=0.018369

U_{red}	U, [m/s]	$U_{i,min}$	$U_{i,max}$	C_L	$y_{f,max}$, [m]	Stress range, [N/mm^2]	Probability	D_i
4.06	9.84	9.63	9.94	0.122521081	0.001193416	0.487615886	0.01918771	1.13001E-12
4.14	10.03	9.94	10.10	0.260532813	0.002537719	2.164583145	0.010378045	4.67685E-09
4.20	10.17	10.10	10.26	0.331071866	0.003224804	3.44689591	0.0100882	7.41267E-08
4.28	10.35	10.26	10.40	0.582897123	0.006482732	12.63568777	0.00857404	0.000152887
4.31	10.44	10.40	10.60	0.698767308	0.008275165	19.24907286	0.012673947	0.002824637
4.44	10.76	10.60	10.82	0.769631227	0.009486778	24.11142946	0.013312589	0.0114602
4.49	10.87	10.82	11.02	0.68907605	0.008231594	19.07929262	0.012872706	0.002720416
4.62	11.18	11.02	11.24	0.614644187	0.007052933	14.64933479	0.012986585	0.000562334
4.66	11.29	11.24	11.39	0.533065877	0.005859431	10.54929758	0.009609017	5.80246E-05
4.75	11.49	11.39	11.54	0.643041263	0.007369961	15.80778295	0.008634465	0.000590273
4.78	11.58	11.54	11.66	0.122804488	0.001407475	0.676812226	0.007329658	3.08663E-12

Table 11.11 Fatigue damage for smooth surface cable, turbulent flow Iu=6.5%, mode 131, fn=66.8717 Hz, Dmode=0.049152

U_{red}	U, [m/s]	$U_{i,min}$	$U_{i,max}$	C_L	$y_{f,max}$, [m]	Stress range, $[N/mm^2]$	Probability	D_i
3.74	9.56	9.49	9.70	0.112727448	0.000982203	0.369117938	0.012764692	1.49432E-13
3.84	9.83	9.70	9.85	0.249805412	0.002176575	1.784598332	0.009725151	1.45405E-09
3.86	9.87	9.85	9.98	0.438680674	0.00382226	5.297866892	0.008279184	8.47296E-07
3.95	10.10	9.98	10.20	0.553159439	0.005276048	9.637871807	0.013821829	5.12736E-05
4.03	10.31	10.20	10.37	0.782689486	0.008279995	21.11319119	0.010129984	0.004153111
4.07	10.42	10.37	10.45	0.86792276	0.009623576	26.94244608	0.005520635	0.009773558
4.10	10.49	10.45	10.62	0.910580276	0.010337389	30.14963116	0.010106633	0.035135006
4.20	10.75	10.62	10.79	0.529916129	0.005189376	9.351918826	0.011025524	3.41386E-05
4.24	10.84	10.79	10.84	0.436911074	0.004025574	5.842404245	0.002966939	5.46135E-07
4.24	10.84	10.84	10.90	0.498201833	0.00464914	7.645439402	0.003603129	3.3307E-06
11.28	28.85	26.65	30.28	0.085736958	0.000800084	0.245260669	0.014834493	1.49445E-14
12.40	31.71	30.28	31.90	0.100958976	0.000942133	0.339725359	0.003048962	2.16951E-14

Table 11.12 Fatigue damage for smooth surface cable, turbulent flow Iu=6.5%, mode 132, fn=67.3822 Hz, Dmode=0.061553

U_{red}	U, [m/s]	$U_{i,min}$	$U_{i,max}$	C_L	$y_{f,max}$, [m]	Stress range, $[N/mm^2]$	Probability	D_i
3.74	9.63	9.57	9.77	0.112727448	0.000992067	0.382284573	0.012862547	1.87237E-13
3.84	9.91	9.77	9.93	0.249805412	0.002198432	1.847255855	0.009796913	1.8155E-09
3.86	9.94	9.93	10.06	0.438680674	0.004045762	5.982653318	0.008338341	1.78315E-06
3.95	10.17	10.06	10.28	0.553159439	0.005335328	9.971685456	0.013916552	6.38098E-05
4.03	10.39	10.28	10.44	0.782689486	0.008394436	21.86926656	0.01019614	0.005202179
4.07	10.50	10.44	10.53	0.86792276	0.009765533	27.90827246	0.005555506	0.01224237
4.10	10.57	10.53	10.70	0.910580276	0.010494641	31.22972181	0.010168275	0.04399468
4.20	10.83	10.70	10.88	0.529916129	0.005257897	9.710913278	0.011089481	4.33726E-05
4.24	10.92	10.88	10.92	0.436911074	0.00407395	6.061242094	0.002983554	6.89998E-07
4.24	10.92	10.92	10.98	0.498201833	0.004704799	7.926242001	0.003622965	4.18998E-06
11.28	29.07	26.85	30.51	0.085736958	0.000809662	0.254990186	0.014108911	1.80875E-14
12.40	31.95	30.51	32.15	0.100958976	0.000953412	0.353187931	0.002859993	2.58907E-14

Table 11.13 Fatigue damage for smooth surface cable, turbulent flow Iu=6.5%, mode 133, fn=67.8927 Hz, Dmode=0.076866

U_{red}	U, [m/s]	$U_{i,min}$	$U_{i,max}$	C_L	$y_{f,max}$, [m]	Stress range, [N/mm^2]	Probability	D_i
3.74	9.70	9.64	9.84	0.112727448	0.001001923	0.395788636	0.012958919	2.34083E-13
3.84	9.98	9.84	10.00	0.249805412	0.002220274	1.911451921	0.009867481	2.26156E-09
3.86	10.02	10.00	10.14	0.438680674	0.004092366	6.200025491	0.008396439	2.24119E-06
3.95	10.25	10.14	10.36	0.553159439	0.005400006	10.33123962	0.014009422	8.00491E-05
4.03	10.47	10.36	10.52	0.782689486	0.008509858	22.64323286	0.010260872	0.006498853
4.07	10.58	10.52	10.61	0.86792276	0.009908824	28.89613523	0.005589577	0.015291122
4.10	10.65	10.61	10.78	0.910580276	0.010653543	32.33450845	0.01022841	0.054932275
4.20	10.91	10.78	10.96	0.529916129	0.005326904	10.07993577	0.01115173	5.49681E-05
4.24	11.01	10.96	11.01	0.436911074	0.004122515	6.285978613	0.002999699	8.69635E-07
4.24	11.01	11.01	11.07	0.498201833	0.004760633	8.210969419	0.003642222	5.24511E-06
11.28	29.29	27.05	30.74	0.085736958	0.000819271	0.265019327	0.013410919	2.18346E-14
12.40	32.20	30.74	32.39	0.100958976	0.000964727	0.367063615	0.002680828	3.08133E-14

Table 11.14 Fatigue damage for smooth surface cable, turbulent flow Iu=6.5%, mode 134, fn=68.4031 Hz, Dmode=0.082958

U_{red}	U, [m/s]	$U_{i,min}$	$U_{i,max}$	C_L	$y_{f,max}$, [m]	Stress range, [N/mm^2]	Probability	D_i
3.74	9.78	9.71	9.92	0.112727448	0.001001654	0.401521656	0.013053785	2.58979E-13
3.84	10.06	9.92	10.08	0.249805412	0.002219678	1.938683591	0.009936841	2.49784E-09
3.86	10.09	10.08	10.21	0.438680674	0.004090957	6.283693455	0.008453467	2.46377E-06
3.95	10.33	10.21	10.44	0.553159439	0.005397852	10.46423233	0.01410042	8.76499E-05
4.03	10.55	10.44	10.60	0.782689486	0.008505005	22.90075838	0.010324164	0.007050649
4.07	10.66	10.60	10.69	0.86792276	0.009902079	29.20601917	0.005622839	0.016522086
4.10	10.73	10.69	10.86	0.910580276	0.010645655	32.67089046	0.010287023	0.059228478
4.20	10.99	10.86	11.04	0.529916129	0.005324199	10.20797975	0.011212256	6.0063E-05
4.24	11.09	11.04	11.09	0.436911074	0.004120939	6.370279334	0.00301537	9.5404E-07
4.24	11.09	11.09	11.15	0.498201833	0.004758849	8.31912614	0.003660898	5.74551E-06
11.28	29.51	27.26	30.97	0.085736958	0.000818964	0.268807015	0.012739981	2.27556E-14
12.40	32.44	30.97	32.63	0.100958976	0.000964365	0.372303323	0.002511104	3.16608E-14

Table 11.15 Fatigue damage for smooth surface cable, turbulent flow Iu=6.5%, mode 135, fn=68.9136 Hz, Dmode=0.10317

U_{red}	U, [m/s]	$U_{i,min}$	$U_{i,max}$	C_L	$y_{f,max}$, [m]	Stress range, [N/mm^2]	Probability	D_i
3.74	9.85	9.78	9.99	0.112727448	0.001011498	0.415522354	0.013147123	3.22776E-13
3.84	10.13	9.99	10.15	0.249805412	0.002241492	2.00513491	0.010004976	3.10157E-09
3.86	10.17	10.15	10.29	0.438680674	0.004137634	6.508651741	0.00850941	3.08567E-06
3.95	10.41	10.29	10.51	0.553159439	0.005462704	10.83557341	0.014189524	0.000109543
4.03	10.62	10.51	10.68	0.782689486	0.00862108	23.69693785	0.010386002	0.008772145
4.07	10.74	10.68	10.77	0.86792276	0.010046452	30.22143875	0.005655286	0.020551779
4.10	10.81	10.77	10.94	0.910580276	0.010805903	33.80613319	0.010344101	0.073649493
4.20	11.07	10.94	11.12	0.529916129	0.0053936	10.59029171	0.011271048	7.58431E-05
4.24	11.17	11.12	11.17	0.436911074	0.00416965	6.603155374	0.003030563	1.19822E-06
4.24	11.17	11.17	11.23	0.498201833	0.004814813	8.616379605	0.003678987	7.18094E-06
11.28	29.73	27.46	31.20	0.085736958	0.000828595	0.279256404	0.012095537	2.7362E-14
12.40	32.68	31.20	32.88	0.100958976	0.000975706	0.386759313	0.002350462	3.75234E-14

Table 11.16 Fatigue damage for smooth surface cable, turbulent flow Iu=12.3%, mode 126, fn=64.3194 Hz, Dmode=15.9922

U_{red}	U, [m/s]	$U_{i,min}$	$U_{i,max}$	C_L	$y_{f,max}$, [m]	Stress range, [N/mm^2]	Probability	D_i
3.23	7.96	7.88	8.00	0.932413427	0.011753407	34.58773608	0.007150236	0.054499683
3.27	8.04	8.00	8.12	0.822113434	0.008922825	22.39695801	0.007279482	0.004090491
3.33	8.19	8.12	8.28	1.104465911	0.013174164	40.99024443	0.01009562	0.213185086
3.40	8.37	8.28	8.50	1.337582083	0.019904989	72.00960112	0.013247515	8.222760175
3.51	8.62	8.50	8.70	1.312307767	0.019389823	69.63244671	0.012478218	6.332326495
3.57	8.77	8.70	8.87	1.161887177	0.015885003	53.42219521	0.010808557	1.118507395
3.65	8.97	8.87	9.08	0.920404903	0.01078177	30.29879631	0.012900767	0.044433299
3.73	9.18	9.08	9.41	0.741742132	0.007596581	17.11287044	0.021140215	0.002363673
3.92	9.64	9.41	9.66	0.538699339	0.004937707	7.952597439	0.015301839	1.72321E-05
3.93	9.67	9.66	9.70	0.491057012	0.004342806	6.26233067	0.002725794	7.31897E-07
3.96	9.73	9.70	9.84	0.455144278	0.003958175	5.258158202	0.008774199	8.25563E-07

Table 11.17 Fatigue damage for smooth surface cable, turbulent flow Iu=12.3%, mode 127, fn=64.8298 Hz, Dmode=20.4768

U_{red}	U, [m/s]	$U_{i,min}$	$U_{i,max}$	C_L	$y_{f,max}$, [m]	Stress range, [N/mm^2]	Probability	D_i
3.23	8.02	7.94	8.06	0.932413427	0.011901849	35.67257512	0.007225124	0.066807624
3.27	8.10	8.06	8.18	0.822113434	0.00904139	23.18282851	0.007354532	0.005123037
3.33	8.26	8.18	8.35	1.104465911	0.01337851	42.40548914	0.010197689	0.266077523
3.40	8.44	8.35	8.56	1.337582083	0.020347591	74.79276108	0.013377849	10.50794126
3.51	8.69	8.56	8.77	1.312307767	0.019827391	72.37734539	0.01259718	8.125745272
3.57	8.84	8.77	8.94	1.161887177	0.01622549	55.59123461	0.010908565	1.44470603
3.65	9.04	8.94	9.15	0.920404903	0.010975465	31.52919864	0.013016377	0.057377509
3.73	9.26	9.15	9.49	0.741742132	0.007704916	17.76720537	0.021320623	0.00300946
3.92	9.72	9.49	9.73	0.538699339	0.004995238	8.240359357	0.015425235	2.16712E-05
3.93	9.75	9.73	9.78	0.491057012	0.004389481	6.484331078	0.002747129	9.16313E-07
3.96	9.81	9.78	9.92	0.455144278	0.00399947	5.443213316	0.008841526	1.03189E-06

Table 11.18 Fatigue damage for smooth surface cable, turbulent flow Iu=12.3%, mode 128, fn=65.3403 Hz, Dmode=26.1793

U_{red}	U, [m/s]	$U_{i,min}$	$U_{i,max}$	C_L	$y_{f,max}$, [m]	Stress range, [N/mm^2]	Probability	D_i
3.23	8.08	8.01	8.13	0.932413427	0.012050775	36.7746339	0.00729958	0.081652262
3.27	8.17	8.13	8.25	0.822113434	0.00916077	23.98600578	0.007429107	0.006398298
3.33	8.32	8.25	8.41	1.104465911	0.013585696	43.85349492	0.010299045	0.331285494
3.40	8.50	8.41	8.63	1.337582083	0.020803492	77.66495709	0.013507147	13.40585377
3.51	8.76	8.63	8.84	1.312307767	0.020279064	75.21561733	0.012715064	10.41230549
3.57	8.91	8.84	9.01	1.161887177	0.016577207	57.83989771	0.011007559	1.863958844
3.65	9.11	9.01	9.22	0.920404903	0.011174653	32.80556884	0.013130681	0.074020648
3.73	9.33	9.22	9.56	0.741742132	0.007815226	18.44278943	0.021498662	0.003826056
3.92	9.80	9.56	9.81	0.538699339	0.005053241	8.539122262	0.015546743	2.72583E-05
3.93	9.83	9.81	9.86	0.491057012	0.004436337	6.712028865	0.002768112	1.14469E-06
3.96	9.89	9.86	10.00	0.455144278	0.004040869	5.632911818	0.008907691	1.28689E-06

Table 11.19 Fatigue damage for smooth surface cable, turbulent flow Iu=12.3%, mode 129, fn=65.8508 Hz, Dmode=33.4194

U_{red}	U, [m/s]	$U_{i,min}$	$U_{i,max}$	C_L	$y_{f,max}$, [m]	Stress range, [N/mm^2]	Probability	D_i
3.23	8.14	8.07	8.19	0.932413427	0.012200173	37.89367466	0.007373589	0.099503689
3.27	8.23	8.19	8.31	0.822113434	0.009280961	24.80646947	0.007503194	0.007968854
3.33	8.39	8.31	8.48	1.104465911	0.013795775	45.33461248	0.010399666	0.411489513
3.40	8.57	8.48	8.70	1.337582083	0.02127309	80.62819273	0.013635382	17.07453179
3.51	8.83	8.70	8.90	1.312307767	0.020745335	78.14972987	0.012831843	13.32336334
3.57	8.98	8.90	9.08	1.161887177	0.016940658	60.17094744	0.011105516	2.40225879
3.65	9.18	9.08	9.29	0.920404903	0.011379633	34.12985669	0.01324365	0.095405722
3.73	9.40	9.29	9.64	0.741742132	0.007927622	19.14037499	0.021674289	0.00485744
3.92	9.87	9.64	9.89	0.538699339	0.005111739	8.846268033	0.015666332	3.42206E-05
3.93	9.90	9.89	9.93	0.491057012	0.004483378	6.945496682	0.002788737	1.42688E-06
3.96	9.96	9.93	10.08	0.455144278	0.004082372	5.827303724	0.008972676	1.60136E-06

Table 11.20 Fatigue damage for smooth surface cable, turbulent flow Iu=12.3%, mode 130, fn=66.3612 Hz, Dmode=44.5324

U_{red}	U, [m/s]	$U_{i,min}$	$U_{i,max}$	C_L	$y_{f,max}$, [m]	Stress range, [N/mm^2]	Probability	D_i
3.23	8.21	8.13	8.25	0.932413427	0.012350026	39.03031501	0.007447135	0.12092474
3.27	8.30	8.25	8.38	0.822113434	0.009401961	25.64465776	0.007576776	0.00989873
3.33	8.45	8.38	8.54	1.104465911	0.0140088	46.85049859	0.01049953	0.509998333
3.40	8.64	8.54	8.77	1.337582083	0.021917947	84.44606265	0.013762525	22.9238805
3.51	8.90	8.77	8.97	1.312307767	0.02133301	81.68614978	0.012947491	17.66809703
3.57	9.05	8.97	9.15	1.161887177	0.017369376	62.84155849	0.011202414	3.168888016
3.65	9.25	9.15	9.37	0.920404903	0.011607178	35.58079447	0.013355258	0.124468577
3.73	9.48	9.37	9.71	0.741742132	0.008045908	19.87632355	0.021847462	0.006187724
3.92	9.95	9.71	9.96	0.538699339	0.005171239	9.163713578	0.015783972	4.29298E-05
3.93	9.98	9.96	10.01	0.491057012	0.00453068	7.185177743	0.002809002	1.77538E-06
3.96	10.04	10.01	10.15	0.455144278	0.00412399	6.026585646	0.009036465	1.98857E-06

Table 11.21 Fatigue damage for helical cable 1x61-12, smooth flow Iu=0.75%, mode 124, fn=63.2984 Hz, Dmode=7.7142e-07

U_{red}	U, [m/s]	$U_{i,min}$	$U_{i,max}$	C_L	$y_{f,max}$, [m]	Stress range, [N/mm^2]	Probability	D_i
4.95	11.99	11.85	12.17	0.508371647	0.003745117	4.591789184	0.018580414	7.63025E-07
5.10	12.34	12.17	12.41	0.349967097	0.002578169	2.232479413	0.014314833	7.76431E-09
5.15	12.48	12.41	12.61	0.287165776	0.002115518	1.515000964	0.011700757	6.19845E-10
5.26	12.74	12.61	12.86	0.193706532	0.001427014	0.695590555	0.014275768	7.08457E-12

Table 11.22 Fatigue damage for helical cable 1x61-12, smooth flow Iu=0.75%, mode 125, fn=63.8089 Hz, Dmode=1.0335e-06

U_{red}	U, [m/s]	$U_{i,min}$	$U_{i,max}$	C_L	$y_{f,max}$, [m]	Stress range, [N/mm^2]	Probability	D_i
4.95	12.09	11.95	12.26	0.508371647	0.003807642	4.81181719	0.018646126	1.02217E-06
5.10	12.44	12.26	12.51	0.349967097	0.002621211	2.342227432	0.014357019	1.04693E-08
5.15	12.58	12.51	12.71	0.287165776	0.002150837	1.590076352	0.011729602	8.37281E-10
5.26	12.85	12.71	12.96	0.193706532	0.001450838	0.730382597	0.01430388	9.5904E-12

Table 11.23 Fatigue damage for helical cable 1x61-12, smooth flow Iu=0.75%, mode 126, fn=64.3194 Hz, Dmode=1.1414e-06

U_{red}	U, [m/s]	$U_{i,min}$	$U_{i,max}$	C_L	$y_{f,max}$, [m]	Stress range, [N/mm^2]	Probability	D_i
4.95	12.18	12.04	12.36	0.508371647	0.003806682	4.882960772	0.018707793	1.12892E-06
5.10	12.54	12.36	12.61	0.349967097	0.00262055	2.377705533	0.01439597	1.15806E-08
5.15	12.68	12.61	12.81	0.287165776	0.002150294	1.614354773	0.01175573	9.2637E-10
5.26	12.95	12.81	13.07	0.193706532	0.001450472	0.741639285	0.014328591	1.06145E-11

Table 11.24 Fatigue damage for helical cable 1x61-12, smooth flow Iu=0.75%, mode 127, fn=64.8298 Hz, Dmode=1.2592e-06

U_{red}	U, [m/s]	$U_{i,min}$	$U_{i,max}$	C_L	$y_{f,max}$, [m]	Stress range, [N/mm^2]	Probability	D_i
4.95	12.28	12.14	12.46	0.508371647	0.003805714	4.954450215	0.018765411	1.24539E-06
5.10	12.64	12.46	12.71	0.349967097	0.002619884	2.413426672	0.014431688	1.27966E-08
5.15	12.78	12.71	12.92	0.287165776	0.002149748	1.638806897	0.011779144	1.02389E-09
5.26	13.05	12.92	13.17	0.193706532	0.001450104	0.752980913	0.014349913	1.17362E-11

Table 11.25 Fatigue damage for helical cable 1x61-12, smooth flow Iu=0.75%, mode 128, fn=65.3403 Hz, Dmode=2.8636e-06

U_{red}	U, [m/s]	$U_{i,min}$	$U_{i,max}$	C_L	$y_{f,max}$, [m]	Stress range, [N/mm^2]	Probability	D_i
4.95	12.38	12.23	12.56	0.508371647	0.004055391	5.671157393	0.018818978	2.83143E-06
5.10	12.74	12.56	12.81	0.349967097	0.002791764	2.772917859	0.014464175	2.97369E-08
5.15	12.88	12.81	13.02	0.287165776	0.002290784	1.885212429	0.011799853	2.39562E-09
5.26	13.16	13.02	13.28	0.193706532	0.001545239	0.867444495	0.014367857	2.76836E-11

Table 11.26 Fatigue damage for helical cable 1x61-12, turbulent flow Iu=4.5%, mode 165, fn=84.2277 Hz, Dmode=1.1777

U_{red}	U, [m/s]	$U_{i,min}$	$U_{i,max}$	C_L	$y_{f,max}$, [m]	Stress range, [N/mm^2]	Probability	D_i
3.66	11.80	11.72	11.95	1.212268267	0.0097828	39.34071349	0.013568386	0.293248481
3.75	12.09	11.95	12.26	1.2387579	0.010083445	41.12834213	0.018679874	0.527078545
3.86	12.43	12.26	12.67	1.08977834	0.008544521	32.08684716	0.023557141	0.149878398
4.00	12.90	12.67	13.02	0.940408612	0.007011675	23.4684475	0.019972928	0.019453694
4.08	13.14	13.02	13.18	1.195780309	0.009586979	38.18119928	0.008852506	0.159888709
4.10	13.22	13.18	13.39	1.007612334	0.007693263	27.23802656	0.011818945	0.028137578

Table 11.27 Fatigue damage for helical cable 1x61-12, turbulent flow Iu=4.5%, mode 166, fn=84.7382 Hz, Dmode=1.4238

U_{red}	U, [m/s]	$U_{i,min}$	$U_{i,max}$	C_L	$y_{f,max}$, [m]	Stress range, [N/mm^2]	Probability	D_i
3.66	11.87	11.79	12.02	1.212268267	0.009924767	40.54155847	0.013608446	0.354396548
3.75	12.16	12.02	12.34	1.2387579	0.01023161	42.38291207	0.018727095	0.636639385
3.86	12.51	12.34	12.74	1.08977834	0.008666574	33.09695519	0.023603052	0.181959504
4.00	12.98	12.74	13.10	0.940408612	0.007106551	24.22187885	0.019999358	0.023688706
4.08	13.22	13.10	13.26	1.195780309	0.009725312	39.34933842	0.008860398	0.192910635
4.10	13.30	13.26	13.47	1.007612334	0.007799976	28.10468702	0.011825698	0.034180437

Table 11.28 Fatigue damage for helical cable 1x61-12, turbulent flow Iu=4.5%, mode 167, fn=85.2487 Hz, Dmode=1.7171

U_{red}	U, [m/s]	$U_{i,min}$	$U_{i,max}$	C_L	$y_{f,max}$, [m]	Stress range, [N/mm^2]	Probability	D_i
3.66	11.95	11.86	12.09	1.212268267	0.01006784	41.76316175	0.013646879	0.427248239
3.75	12.24	12.09	12.41	1.2387579	0.010381008	43.65939817	0.018771989	0.767120305
3.86	12.58	12.41	12.82	1.08977834	0.008789596	34.12598441	0.023645889	0.220370508
4.00	13.06	12.82	13.18	0.940408612	0.007202056	24.9902019	0.020023068	0.028776364
4.08	13.30	13.18	13.34	1.195780309	0.009864729	40.53789003	0.008867054	0.23218433
4.10	13.38	13.34	13.55	1.007612334	0.007907451	28.98798534	0.011830773	0.041419803

Table 11.29 Fatigue damage for helical cable 1x61-12, turbulent flow Iu=4.5%, mode 168, fn=85.7591 Hz, Dmode=1.8106

U_{red}	U, [m/s]	$U_{i,min}$	$U_{i,max}$	C_L	$y_{f,max}$, [m]	Stress range, [N/mm^2]	Probability	D_i
3.66	12.02	11.93	12.16	1.212268267	0.010059263	42.07620306	0.013683685	0.450714821
3.75	12.31	12.16	12.48	1.2387579	0.010371842	43.98166451	0.018814556	0.808357458
3.86	12.66	12.48	12.90	1.08977834	0.008782448	34.39458891	0.023685654	0.232758545
4.00	13.14	12.90	13.26	0.940408612	0.007197063	25.2034842	0.020044066	0.030495014
4.08	13.38	13.26	13.42	1.195780309	0.009856482	40.84458896	0.008872479	0.244529726
4.10	13.46	13.42	13.63	1.007612334	0.007901558	29.22653183	0.011834179	0.043780562

Table 11.30 Fatigue damage for helical cable 1x61-12, turbulent flow Iu=4.5%, mode 169, fn=86.2696 Hz, Dmode=2.1763

U_{red}	U, [m/s]	$U_{i,min}$	$U_{i,max}$	C_L	$y_{f,max}$, [m]	Stress range, [N/mm^2]	Probability	D_i
3.66	12.09	12.00	12.24	1.212268267	0.010203138	43.32168839	0.01371886	0.541510923
3.75	12.38	12.24	12.56	1.2387579	0.010522138	45.28310237	0.018854793	0.970723961
3.86	12.74	12.56	12.97	1.08977834	0.008906186	35.44573614	0.023722352	0.280930373
4.00	13.21	12.97	13.33	0.940408612	0.007293032	25.98984479	0.02006236	0.036919947
4.08	13.45	13.33	13.50	1.195780309	0.00999669	42.05671443	0.008876677	0.293304965
4.10	13.54	13.50	13.71	1.007612334	0.008009596	30.12968341	0.011835923	0.052872091

Table 11.31 Fatigue damage for helical cable 1x61-24, smooth flow Iu=0.75%, mode 91, fn=47.0197 Hz, Dmode=0.0004173

U_{red}	U, [m/s]	$U_{i,min}$	$U_{i,max}$	C_L	$y_{f,max}$, [m]	Stress range, [N/mm^2]	Probability	D_i
4.75	8.55	8.46	8.64	0.097834018	0.000980143	0.177748764	0.011304962	1.16035E-15
4.85	8.73	8.64	8.85	0.386545793	0.004064651	2.964735501	0.013105073	2.89623E-08
4.99	8.97	8.85	9.03	0.599293639	0.006998685	8.300619787	0.011483824	1.22244E-05
5.06	9.10	9.03	9.25	0.616928841	0.007266426	8.892288759	0.013435497	2.16179E-05
5.23	9.40	9.25	9.55	0.600076214	0.007033462	8.376600429	0.018895774	2.12447E-05
5.39	9.70	9.55	9.84	0.515347702	0.005822225	5.893449426	0.018120529	2.47097E-06
5.55	9.98	9.84	10.10	0.487405853	0.005402198	5.116300739	0.016402576	9.57474E-07
5.68	10.22	10.10	10.35	0.495024459	0.005482724	5.261729679	0.01589695	1.0979E-06
5.83	10.48	10.35	10.64	0.436311883	0.004720355	3.955661102	0.01811677	2.25878E-07
6.01	10.80	10.64	10.93	0.691102206	0.008507465	11.82298823	0.017814621	0.00015835
6.15	11.06	10.93	11.19	0.388699962	0.004198082	3.15600445	0.01583638	5.09284E-08
6.29	11.32	11.19	11.45	0.669569234	0.008137902	10.91958943	0.015853046	8.7464E-05
6.44	11.58	11.45	11.71	0.677245537	0.008274815	11.25138336	0.016128703	0.000106491
6.59	11.85	11.71	12.01	0.536953862	0.006180416	6.591535709	0.017415982	4.64886E-06
6.76	12.16	12.01	12.22	0.466817414	0.005149311	4.670871033	0.012459615	4.21086E-07
6.82	12.27	12.22	12.33	0.303925974	0.003352509	2.037399424	0.006841055	1.59242E-09

Table 11.32 Fatigue damage for helical cable 1x61-24, smooth flow Iu=0.75%, mode 92, fn=47.5364 Hz, Dmode=0.00047562

U_{red}	U, [m/s]	$U_{i,min}$	$U_{i,max}$	C_L	$y_{f,max}$, [m]	Stress range, [N/mm^2]	Probability	D_i
4.75	8.64	8.55	8.74	0.097834018	0.000979963	0.181599962	0.011455055	1.35181E-15
4.85	8.83	8.74	8.95	0.386545793	0.004063695	3.026758647	0.013273716	3.35803E-08
4.99	9.07	8.95	9.13	0.599293639	0.006996372	8.463000614	0.011626797	1.4055E-05
5.06	9.20	9.13	9.35	0.616928841	0.007263953	9.064903327	0.013596958	2.48225E-05
5.23	9.50	9.35	9.65	0.600076214	0.007031079	8.540197826	0.019112014	2.43971E-05
5.39	9.81	9.65	9.95	0.515347702	0.005820434	6.013000676	0.018315675	2.84836E-06
5.55	10.09	9.95	10.21	0.487405853	0.005400653	5.220884634	0.016568601	1.10402E-06
5.68	10.34	10.21	10.47	0.495024459	0.005481182	5.369216604	0.016047954	1.26506E-06
5.83	10.60	10.47	10.76	0.436311883	0.004719112	4.03737466	0.018276628	2.60445E-07
6.01	10.92	10.76	11.05	0.691102206	0.008504134	12.04321714	0.017958711	0.000180283
6.15	11.18	11.05	11.31	0.388699962	0.004196903	3.221613702	0.015953214	5.86832E-08
6.29	11.44	11.31	11.57	0.669569234	0.008134839	11.12569971	0.015959056	9.95855E-05
6.44	11.70	11.57	11.84	0.677245537	0.008271623	11.46266086	0.016224963	0.000121094
6.59	11.98	11.84	12.14	0.536953862	0.006178351	6.724329703	0.017506352	5.32494E-06
6.76	12.29	12.14	12.35	0.466817414	0.005147831	4.766674485	0.01251534	4.83015E-07
6.82	12.41	12.35	12.47	0.303925974	0.003351545	2.080225857	0.006868401	1.83123E-09

Table 11.33 Fatigue damage for helical cable 1x61-24, smooth flow Iu=0.75%, mode 93, fn=48.0531 Hz, Dmode=0.00064711

U_{red}	U, [m/s]	$U_{i,min}$	$U_{i,max}$	C_L	$y_{f,max}$, [m]	Stress range, [N/mm^2]	Probability	D_i
4.75	8.74	8.64	8.83	0.097834018	0.000991446	0.189925931	0.0116033	1.81137E-15
4.85	8.92	8.83	9.05	0.386545793	0.004119198	3.1729331	0.01344002	4.56127E-08
4.99	9.17	9.05	9.23	0.599293639	0.007104877	8.879155766	0.011767549	1.91795E-05
5.06	9.30	9.23	9.45	0.616928841	0.007377905	9.511127645	0.013755619	3.38682E-05
5.23	9.61	9.45	9.76	0.600076214	0.007141185	8.962271883	0.019323948	3.33062E-05
5.39	9.91	9.76	10.05	0.515347702	0.00590829	6.311284931	0.018506294	3.88997E-06
5.55	10.19	10.05	10.32	0.487405853	0.005479987	5.477816609	0.016730197	1.50337E-06
5.68	10.45	10.32	10.58	0.495024459	0.005561201	5.632097843	0.01619437	1.71912E-06
5.83	10.71	10.58	10.88	0.436311883	0.004786346	4.23497358	0.018430906	3.53648E-07
6.01	11.04	10.88	11.17	0.691102206	0.008645003	12.63920048	0.018096959	0.000245382
6.15	11.30	11.17	11.43	0.388699962	0.004258029	3.382700555	0.016064565	8.00517E-08
6.29	11.57	11.43	11.70	0.669569234	0.008267533	11.67570484	0.016059313	0.000135315
6.44	11.83	11.70	11.97	0.677245537	0.008407892	12.03100325	0.016315105	0.000164559
6.59	12.11	11.97	12.27	0.536953862	0.006274557	7.061755562	0.017589828	7.25534E-06
6.76	12.43	12.27	12.48	0.466817414	0.005223569	5.002559022	0.012565955	6.55042E-07
6.82	12.54	12.48	12.60	0.303925974	0.003400855	2.186167454	0.00689288	2.50277E-09

Table 11.34 Fatigue damage for helical cable 1x61-24, smooth flow Iu=0.75%, mode 94, fn=48.5698 Hz, Dmode=0.00087669

U_{red}	U, [m/s]	$U_{i,min}$	$U_{i,max}$	C_L	$y_{f,max}$, [m]	Stress range, [N/mm^2]	Probability	D_i
4.75	8.83	8.74	8.92	0.097834018	0.001002922	0.198531251	0.011749633	2.41859E-15
4.85	9.02	8.92	9.14	0.386545793	0.004174883	3.324299123	0.013603913	6.17205E-08
4.99	9.27	9.14	9.33	0.599293639	0.007214198	9.310032465	0.011906016	2.60639E-05
5.06	9.40	9.33	9.55	0.616928841	0.007492772	9.973145641	0.013911407	4.60181E-05
5.23	9.71	9.55	9.86	0.600076214	0.007252184	9.399478013	0.019531479	4.52817E-05
5.39	10.02	9.86	10.16	0.515347702	0.005996768	6.620563923	0.018692297	5.29173E-06
5.55	10.30	10.16	10.43	0.487405853	0.005559803	5.744110737	0.016887288	2.03921E-06
5.68	10.56	10.43	10.69	0.495024459	0.005641673	5.904431581	0.016336128	2.32693E-06
5.83	10.83	10.69	10.99	0.436311883	0.004853912	4.439741582	0.018579535	4.7835E-07
6.01	11.16	10.99	11.29	0.691102206	0.008787277	13.25619075	0.018229306	0.000332543
6.15	11.42	11.29	11.56	0.388699962	0.004319547	3.549971666	0.01617039	1.08802E-07
6.29	11.69	11.56	11.83	0.669569234	0.008401483	12.24514822	0.016153781	0.000183073
6.44	11.96	11.83	12.10	0.677245537	0.008545525	12.61957865	0.016399105	0.000222666
6.59	12.24	12.10	12.40	0.536953862	0.006371577	7.411893449	0.017666394	9.84664E-06
6.76	12.56	12.40	12.62	0.466817414	0.005299792	5.247190776	0.01261146	8.84895E-07
6.82	12.68	12.62	12.74	0.303925974	0.003450481	2.296322965	0.006914497	3.40819E-09

Table 11.35 Fatigue damage for helical cable 1x61-24, smooth flow Iu=0.75%, mode 95, fn=49.0865 Hz, Dmode=0.0011827

U_{red}	U, [m/s]	$U_{i,min}$	$U_{i,max}$	C_L	$y_{f,max}$, [m]	Stress range, [N/mm^2]	Probability	D_i
4.75	8.92	8.83	9.02	0.097834018	0.001014392	0.207422326	0.011893991	3.21826E-15
4.85	9.12	9.02	9.24	0.386545793	0.004230751	3.480967462	0.013765323	8.32045E-08
4.99	9.36	9.24	9.43	0.599293639	0.007324346	9.755898367	0.012042138	3.52751E-05
5.06	9.50	9.43	9.66	0.616928841	0.007608568	10.45124524	0.014064251	6.2271E-05
5.23	9.81	9.66	9.97	0.600076214	0.007364092	9.852106057	0.019734511	6.13143E-05
5.39	10.13	9.97	10.27	0.515347702	0.006085877	6.941081696	0.018873598	7.17098E-06
5.55	10.41	10.27	10.54	0.487405853	0.005640106	6.019971305	0.017039801	2.75545E-06
5.68	10.67	10.54	10.81	0.495024459	0.005722605	6.186414899	0.016473165	3.13742E-06
5.83	10.94	10.81	11.11	0.436311883	0.004921812	4.651837481	0.01872245	6.44571E-07
6.01	11.28	11.11	11.41	0.691102206	0.008930979	13.8945508	0.018355697	0.000448744
6.15	11.54	11.41	11.68	0.388699962	0.004381464	3.723591598	0.016270648	1.47346E-07
6.29	11.82	11.68	11.95	0.669569234	0.008536708	12.83437829	0.016242431	0.000246638
6.44	12.09	11.95	12.23	0.677245537	0.008684547	13.22876018	0.016476941	0.000300021
6.59	12.37	12.23	12.53	0.536953862	0.006469428	7.775055647	0.017736045	1.33119E-05
6.76	12.69	12.53	12.75	0.466817414	0.005376508	5.500775819	0.012651859	1.19085E-06
6.82	12.81	12.75	12.87	0.303925974	0.003500427	2.410818281	0.006933258	4.62472E-09

Table 11.36 Fatigue damage for helical cable 1x61-24, turbulent flow Iu=4.5%, mode 146, fn=75.4381 Hz, Dmode=38.1556

U_{red}	U, [m/s]	$U_{i,min}$	$U_{i,max}$	C_L	$y_{f,max}$, [m]	Stress range, [N/mm^2]	Probability	D_i
3.52	10.16	10.12	10.45	1.397644741	0.016526896	68.52582138	0.020633715	11.15560188
3.72	10.73	10.45	11.06	1.20274962	0.013241522	50.92199577	0.038403449	3.496172117
3.95	11.40	11.06	11.49	0.962440487	0.009388402	30.72229325	0.025908169	0.113749262
4.01	11.58	11.49	11.72	0.883668503	0.008060284	24.12606506	0.013872093	0.014284039
4.11	11.86	11.72	11.90	1.432449791	0.017460698	73.51794652	0.010729756	8.845861111
4.14	11.93	11.90	12.09	1.462321051	0.018242412	77.68484717	0.011378374	13.05834568
4.24	12.24	12.09	12.59	1.073021668	0.011491524	41.63414867	0.029404897	0.799664609
4.48	12.94	12.59	13.07	1.113811882	0.011363046	40.95631489	0.027266625	0.67196509
4.57	13.20	13.07	13.37	0.306073814	0.003122548	4.432767139	0.016846463	6.67342E-07

Table 11.37 Fatigue damage for helical cable 1x61-24, turbulent flow Iu=4.5%, mode 147, fn=75.9548 Hz, Dmode=45.8585

U_{red}	U, [m/s]	$U_{i,min}$	$U_{i,max}$	C_L	$y_{f,max}$, [m]	Stress range, [N/mm^2]	Probability	D_i
3.52	10.23	10.19	10.52	1.397644741	0.01677861	70.48749907	0.02075486	13.38279968
3.72	10.80	10.52	11.14	1.20274962	0.013435099	52.44902631	0.038600467	4.224464846
3.95	11.48	11.14	11.57	0.962440487	0.009509265	31.6680449	0.026019051	0.137966462
4.01	11.66	11.57	11.80	0.883668503	0.008152911	24.84769019	0.01392379	0.017227735
4.11	11.94	11.80	11.98	1.432449791	0.017740176	75.65694523	0.010765946	10.61450086
4.14	12.02	11.98	12.17	1.462321051	0.018545827	79.97372296	0.011413043	15.69783941
4.24	12.33	12.17	12.68	1.073021668	0.011662906	42.96300384	0.029476139	0.974525006
4.48	13.03	12.68	13.16	1.113811882	0.011517004	42.18559121	0.027307794	0.809144369
4.57	13.29	13.16	13.46	0.306073814	0.003164855	4.607614965	0.016859212	8.48104E-07

Table 11.38 Fatigue damage for helical cable 1x61-24, turbulent flow Iu=4.5%, mode 148, fn=76.4715 Hz, Dmode=55.0012

U_{red}	U, [m/s]	$U_{i,min}$	$U_{i,max}$	C_L	$y_{f,max}$, [m]	Stress range, [N/mm^2]	Probability	D_i
3.52	10.30	10.25	10.59	1.397644741	0.017033685	72.48368737	0.020873673	16.02283986
3.72	10.88	10.59	11.22	1.20274962	0.013631344	54.00628143	0.038792649	5.094646129
3.95	11.56	11.22	11.65	0.962440487	0.009631544	32.63407357	0.026126317	0.167033993
4.01	11.73	11.65	11.88	0.883668503	0.008246324	25.58381601	0.01397344	0.020739306
4.11	12.02	11.88	12.06	1.432449791	0.018023867	77.83571375	0.010800501	12.71207104
4.14	12.10	12.06	12.25	1.462321051	0.018854267	82.30733312	0.011445929	18.83567425
4.24	12.41	12.25	12.76	1.073021668	0.011837036	44.32305678	0.029542556	1.185564636
4.48	13.12	12.76	13.25	1.113811882	0.011673076	43.44095299	0.027344229	0.972659164
4.57	13.38	13.25	13.56	0.306073814	0.003207744	4.78862999	0.016868926	1.0766E-06

Table 11.39 Fatigue damage for helical cable 1x61-24, turbulent flow Iu=4.5%, mode 149, fn=76.9882 Hz, Dmode=65.8664

U_{red}	U, [m/s]	$U_{i,min}$	$U_{i,max}$	C_L	$y_{f,max}$, [m]	Stress range, [N/mm^2]	Probability	D_i
3.52	10.37	10.32	10.66	1.397644741	0.017292118	74.51444472	0.020990133	19.14615222
3.72	10.95	10.66	11.29	1.20274962	0.013830277	55.5939669	0.038979959	6.132405469
3.95	11.63	11.29	11.72	0.962440487	0.009755259	33.62064604	0.026229951	0.201863271
4.01	11.81	11.72	11.96	0.883668503	0.008340534	26.33462188	0.014021036	0.024921037
4.11	12.10	11.96	12.14	1.432449791	0.018311768	80.05437024	0.010833417	15.19494801
4.14	12.18	12.14	12.34	1.462321051	0.019167728	84.68591947	0.011477031	22.55902332
4.24	12.49	12.34	12.85	1.073021668	0.012013945	45.71476517	0.029604152	1.439842782
4.48	13.21	12.85	13.34	1.113811882	0.011831302	44.7228357	0.027375945	1.167262696
4.57	13.47	13.34	13.65	0.306073814	0.003251224	4.976014406	0.016875619	1.36513E-06

Table 11.40 Fatigue damage for helical cable 1x61-24, turbulent flow Iu=4.5%, mode 150, fn=77.5049 Hz, Dmode=78.7053

U_{red}	U, [m/s]	$U_{i,min}$	$U_{i,max}$	C_L	$y_{f,max}$, [m]	Stress range, [N/mm^2]	Probability	D_i
3.52	10.44	10.39	10.73	1.397644741	0.017553902	76.57793011	0.021104219	22.83071445
3.72	11.02	10.73	11.37	1.20274962	0.01403191	57.21076911	0.039162368	7.366550114
3.95	11.71	11.37	11.80	0.962440487	0.00988043	34.62701167	0.02632994	0.243482879
4.01	11.89	11.80	12.04	0.883668503	0.008435556	27.0994562	0.014066573	0.029886857
4.11	12.18	12.04	12.22	1.432449791	0.018603866	82.31104502	0.010864691	18.12569122
4.14	12.26	12.22	12.42	1.462321051	0.019486182	87.10768189	0.011506348	26.96526586
4.24	12.58	12.42	12.94	1.073021668	0.012193653	47.13727298	0.029660931	1.745420165
4.48	13.29	12.94	13.43	1.113811882	0.011991713	46.03040572	0.027402959	1.398281993
4.57	13.56	13.43	13.74	0.306073814	0.003295305	5.169786284	0.016879308	1.7287E-06

Table 11.41 Fatigue damage for helical cable 1x91-12, smooth flow Iu=0.75%, mode 108, fn=55.1634 Hz, Dmode=1.2378e-05

U_{red}	U, [m/s]	$U_{i,min}$	$U_{i,max}$	C_L	$y_{f,max}$, [m]	Stress range, [N/mm^2]	Probability	D_i
4.79	10.10	9.94	10.25	0.169301837	0.00174335	0.786751365	0.019314298	1.74886E-11
4.93	10.40	10.25	10.58	0.320140075	0.003296575	2.753233878	0.02087767	3.47209E-08
5.10	10.77	10.58	10.92	0.368920123	0.003798878	3.621884733	0.020893452	1.80081E-07
5.25	11.08	10.92	11.23	0.453351597	0.005081108	6.296502372	0.018807336	4.4748E-06
5.39	11.38	11.23	11.52	0.427297696	0.004741446	5.527815463	0.018084981	1.97011E-06
5.53	11.67	11.52	11.84	0.36605005	0.003957923	3.918904486	0.01940343	2.68359E-07
5.70	12.02	11.84	12.18	0.318365074	0.003442328	2.99421893	0.020132981	5.53936E-08
5.85	12.35	12.18	12.49	0.457021637	0.005127493	6.404642608	0.018080904	4.76474E-06
6.10	12.87	12.76	12.96	0.390035313	0.004264748	4.520661083	0.011498488	3.74716E-07
6.18	13.04	12.96	13.20	0.366170042	0.003951037	3.90583313	0.013392069	1.81543E-07
6.33	13.35	13.20	13.41	0.342604409	0.00369676	3.43666495	0.011640376	7.32218E-08

Table 11.42 Fatigue damage for helical cable 1x91-12, smooth flow Iu=0.75%, mode 109, fn=55.6742 Hz, Dmode=1.6325e-05

U_{red}	U, [m/s]	$U_{i,min}$	$U_{i,max}$	C_L	$y_{f,max}$, [m]	Stress range, [N/mm^2]	Probability	D_i
4.79	10.19	10.03	10.34	0.169301837	0.001763005	0.819267424	0.019474407	2.26919E-11
4.93	10.50	10.34	10.68	0.320140075	0.003333742	2.864577488	0.021036897	4.47917E-08
5.10	10.87	10.68	11.02	0.368920123	0.004025288	4.119912808	0.021037877	3.96445E-07
5.25	11.18	11.02	11.33	0.453351597	0.005146515	6.5613995	0.018924095	5.81898E-06
5.39	11.48	11.33	11.63	0.427297696	0.004805256	5.768425652	0.018184981	2.58172E-06
5.53	11.78	11.63	11.95	0.36605005	0.004010257	4.090498124	0.019496834	3.51944E-07
5.70	12.13	11.95	12.30	0.318365074	0.003487845	3.126616308	0.020214092	7.27704E-08
5.85	12.46	12.30	12.61	0.457021637	0.005197872	6.684313432	0.018139456	6.23473E-06
6.10	12.99	12.87	13.08	0.390035313	0.00432194	4.719033129	0.011520653	4.90284E-07
6.18	13.17	13.08	13.32	0.366170042	0.004003147	4.076615975	0.013410222	2.37185E-07
6.33	13.48	13.32	13.53	0.342604409	0.003745516	3.587680401	0.011649254	9.57268E-08

Table 11.43 Fatigue damage for helical cable 1x91-12, smooth flow Iu=0.75%, mode 110, fn=56.1849 Hz, Dmode=2.1323e-05

U_{red}	U, [m/s]	$U_{i,min}$	$U_{i,max}$	C_L	$y_{f,max}$, [m]	Stress range, [N/mm^2]	Probability	D_i
4.79	10.28	10.13	10.44	0.169301837	0.001782648	0.852749587	0.019630698	2.93551E-11
4.93	10.59	10.44	10.78	0.320140075	0.003370884	2.979040561	0.021191655	5.76026E-08
5.10	10.97	10.78	11.12	0.368920123	0.004077401	4.296995239	0.021177483	5.18421E-07
5.25	11.28	11.12	11.43	0.453351597	0.005216329	6.844380891	0.019036227	7.61036E-06
5.39	11.59	11.43	11.74	0.427297696	0.004869992	6.01810618	0.01828028	3.37723E-06
5.53	11.88	11.74	12.06	0.36605005	0.004062855	4.267734672	0.01958493	4.60178E-07
5.70	12.24	12.06	12.41	0.318365074	0.003533591	3.263475155	0.02028942	9.5317E-08
5.85	12.57	12.41	12.72	0.457021637	0.005268563	6.972698683	0.018192587	8.13053E-06
6.10	13.11	12.99	13.20	0.390035313	0.004379355	4.923736193	0.011539163	6.39384E-07
6.18	13.29	13.20	13.44	0.366170042	0.004055432	4.252837894	0.013424027	3.08869E-07
6.33	13.60	13.44	13.66	0.342604409	0.003794437	3.743563687	0.011654277	1.24743E-07

Table 11.44 Fatigue damage for helical cable 1x91-12, smooth flow Iu=0.75%, mode 111, fn=56.6957 Hz, Dmode=2.7739e-05

U_{red}	U, [m/s]	$U_{i,min}$	$U_{i,max}$	C_L	$y_{f,max}$, [m]	Stress range, [N/mm^2]	Probability	D_i
4.79	10.38	10.22	10.53	0.169301837	0.001802278	0.887216808	0.019783117	3.78637E-11
4.93	10.69	10.53	10.88	0.320140075	0.003408004	3.096667407	0.021341893	7.38499E-08
5.10	11.07	10.88	11.22	0.368920123	0.004129665	4.47955886	0.021312224	6.75756E-07
5.25	11.38	11.22	11.54	0.453351597	0.005286444	7.136037537	0.019143698	9.92014E-06
5.39	11.69	11.54	11.84	0.427297696	0.004935	6.275550022	0.018370854	4.40341E-06
5.53	11.99	11.84	12.17	0.36605005	0.004115639	4.450567223	0.019667702	5.99784E-07
5.70	12.36	12.17	12.52	0.318365074	0.003579499	3.404769293	0.020358959	1.2446E-07
5.85	12.69	12.52	12.84	0.457021637	0.005339565	7.269929614	0.018240303	1.05673E-05
6.10	13.23	13.11	13.32	0.390035313	0.004436992	5.134883314	0.011554034	8.31125E-07
6.18	13.41	13.32	13.56	0.366170042	0.004107895	4.43459638	0.01343351	4.00925E-07
6.33	13.72	13.56	13.78	0.342604409	0.003799712	3.819411467	0.011655478	1.4199E-07

Table 11.45 Fatigue damage for helical cable 1x91-12, smooth flow Iu=0.75%, mode 112, fn=57.2065 Hz, Dmode=3.095e-05

U_{red}	U, [m/s]	$U_{i,min}$	$U_{i,max}$	C_L	$y_{f,max}$, [m]	Stress range, [N/mm^2]	Probability	D_i
4.79	10.47	10.31	10.63	0.169301837	0.001801875	0.902717171	0.019931615	4.27068E-11
4.93	10.79	10.63	10.98	0.320140075	0.003407242	3.149499429	0.021487561	8.30387E-08
5.10	11.17	10.98	11.33	0.368920123	0.004128474	4.554344286	0.021442061	7.57646E-07
5.25	11.49	11.33	11.64	0.453351597	0.005284702	7.251593939	0.01924648	1.10814E-05
5.39	11.80	11.64	11.95	0.427297696	0.004933406	6.378074424	0.018456683	4.91966E-06
5.53	12.10	11.95	12.28	0.36605005	0.004114408	4.524801081	0.019745139	6.70968E-07
5.70	12.47	12.28	12.63	0.318365074	0.003578429	3.462169505	0.020422708	1.39267E-07
5.85	12.80	12.63	12.96	0.457021637	0.005337794	7.387472276	0.018282615	1.17668E-05
6.10	13.35	13.23	13.44	0.390035313	0.004435615	5.219835422	0.011565287	9.26279E-07
6.18	13.53	13.44	13.69	0.366170042	0.004106682	4.508607032	0.013438704	4.46947E-07
6.33	13.85	13.69	13.91	0.342604409	0.003798633	3.883640025	0.011652889	1.58311E-07

Table 11.46 Fatigue damage for helical cable 1x91-12, turbulent flow Iu=4.5%, mode 160, fn=81.7236 Hz, Dmode=0.049937

U_{red}	U, [m/s]	$U_{i,min}$	$U_{i,max}$	C_L	$y_{f,max}$, [m]	Stress range, [N/mm^2]	Probability	D_i
3.95	12.35	12.30	12.40	0.997569498	0.007452701	24.65275242	0.005636846	0.007157725
3.98	12.44	12.40	12.56	0.960927541	0.007125386	22.919592	0.009830732	0.008060713
4.06	12.69	12.56	12.78	0.88071255	0.006388075	19.12684291	0.012244523	0.003391157
4.12	12.87	12.78	13.01	0.793768449	0.005607374	15.31557768	0.013070624	0.000954208
4.21	13.15	13.01	13.21	0.696943622	0.004784518	11.58671836	0.011134318	0.000152396
4.24	13.27	13.21	13.40	1.056620029	0.008060495	27.93811946	0.010844089	0.029169059
4.33	13.54	13.40	13.56	0.822761583	0.005916234	16.79499142	0.008287269	0.00105205

Table 11.47 Fatigue damage for helical cable 1x91-12, turbulent flow Iu=4.5%, mode 161, fn=82.2343 Hz, Dmode=0.05309

U_{red}	U, [m/s]	$U_{i,min}$	$U_{i,max}$	C_L	$y_{f,max}$, [m]	Stress range, [N/mm^2]	Probability	D_i
3.95	12.42	12.38	12.47	0.997569498	0.007448214	24.87708719	0.005649272	0.007621525
3.98	12.52	12.47	12.64	0.960927541	0.007121125	23.1308815	0.009850216	0.008587191
4.06	12.76	12.64	12.86	0.88071255	0.006384478	19.30931826	0.012264822	0.003618388
4.12	12.95	12.86	13.09	0.793768449	0.005604475	15.46740409	0.0130873	0.001020016
4.21	13.23	13.09	13.29	0.696943622	0.004782274	11.70627898	0.011144334	0.000163237
4.24	13.35	13.29	13.49	1.056620029	0.00805526	28.1846623	0.010850031	0.030957098
4.33	13.62	13.49	13.64	0.822761583	0.005912915	16.95822639	0.008289208	0.001122142

Table 11.48 Fatigue damage for helical cable 1x91-12, turbulent flow Iu=4.5%, mode 162, fn=82.7451 Hz, Dmode=0.06514

U_{red}	U, [m/s]	$U_{i,min}$	$U_{i,max}$	C_L	$y_{f,max}$, [m]	Stress range, [N/mm^2]	Probability	D_i
3.95	12.50	12.45	12.55	0.997569498	0.007554903	25.70630342	0.005660927	0.009355493
3.98	12.60	12.55	12.72	0.960927541	0.007222981	23.91074788	0.009868334	0.010561951
4.06	12.84	12.72	12.94	0.88071255	0.006473946	19.96972115	0.012283381	0.004461607
4.12	13.03	12.94	13.17	0.793768449	0.005680758	16.00206544	0.013102072	0.001259904
4.21	13.31	13.17	13.37	0.696943622	0.004845271	12.11497144	0.011152696	0.000201955
4.24	13.43	13.37	13.57	1.056620029	0.008173832	29.12096756	0.010854334	0.037912232
4.33	13.71	13.57	13.72	0.822761583	0.005995642	17.54845753	0.008289876	0.00138651

Table 11.49 Fatigue damage for helical cable 1x91-12, turbulent flow Iu=4.5%, mode 163, fn=83.2559 Hz, Dmode=0.069145

U_{red}	U, [m/s]	$U_{i,min}$	$U_{i,max}$	C_L	$y_{f,max}$, [m]	Stress range, [N/mm^2]	Probability	D_i
3.95	12.58	12.53	12.63	0.997569498	0.007550248	25.93513958	0.00567181	0.009946429
3.98	12.68	12.63	12.80	0.960927541	0.007218559	24.12641351	0.009885086	0.011234429
4.06	12.92	12.80	13.02	0.88071255	0.006470216	20.15628442	0.012300202	0.004753233
4.12	13.11	13.02	13.25	0.793768449	0.005677757	16.15758662	0.013114948	0.001344744
4.21	13.39	13.25	13.45	0.696943622	0.004842951	12.23769028	0.01115941	0.000215999
4.24	13.52	13.45	13.65	1.056620029	0.008168391	29.37214686	0.010857005	0.04017336
4.33	13.79	13.65	13.81	0.822761583	0.005992198	17.71553178	0.008289282	0.001476577

Table 11.50 Fatigue damage for helical cable 1x91-12, turbulent flow Iu=4.5%, mode 164, fn=83.7666 Hz, Dmode=0.084524

U_{red}	U, [m/s]	$U_{i,min}$	$U_{i,max}$	C_L	$y_{f,max}$, [m]	Stress range, [N/mm^2]	Probability	D_i
3.95	12.66	12.61	12.70	0.997569498	0.007657405	26.78454769	0.005681924	0.012163863
3.98	12.75	12.70	12.88	0.960927541	0.007320882	24.92595141	0.009900474	0.013766916
4.06	13.00	12.88	13.10	0.88071255	0.006560066	20.83425108	0.012315291	0.005839588
4.12	13.19	13.10	13.33	0.793768449	0.005754316	16.70718344	0.013125933	0.001655083
4.21	13.47	13.33	13.54	0.696943622	0.004906127	12.65839849	0.011164483	0.000266306
4.24	13.60	13.54	13.74	1.056620029	0.008287577	30.33080507	0.010858054	0.04901464
4.33	13.88	13.74	13.89	0.822761583	0.006075287	18.32224106	0.008287432	0.001817865

12. Appendix C: Matlab code for Comsol Multyphisics

```
function [Stresses, StressMax, StressMin, Forces, ForceMax, ForceMin] = COMSOL_cable_routine(cable_length,n_el,Young_E,Poiss_nu,Dens_ro,Area_cab,IntStrs,load_vctr)
np=n_el+1;% number of points
step=cable_length/n_el;
xcoord=char( ['range,(',num2str(0),',',num2str(step),',',num2str(cable_length),')']);
ycoord=char( ['range,(',num2str(0),',',num2str(step),',',num2str(0),')']);
import com.comsol.model.*
import com.comsol.model.util.*

%% Create model in matlab
model = ModelUtil.create('Model');
ModelUtil.setServerBusyHandler(ServerBusyHandler(2));
model.modelPath('D:\EXPERIMENT GACR\MATLAB');
model.comments(['Untitled\n\n']);
model.modelNode.create('comp1');

%% Create Geometry
model.geom.create('geom1', 2);
model.mesh.create('mesh1', 'geom1');
model.physics.create('truss', 'Truss', 'geom1');
model.study.create('std1');
model.study('std1').create('stat', 'Stationary');
model.study('std1').feature('stat').activate('truss', true);
model.geom('geom1').create('pol1', 'Polygon');

% coordinates from range
model.geom('geom1').feature('pol1').set('source', 'table');
for n=1:np
model.geom('geom1').feature('pol1').setIndex('table', num2str((n-1)*step), (n-1), 0);
model.geom('geom1').feature('pol1').setIndex('table', '0', (n-1), 1);
end
model.geom('geom1').feature('pol1').set('type', 'open');
model.geom('geom1').run('pol1');
model.geom('geom1').run;

%% Material Properties
model.material.create('mat1', 'Common', 'comp1');
model.material('mat1').propertyGroup('def').set('youngsmodulus', {char([num2str(Young_E),'*(1-0.9999*(truss.en<0))'])});
```

```
model.material('mat1').propertyGroup('def').set('poissonsratio', {num2str(Poiss_nu)});
model.material('mat1').propertyGroup('def').set('density', {num2str(Dens_ro)});


%% Cross section, bearing and initial values
model.physics('truss').feature('csd1').set('area', {num2str(Area_cab)});
model.physics('truss').feature.create('pin1', 'Pinned', 0);
model.physics('truss').feature('pin1').selection.set([1 n_el+1]);
model.physics('truss').feature('sec1').active(false);
model.physics('truss').feature('emm1').feature.create('iss1', 'InitialStressandStrain', 1);
model.physics('truss').feature('emm1').feature('iss1').set('sni', {num2str(IntStrs)});

%% FEM features
model.mesh('mesh1').create('edg1', 'Edge');
model.mesh('mesh1').feature('edg1').selection.all;
model.mesh('mesh1').run('edg1');
model.study('std1').feature('stat').set('geometricNonlinearity', 'on');

%% Loads correponds to load from matlab
for n=1:np
loadname=char(['pl',num2str(n)]);
loadval={'0',num2str(load_vctr(n)),'0'};
model.physics('truss').feature.create(loadname, 'PointLoad', 0);
model.physics('truss').feature(loadname).selection.set([n]);
model.physics('truss').feature(loadname).set('Fp', loadval);
end

%% Solver
model.sol.create('sol1');
model.sol('sol1').study('std1');
model.study('std1').feature('stat').set('notlistsolnum', 1);
model.study('std1').feature('stat').set('notsolnum', '1');
model.study('std1').feature('stat').set('listsolnum', 1);
model.study('std1').feature('stat').set('solnum', '1');
model.sol('sol1').create('st1', 'StudyStep');
model.sol('sol1').feature('st1').set('study', 'std1');
model.sol('sol1').feature('st1').set('studystep', 'stat');
model.sol('sol1').create('v1', 'Variables');
model.sol('sol1').feature('v1').set('control', 'stat');
model.sol('sol1').create('s1', 'Stationary');
model.sol('sol1').feature('s1').create('fc1', 'FullyCoupled');
```

```
model.sol('sol1').feature('s1').feature('fc1').set('linsolver', 'dDef');
model.sol('sol1').feature('s1').feature.remove('fcDef');
model.sol('sol1').attach('std1');
model.result.create('pg1', 'PlotGroup2D');
model.result('pg1').label('Force (truss)');
model.result('pg1').set('oldanalysistype', 'noneavailable');
model.result('pg1').set('data', 'dset1');
model.result('pg1').feature.create('line1', 'Line');
model.result('pg1').feature('line1').set('oldanalysistype', 'noneavailable');
model.result('pg1').feature('line1').set('expr', 'truss.Nxl');
model.result('pg1').feature('line1').set('const', {'truss.refpntx' '0' 'Reference point for moment computation, x component'; 'truss.refpnty' '0' 'Reference point for moment computation, y component'; 'truss.refpntz' '0' 'Reference point for moment computation, z component'});
model.result('pg1').feature('line1').set('linetype', 'tube');
model.result('pg1').feature('line1').set('radiusexpr', 'sqrt(truss.area/pi)');
model.result('pg1').feature('line1').set('resolution', 'extrafine');
model.result('pg1').feature('line1').set('const', {'truss.refpntx' '0' 'Reference point for moment computation, x component'; 'truss.refpnty' '0' 'Reference point for moment computation, y component'; 'truss.refpntz' '0' 'Reference point for moment computation, z component'});
model.result('pg1').feature('line1').set('data', 'parent');
model.result('pg1').feature('line1').feature.create('def1', 'Deform');
model.result.create('pg2', 'PlotGroup2D');
model.result('pg2').label('Stress (truss)');
model.result('pg2').set('oldanalysistype', 'noneavailable');
model.result('pg2').set('data', 'dset1');
model.result('pg2').feature.create('line1', 'Line');
model.result('pg2').feature('line1').set('oldanalysistype', 'noneavailable');
model.result('pg2').feature('line1').set('expr', 'truss.sn');
model.result('pg2').feature('line1').set('const', {'truss.refpntx' '0' 'Reference point for moment computation, x component'; 'truss.refpnty' '0' 'Reference point for moment computation, y component'; 'truss.refpntz' '0' 'Reference point for moment computation, z component'});
model.result('pg2').feature('line1').set('linetype', 'tube');
model.result('pg2').feature('line1').set('radiusexpr', 'sqrt(truss.area/pi)');
model.result('pg2').feature('line1').set('resolution', 'extrafine');
model.result('pg2').feature('line1').set('const', {'truss.refpntx' '0' 'Reference point for moment computation, x component'; 'truss.refpnty' '0' 'Reference point for moment computation, y component'; 'truss.refpntz' '0' 'Reference point for moment computation, z component'});
model.result('pg2').feature('line1').set('data', 'parent');
model.result('pg2').feature('line1').feature.create('def1', 'Deform');
model.sol('sol1').runAll;
model.result('pg1').run;

%% Results
Stresses=mphevalpoint(model,'truss.sn','selection',[1:np]);
StressMin=mphmin(model,'truss.sn','line');
```

```
StressMax=mphmax(model,'truss.sn','line');
Forces=mphevalpoint(model,'truss.Nxl','selection',[1:np]);
ForceMin=mphmin(model,'truss.Nxl','line');
ForceMax=mphmax(model,'truss.Nxl','line');
ModelUtil.remove('Model');
end
```